SYNTHESIS OF BIO-FUNCTIONAL NANOMATERIALS IN REACTIVE PLASMA DISCHARGES

Miguel Santos

A thesis submitted in fulfilment of the requirements for the degree of *Doctor of Philosophy*

Sydney Medical School

University of Sydney

February 2018

DECLARATION

I declare that the work described in this thesis is entirely my own except where otherwise stated in the text. This work has not been previously submitted for any degree at any institution.

Miguel Santos

ABSTRACT

Plasma processing technologies have been extensively used as surface modification platforms in many biomedical applications. Particularly, plasma polymerization (PP) is a versatile deposition technology which has the potential to deliver biocompatible interfaces for a myriad of medical devices. To successfully translate new materials for specific clinical applications, the plasma process needs to be scalable and incorporate appropriate control feedback strategies. Comprehensive process parameterization is an essential first step towards identifying optimal deposition windows, which will vary depending on the required interface specifications. However, the plasma medium in PP is exceptionally complex and identifying the main physical quantities that allow a suitable formulation and description of the interface growth mechanisms is challenging.

The first part of the thesis reports the design and optimization of a single step ion assisted PP process to create plasma-activated coatings (PAC) that meet the extreme mechanical demands for cardiovascular implants and in particular stents. An ideal working window in the parameter space is identified, and found suitable for the synthesis of PAC interfaces that are mechanically robust, hemocompatibility and allow one step covalent protein immobilization without the need for chemical processes. This window is identified by combining plasma optical emission spectroscopy (OES) with a comprehensive macroscopic process description that isolates key coating growth mechanisms. To further narrow the working conditions best suited for stent applications the best surfaces were screened for covalent protein binding and compatibility with platelet rich plasma and whole human blood. During process scalability, OES diagnostics revealed the formation of plasma polymer nanoparticles (nanoP^3), usually known as plasma dust, in parallel with the deposition of PAC coatings. Plasma dust is usually regarded as a contaminant in

plasma-based manufacturing industries. However, as both PAC coatings and nanoP^3 are synthesized in parallel inside the plasma reactor, it is first hypothesized that both are constituted from the same material, and therefore share similar physical-chemical properties, suggesting that nanoP^3 may also be capable of the spontaneous immobilization of bioactive molecules on its surface.

The second part of the thesis reports the demonstration of carbonaceous plasma nanoparticles for nanomedicine applications. By controlling nanoparticle formation and collection, nanoP^3 were engineered with unique immobilization capabilities facilitating multifunctional nanocarriers. The unique surface chemistry of nanoP^3, allowing a robust immobilization of the cargo without the need for intermediate functionalization strategies, has great potential to overcome major limitations of currently proposed platforms. Since unpaired electrons and surface functionalities are preserved and crosslinked on the nanoP^3 during their formation, the PP process provides a cost and time effective synthesis route for multifunctional nanocarriers with a long shelf-life. The universal binding surface of nanoP^3 paves the way for the design of personalized nanocarriers, allowing theranostic agents to be fabricated in a one-step incubation and according to specific treatment requirements. As many of the favorable characteristics of nanoP^3 are inherent to the fabrication process, this work proposes PP as a nanoparticle synthesis route with valuable potential for broad clinical and commercial applications.

ACKNOWLEDGEMENTS

First and foremost, I would like to thank my supervisor Dr. Steven Wise for his guidance and support. For welcoming a lost theoretical plasma physicist into the unknown realms of cardiovascular research and bioengineering. For giving me the freedom to pursue and explore the research endeavors that absorbed me the most but importantly, for always being there when those endeavors did not go as planned. Without his encouragement and mentorship, I could not have finished this thesis.

Special gratitude extends to my co-supervisor Professor Marcela Bilek for the fruitful Tuesday morning meetings, her scientific input in all stages of this work and for diligently proofreading this thesis.

I am grateful to my fellow lab colleagues at the Applied Materials Group Alex Chan, Richard Tan and Bob Lee for their support and friendship. Particularly, I would like to express my gratitude to Praveesuda Michael for her unfailing support and for taking some of the research reported here to the "next level". I also thank Juichien Hung for her tireless support and expertise with tissue culture and blood work.

I extend my gratitude to all my colleagues at the Applied and Plasma Physics group, especially Dr. Ian Falconer for his mentorship, positive attitude and encouragement as well as Dr. Rajesh Ganesan for his friendship and energizing "coffee times". I thank Dr. Alexey Kondyurin for his technical support and help in interpreting initial FTIR and XPS measurements on PAC. The SEM and TEM data reported here would not have been

possible without the friendly support from Dr. Minh Hyunh, Dr. Patrick Trimby and Dr. Hongwei Liu, thank you.

For supporting and encouraging me through this journey, I thank my proud family and friends. Thank you Mãe, Pai, Ana Sofia, Avô, Avó, Luis Miguel, Dina, Tony, Lourdes, Daniel, Nuno, Adriana and Chris.

Most importantly, to my colleague and partner in life Elysse, I thank you for your love, friendship, unconditional support and the brainstorming sessions over dinner. We did it together!

To my son Isaac.

PUBLICATIONS ARISING FROM THIS WORK

Patents

M Santos, E C Filipe, P L Michael, M M M Bilek and S G Wise, "*Nanoparticles*", Australian Patent Application No. 2016905306, 21 December 2016

Journal publications

Miguel Santos, Praveesuda L. Michael, Elysse C. Filipe, Alex H.P. Chan, Juichien Hung, Richard P. Tan, Bob S.L. Lee, Minh Huynh, Clare Hawkins, Anna Waterhouse, Marcela M. M. Bilek and Steven G. Wise, *Plasma synthesis of carbon-based nanocarriers for linker-free immobilization of bioactive cargo*, under review at ACS Applied Nanomaterials (2017) [1]

Miguel Santos, Praveesuda L. Michael, Marcela M. M. Bilek and Steven G. Wise, *Plasma polymerization of nanoparticles in dusty plasmas for applications in nanomedicine,* under preparation for submission to Scientific Reports [2]

Miguel Santos, Praveesuda L. Michael, Marcela M. M. Bilek and Steven G. Wise, *Fluorescent properties of plasma polymerized amorphous carbon nanoparticles*, under preparation for submission to Scientific Reports [3]

M Santos, E C Filipe, P L Michael, J Hung, S G Wise and M M M Bilek, *Mechanically Robust Plasma-Activated Interfaces Optimized for Vascular Stent Applications*, ACS Applied Materials & Interfaces (2016) [4]

M Santos, M M M Bilek, S G Wise, *Plasma-Synthesised Carbon-Based Coatings For Cardiovascular Applications*, Biosurface and Biotribology (2015) [5]

Laura Z. Vanags, Joanne T.M. Tan, **M Santos**, Praveesuda S. Michael, Ziad Ali, Marcela M.M. Bilek, Steven G. Wise, Christina A. Bursill, *Plasma activated coating immobilizes apolipoprotein A-I to stainless steel surfaces in its bioactive form and enhances biocompatibility*, Nanomedicine: Nanotechnology, Biology, and Medicine (2017) [6]

G C Yeo, **M Santos***, A Kondyurin, J Liskova, A S Weiss, and M M M Bilek, *Plasma-Activated Tropoelastin Functionalization of Zirconium For Improved Bone Response*, ACS Biomaterials Science & Engineering (2016) [7]

S G Wise, P L Michael, A Waterhouse, **M Santos**, E Filipe, J Hung, A Kondyurin, M M M Bilek, Martin K C Ng, *Immobilization Of Bioactive Plasmin Reduces The Thrombogenicity Of Metal Surfaces*, Colloids and Surfaces B: Biointerfaces (2015) [8]

Book chapters

M. Santos, A. Waterhouse, S.L. Lee, A.H.P. Chan, R.P. Tan, P.L. Michael, E.C. Filipe, J. Hung, S.G. Wise, M.M.M. Bilek., *Simple one-step immobilization of bioactive agents without use of chemicals on plasma-activated non thrombogenic coatings*, Functionalised Cardiovascular Stents. Elsevier Press (2018) [9]

Conference proceedings

M Santos, P. Michael, J Hung, E Filipe, S G Wise, M M M Bilek, *Control Feedback Strategies For Plasma Processing: Bioengineering Biocompatible And Mechanically*

Robust Coatings For Medical Implants, Gaseous Electronics Meeting, Geelong, Australia, February 14-17, 2016

M Santos, P L Michael, E C Filipe, S G Wise, M M M Bilek, *Optical Emission Spectroscopy in PECVD Helps Modulating Key Features in Biofunctional Coatings for Medical Implants*, 68th Gaseous Electronics Conference, Honolulu October 12-16, 2015

M Santos, S G Wise, J C Hung, P Michael, E C Filipe, M K C Ng, A Kondyurin and M M M Bilek, *Capacitively Coupled Radio-Frequency Plasmas in C_2H_2-Ar-N_2 Mixtures: Enhancing the Hemocompatibility of Metallic Substrates*, 27th Summer School and International Symposium on the Physics of Ionized Gases, Belgrade, Serbia Aug 26-29, 2014

AUTHORSHIP ATTRIBUTION STATEMENT

Chapter 1 of this thesis is partially published as

M Santos, M M M Bilek, S G Wise, *Plasma-Synthesised Carbon-Based Coatings For Cardiovascular Applications*, Biosurface and Biotribology (2015) [5]

I performed the literature research and wrote the review.

Chapters 3 and 4 of this thesis are published as

M Santos, E C Filipe, P L Michael, J Hung, S G Wise and M M M Bilek, *Mechanically Robust Plasma-Activated Interfaces Optimized for Vascular Stent Applications*, ACS Applied Materials & Interfaces (2016) [4]

I designed the study, co-acquired, analysed and interpreted the data and wrote the manuscript.

M. Santos, A. Waterhouse, S.L. Lee, A.H.P. Chan, R.P. Tan, P.L. Michael, E.C. Filipe, J. Hung, S.G. Wise, M.M.M. Bilek., *Simple one-step immobilization of bioactive agents without use of chemicals on plasma-activated non thrombogenic coatings*, Functionalised Cardiovascular Stents. Elsevier Press (2018) [9]

I co-designed the study and co-wrote the book chapter with co-authors.

Chapters 5 and 6 of this thesis are under review as

Miguel Santos, Praveesuda L. Michael, Elysse C. Filipe, Alex H.P. Chan, Juichien Hung, Richard P. Tan, Bob S.L. Lee, Minh Huynh, Clare Hawkins, Anna Waterhouse, Marcela M. M. Bilek and Steven G. Wise, *Plasma synthesis of carbon-based nanocarriers for*

linker-free immobilization of bioactive cargo, under review at ACS Applied Nano Materials (2017) [1]

I designed the study, co-acquired, analysed and interpreted the data and wrote the manuscript.

M Santos, E C Filipe, P L Michael, M M M Bilek and S G Wise, "*Nanoparticles*", Australian Patent Application No. 2016905306, 21 December 2016

I invented the nanoparticles and designed their collection, co-designed the overall idea, co-acquired, analysed and interpreted the data and co-wrote the patent application with the co-authors.

I am the corresponding author of the items above.

The following journal publications resulted from collaborative work during my PhD but their corresponding literature review, results and discussion are not presented in this thesis.

Laura Z. Vanags, Joanne T.M. Tan, **M Santos**, Praveesuda S. Michael, Ziad Ali, Marcela M.M. Bilek, Steven G. Wise, Christina A. Bursill, *Plasma activated coating immobilizes apolipoprotein A-I to stainless steel surfaces in its bioactive form and enhances biocompatibility*, Nanomedicine: Nanotechnology, Biology, and Medicine (2017) [6]

G C Yeo, **M Santos***, A Kondyurin, J Liskova, A S Weiss, and M M M Bilek, *Plasma-Activated Tropoelastin Functionalization of Zirconium For Improved Bone Response*, ACS Biomaterials Science & Engineering (2016) [7]

S G Wise, P L Michael, A Waterhouse, **M Santos**, E Filipe, J Hung, A Kondyurin, M M M Bilek, Martin K C Ng, *Immobilization Of Bioactive Plasmin Reduces The Thrombogenicity Of Metal Surfaces*, Colloids and Surfaces B: Biointerfaces (2015) [8]

Miguel Santos

14, December 2017

As supervisor for the candidature upon which this thesis is based, I can confirm that the authorship attribution statements above are correct.

Dr. Steven Wise

14, December 2017

CONTENTS

LIST OF TABLES

LIST OF FIGURES

LIST OF ABBREVIATIONS AND ACRONYMS

Φ_d	Coupled power per unit monomer mass
ω_e	Fundamental frequency of vibration
A_{act}	Active discharge cross-sectional area
ABTS	2,2'-azino-bis(3-ethylbenzothiazoline-6-sulphonic acid)
a-C	Amorphous carbon
a-C:H	Hydrogenated amorphous carbon
A_{gas}	Cross-sectional (gas flow)
AIM	Atomic interfacial mixing
ATR	Attenuated total reflectance
c	Speed of light
CAP	Competitive ablation polymerization
CCRF	Capacitively coupled radiofrequency
DAPI	4',6-diamidino-2-phenylindole
DC	Direct current
DES	Drug eluting stents
DLC	Diamond like carbon
DPPH	2,2-diphenyl-1-picrylhydrazyl
e	Electron charge
E	Excitation energy
E_e	Electronic excitation energy
E_a	Monomer activation energy
EEDF	Electron energy distribution function
ELISA	Enzyme-linked immunosorbent assay
E_r	Rotational energy
EPR	Electron paramagnetic resonance
E_v	Vibrational energy
F	Flow rate of the precursor (in $cm^3\ s^{-1}$)
F_{est}	Electrostatic force
Fib	Fibrinogen
FNS	First negative system

FPS	First positive system
FTIR	Fourier transform infrared spectroscopy
GNP	Gold nanoparticle
h	Planck's constant
hCAEC	Human coronary endothelial cells
HCM	Hollow cathode magnetron
H_r	Hardness
HRP	Horseradish peroxidase
HSA	Human serum albumin
HV	High voltage
I	Emission intensity
I_{bias}	Pulsed bias current
ICCD	Intensified charged-coupled device
ICG	Indocyanine green (Cardiogreen)
ISM	Interstellar medium
k_B	Boltzmann constant
l_{act}	Active discharge length
LST	Late stent thrombosis
MCF7	Cancerous human mammary epithelial cell line
MCF10A	Human mammary epithelial cell line
M	Molecular weight of the precursor
m_e	Electron mass
m_p	Dust particle mass
n	Density
N	Number density
NanoP^3	Plasma polymerised nanoparticles
n_d	Dust particle density
n_e	Electron density
n_g	Gas density
n_i	Ion density
OES	Optical emission spectroscopy
p	Discharge pressure
p_0	Pressure at standard conditions

PAC	Plasma activated coating
PBS	Phosphate buffer saline
PCN	Primary carbonaceous nanoclusters
PDI	Polydispersity index
PDP	Plasma dust particles
PECVD	Plasma enhanced chemical vapor deposition
PEG	Polyether glycol
PMS	Plasma magnetron sputtering
PP	Plasma polymerization
PPC	Plasma polymerised coatings
PRP	Platelet rich plasma
PS	Polystyrene
Q	Flow rate (in sccm)
RF	Radiofrequency
r_p	Dust particle radius
RSGP	Rapid step growth polymerization
RT-PCR	Reverse transcription-polymerase chain reaction
SDS	Sodium dodecyl sulfate
SBF	Serial block face
SE	Spectroscopic ellipsometry
SEM	Scanning electron microscopy
siRNA	Small interfering Ribonucleic acid
SMC	Smooth muscle cells
SPS	Second positive system
SS	Stainless Steel
T_0	Temperature at standard conditions
ta-C	Tetrahedral amorphous carbon
T_e	Electron temperature
TE	Tropoelastin
TEM	Transmission electron microscopy
T_{exc}	Excitation temperature
T_g	Gas temperature
T_i	Ion temperature

T_{rot}	Rotational temperature
T_{vib}	Vibrational temperature
V_{bias}	Pulsed bias voltage
V_{disc}	Discharge volume
V_{disc}	Discharge volume
v_e	Electron thermal velocity
V_{gas}	Volume occupied by the gas
v_i	Ion thermal velocity
v_p	Dust particle mass
V_{rf}	Radiofrequency voltage
Y_r	nanoP^3 mass yield per unit area
W	Total coupled power
W_{bias}	Pulsed bias power
W_{rf}	Radiofrequency power
XPS	X-Ray photoelectron spectroscopy
A	Einstein coefficient
ζ_V	Zeta potential
λ	Emission wavelength
τ	Residence time
ϵ	Radiative intensity

1 GENERAL INTRODUCTION

1.1 Current demands for new bio-functional nanomaterials

1.1.1 Biointerfaces for medical devices

Every year more than 6 million people undergo surgery around the world for the insertion of medical implants such as hip and knees prostheses, pacemakers, heart valves and coronary stents [10, 11]. In the US alone around 1 million orthopaedic implants are inserted annually for knee and hip replacements [12] and these numbers are expected to rapidly increase to around 3 million by the year 2030 [13]. The increasing life expectancy of the population elevates demands for medical implants with a superior life span that can resist corrosion and wear, especially in load bearing and blood and/or tissue contacting applications. Additionally, insertion of exogenous materials into the body triggers immune responses in the areas surrounding the implant which can compromise implant performance and even necessitate revision surgery for implant replacement or extraction. Novel surface modification technologies that could mediate interactions between the implant and the host to prevent adverse reactions would clearly benefit the biomedical devices industry. In particular, there is a great demand for a universal technology capable of producing tailored biofunctional interfaces to simultaneously address a number of specific tasks depending on the application. Modulation of the surface properties such as hemocompatibility, protein adsorption / immobilization, as well as differential attachment, proliferation and differentiation of cells are highly desirable.

1.1.1.1 Cardiovascular stents

The World Health Organization [13] estimates that cardiovascular diseases represent 30% of total deaths worldwide, with coronary heart complications, including atherosclerosis, leading

the list with a total of 7.3 million deaths every year. The same organization predicts that these numbers will rise to 8% within the next 15 years, exacerbating an already serious problem. In the last three decades, percutaneous coronary interventions became widely used in the treatment of cardiovascular diseases and have been established as the first-line technique for revascularization of the coronary arteries. Among implantable biomedical devices, coronary stents are now the dominant vascular implant in percutaneous coronary interventions [14] with around 800 000 stents implanted annually in the US alone [15]. Stents are expandable cylindrical meshes used to re-establish the normal blood flow in blocked atherosclerotic coronary arteries, resupplying ischemic tissue (see Figure 1.1). However, despite their widespread use, current stent platforms have only sub-optimal biocompatibility, interacting poorly with vascular cells and promoting blood clot formation (see Figure 1.2).

The first commercially available stent platform was based on metallic alloys such as stainless steel (SS). Despite the extraordinary results in reducing the rate of abrupt vessel closure, one of the major pitfalls of coronary angioplasty, post-procedure complications related to stent implantation started to arise. The most common was in-stent restenosis, triggered by an inflammatory response due to blood vessel intima injury during stent deployment. Damage to the endothelium led to the migration and over-proliferation of underlying smooth muscle cells (SMC), causing vessel re-narrowing in a process called neointimal hyperplasia [16]. To overcome the draw-backs of bare metal stents, drug eluting stents (DES) were introduced. DESs are grafted with layers of biodegradable [17-19] or non-biodegradable [20-22] polymers, in which a pharmacological agent is loaded and can be locally released within a given period

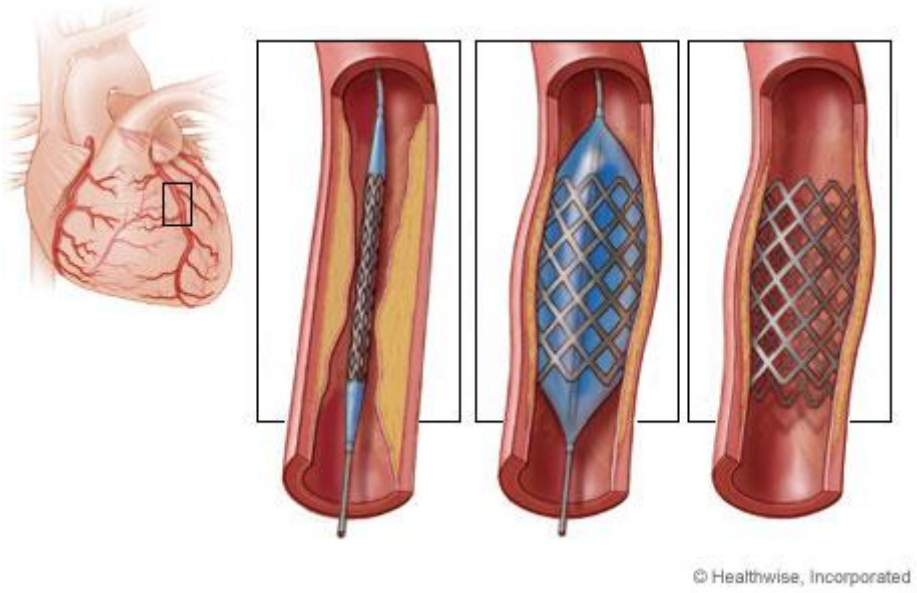

Figure 1.1: Schematic illustration of a stent implantation at the site of a clogged coronary artery with atherosclerotic plaque. The stent unblocks the artery and provides mechanical support, preventing recoil of the blood vessel [https://www.healthlinkbc.ca/health-topics/zm2311].

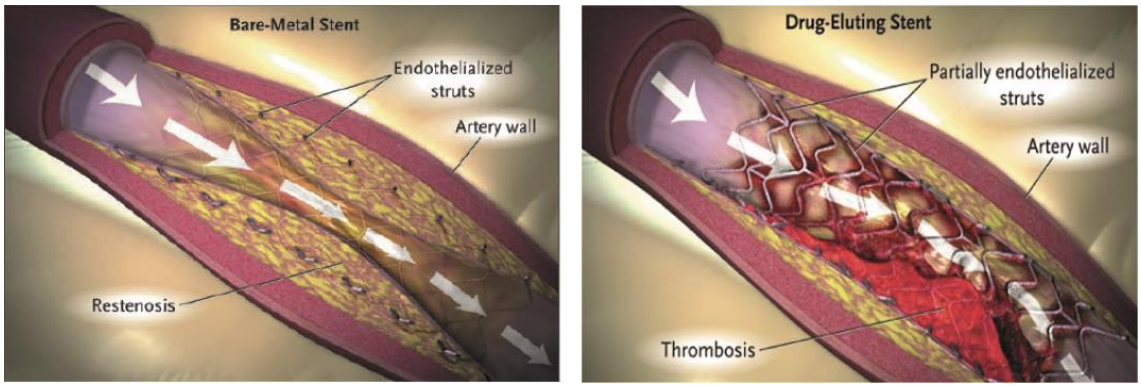

Figure 1.2: Schematic depiction of restenosis (left) around an implanted bare metal stent and driven by over-proliferation of smooth muscle cells. Late stent thrombosis (right) is typically observed in drug-eluting stents, which is triggered due to lack of stent endothelialisation. Image taken from [23]. By incorporating anti-proliferative agents, drug-eluting stents were successful in inhibiting the over-proliferation of SMC, hence reducing the effects of hyperplasia.

However, an unintended consequence of DES was a substantially increased risk of long-term stent thrombosis, termed late stent thrombosis (LST) [24]. LST is mainly associated with reduced re-endothelialisation of the stent, leading to a delayed healing of the vessel and over-exposure of the stent struts to the blood. Another possible reason for late thrombosis could be associated with adverse inflammatory responses to the drugs and the grafted polymer used in these stents. Extensive research has been undertaken to address the issues of in-stent restenosis and late-stent thrombosis, either through the development of more biocompatible polymer-based coatings [25, 26] or by integrating specific antibodies with the ability to recruit and immobilize endothelial progenitor cells [27-29], thus promoting re-endothelialisation. The incorporation of nitric oxide (NO) donors in the stent design has also been considered as an encouraging alternative platform to reduce in-stent restenosis and LST. NO is an endogenous signalling molecule that participates in important biological processes and possesses several vasculoprotective properties [30]. It has been shown that the administration of different NO donors inhibits the proliferation and migration of SMC [31, 32], enhances the proliferation of endothelial cells [33], prevents platelet aggregation [34] and adhesion [35] to the vascular endothelium and reduces intimal hyperplasia following vascular injury [36]. The delivery of NO through eluting stent platforms has been achieved by incorporating NO donors in a polyurethane polymer which was then coated onto the stents [37] or by incorporating the NO donor with paclitaxel [38] (an anti-proliferative agent extensively used in the prevention of restenosis). However, no significant improvements in preventing restenosis were shown so far relative to the controls in different *in-vivo* animal trials.

A new generation of bioabsorbable stents [39-41] have been prompting increasing interest from the scientific community. In theory, these stents can be temporarily used has a treatment for atherosclerosis as they are dissolved in the body after a period of time, leaving behind a structurally normal and recovered blood vessel. Although promising, some issues regarding their mechanical properties, which are paramount for a proper stent deployment, radio-opacity and control over the rate that they are absorbed in the body still need to be addressed [42].

Currently used DES platforms still carry an ongoing risk of thrombosis requiring patients to be on pharmacological dual anti-platelet therapies, which can result in bleeding and is not feasible for patients requiring additional surgery. A drug-free coating technology, with all the necessary mechanical and biological properties for enhancement of the clinical performance of coronary stents, would provide a clear benefit over current stent platforms. In particular, the coating should be able to resist cracking and delamination during and after stent deployment in order to avoid the contact of the struts with the blood stream. It should also be multi-functional, promoting the adhesion and proliferation of endothelial progenitor cells, for re-endothelialisation, while also inhibiting the over-proliferation of smooth muscle cells to avoid hyperplasia. In this work, chapters 3 and 4 focus on the feasibility of using PAC coatings for implantable medical devices, with particular focus on coronary stents. The deposition of biofunctional surfaces on coronary stents is a particularly interesting and complex case study as it combines: (i) physical-chemical, (ii) mechanical, (iii) geometric, (iv) blood clotting and (v) cellular response considerations.

1.1.2 Multifunctional nanocarriers for nanomedicine

In nanomedicine, multifunctional nanocarriers, capable of delivering multiple molecular cargos within the same structure, are expected to greatly improve theranostic outcomes in numerous diseases. Over the last decade, the number of nanoparticle platforms proposed for use in custom-made nanomedicine has vastly increased [43, 44] (see Figure 1.3). Nanocarriers have been designed for the specific treatment of a great number of conditions using cocktails of drugs, nucleic acids, photosensitive dyes and diagnostic agents [45-49].

However, the upscaling of current synthetic routes into the clinic relies on multistep wet-chemistry approaches for functionalisation with linkers [50, 51] (see Figure 1.4), and has thus been largely hampered by the complexity and cost involved in producing nanocarriers capable of carrying multiple cargo [52]. Typically, the proposed nanocarriers utilize materials that are not inherently bioactive and do not allow a direct and simple conjugation with pharmaceutical cargo. Functionalisation strategies with chemical cross linkers have been proposed to impart functionalities on the surface of various nanoparticle materials (e.g. gold, iron-oxide, polymeric, quantum dots, etc.). Alternative conjugation strategies involve the pre-conjugation of molecules with the nanoparticle material in self-assembly processes [53, 54]. Other promising approaches utilize mesoporous polymeric materials with large surface/volume ratios, which electrostatically entrap high loads of molecular cargo [55] that can be released in targeted cells upon photo-chemical stimuli [56]. These nanoparticles are usually PEGylated

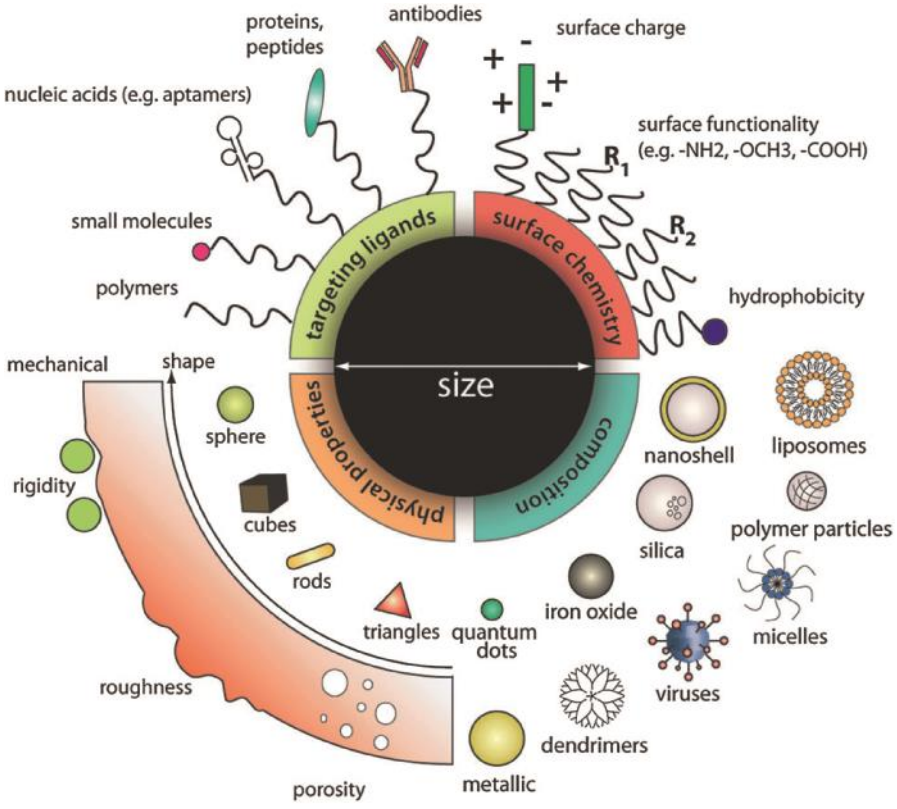

Figure 1.3: Schematic illustration of various nanoparticle materials, architectures, properties and functionalities for nanomedicine applications. Image taken from [43].

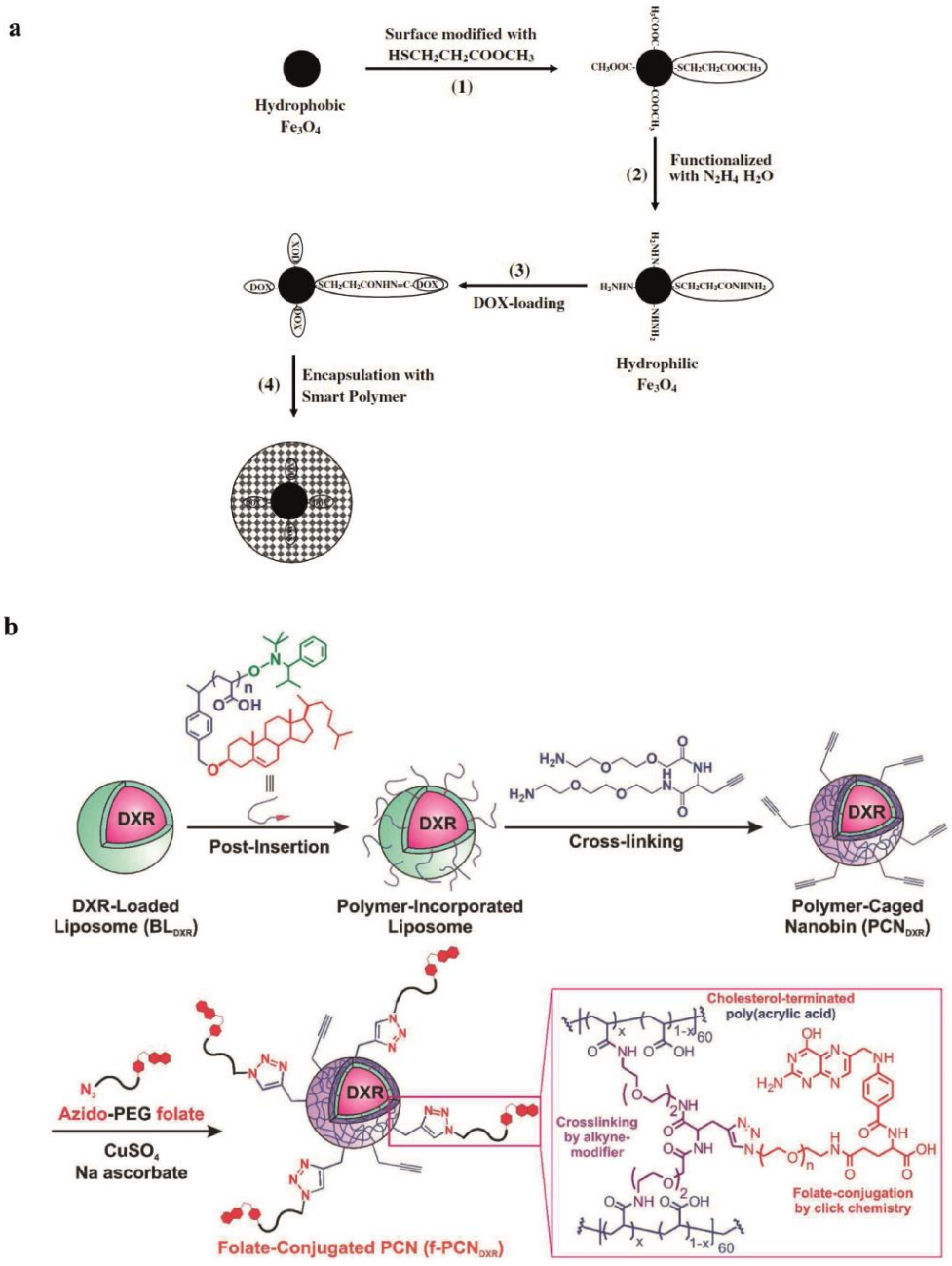

Figure 1.4: a, Schematic depicting a multi-step functionalization approach typically necessary to bind one drug type (doxorubicin) to iron oxide nanoparticles. Image taken from [57]. b, An alternative strategy based on click chemistry to bind doxorubicin to liposome templates using cross-linkers and PEG-based targeting ligands. Image taken from [58]. Note that in both cases additional synthesis steps are necessary to fabricate the initial nanomaterial.

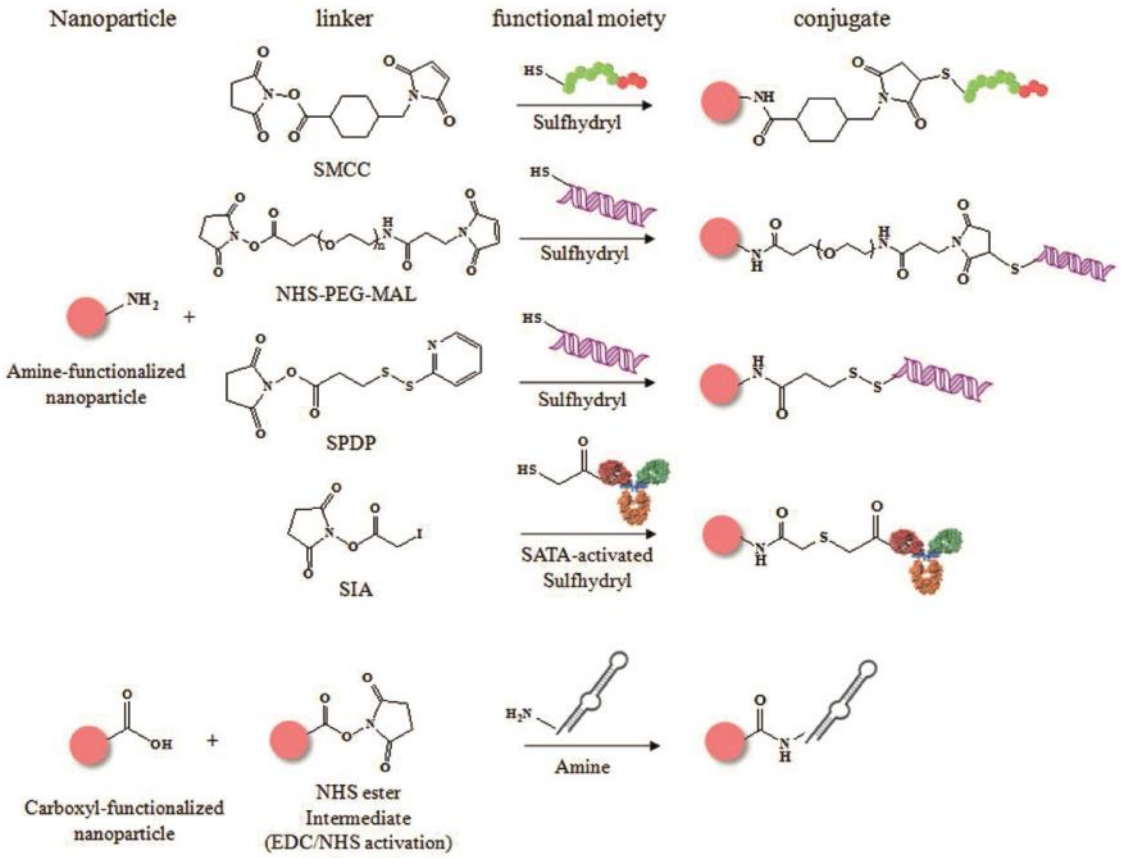

Figure 1.5: Functionalisation of nanoparticles with small molecules, therapeutic genes, antibodies and oligonucleotides require different chemical linkers to achieve specific and robust immobilization. Image taken from[51].

to enhanced stability and circulation in vivo [59], or combined with stabilized and functional lipid bilayers [55, 56]. However, wet-chemistry-based approaches are usually, often extremely, complex and rely on time-consuming, multi-step protocols to achieve a robust conjugation between the nanocarrier surface and the molecular cargo (see Figure 1.4b). Moreover, the optimization, reproducibility and control over a suitable surface concentration and thickness of the surface coatings with functional linkers are difficult to achieve. Typically, the terminal groups of the linkers also limit the range of biomolecules that can be immobilized (see Figure 1.5). Such approaches also rely on the usage of organic solvents and multiple purification steps that compromise the native conformation and functionality of the molecular cargos and present safety or disposal difficulties. Despite the recent rapid growth of nanomedicine research, the need for new up-scalable nanofabrication strategies that can deliver novel products with improved performance, functionality and safety for the patient remains. Ideally, the rational design of nanoparticles should address multiple functionalization using simple approaches [45] such as direct incubation with biomolecule solutions.

While it is regarded as a major contaminant in manufacturing and energy applications, chapters 5, 6 and 7 propose that carbonaceous plasma dust can be tailored to function as multifunctional plasma polymer nanoparticles (nanoP^3). Particularly, it is shown that PP technology can be operated in a suitable window of parameters to synthesize nanoP^3 in a controlled fashion. By identifying relevant macroscopic parameters, it is further demonstrated that significant features of nanoP^3, such as yield, size, aggregation, surface chemistry and

charge can be tailored and reproducibly attained. NanoP^3 retain a surface activity characteristic of thin film coatings synthesized by the PP process [5, 60, 61]. Radicals and functional moieties formed during dust formation are preserved within the nanoP^3 structure, enabling surface immobilization of bioactive cargo with wide ranges of molecular weights and chemical structures.

1.2 Plasma discharges

1.2.1 The plasma medium

Among the four fundamental states of matter, (i.e. solid, liquid, gaseous and plasma), plasma is the most abundant in the Universe. For instance, the stars, interstellar and intergalactic space, nebulae, lightning and auroras borealis are all in the form of plasma. A plasma is achieved when enough energy is supplied to a gas, or a gaseous mixture in thermal equilibrium so that a fraction of the atoms (or molecules) that constitutes the medium becomes ionised. In contrast to a gas, formed only by neutral species (atoms and/or molecules), the plasma medium is also comprised by freely moving charged species (ions and electrons) and photons. Therefore, the electrical and thermodynamical properties inherent to a plasma medium are far more complex and subtle than in the gaseous state. The complex interaction between positively and negatively charged particles, governed by Coulomb interactions, gives rise to complex phenomena and collective behaviours and are unique to the plasma and may vary depending on the conditions in which the plasma is produced and sustained. To generate a plasma, energy can be coupled to a gas either through an increase of its temperature or by applying a sufficiently strong electric field. The medium becomes ionized when some of the

background electrons, heated to a thermal energy greater than the gas ionization threshold, collide with the gas atoms. These inelastic collisions are categorised as ionization collisions, and result in the creation of electron-ion pairs. Since electrons and ions are created in pairs, the plasma medium is quasi-neutral and can be characterised by a single particle density, $n \approx n_e \approx n_i$ [62]. Plasmas can range from weakly ionized, where n is only a fraction of the neutral gas density $n \ll n_g$, to fully ionized discharges where $n \approx n_e \approx n_i \gg n_g$. Here, the subscripts e, i and g denote electrons, ions and gas particles respectively.

Because electrons are significantly lighter and more mobile than ions, the power applied to the discharge is mainly absorbed by the electron population. Therefore, electrons play a fundamental role in generating and sustaining the plasma, and different classes of discharges are often categorised by their range in electron temperature, T_e and density, n_e (Figure 1.6). Thermal (or hot) plasmas are characterised by a thermodynamical equilibrium between electrons and heavy species (atoms, molecules and ions) and very high ionization degrees. Examples of hot plasmas include the Sun and nuclear fusion devices. Thermal plasma torches and arc discharges operated at atmospheric pressure are examples of hot plasmas used in the industry for materials processing. Low pressure, weakly ionized glow discharges generated by electrical excitation are an important kind of plasma for the synthesis of materials in a vast number of industries. Importantly, these discharges are distinguished by a strong non-equilibrium between electrons and heavy species, i.e. $T_e \gg T_i \approx T_g$. Therefore, the rich composition of these discharges (e.g. ions, excited species, reactive radicals and photons), and incidentally its unique characteristics, are mostly driven by collisional mechanisms

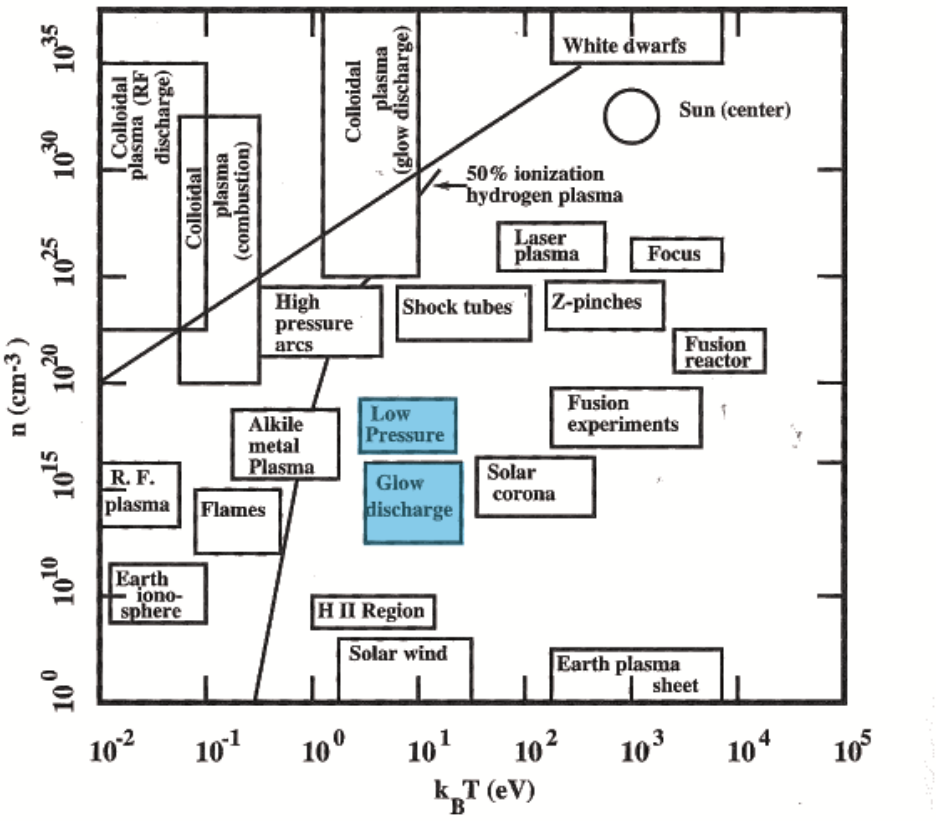

Figure 1.6: Space and laboratory plasmas in a density and temperature phase diagram. The regions highlighted in blue represent the plasmas used in this work. Image adapted from [63]

between energetic electrons and the background gas. These discharges are typically sustained close to room temperature, $k_B T_i \approx 0.025$ eV, low pressures $p \approx 1$ mTorr $- 1$ Torr, and feature electron densities and temperatures usually ranging $n \approx 10^8 - 10^{13}$ cm^{-3} and $k_B T_e \approx 1 - 10$ eV respectively. This work deals with low-pressure and low temperature discharges and their use for the synthesis of plasma polymer nanomaterials.

1.2.2 Generation of plasma discharges for materials processing

Plasmas can be produced in laboratory conditions. Humankind has been studying and developing different ways to produce and control plasmas for its own benefit for more than 130 years. Plasma discharges have found a large number of applications from illumination, metallurgy, micro-electronics, environment, materials engineering, analytical spectroscopy, medicine, etc [64]. The success of man-made plasma discharges is a result of the unique physical and chemical characteristics inherent to this medium, as well as the extraordinary flexibility achieved so far in controlling a large window of working conditions. Plasma can be artificially produced in a wide range of size scales (from micrometre up to several metres), geometries (planar, cylindrical, spherical, etc.), densities (from 10^7 up to 10^{32} particles per cubic meter), pressures (from a few mTorr up to atmospheric pressure), temperatures (from negative values up to 10^8 degrees Celsius) and lifetimes (from femtoseconds up to years).

Depending on the type of application, many different techniques of plasma generation can be used. For instance, in surface modification and deposition applications it is desirable to achieve high levels of purity in the coatings. The use of a vacuum chamber, where the system

is pumped down to very low pressures, allows control of the plasma composition and, therefore, also the coating composition. Magnetic fields and high voltage sources can also be used to gain control over trajectory and energy of the charged species that reach the surfaces to be coated. In the last decades for instance, different types of plasma discharges have proven their potential for biomedical applications, for a wide range of tasks such as sterilisation, cell proliferation, treatment of oral pathogens and healing of burn wounds [65].

Low pressure and low temperature plasmas have become widely used for surface modification in different applications, including the deposition of thin-films on implantable biomedical devices. Organosilicon and hydrocarbon precursors are commonly used for the creation of hydrogenated silicon films and amorphous hydrogenated carbon films (frequently named diamond-like carbon films) for a wide range of applications. The rich composition of the plasma medium, i.e., electrons, ions, atoms, radicals, molecules and photons, is achieved through efficient dissociation and ionization of precursor and carrier gas atoms and molecules, which takes place via many different kinetic mechanisms and energy transfer channels. The resulting precursor ions and radicals then diffuse towards the substrate, initiating a set of surface chemical reactions and ultimately leading to the deposition and growth of a coating on the substrate surface.

For instance, capacitively coupled radio frequency (ccrf) discharges have become very popular in plasma-assisted processing of materials. The plasma is usually generated at low temperatures (close to ambient temperature) inside a vacuum chamber and is typically sustained at a frequency of 13.56 MHz. The radio frequency power is usually coupled to a

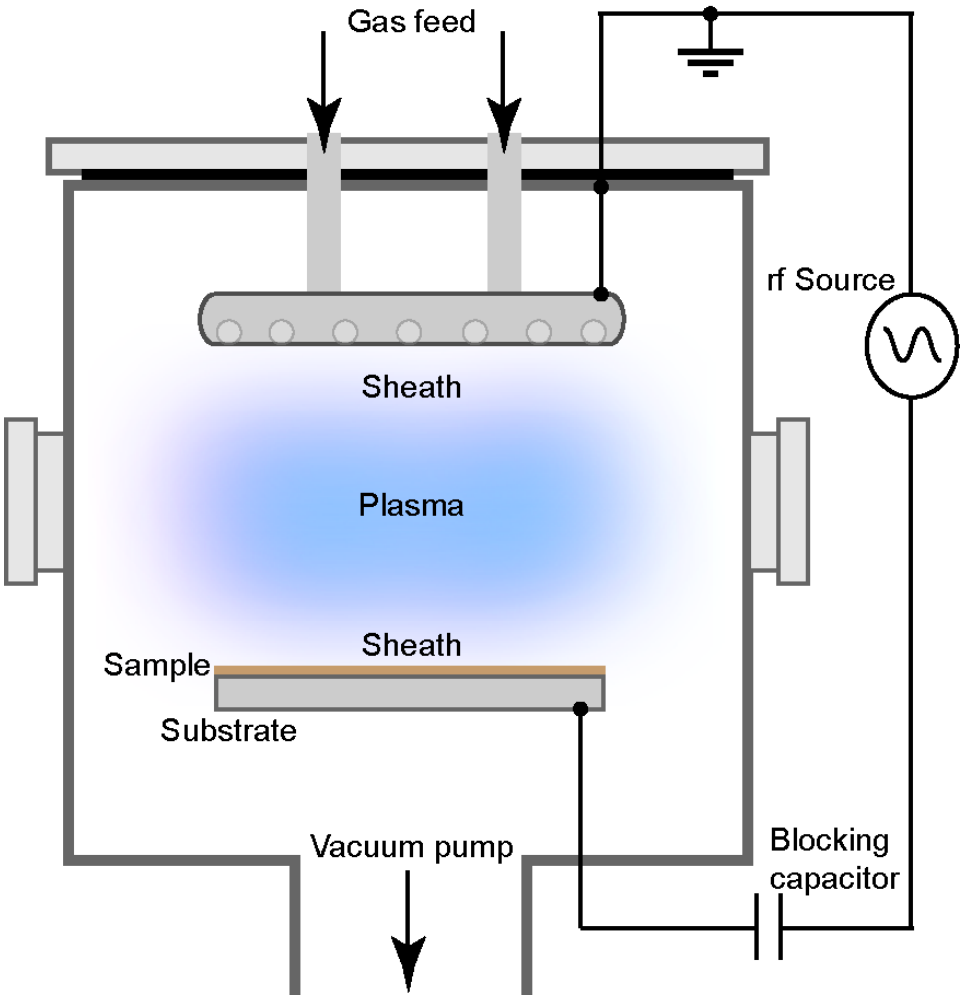

Figure 1.7: Schematic illustration of a typical capacitively-coupled radio-frequency (rf) reactor used in surface modification of materials. The plasma is generated between the two electrodes and interact with surfaces through positively charged sheaths. Adapted from [62].

driving electrode using a matching network that matches the impedance of the power source to the impedance of the plasma, to minimise power losses within the external circuit. Figure 1.7 illustrates a typical asymmetric planar ccrf apparatus used for materials processing. Here, the sample is electrically connected to the rf (bottom) electrode and the gas is introduced at the top and flows downstream throughout the enclosed reactor. The gas atoms are ionised between the two electrodes, forming a plasma that interacts with the surfaces of the sample and electrodes through positively charged sheaths. The sheath is initially formed because electrons acquire a significantly higher thermal velocity than the ions, $v_i \ll v_e \equiv (eT_e/m_e)$, causing their excessive diffusion towards the walls. This excessive electron diffusion results in an abrupt decrease in the electron density, which creates a positive net space charge separation ($n_i > n_e$) along the sheath. The formation of this ionic sheath eventually produces a plasma potential that confines the electrons within the discharge boundaries and accelerates ions towards the surfaces. Therefore, plasma sheaths play a paramount role in plasma processing since, they not only confine electrons that sustain the discharge, but it also accelerate ions with sufficiently high energy – typically up to ~100 eV – that can be utilised to modify the surface of the samples.

The versatility of ccrf discharges allows to easily tailor different input parameters according to specific needs. For instance, the rf power can be coupled to the plasma either in continuous or in pulsed regimes [66]. A pulsed power modulation regime is frequently used in plasma polymerization to provide an extra degree of freedom in the deposition process. The substrate holder can also be electrically biased to accelerate the plasma ions towards the growing film. The applied bias can be either continuous DC [67], radio-frequency [68] or pulsed [69].

Control over the chemical composition of the coatings is achieved by choosing different gases (or gaseous mixtures) to generate the plasma. The coatings deposited by ccrf, especially when bias is used to increase the energy of the depositing species, are characterised by superior adhesion to the substrates, high cross-linking, improved biocompatibility and chemically active and functional surfaces. This deposition technology also allows a level of control over different properties of the films, such as roughness, wettability, hardness, density, flexibility and composition without changing the properties of the underlying substrate. This control is achieved by tuning the different process parameters - a difficult task given the complexity of the plasma and the use of reactive gaseous mixtures.

1.2.3 Plasma polymerization

Reactive plasma polymerization (PP) is an extremely versatile plasma-assisted technology used for the deposition of thin films coatings [66, 70-77]. The plasma is usually sustained using a ccrf discharge but other plasma generation platforms, such as DC [78, 79] or microwave discharges [80], can be adopted. A number of models have been proposed to describe the evolution of the plasma/gas phase chemistry during formation of plasma polymer coatings [81]. However, the fundamental mechanisms of PP are extremely complex and not yet fully understood. The two most accepted models in PP, the rapid step growth polymerization (RSGP) [77] and competitive ablation and polymerization (CAP) by Yasuda [72], are shortly reviewed below.

In PP, the power coupled to the plasma is partially channelled to fragment and activate a carbon- or silicon-based organic precursor. The activation of the precursor is mostly driven by electron impact collisions, resulting in the formation of a myriad of reactive (radicals), charged (ions) and excited species. The radicals, containing unpaired electrons, easily recombine with other species to form more complex molecules. These molecules, formed in the plasma phase, can be deposited on any surface inside the chamber to form a thin-film coating that grows by continuous plasma-surface interactions. Figure 1.8 shows two possible pathways for PP based on the radical-chain growth mechanism proposed by the RSGP model. In the first cycle, a radical specie, $M_i^{\cdot}$, containing one unpaired electron is initially formed by the activation of the precursor, M_i, in a collisional process, e.g. an electron impact collision. Several radical-chain growth reactions can take place as $M_i^{\cdot}$ may: (i) react with a neutral specie, M, to form a reactive radical molecule, $M_i - M^{\cdot}$; (ii) be neutralised by reacting with another radical specie, $M_j^{\cdot}$, to form a stable molecule, $M_i - M_j$ or (iii) react with a bi-radical specie, $^{\cdot}M_k$, to form a reactive radical molecule $M_i - M^{\cdot}{}_k$. The radical species formed in (i) and (iii) will continuously grow through propagation reactions with other species in the plasma (neutrals and radicals) and form larger molecules. The stable molecule $M_i - M_j$ can in turn be re-activated in the plasma in inelastic collisions with electrons (or heavy species) and also undergo propagation reactions to form large molecules. The second cycle starts with the bi-radical specie $^{\cdot}M_k$ and involves several propagation reactions – (iv) and (v) – in a similar fashion to the first cycle. However, $^{\cdot}M_k$ does not participate in termination reactions as in step (ii). Consequently, the products of any reaction in the second cycle will always

feature radical species and the polymerization is auto-sustained for as long as the plasma is left on.

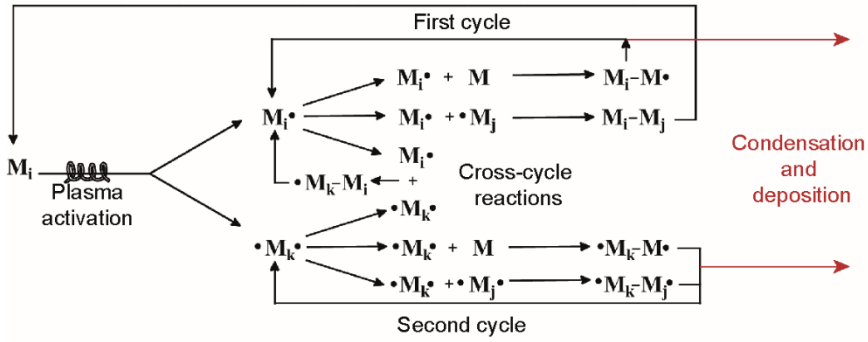

Figure 1.8: Schematic showing the two cycles of the rapid step growth polymerization model (RSGP) proposed by Yasuda. Image adapted from [77]. Radical species and the polymerization is auto-sustained for as long as the plasma is left on.

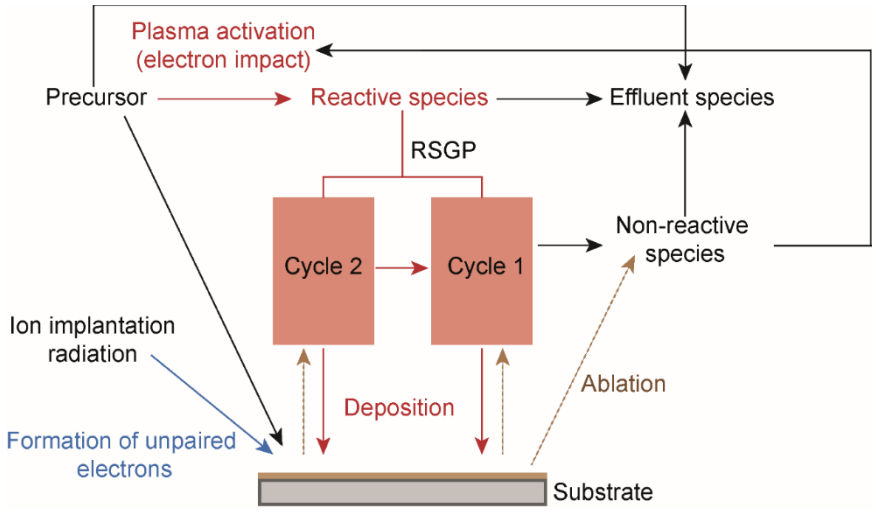

Figure 1.9: Schematic representing the deposition process of a plasma polymer coating. Coating deposition is a competition between polymerization (described by the RSGP model[77]), surface ablation (predicted by the CAP model [72]) and formation of additional unpaired electrons due to ion bombardment and irradiation (as described by the ion-activated growth of plasma polymers [82]). Image adapted from [83].

The large molecules formed by plasma polymerization eventually diffuse out of the active plasma boundaries and condense on surfaces of the reactor (e.g. electrodes, walls or substrates), initiating the growth of a solid plasma polymerized coating. Further coating growth occurs spontaneously via plasma-surface interactions between plasma species and radical sites in the condensed polymerised molecules. Additional unpaired electrons can be formed on the surface of the coating if the energy gained by the ions in the plasma sheath is sufficiently high to break chemical bonds between atoms. Therefore, stable molecules can still be activated upon the impact of energetic ions or UV irradiation on the coating, even if they were formed in termination reactions occurred previously in the plasma. Coating growth is exacerbated when the newly created radicals at the interface react with other carbon-based radical species from the plasma, a process often known as ion-activated growth of plasma polymers [82]. However, chemical etching can also occur if the surface radicals react with non-carbon-based radicals, such as $O^{\cdot}$ and $S^{\cdot}$. These radicals are prone to react with the interface and form stable compounds (e.g. CO and CO_2) that can desorb from the growing coating and are eventually removed from the reactor [83] by the pumping system. Additionally, coating ablation can also take place if the energetic ions bombard the coating interface with a sufficient energy to remove material from the coating (i.e. physical etching). Therefore, the deposition of plasma polymerised coatings is a competition between material growth, assisted by radical chain reactions, and ablation caused by the impact of energetic ions on the surface of the coating (see Figure 1.9). The polymerization reactions envisaged by the RSGP model combined with the mechanism of ion-assisted etching at the plasma-coating interface are described by the competitive ablation and polymerization (CAP) model initially proposed by Yasuda [72].

The energy range acquired by the electrons in the plasma is characterised by a probability density function, the electron energy distribution function (EEDF). For instance, electron energies are distributed according to a Maxwellian EEDF at a given electron temperature, T_e, if they are allowed to reach a thermal equilibrium via energy re-distribution (e.g. in electron-electron collisions). Due to this energy distribution, the activation of the precursor via electron inelastic collisions is a manyfold process that results in the creation of several populations of radical species. The array of different radical species in each process mainly relies on: (i) the type of precursor; (ii) power coupled to the discharge (electrons) and (iii) the introduction of buffer gases that can in turn be excited and react with the radical species. For this reason, the plasma-phase chemistry during PP is extremely rich and comprise a vast number of the radical-assisted propagation reactions. Consequently, plasma polymer coatings do not usually retain the same homogeneous and repeating structure which is typical of conventional polymers. In contrast, plasma polymer coatings are usually denser, more cross-linked and characterised by a complex, highly-branched, heterogeneous and random network of structural units. Figure 1.10 illustrates the primary differences between two polymers synthesised from the same precursor using plasma polymerization and conventional polymerization processes.

The density, the cross-linking degree and structural complexity of plasma polymers, can be tailored by a suitable manipulation of the plasma parameters. However, this manipulation is limited and control over the coating chemistry becomes hard to achieve due to the complexity of the reactions that take place in PP processes. Pulsed radiofrequency discharges are often used in order to circumvent this problem and gain some control over the coating surface [84].

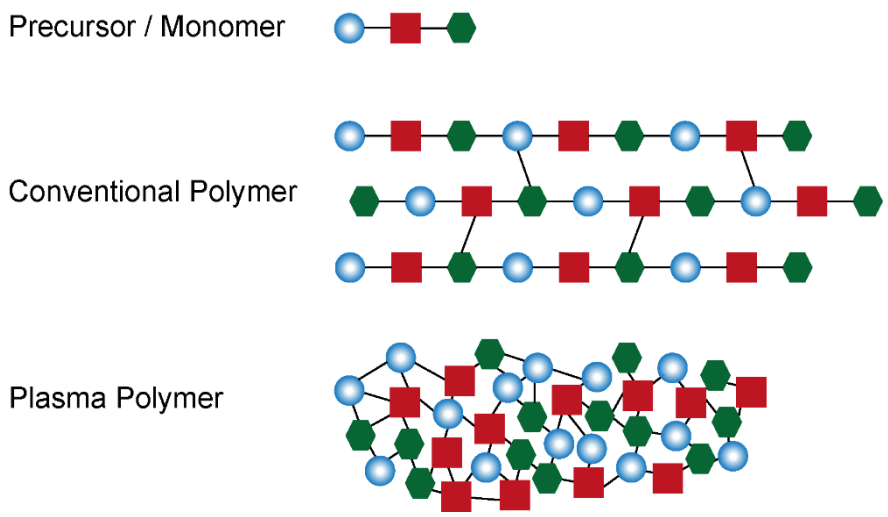

Figure 1.10: A comparison between a conventional polymer and a plasma polymer synthesized from the same monomer. Image adapted from [85].

This approach allows to generate the plasma for short instants (plasma on-time) between intervals where there is no active discharge (plasma off-time). Since there is no ionization and excitation during the plasma off-time, the precursor (or stable fragments of the precursor) can bind to reactive sites at the coating interface. Coatings synthesised by this approach benefit from a more controlled surface chemistry, featuring functional moieties of the original precursor molecules [86-88] and a reduced number of unspecific reactive sites. In contrast, the radical density in plasma polymer coatings can be significantly bolstered if the precursor is fully activated in higher energy plasma processes [89, 90]. Moreover, substrate electrical bias accelerates ions with energies up to 1kV towards the growing film and has been used to substantially increase the reactivity of plasma polymer coatings [89]. These polymers comprise a reservoir of long-lived radicals that can be harvested for surface bio-functionalisation of a range of substrates with bioactive molecules.

As previously demonstrated in figure 1.8, the extension at which the polymerization reactions propagate depend on the feedstock of radicals available in the discharge. Therefore, the growth and properties of the plasma polymer coating are ultimately modulated by the degree of activation of the precursor molecules, and hence on the parameters at which the plasma is sustained. For instance, the precursor flow rate together with the pumping speed defines the density of precursor molecules and their residence time in the discharge. An increase in density will naturally result in the creation of more radical species, provided that the power coupled to the discharge is sufficiently high to promote dissociation and fragmentation of additional molecules. The precursor flow rate together with the pumping speed also determines the total discharge pressure. At higher pressure, the mean-free path between

species in the plasma decreases, resulting in higher electron-molecule collision frequencies and an enhanced activation of the precursor provided that the energy provided to the electrons over the shorter distance they now travel is sufficient to ionise the precursor molecules. A suitable modulation of the power delivered to the discharge is equally important in the deposition of plasma polymerised coatings. Since electrons absorb most of the coupled power, and the activation of the precursor occurs mostly via electron inelastic collisions, the feedstock of available radicals increases with further power delivery.

The deposition regime of plasma polymerised coatings is described empirically by two distinct domains, which depend on the overall energy per unit mass of the precursor, W/MF, often known as the Yasuda's parameter. Here, W is the power coupled to the discharge and M and F the molecular weight and the flow rate of the precursor. In the first domain, the energy deficiency domain, the coating deposition rate increases monotonically with an increase in W/MF. This domain takes place, for instance, when W is increased and the feedstock of precursor is maintained at a saturation level. Since an increase in the coupled power produces additional radical species that feed the polymerization reactions, the deposition rate continues to trend linearly with increasing W. The deposition rate eventually reaches a maximum and stabilises in the second domain, the monomer deficiency domain, where the power is increased to a point at which the whole reservoir of precursor molecules has become activated. A decrease in the deposition rate is generally observed at a higher W/MF as etching processes, driven by the impact of energetic ions, ablate the deposited coating. Overall, the macroscopic description of PP is a useful tool that enables the identification of different coating deposition modes based on simple analysis of the process

input parameters and the properties of the coating. Several works have been dedicated to developing more sophisticated macroscopic tools envisaging process upscaling into various industrial applications. Further details on these works and their limitations are discussed in chapter 3.

1.2.4 Dusty plasmas

Dusty plasmas are ionised gases that contain solidified particulates trapped within the plasma boundaries [91]. The natural occurrence and formation of dusty plasmas in the Universe has been widely documented. Incidentally, the list of astrophysical dusty plasmas is rather extensive and comprises most of the known forms of plasmas, including the interstellar, circumstellar and interplanetary media, nebulae, comets and planetary rings [63, 92, 93]. The occurrence of dust particles in man-made plasmas is also well known, but mostly regarded as an inconvenient source of contamination, compromising process efficiency in plasma-based manufacturing and energy applications. For instance, the formation of plasma dust grains is known to severely contaminate and render non-functional circuit components for microelectronics fabricated in plasma-assisted etching and deposition reactors [63, 94, 95]. The ablation of deposited material on the walls of Tokamaks and its subsequent condensation into dust particles is also one of the current major scientific challenges in nuclear fusion science [96].

1.2.4.1 Formation and growth of plasma dust particles (PDP)

Plasma dust particles (PDP) can be formed spontaneously through reactive plasma polymerization (see section 1.2.3) of particular precursors such as acetylene [97-99], silane [100, 101] or methane [97, 98]. Depending on the parameters chosen to sustain the discharge, the surface growth of plasma polymer coatings can occur simultaneously with the growth of PDP within the plasma boundaries. Early studies by Kobayashi et al in the 1970s established parameter windows for the formation of plasma polymerized ethylene materials in the form of thin-film, powder and oil [102, 103]. The chemical and physical phenomena of formation and growth models of PDP from a plasma-vapor phase to micrometer-sized solid particles is commonly described as multi-phase process [95, 101], depicted here in Figure 1.11. The first phase of the PDP growth model describes the plasma chemistry governing the formation of primary clusters of a few atoms (from ~10 to about ~100 atoms) from the precursor gas molecules. The spontaneous formation of these primary clusters has been hypothesized to take place via several chemical pathways but is dominantly expected to occur via ion- and/or radical-induced propagation reactions. The ionic pathway has been considered a central candidate for the formation of PDP in low-pressure and low-power regimes in both acetylene [99, 104] and silane plasmas [105]. In the first phase, the products of dissociation and activation of the precursor molecules continuously recombine with negatively-charged clusters. The clusters are mostly single charged and generally thought to be initially formed by dissociative attachment of the precursor molecule:

$$A_xB_y + \mathbf{e}^- \rightarrow A_xB_{y-1}{}^- + B \qquad (1.1)$$

followed by a sequence of addition reactions with neutrals

$$A_xB_{y-1}^- + A_xB_y \rightarrow A_{x+1}B_z^- + (\text{B products}) \quad (1.2)$$

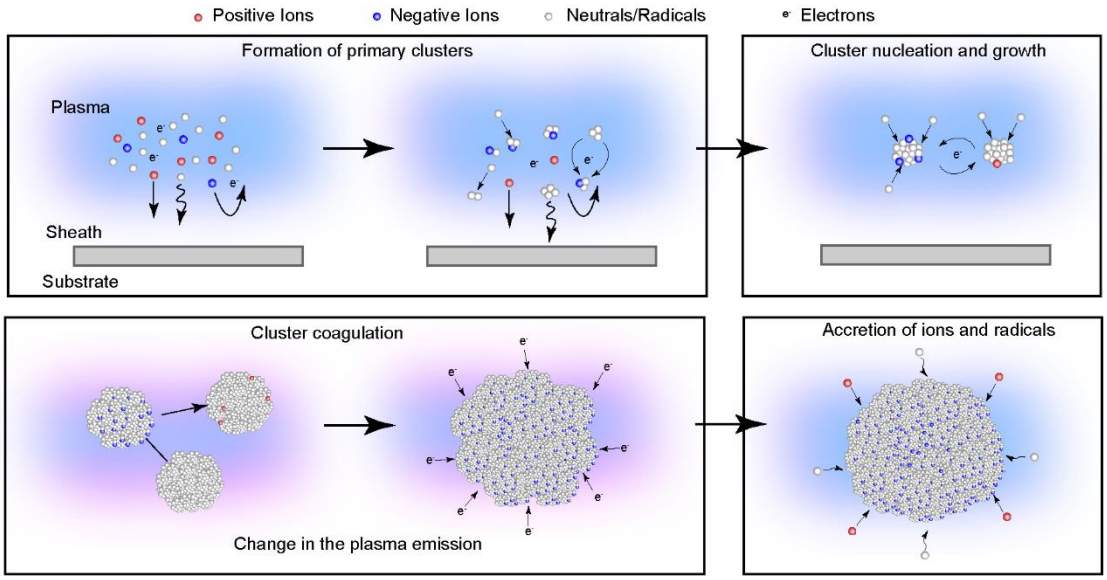

Figure 1.11: Schematic showing the various phases involved in the formation of plasma dust particles. In the first phase, the reactive nature of the plasma favours the formation of primary clusters. The primary clusters nucleate and grow in the second phase. In a third phase, rapid coagulation between clusters forms larger particles. Electron diffusion towards the particle surface drastically changes the plasma characteristics. The particles grow further via ion diffusion and radical accretion in the fourth phase. Adapted from [95].

For instance, in silane discharges the reactions (1.1) and (1.2) read

$$SiH_4 + \mathbf{e}^- \rightarrow SiH_3^- + H \tag{1.3}$$

$$Si_xH_i^- + SiH_j \rightarrow Si_{x+1}H_k^- + (H \text{ and } H_2 \text{ products}) \tag{1.4}$$

In acetylene discharges, it has been proposed [97] that the dissociative attachment reaction 1.1 generates ethynyl anions and atomic hydrogen

$$C_2H_2 + e^- \rightarrow C_2H^- + H$$

The ethynyl ions can subsequently react with the precursor molecules and initiate a sequence of polymerization reactions to form the primary hydrocarbon clusters

$$C_{2n}H^- + C_2H_2 \rightarrow C_{2n+2}H^- + H_2, \qquad n = 1, 2, 3, \ldots$$

Alternatively, it was proposed that dissociative attachment of acetylene by electron impact produces the vinylidene anion [99]

$$C_2H_2 + e^- \rightarrow H_2CC^-$$

which can also trigger the propagation reactions necessary for the formation of hydrocarbonaceous clusters

$$H_2CC^- + C_2H_2 \rightarrow C_4H_2^- + H_2$$

$$C_{2n}H_2^- + C_2H_2 \rightarrow C_{2n+2}H_2^- + H_2, n = 2, 3, 4, \ldots$$

It should be noted that both the anions and the growing negative clusters are confined by the positive plasma potential. In contrast, positive ions are lost by diffusion in the sheaths at a

faster time-scale than the rapid growth period of the clusters [62]. Therefore, cluster formation is unlikely to result from the build-up of radical neutrals with positive ions at lower pressures. However, at higher pressures the precursor fragmentation, and thus formation of clusters, is expected to occur at a faster time-scale due to an increase in electron-neutral collision frequency. Consequently, the neutral and positive ion diffusion rates may be slower than the time necessary for cluster build-up and the initial clusters may randomly be neutral, positively or negatively charged in higher pressure regimes. Note that the formation mechanisms based exclusively on the radical pathway are similar to those discussed in the RSGP model for PP of thin films in the previous section. At sufficiently high pressures some the large molecules formed in the propagation reactions will not condense on surfaces and will rather nucleate to form the initial clusters within the plasma volume [62].

During the second phase of the PDP growth model the primary clusters rapidly grow through nucleation processes up to ~5-10 nm. In this phase, the clusters may randomly acquire a positive, negative or neutral net charge, depending on the collisional mechanisms in which they participate. Since in the second phase the net charge of the clusters is only a few elementary charges, cluster charging is essentially a stochastic-type mechanism and they are allowed to easily change sign upon ionization, electron attachment or charge transfer mechanisms. In a third phase an abrupt coagulation of the clusters into larger particles is triggered when the density of the clusters reaches a critical value and exceeds the ion density [101]. In this phase particles can grow up to around 100 nm through cluster coagulation and their charging is governed by the diffusion of electrons and ions. Since the flux of electrons exceeds the ion flux the larger particles eventually build-up a significant negative net charge,

and further coagulation is prevented by inter-particle electrostatic repulsion. In this phase, the loss of electrons on the particles is substantial and may surpass electron losses in diffusion and recombination processes. Consequently, the discharge characteristics are strikingly altered during the coagulation phase. The abrupt decrease in the electron density [106] is followed by a significant increase in electron temperature [105] since less electrons share the same delivered power. The increase in electron temperature changes the ionization profile in the discharge [62] and an enhancement in the plasma emission intensity is generally observed [97, 98]. The bigger particles behave like a microscopic probe in the plasma and develop a sheath that accelerates positive ions. At this stage, the fourth phase of the PDP growth model, particles grow in size by the diffusion of ions and accretion of neutral radicals on their surface.

1.2.4.2 Charging mechanisms of plasma

Charging of dust particles in the plasma is paramount to understand their dynamics and confinement throughout the different growth phases. As discussed above, PDP acquire a net charge that is controlled by the flux of electrons and ions. Since electron are more mobile than ions, the particles usually acquire a negative net charge. In a steady-state situation, a sheath develops around sufficiently large particles so that the net current through their surface is zero. While the diffusion of charged species on PDP may dominate their charging and electric potential in most plasmas conditions, other charging mechanisms can also take place. For instance, secondary electron emission can occur upon the bombardment of energetic charged species on the particle surface. Photoelectrons can also be produced if the energy flux of photons reaching the dust particle surface is larger than its photoelectric work function. Dust particles can also emit electrons or ions through thermionic or field emission caused by

particle heating to high temperatures or a very high surface electric fields, respectively. A comprehensive review on the charging mechanisms of PDP is given in references [63] and [95].

1.2.4.3 Dynamics of plasma dust particles

The confinement of PDP within the plasma boundaries is governed by the balance of several forces acting on the particles. Generally, the electrostatic force is the restraining force that traps the charged dust particles in the plasma since the discharge potential is higher than the potential at the walls [62]. Conversely, other forces tend to drag the particles out of the active plasma toward surfaces or the pumping system (see Figure 1.12). The equation of motion for a charged PDP of mass m_p and velocity $\boldsymbol{v}_p$ in the plasma is given by [63, 101, 107]

$$m_p \frac{d\boldsymbol{v}_p}{dt} = \boldsymbol{F}_e + \boldsymbol{F}_g + \boldsymbol{F}_i + \boldsymbol{F}_n + \boldsymbol{F}_t + \boldsymbol{F}_p$$

In the equation of motion $\boldsymbol{F}_e$ is the total electric force experienced by the dust particle. In the case where particle-particle interactions and polarization forces can be ruled-out, i.e. no mutual Coulomb interactions or sheath deformation forces, the electric force term becomes purely electrostatic, $\boldsymbol{F}_{est}$. For a uniform plasma with an electric field $\boldsymbol{E}_0$ and particles smaller than the Debye length, the electric force is given in very good approximation by

$$\boldsymbol{F}_e = Q_p(\propto r_p)\boldsymbol{E}_0$$

where Q_p is the charge and r_p the radius of the dust particle. For smaller spherical dust particles (less than a micrometer) of radius r_p and mass density ρ_p the gravitational force

$$\boldsymbol{F}_g = m_p \boldsymbol{g} = \frac{4}{3}\pi {r_p}^3 \rho_p \boldsymbol{g}$$

may be negligible when compared with other forces. However, $\boldsymbol{F}_g$ becomes dominant if the particles grow to several micrometers and can exceed the applied electric force, pushing the

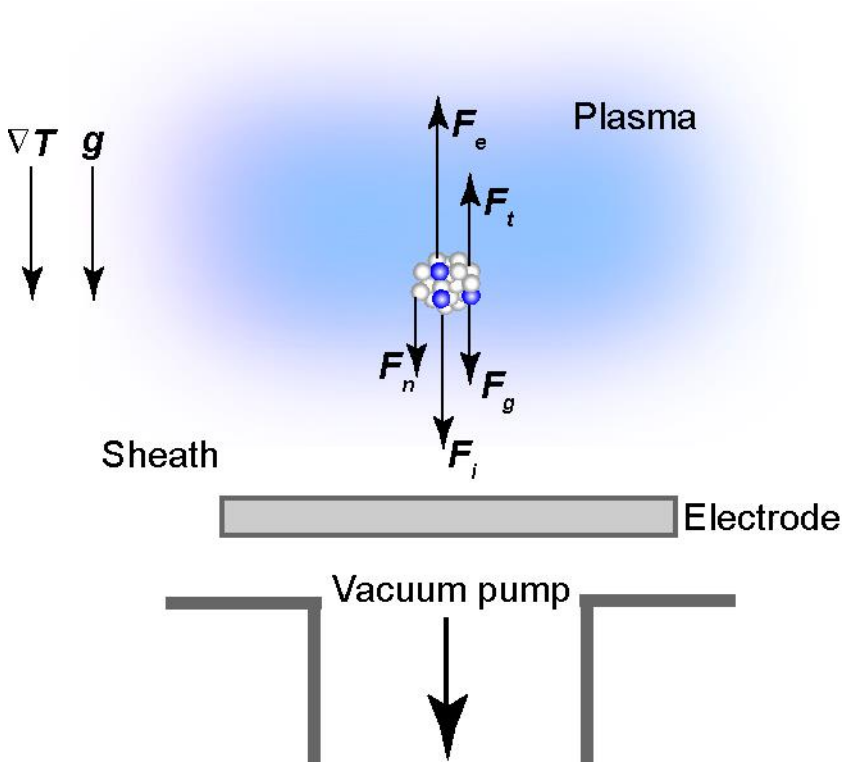

Figure 1.12: A schematic depicting the forces acting on a negatively charged plasma dust particle. The particle is repelled by the sheath and the electric force confines it in the plasma. All other forces drag the particle out of the plasma active zone. Inter-particle interactions and radiation pressure is neglected.

particles out of the plasma. The ion drag force, $\boldsymbol{F}_i$, is the force communicated to dust particles arising from a momentum transfer with positively charged ions. This force has two components arising from: (i) momentum transfer in impact collisions where the ion is collected by the dust particle, i.e. the ion drag force, $\boldsymbol{F}_i^c$, and (ii) momentum transfer in Coulomb interactions where the trajectory of the ions is deflected by the charged dust particle potential, i.e. the orbital ion drag force, $\boldsymbol{F}_i^o$. The total ion drag force can be written as

$$\boldsymbol{F}_i = \boldsymbol{F}_i^c + \mathbf{F}_i^o = \pi n_i m_i u_i \boldsymbol{u}_i (b_{\mathrm{c}}^2 + 4\Lambda b_{\mathrm{o}}^2)$$

where u_i is the total ion velocity related to the ion mean thermal and drift energy, $\boldsymbol{u}_i$ is the ion velocity acquired when subjected to the local electric field, $b_{\mathrm{c}}(\propto r_p)$ and b_{o} the impact parameters for the collection and orbital components and Λ the Coulomb logarithm. The gas drag force, $\boldsymbol{F}_n$ arises from the momentum transfer between the dust particle and neutral atoms and molecules flowing in the plasma and can be expressed, in good approximation for a stationary dust particle and specular reflection, by

$$\boldsymbol{F}_n = \frac{4}{3}\pi {r_p}^2 m_n n_n u_n^{\mathrm{th}} \boldsymbol{u}_n$$

where m_n, is the mass, n_n the density, u_n^{th} the thermal speed and $\boldsymbol{u}_n$ the velocity of the neutral gas particle. The themophoretic force, $\boldsymbol{F}_t$, arises from a higher momentum efficiency between the plasma/gas species and the particles in higher temperature regions. Therefore, this force depends on temperature gradients that pushes the particles from hotter to colder regions and can be expressed as

$$\boldsymbol{F}_t \approx -\frac{5}{4\sqrt{2}}\left(\frac{r_p}{\sigma_{\mathrm{LJ}}}\right)^2 k_b \boldsymbol{\nabla} T_g$$

where σ_{LJ} is the Lennar-Jones collision diameter for gas particles and k_b the Boltzmann constant. The radiation pressure force, $\boldsymbol{F}_p$, results from the momentum transfer between photons and the dust particles and can be written as

$$\boldsymbol{F}_p \approx \frac{n\pi {r_p}^2}{c} I_0 \hat{\boldsymbol{e}}_{\boldsymbol{r}}$$

with n the refractive index of the medium surrounding the dust particle, c and I_0 the speed and irradiance of the radiation and $\hat{\boldsymbol{e}}_{\boldsymbol{r}}$ the unit vector along the incident wave vector. Table 1.1 summarises the forces discussed above and their dependence on the dust particle radius, r_p. While the electric and gravitational forces trend linearly and with the cube of the particle radius respectively, the ion and neutral drag forces, thermophoretic force and radiation pressure force are proportional to ${r_p}^2$. Therefore, the electric force is dominant in low pressure and low temperature discharges, trapping smaller dust particles (typically up to a few tens of nanometers) within the plasma boundaries. The ion drag force competes with the electric force for particles of a few hundreds of nanometers and pushes them out of the plasma towards the walls of the reactor. Gravity takes over only when particles grow larger than a few micrometers. The dynamics of PDP and the potential dominant forces acting on the particle are discussed in chapter 5 from the analysis of the plasma emission spectra. The control of PDP dynamics in the plasma is shown to be of great importance in harvesting nanoparticles with specific physical and chemical properties.

Force	Expression	Radius dependence
Electrostatic	$Q_p(\propto r_p)\boldsymbol{E}_0$	r_p
Gravity	$m_p\boldsymbol{g}$	${r_p}^3$
Ion drag	$n_i m_i u_i \boldsymbol{u}_i (b_c^2 + 4\Lambda b_o^2)$	${r_p}^2$
Gas drag	$\frac{4}{3}\pi {r_p}^2 m_n n_n u_n^{\text{th}} \boldsymbol{u}_n$	${r_p}^2$
Thermophoretic	$-\frac{5}{4\sqrt{2}}\left(\frac{r_p}{\sigma_{\text{LJ}}}\right)^2 k_b \boldsymbol{\nabla} T_g$	${r_p}^2$
Radiation pressure	$\frac{n\pi {r_p}^2}{c} I_0 \hat{\boldsymbol{e}}_{\boldsymbol{r}}$	${r_p}^2$

Table 1.1: Forces acting on a single plasma dust nanoparticle as a function of its radius.

1.3 Plasma synthesised nanomaterials

1.3.1 Plasma-synthesised coatings

Plasma deposition technologies have been extensively used as surface modification platforms in various biomedical applications [73, 108, 109]. Plasma polymerization (PP) processes [74] that utilize carbon precursor gases are versatile deposition technologies previously employed for the bioactivation of materials used in orthopedic [60, 110] and cardiovascular devices [4, 111-113]. These techniques have the potential to deliver coatings that can be tailored to specific needs. For instance, an appropriate choice of gaseous mixtures allows for modulation of the coating chemical composition without changing the mechanical properties of the underlying implant material. This approach has been extensively explored for surface

coatings functionalized with carboxyl [114], hydroxyl [115] or amine groups [116]. The incorporation and modulation of nitrogen-rich functional groups in a variety of thin films has been shown to increase protein binding capability and regulate favorable cellular responses, including cell adhesion, proliferation and differentiation [117].

The extreme versatility of plasma-based systems could be fostered to provide a universal coating platform for biocompatible and multi-functional cardiovascular implants. A considerable number of publications have reported the viability of using plasma-based technologies for the manufacture of biofunctional coatings for cardiovascular implants. These works were recently reviewed by Wise *et al* [118]. Efforts have been made to deliver mechanically robust coatings with sufficient adhesion strength to metallic substrates. Wear and corrosion resistance due to fluid permeation after prolonged exposures to body fluids has also been a concern. With regards to coating biocompatibility, it is still not clear which physical and/or chemical properties play the most important roles. Bonding configuration, chemical composition, presence of dopants, surface roughness and wettability have been regarded has important factors predominantly affecting blood protein adsorption and cellular response such as platelet adhesion and activation.

1.3.1.1 Diamond-like and amorphous carbon coatings

The exceptional physical, chemical and tribology properties of plasma synthesised diamond-like carbon (DLC) have prompted an increasing volume of research since they were first synthesized in the form of thin films in 1971 [119]. The potential use of DLC as a biocompatible coating for medical implants in a wide range of applications has been

extensively investigated in the last two decades. A considerable number of review papers covering these investigations are now available [120-124]. The use of DLC coating for orthopaedic prostheses [110] and cardiovascular implants such as heart valves [125], guiding wires and coronary stents [113] are among the most common examples.

The designation DLC is commonly attributed to a variety of amorphous carbon-based materials that may contain different sp^2 and sp^3 carbon bond ratios as well as different hydrogen contents. Depending on the bonding configuration and the hydrogen content, DLC materials are usually sub-classified into: (i) tetrahedral amorphous carbon (ta-C) for higher sp^3 contents (typically > 70%) and low levels of hydrogen; (ii) amorphous carbon (a-C) if the ratio sp^3/sp^2 ranges between 0.4 and 0.7 and (iii) hydrogenated amorphous carbon (a-C:H) for hydrogen containing materials which are typically characterised by higher sp^3/sp^2 ratios. The properties of DLC thin films, their mechanisms of deposition and their characterization techniques were extensively reviewed in [126] and [127]. Highly hydrogenated amorphous a-C:H thin films are usually denominated by hydrocarbon plasma polymers [70, 75, 128]. As discussed in previous sections, these films are characterised by a polymer-like structure which is deposited on the substrate material. The atomic arrangement of this structure is strictly dependent on the type of carbon precursor and the process parameters used during the deposition. Carbon-based polymer-like deposits are usually highly cross-linked and may contain large concentrations of imprisoned radicals.

Carbon-based materials can be prepared as a coating in the form of a film using a wide range of plasma-based deposition techniques. Different properties of the DLC and polymer-like

carbon coatings can be tuned by setting adequate deposition parameters. For instance, ta-C thin-films prepared by arc vapour deposition [129, 130, 131] are characterised by extreme hardness (up to 80 GPa), great wear and corrosion resistance and chemical inertness. These properties make ta-C potential coating candidates for load-bearing biomedical applications . These properties make ta-C potential coating candidates for load-bearing biomedical applications [129]. However, the high internal compressive stress characteristic of thick ta-C films still remains the primary source of coating failure in orthopaedic implants [131]. The exposure of the underlying metallic substrate due to poor adhesion and delamination presents one of the major obstacles to the commercial success of DLC coatings. a-C films can be prepared using a variety of plasma-based deposition technologies. For instance, a-C materials are usually made by plasma magnetron sputtering (PMS) where a graphite target is exposed to argon plasma [132, 133]. Carbon atoms and ions are sputtered from the graphite target and are then deposited onto the substrates. Substrates to be coated are usually electrically biased [134] which allows control over the kinetic energy of the ions reaching the samples. The majority of the ions are argon and often diffuse out of the film after delivering their energy but a small fraction remains trapped in the film. Control over the bias voltage and hence the energy delivered to the growing film is characteristically used to produce films with different physical structures, surface topographies and sp^3/sp^2 ratios.

a-C:H are commonly prepared by PMS [135, 136] or by plasma polymerization [70, 75, 128, 137, 138]. In the first case, a reactive mixture of argon and hydrogen is injected in the PMS reactor. Hydrogen atoms bind with the sputtered carbon atoms leading to the deposition and growth of a hydrogenated carbon thin film. The concentration of hydrogen gas during the

deposition process can also be adjusted to yield films with different hydrogen contents, hence with diverse properties as well. Highly hydrogenated a-C:H have reduced internal stress [121] resulting in improved film adhesion to the underlying substrates [139]. Hydrogen also behaves as an etching element and increasing the hydrogen concentration in the plasma was reported to promote surface smoothness of the films [126]. Control over the chemical composition of the DLC coating by plasma polymerization is achieved by choosing different gases, or gaseous mixtures, to generate the plasma. While argon is commonly used as the background gas, different hydrocarbon precursors (acetylene, methane, ethylene, ethane, butane, etc.) are used to tailor different chemical and physical structures of the a-C:H films. For instance, increased hydrogen contents and smoother surfaces can be created by using methane (CH_4) instead of acetylene (C_2H_2) as the precursor gas [140]. Also, the incorporation of hydrogen in CH_4 plasmas was shown to reduce the coating friction and wear when deposited on steel substrates [141]. The incorporation of dopants, such as nitrogen, phosphorous, fluorine or silicon can also be easily performed by choosing the appropriate gaseous mixture. This feature is particularly interesting since the combination of these elements with DLC was shown to be paramount in tailoring the mechanical and biological performance of the a-C:H coatings. It is now generally accepted that sample bias is a fundamental process parameter in the production of DLC coatings. Films with variable sp^3 fraction [142], residual stress [143], substrate adhesion [144], refractive index [145] and hemocompatibility [146] can be prepared by adjusting solely the sample bias while maintaining constant the other process parameters. Importantly, sample bias promotes the creation of radicals in the coating's surface and bulk, allowing for a further functionalization of the coated materials with bioactive proteins, peptides and other biomolecules [89, 90].

1.3.1.2 Translation of plasma-based coatings to coronary stents – challenges

Significant efforts have been made to develop biocompatible coatings for metallic cardiovascular implants and especially for coronary stents. Although plasma discharges are perceived as a promising solution to fulfil this task, a great deal of research still needs to be carried out. Despite the increasing volume of investment and research, there is still no available plasma-based coating technology for stents proved to successfully address all the aspects of biocompatibility in humans.

Stents are three-dimensional objects with wide-ranging dimensions, aspect ratios, complex geometries and strut designs. Consequently, coating uniformity using appropriate plasma discharges such as low-pressure PP or PMS is a non-trivial task. One of the main challenges is to avoid edge and shadowing effects on the stent struts caused either by adjacent struts or by the electrical connections used to support the stent in the discharge. PP can provide stable plasma media that uniformly surround flat surfaces during the deposition process. Also, when using sample biasing, ions are accelerated uniformly towards the full length of flat surfaces when a uniform sheath lies between the plasma and the sample surface. However, the intricate design of a stent and the use of electrical and supporting contacts give rise to the development of complex plasma sheaths that are not completely conformal to the stents. For this reason, a thickness gradient in the coating across the stent outer surface is usually hard to avoid. Moreover, while the outside struts are directly coated and bombarded with energetic ions from the surrounding reactive plasma, the inner struts are exposed only to the poor plasma and less energetic ion flux inside the stent. Therefore, the physical and chemical properties of the coating are generally spatially dependent. Coating thickness, for instance, is usually thinner

on the inside struts. Importantly, the bonding configuration has also been reported to be different in the outer and inner struts with the latter showing lower sp^3/sp^2 ratios [147].

Strut shadowing is particularly accentuated when using PMS discharges as the great majority of these platforms are built with planar magnetrons providing only unidirectional sputtering. When no rotation is applied to the stent, gradients in the thickness of the coating are to be expected as thicker layers are deposited on the struts facing the magnetron. An enhancement of the coating uniformity could be achieved using, for instance, hollow cathode magnetrons (HCM) instead of planar ones. HCM discharges [148-150] use cylindrical targets that surround the samples to be coated. When the plasma is generated the sputtered material covers the outer layers of the samples facing the target. In addition, rotation can be applied to minimise shadowing of the inner struts. Using this technology could, however, still face some possible drawbacks. Shadowing would not be totally eliminated since a mechanical support to hold and rotate the stent inside the magnetron would still be required. Additionally, it is known that coating properties, such as thickness, are strictly dependent on the aspect-ratio (radius to length ratio) of the magnetron [150]. Therefore, custom-made HCM reactors would need to be built to fit specific stent dimensions, a demand that could largely decrease the cost efficiency and compromise the universality of the process.

Stent design imposes a further obstacle with regards to its surface characterization. An accurate determination of the bulk and the surface physical (roughness, wettability, etc.) and chemical (elemental composition, atomic bonding configuration, etc.) properties using the standard characterisation and spectroscopic techniques is difficult to achieve. The biocompatibility of coatings deposited on stents is even more challenging to assess *in-vitro*

since it is hard to reproduce and quantify cellular attachment and proliferation on non-two-dimensional flat surfaces.

a-C and a-C:H made by PMS and PP are generally characterised by a reduced internal stress and improved substrate adhesion when compared to ta-C films. However, and despite their excellent biocompatibility, these materials still can't fulfil all the requirements necessary for a permanent and successful translation to real medical implants, such as stents. These coatings are particularly sensitive to wear and corrosion, especially when deposited on metal substrates and exposed to saline solutions or biological fluids. It has been observed that the prolonged exposure of the coatings to fluids reduces the interfacial strength, ultimately leading to delamination and spallation at the coating / substrate interface [113, 151, 152]. Chandra *et al* [152] proposed that failure of DLC coatings after exposure to fluids, such as water and phosphate buffered saline (PBS), was related with the permeation and perforation of the solution through porosities and failures localised at the coating surface.

Polyethylene glycol (PEG) conjugated DLC coatings on nitinol flat samples revealed superior *in-vitro* hemocompatibility presenting higher albumin/fibrinogen adsorption rates and decreased platelet adhesion when compared with bare metal and DLC surfaces [153]. However, PEG/DLC coated nitinol stent performance in canine iliac arteries was substantially inferior revealing more developed neointimal hyperplasia areas compared to DLC stents and even to control non-coated nitinol stents [154]. The authors associated restenosis with the accumulation of a thick collagen layer formed due to over proliferation of fibroblasts on the PEG surface, a factor that had been overlooked in the previous *in-vitro* assays.

Kim *et al* [155] studied the mechanical properties of DLC coatings deposited on self-expandable nitinol vascular stents using a focused ion beam system and acetylene gas as a carbon precursor. Interlayers of Si were also deposited by magnetron sputtering between the stent surface and the DLC layer for assessment of potential enhancement of the coating adhesion strength. Stents were exposed to high stresses through a mechanism of stent contraction and expansion. DLC coatings deposited without Si interlayers were found not to withstand stress as delamination and spallation occurred at the strut / coating interface. Cracking and delamination was prevented when a-Si interlayer thicker than 0.6 nm was used. Unfortunately, there is no detailed information on the chemical, physical and biological characteristics of these DLC coatings. Similar results were found elsewhere [113] on DLC coated stainless steel stents. The addition of an a-Si:H interlayer substantially enhanced the mechanical stability of the carbon coatings following stent expansion. However, the adhesion of similar coatings to stainless steel flat substrates was significantly compromised after 1 month of incubation in biofluids. Endothelial cell and platelet attachment was also studied on DLC coatings deposited on Si substrates. Superior endothelialisation and reduced platelet adhesion were found for thermally annealed a-C:H films doped with Si. Unfortunately, these results were not confirmed on stents prepared in the same conditions.

Previous studies [90, 156, 157], also showed that carbon-based polymer-like coatings produced by PP with enhanced ion-bombardment possess superior biological qualities over conventional coating alternatives (e.g. chemical vapour deposition, physical vapour deposition and wet techniques such as solvent dipping). Importantly, these coatings also allow the covalent immobilization of biomolecules [157]. The possibility to conjugate bioactive

molecules to biomedical implants is particularly interesting. The development of more biocompatible stents may be achievable through a specific and controlled functionalization via the stable immobilization of bioactive proteins or peptides that can interact with the vasculature, especially by promoting endothelialisation, inhibiting the proliferation of smooth muscle cells and reducing the formation of thrombus.

Waterhouse *et al* [112] reported the feasibility and safety of delivering a prototype plasma-activated coating (PAC) *in vivo*. This coating was deposited using hydrocarbon-based radio-frequency plasma discharges and prepared with energetic ions and a graded interface between the stainless steel surface and the PAC coating to provide sufficient adhesion. Following some initial optimisation of mechanical and biological properties the coating was applied to a stent and implanted in rabbit iliac arteries. Results showed that PAC had sufficient adhesion, undergoing stent crimping and expansion, and performed equivalently in terms of re-endothelialisation when compared to bare metal stent platforms.

PAC coated 316L SS stents have been tested for both mechanical stability and *in-vivo* performance [111, 112]. The inclusion of nitrogen in acetylene/argon plasma polymerization provided improvements in the mechanical properties by reducing the compressive stress and by increasing the elasticity of the coatings. Superior ability for tropoelastin covalent immobilization on 316L flat samples was observed for coatings prepared under such conditions, which was congruent with an enhancement in endothelialisation. PAC coated directly onto stents prepared in such circumstances resisted delamination and spallation following a balloon expansion with only nano-sized cracks emerging but without exposing

the underlying strut. Graded interfaces between the metallic strut surface and PAC coatings can be made to further enhance PAC mechanical stability in animal trials [112, 157]. Although PAC alone did not present significant *in-vivo* improvements in stent biocompatibility, further functionalization of PAC surfaces with specific strongly bounded bioactive biomolecules could overcome the limitations of current stent platforms.

1.3.2 Plasma dust nanoparticles in industry and space

Fundamental research in dusty plasmas has been driven over the last decades by industry demands, mostly with the aim to supress sample contamination caused by the formation of plasma dust nanoparticles. Industrial upscaling of reactive plasma-assisted platforms, e.g. etching, sputtering and deposition, has been largely fraught by the spontaneous and undesirable formation of PDP. The unintended growth of dust nanoparticles severely compromises yield and overall process efficiency, particularly in reactive plasma etching lithography and semiconductor manufacturing using silane discharges [63]. While plasma dust nanoparticles are usually unwanted, their growth and harvesting for potential technological applications has been previously envisaged [158]. Reactive dusty plasmas provide an optimal tool that allows the incorporation of nanoparticles into thin-films using a single-step process. The inclusion of nanoparticles grown in dusty silicon-based discharges offers means to modulate the properties of nanostructured thin-films, with potential applications in microelectronics and photo-voltaic cells. However, the beneficial use of nanoparticulates in dusty plasmas is still illusive in the field and lacks further fundamental studies.

Dusty plasmas have also been studied in different scientific and technological contexts. Incidentally, our knowledge of the formation, growth and dynamics of PDP was significantly driven by the discovery of Coulomb crystals [159], formed in strongly coupled dusty plasmas, and bolstered by the development of advanced plasma diagnostic techniques. In astrophysics, carbonaceous nanoparticles produced in acetylene dusty plasmas have been proposed as analogues to the dust grains formed in the interstellar medium [160]. Comparison between the infrared spectra of the carbonaceous plasma dust and the dust grains found in the diffuse interstellar medium revealed remarkable similarities in the aliphatic carbon component, a common tracer of the carbonaceous component of the ISM dust [161, 162]. More recently, a plasma facility (COSmIC) [163] was used to simulate the environments found in the interstellar medium and study the formation and destruction mechanisms of the ISM dust. Results have suggested that plasma polymerization of acetylene can trigger the formation of polycyclic aromatic hydrocarbons, which are thought to be the building blocks of carbonaceous particles in the outflow of carbon stars [163].

Whether dusty plasmas are considered a challenge in manufacturing industries, or provide a rather versatile platform for industrial applications or a simulation tool for astrophysical plasma environments, the potential of PDP in nanomedicine has been entirely overlooked. The ability of producing nanoparticles in a wet-chemistry-free plasma environment could potentially pave the way for a cost-effective synthesis of unique multifunctional nanocarriers with selected physical and chemical properties. This work shows for the first time evidence that nanoparticles can be synthesised and harvested in a reactive dusty plasma with easily

modulated properties suitable for personalised nanomedicine. The results presented in this work could potentially represent a paradigm shift in the technological impact of plasma science, in particular dusty plasmas.

1.4 Thesis aims and chapter organization

Including the General Introduction (**Chapter 1**) and Final Remarks (**Chapter 7**) chapters, this thesis comprises of a total of seven chapters, and is organised as follow:

- **Chapter 2** reports the methods and materials used throughout multiple chapters in this work, including a detailed description of the plasma polymerization apparatus, optical emission spectroscopy (OES) and materials characterization methods such as X-Ray photoelectron spectroscopy (XPS), Fourier transform infrared spectroscopy (FTIR) and electron spin resonance spectroscopy (ESR).

- **Chapter 3** carries out a comprehensive characterization and optimization of plasma activated coatings (PAC) produced under various plasma polymerization process parameters. Optimal PAC formulations characterised by exceptional mechanical and substrate adhesion properties are identified. A PAC growth mechanism is proposed based on correlations between OES diagnostics and coating characterization.

- **Chapter 4** demonstrates the feasibility of translating the optimal PAC formulations identified on Chapter 3 to vascular stents of various designs and made of various alloy compositions. The hemocompatibility of PAC is also assessed using human blood under both static and flow conditions.

- **Chapter 5** identifies the formation of plasma polymerized nanoparticles (nanoP^3) through OES measurements during the deposition PAC. The removal and collection of nanoP^3 from the plasma is optimised by identifying the mechanisms involved in the formation, growth and removal of the particles in the plasma, and by exploring a wide range of process parameters and adopting three-dimensional well-shaped substrates.

- **Chapter 6** bioengineers nanoP^3 with modulated physical, chemical and biological properties and demonstrates for the first-time that carbonaceous nanoP^3 produced in dusty plasmas can be adopted as multifunctional nanocarriers. It is shown that a wide range of biomolecules with various molecular weights, structures and biological functions can be immobilized on the nanoP^3 surface in a simple one-step incubation process and without the use of conventional chemistry that is usually adopted on commercially available nanoparticle platforms.

2 GENERAL METHODOLOGY

This chapter reports the materials and methods used throughout multiple sections in the thesis. The methodology particular to a given chapter is defined within.

2.1 Plasma polymerization process

2.1.1 Apparatus

Plasma polymerization was carried out using a cylindrical stainless steel capacitively coupled radio-frequency (ccrf) reactor with enhanced ion bombardment provided by dc high voltage pulsing of the substrate (see Figure 2.1 and 2.2). Prior to each run the reactor was pumped down to a base pressure of ~10^{-6} Torr using a dual dry vacuum pump system comprised of an Ebara PDV250 and a turbomolecular pump (Edwards NEXT400). Reactive gas mixtures of argon, nitrogen and acetylene were used to sustain the plasma discharge and were introduced through a shower-head like apparatus located at the top of the chamber. The flow rate of each gas was individually controlled by an Allicat Scientific mass flow controller and the working pressure, measured by a full range gauge (PFEIFFER PKR251). A butterfly-type valve was placed between the chamber and the pumping system and was adjusted to control the pumping efficiency and therefore the residence time of the species in the active plasma. Plasma discharges were generated and sustained by coupling the rf power, supplied by a 13.56 MHz (Eni OEM-6) frequency generator, to the top electrode using a purpose built matching network. A second electrode 10 cm from the rf electrode was electrically connected to a DC high voltage pulse generator (RUP 6-25) to provide bias voltage, V_{bias} pulses. Pulse frequency and duration were set at f_{bias} = 3 kHz and τ_{bias} = 20 μs respectively for all runs except where stated otherwise. All current and voltage waveforms were recorded by a digital oscilloscope (Agilent DSO-X 3024A with a bandwidth of 200 MHz and a sampling rate of 5 GSamples s^{-1}). Rf and pulsed bias current and voltage waveforms were measured using custom-built current and voltage probes placed as close as possible to the rf and pulsed biased electrodes. The rf power coupled to the discharge was determined by evaluating the incident power

Figure 2.1: Photograph of plasma polymerization apparatus in the School of Physics used in this work. The cylindrical SS chamber was used here for PAC deposition and synthesis of nanoP^3.

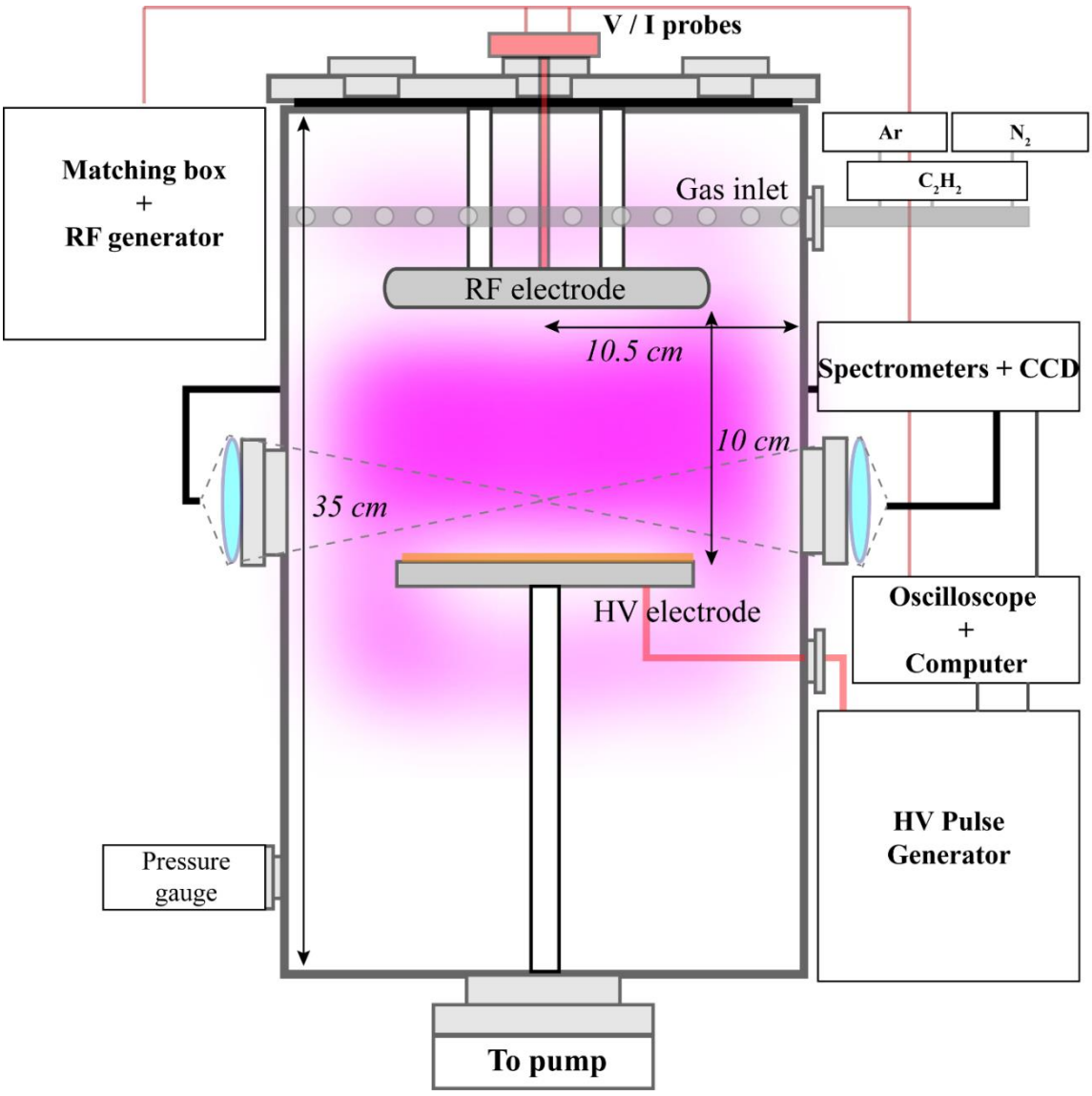

Figure 2.2: Schematic representation of a longitudinal section of the plasma polymerization chamber used in this work.

measured at the frequency generator with and without the plasma discharge for equivalent V_{rf} values. This method has been applied to correctly obtain the power coupled in ccrf discharges by taking into account power losses in the external electric circuit provided that V_{rf} is measured sufficiently close to the rf electrode [62].

2.2 Optical emission spectroscopy (OES)

2.2.1 Theoretical background

Optical emission spectroscopy (OES) is a well-established and essential diagnostic tool for low-temperature plasmas. OES is non-invasive, providing measurements on a wide range of collisional processes and plasma macroscopic parameters without affecting the plasma characteristics. The versatility of this diagnostic tool makes it valuable for various plasma-assisted applications, ranging from material processing to nuclear fusion. Using a spectrometer, the radiation emitted by excited atoms, molecules and their ions is collected and decomposed into an emission spectrum, i.e. several radiative lines or bands with well-defined central wavelengths. The spectral fingerprint of each spectrum is exclusively dependent on the gas used to generate the plasma. The collisional and radiative mechanisms that take place in the plasma govern the relative intensity and shape of the different emission lines and bands.

The discharge emission in the visible spectral range originates from transitions between electronically excited atoms and molecules. Analysis of the emission spectrum allows determination of the atomic and molecular species that populate the plasma, which can in turn

be correlated with their mechanisms of excitation and various plasma macroscopic parameters. The central wavelength, λ_i^j, for a given radiative transition $i \longrightarrow j < i$ is related with the energy gap between the upper i and the lower j states:

$$\lambda_i^j = \frac{hc}{E_i - E_j}$$

where E the energy of the excited state, h the Planck's constant and c the speed of light. The radiative intensity of a given atomic line or molecular band is proportional to the number density of the upper (emitter) state, N_i, and given by:

$$\epsilon_i^{\ j} \propto N_i A_i^j \frac{hc}{\lambda_i^j}$$

with A_i^j the Einstein coefficient (or transition probability) for the spontaneous radiative emission $i \longrightarrow j$. In this work, the plasmas are generated in $C_2H_2/N_2/Ar$ atmospheres. Therefore, the optical fingerprint is mostly dominated by molecular emission bands. As in atoms, the molecular electronic states can also be specified by their molecular term symbols

$$M(n^{2S+1}\Lambda_{u,g}^{+,-})$$

with $\Lambda = 0, \pm 1, \pm 2, \pm 3$ (corresponding to the Greek symbols $\Sigma, \Pi, \Delta, \Phi$) describing the overall angular momentum on the internuclear axis. For the Σ states, the right-hand superscripts $+, -$ indicate if the wave function is symmetric $(+)$ or anti-symmetric $(-)$ with respect to reflection at any plane, including the internuclear axis. The subscripts u, g denote whether the wave function is symmetric (g) or anti-symmetric (u) with respect to inversion through the centre of symmetry of the molecule. For instance, the ground electronic state of N_2 is $X^1\Sigma_g^+$ with $n = X$. The selection rules for electric dipole radiation of excited molecules require:

$$\Delta S = 0;\ \Delta \Lambda = 0\ or\ \pm\ 1;\ \mathrm{g} \leftrightarrow u$$

Diatomic molecules have additional degrees of freedom and quantization of their energy levels varies greatly from the atomic case. The atomic nuclei in a molecule vibrate (i.e. stretch and compress) about an equilibrium separation and the energy associated with this movement cannot be neglected. In addition, the whole molecule can also rotate about its centre of mass. For each electronic state, the total potential energy of the molecule depends on the internuclear distance, giving rise to multiple bound vibrational states for a given electronic configuration. In turn, multiple bound rotational states can also exist for each vibrational state. Therefore, the total energy of a diatomic molecule for a given electronic state, E, is given by:

$$E = E_e + E_\upsilon + E_r$$

where E_e is the minimum energy of each electronic state, E_υ is the vibrational energy and E_r the rotational energy. Figure 2.3 shows an example of a potential energy curve as a function of the internuclear distance for two electronic states. The asymmetrical potential curve of a diatomic molecule can be emulated by a Morse potential:

$$V(r) = D_e\left[1 - \exp\left(-\beta(r - r_0)\right)\right]^2$$

where D_e is the dissociation energy given by the depth of the potential well and β a constant associated with the force constant of the bond at equilibrium. Solving the Schrodinger equation for the molecule electronic wave function using the Morse potential, one can find the energy E_υ for each vibrational level:

$$E_\upsilon = \hbar\omega_e\left(\upsilon + \frac{1}{2}\right) - \hbar\omega_e x_e\left(\upsilon + \frac{1}{2}\right)^2$$

with $\omega_e = \beta\sqrt{2D_e/\mu}$ the fundamental frequency of the vibration, μ the reduced mass of the molecule and $x_e = \hbar\omega_e/4\,D_e$. Note that the first term corresponds to the quantization of

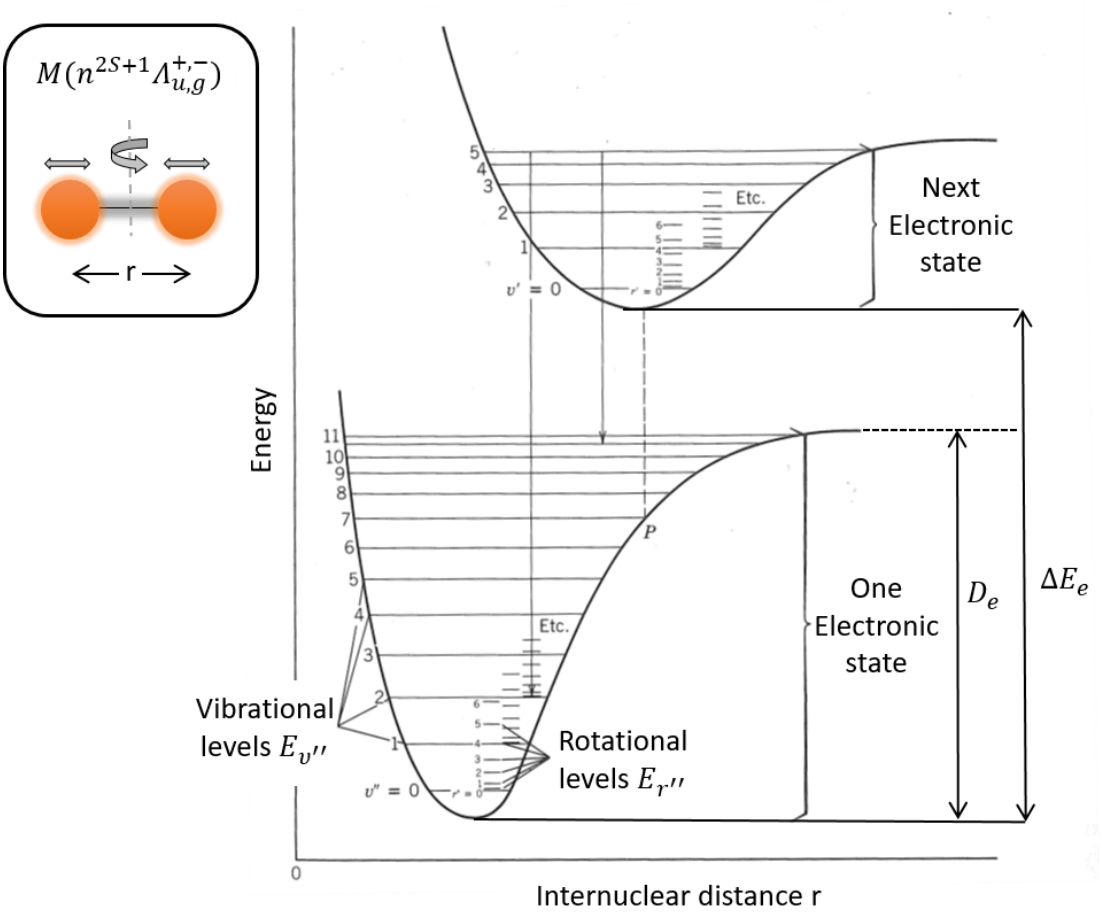

Figure 2.3: Energy diagram of a diatomic molecule. Figure adapted from [164].

levels in a harmonic oscillator, valid here for low ν values, i.e. when the potential curve is described approximately by a parabola.

The vibrational and rotational processes play a fundamental role in a plasma. Rotational excitations play the role of plasma thermometer, whereas the vibrational excitations can trap energy, due to their adiabatic character, and play the role of energy reservoir, through which the plasma becomes chemically reactive. Vibrational levels of diatomic molecules are not degenerate and the number density of molecules with a given vibrational quanta υ should follow a Boltzmann distribution at a vibrational temperature T_υ:

$$N(\upsilon') = N(0)\exp\left(-\frac{E_{\upsilon'}}{k_B T_\upsilon}\right)$$

Because the rotational quanta are generally small (see Figure 2.3), energy transfer (relaxation) in rotational-rotational (RR) and rotational-translational (RT) collisional processes within molecules are usually non-adiabatic. In general RT relaxation is a fast process usually requiring only several collisions. In most systems, the rates of the rotational relaxation processes are comparable with the rate of thermalization, i.e. translational-translational (TT) relaxation. Consequently, the rotational and translational degrees of freedom of N_2 molecules can usually be assumed in thermal equilibrium with each other, and the rotational temperature, T_{rot}, is assumed to represent the gas temperature, T_{g}. When the spectral resolution of the spectrometer is sufficiently high to separate the different rotational structures ($\delta\lambda \lesssim 0.02$ nm), T_{rot} can be calculated using a Boltzmann plot or by appropriate fitting the rotational-vibrational band-head envelope. However, this approach is limited when lower resolution spectrometers are used to record the discharge emission. Alternatively, the rotational

temperature can be determined by taking into account the strong dependence of the emission intensity of band-heads in the nitrogen first positive system (FPS), $B^3\Pi_g \longrightarrow A^3\Sigma_u^+$ with T_{rot}. This method compares experimentally measured and theoretical spectra of the band head of the FPS (2-0) at a given spectral resolution and proposes a semi-empirical formula for T_{rot} that depends on the ratio of the emission intensities related with the band sub-heads at 774.3 nm and 775.8 nm [165]:

$$T_{\text{rot}} = \frac{195}{[I(775.8\text{ nm})/I(774.3\text{ nm})] - 0.52}$$

2.2.2 Apparatus

The radiation emitted by the plasma was captured by two different optical fibers placed in line of sight with the plasma region immediately above the sample holder and optically coupled to two UV-VIS-NIR spectrometers. An Ocean Optics HR 4000, with a spectral resolution of ~ 0.2 nm, was used to obtain spectra covering a wavelength range of 200 – 1000 nm from the discharge. For an improved signal-to-noise ratio, 10 scans at integration time 300 ms were averaged for each acquisition. The line intensities were obtained by averaging all of the acquisitions for each deposition run. High resolution spectra were obtained using an Acton SpectraPro 2750 spectrometer (Princeton Instruments, USA) equipped with a 1200 grooves mm^{-1} grating, resulting in a nominal resolution of 0.014 nm for an entrance slit opened at 50 μm. Discharge emission spectra were captured by a PI-MAX (Princeton Instruments, USA) intensified charge-coupled device (ICCD) with a 1024 x 1024 pixel array optically coupled with the spectrometer's exit plane. The ICCD exposure time was 300 μs and 150 consecutive acquisitions were averaged to maximize the signal-to-noise ratio. The entire optical setup remained unchanged throughout the experiments.

2.3 X-ray photoelectron spectroscopy

Surface chemistry characterization of PAC and nanoP[3] was performed using X-ray photoelectron spectroscopy (XPS) with a SPECS-XPS instrument (Germany) equipped with a hemispherical analyzer and an Al Kα monochromatic X-ray source. The system was operated at a constant pressure of ~10^{-9} torr, with a takeoff angle of 90 ° at a power of 200 W. Survey spectra of the samples were scanned in the energy range 100 eV – 1400 eV using a step energy of 1 eV and a pass energy of 30 eV. High resolution scans for C1s, N1s and O1s were recorded with a step energy of 0.03 eV and a pass energy of 23 eV. Analysis was performed using CasaXPS software. The atomic fraction in the samples was determined by calculating the integrated areas of the C1s, N1s and O1s peaks. Peak fitting was carried out by adopting a Shirley background and convoluted Lorentzian (30%) – Gaussian (70%) line shapes with identical full-width half maximum for each component. Charge compensation was applied in all spectra by setting the C-C/C-H component in the C1s peak to a binding energy of ~285 eV.

2.4 Fourier transform spectroscopy in attenuated total reflectance mode (FTIR – ATR)

Infrared spectra were recorded by means of Fourier transform spectroscopy in attenuated total reflectance mode (FTIR-ATR) using a Digilab FTS7000 spectrometer (Holliston, MA, USA) equipped with a trapezium germanium crystal. Spectra were acquired by averaging a total of 500 scans at a spectral resolution of 4 cm^{-1} in the wavenumber range 650 cm^{-1} – 4000 cm^{-1}. Spectral subtraction and baseline correction was applied to eliminate background signals from the underlying substrates.

2.5 Electron paramagnetic resonance spectroscopy

The detection of unpaired electrons was carried out by means of EPR spectroscopy using a Bruker EMXplus X-band spectrometer on PAC coated polystyrene substrates (6 cm x 6 cm x 25 μm). Spectra were collected with a center field of 3510 G, sampling time of 90 ms, modulation amplitude of 3 G, modulation frequency of 105 Hz and microwave frequency and power of 9.8 GHz and 25 mW respectively. To exclude spin activation due to ion bombardment of the substrate, the EPR spectrum of plasma treated PS substrates in N_2+Ar atmospheres was measured for the various $|V_{bias}|$ values adopted in this work. Quantitative analysis using a weak pitch (~10^{13} spins / cm) Bruker standard sample was carried out to estimate the spin density of background subtracted PAC coated PS substrates.

2.6 Scanning electron microscopy

SEM was performed with a Zeiss ULTRA Plus or a Zeiss Sigma HD FEG scanning electron microscope at acceleration voltages ranging 3 – 10 kV and a working distance between 3 and 12 mm.

3 PLASMA-ACTIVATED COATINGS (PAC)

3.1 Introduction

The ultimate aim for biomimetic interfaces for medical implants is complete implant integration free of unwanted adverse foreign-body responses and the associated post-surgery complications [90]. For cardiovascular devices, and in particular stents, there are multiple physical and biological demands for a successful coating. In addition to outstanding adhesion strength and structural integrity following plastic deformation during deployment, biofunctional stent coatings should reduce the thrombogenicity intrinsic to many implantable devices [166] and address the exaggerated healing response which leads to vessel re-narrowing, called restenosis, over time. This can either be through the enhanced recruitment of luminal endothelial cells [167] or the active suppression medial smooth muscle cells [168] or a combination of these two strategies. Contemporary drug-eluting stents have ongoing problems with thrombosis and appropriate healing [169], leading to continued research into stent functionalization with biomolecules found in the vasculature [118]. For this purpose, a strong covalent coupling between the surface coating and the biomolecule layer is preferable over weak physisorptions, while the bioactivity of biomolecules after immobilization must be preserved. Accordingly, new platforms that combine robust mechanical performance with hemocompatibility and facilitate rapid and robust coupling with bioactive molecules [5] would be advantageous. Sample to sample reproducibility is also paramount, especially since process upscaling is ultimately necessary for industrial and commercial applications. Addressing these issues is technologically challenging, and necessitates the identification of ideal parameters windows for process optimization and stability as well as the development of feedback control strategies to keep the process within the desired operation windows.

3.1.1 Mechanical performance of plasma-synthesised coatings

In addressing coating implant adhesion and corrosion resistance under exposure to biological fluids, Si-containing interlayers have been previously deposited between the coating and the substrate [151, 170]. Using a combination of magnetron sputtering and plasma polymerization, metal to carbon graded interfaces have also been shown to impart enhanced coating adhesion strength for in vivo deployment of coronary stents [112, 157]. The majority of studies reported so far address only specific aspects of the coatings and there are no approaches as yet that draw together, in a single step process, all the necessary coating properties and characteristics for medical implants.

A great amount of research has been undertaken to address the issue of coating failure due to poor substrate adhesion, wear and corrosion. A popular approach directed to improving adhesion is to increase the interfacial strength between substrates and carbon-based coatings through the addition of interlayers [151, 152, 155, 170-173]. The deposition of silicon-based thin layers between metallic substrates and DLC coatings, prepared by rf – PP, can significantly increase the adhesion strength of DLC to stainless steel (SS) substrates. SiN_x interlayers have been reported as particularly effective for the enhancement of both adhesion and coating corrosion resistance of samples incubated in saline solution up to 2 years [151]. The deployment of an a-Si:H to a-C:H graded interface (also prepared by rf – PP) was shown to increase the adhesion strength and corrosion resistance of DLC on Ti alloys [152]. The addition of 90 nm thick Si interlayers prior to DLC deposition on CoCrMo substrates resulted in a substantial enhancement in the adhesion strength when compared to samples without the interlayers [173].

Further enhancement of DLC adhesion strength to metallic substrates can be fostered by creating a graded interface between the metal surface and the carbon layer. Graded metallic interfaces were previously reported and performed on SS substrates prior to the deposition of carbon-based plasma polymers (a-C:H) using a low pressure plasma magnetron sputtering system [157]. A SS target is bombarded by energetic argon atoms coming from the plasma, which ultimately leads to the sputtering of metallic species from the target and their subsequent deposition on the substrate surface. If a hydrocarbon precursor (such as acetylene) is gradually added to the plasma during the sputtering process, it is possible to create a metal-carbon graded interface. This graded interface is characterised by an increasing carbon to metal content from bottom to top with the top layer being exclusively composed of DLC or a carbon-based plasma polymer. The adhesion strength of DLC coatings to SS substrates prepared with graded layers was reported to be greater than 26 MPa. This value represents an improvement of at least 260% when compared to coating deposited directly on the same substrates [157].

3.1.2 Macroscopic description of plasma polymerization

To successfully translate new device coatings for clinical applications, the process needs to be scalable and incorporate appropriate feedback control strategies. Comprehensive process parameterization is an essential first step toward identifying optimal deposition windows, which will vary depending on the required coating specifications. However, the plasma medium in PP is exceptionally complex and identifying the main physical quantities that allow a suitable formulation and description of the coating growth mechanisms is challenging. Macroscopic descriptions have been used to provide simplified interpretations of the

deposition mechanisms in PP [75, 174, 175]. Typically, these strategies rely on the control of the energy coupled to the discharge and the flow of the monomer gas to estimate the monomer activation energy and the deposition regime. Higher energy inputs per monomer molecule in the discharge provide enhanced coating adhesion strengths [72, 176]. However, when surface functionalization is necessary, very high energy inputs can lead to a complete and unintended fragmentation of functional groups in monomers such as acrylic acid and allylamine [114, 177, 178]. The use of a macroscopic description alone is an inherently over simplistic approach since it fails to predict the channels of creation and destruction of relevant species in the plasma. In situ screening of the discharge can be used to pinpoint energetic and reactive species (ions and reactive radical molecules) that play competing roles in coating ablation and growth. Non-invasive plasma diagnostic tools, such as optical emission spectroscopy (OES) [179, 180], can thus be used to gain a more detailed understanding of the plasma medium during coating deposition. Combination of a macroscopic description with OES [175] and coating physicochemical and biological characterization can ultimately lead to the development of universal process parameterization strategies and the identification of suitable working windows.

This chapter reports the design and optimization of a single step ion assisted plasma deposition process to create plasma-activated coatings (PAC) that meet the extreme mechanical demands for cardiovascular implants and in particular stents. By combining OES diagnostics with a comprehensive macroscopic process description to isolate key growth mechanisms, an ideal working window in the parameter space is identified and effective process control is enabled. It was found that high energy input per gas molecule and mild

applied substrate bias enables the formation of coatings that resist delamination under the harsh implant deployment conditions.

3.2 Materials and methods

3.2.1 Substrates

Plasma-activated coating (PAC) was deposited on a variety of flat substrates including: (i) 8 cm x 10cm x 35 μm stainless steel (SS) alloy 316L (Brown metals, USA), (ii) 8 cm x 10cm x 250 μm cobalt chromium (CoCr) alloy L605 (High Temp Metals, Inc. Sylmar, USA), (iii) 8 cm x 10cm x 70 μm Zirconium (Firmetal, China), (iv) 1 cm x 1cm x 300 μm Boron doped silicon double side polished wafers (Addison Engineering, USA) and (v) 6 cm x 6 cm x 25 μm Polystyrene (GoodFellow, England). All substrates (excluding polystyrene) were cleaned prior to PAC deposition using a cleaning protocol with solvents followed by an argon plasma cleaning to remove surface contaminants arising from the material production process and exposure to the laboratory environment. The cleaning protocol with solvents was performed using high purity (>99.5%) ethanol, acetone and toluene, all purchased from Sigma-Aldrich, USA. Samples were immersed and sequentially ultrasonicated in toluene, acetone and ethanol for 10 minutes and dried with high purity compressed nitrogen. Following washing, substrates were loaded to the plasma polymerization chamber for further surface cleaning with an argon plasma. The plasma was sustained for 15 min at a radiofrequency power of 75 W. The flow of argon was 40 sccm and the pumping efficiency was set to achieve a constant pressure in the chamber of 80 mTorr. A high voltage pulsed bias (V_{bias} = -750 V) was applied to the sample holder for an enhanced ion-bombardment on the surface of the substrates.

3.2.2 Plasma polymerization deposition parameters

Process parameters were varied in two different experimental series to tailor specific physico-chemical properties in the coatings. In the first series, only the carbon precursor flow rate, $Q_{acetylene}$, was changed while maintaining all other process parameters constant. The minimum and maximum values for $Q_{acetylene}$ were 1 sccm and 10 sccm corresponding to hydrocarbon contents in the plasma of 7.1% and 43.5% respectively. The second series dealt with changes in V_{bias} applied to the bottom electrode (sample holder). Here V_{bias} was increased from floating potential, $|V_{bias}| = V_f$ where V_f is the floating potential, to -1 kV for each value of $Q_{acetylene}$ of the first series. In total 30 different set of samples were prepared and characterized.

3.2.3 Nanoindentation

Nanoindentation was performed using a G200 Nano Indenter (Agilent) with a displacement and loading resolution of 0.01 nm and 50 nN respectively. The nanoindenter was equipped with a calibrated Berkovich diamond tip with a Poisson ratio of 0.18. Thermal drift corrections were applied and the allowable maximum drift rate was 0.05 nm/s. The loading rate was set at 0.02 nm/s and the applied load ranged between 0.02 mN and 19 mN. 375 indentations were performed on each sample and the results presented here are averages of 25 indentation cycles made in different regions of the sample. Contact stiffness, residual area, indentation depth and reduced Young's Modulus were determined by analysing the unloading curves using the Oliver-Pharr method [181]. The maximum indentation depth was no more than 10 % of the total film thickness to minimize the substrate influence.

3.2.4 Substrate adhesion assay

To test PAC adhesion to SS substrates tensile and compressive forces were applied by bending and folding the coated samples inward and outward with small radii of curvature[182]. Whenever possible, samples were coated with coatings of the same thickness so as to eliminate thickness dependencies and adhesion was qualitatively assessed by imaging the deformed samples with optical and electron microscopies.

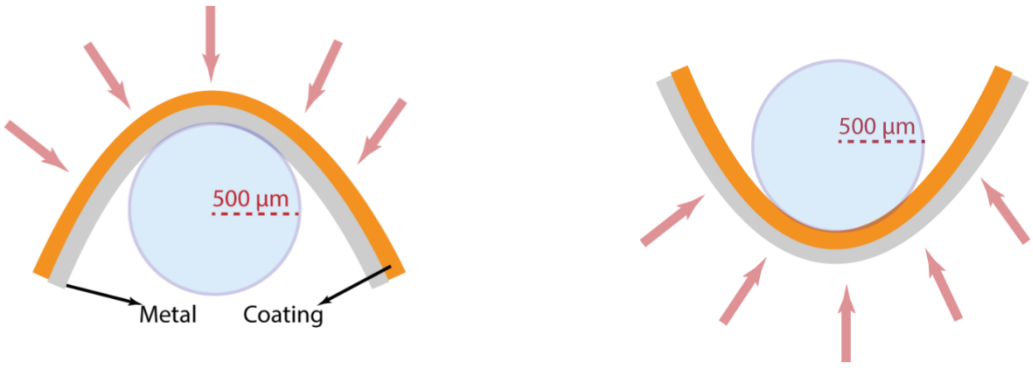

Figure 3.1: Schematic diagram showing the adhesion assay used in this work to test the mechanical properties of PAC deposited in flat metallic substrates. Tensile stress was emulated by bending the coated substrates against a rod (500 µm diameter) with PAC on the outside of the sample (left). Compressive stress was applied by folding the sample against the rod with PAC in the inside of the sample (right).

3.2.5 Spectroscopic ellipsometry

The thickness and optical constants of the coatings deposited onto Si substrates were determined by spectroscopic ellipsometry using a Woollam M2000V spectrometer and the WVASE32® software. SE data acquisition was performed at three angles of incidence (65º, 70º and 75º) and covering a spectral region ranging from 200 nm up to 1000 nm. A Cauchy

layer was implemented in the model to represent the coating on top of Si substrates of which the oxide layer thickness and optical parameters were previously determined. A point-by-point fit of the experimental SE data was performed until model convergence was achieved. The error between the measured and calculated ellipsometry parameters was monitored and a convergence criterion mandating relative errors smaller than 8% was used.

3.3 Results and discussion

3.3.1 Process parameterization and deposition rate

The key parameter generally adopted to describe macroscopically the deposition of thin films in PP processes is the energy input per monomer unit mass *W/F*, where *W* is the power (in Watts) coupled to the discharge and *F* the monomer mass flow (in kg/s) [75]. In this work, the deposition of plasma-activated coatings (PAC) is performed on biased substrates and inside an asymmetric ccrf discharge wherein the plasma is sustained in reactive $C_2H_2/N_2/Ar$ atmospheres. Therefore, a suitable macroscopic description of the deposition process must consider additional physical and geometric considerations such as: (i) power consumption and gas flows outside the active plasma region [183], which do not contribute to PAC deposition at the substrate and (ii) the contribution of reactive but non-polymerizable (N_2) and carrier (Ar) gases to film growth [174].

Therefore, the overall energy coupled to the gas particles that are expected to contribute to PAC deposition at the substrate and within the active plasma region must be estimated. In the current reactor configuration (see Figure 3.2) the total discharge volume (V_{disc}) is not

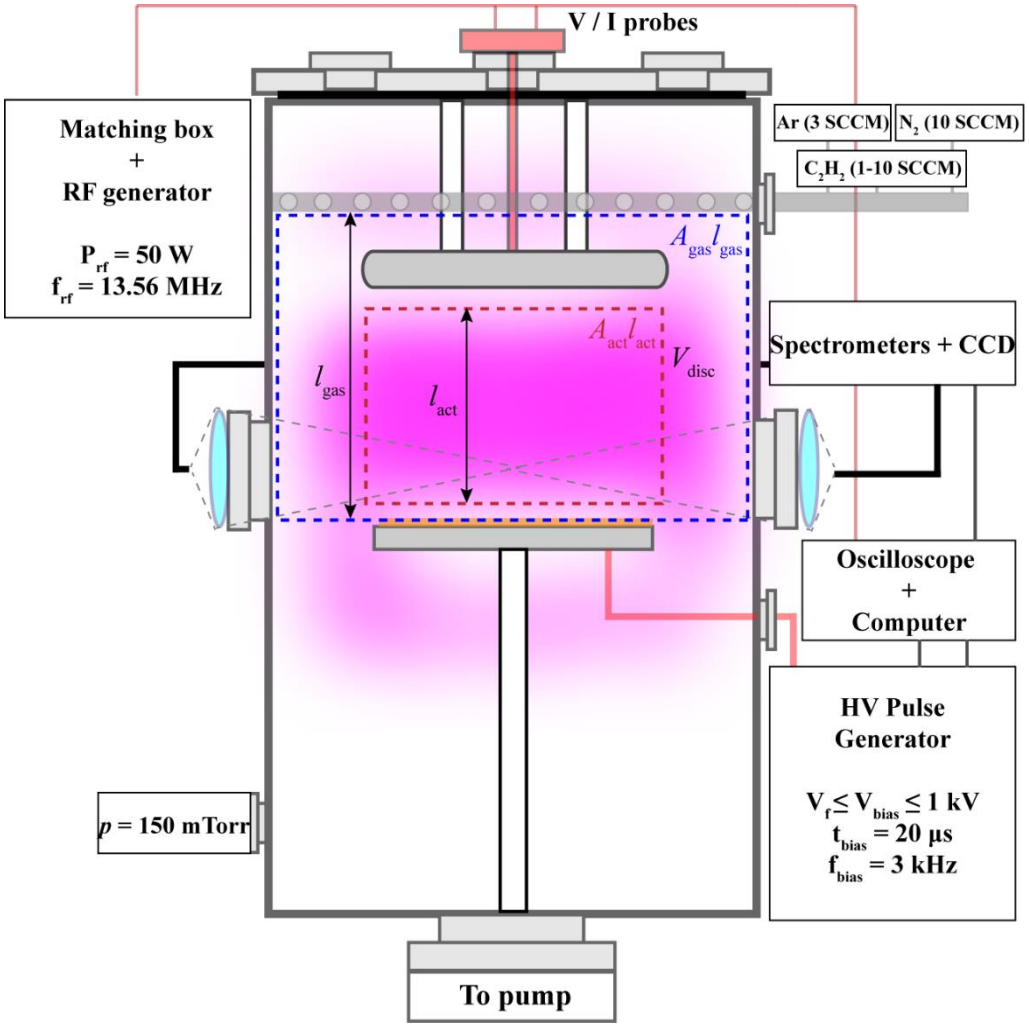

Figure 3.2: Schematic of the plasma polymerization system used in this work. The radiofrequency power is coupled to the top electrode while samples to be coated are electrically connected to the pulsed bias high voltage (HV) bottom electrode. The gaseous mixture is introduced at the top of the chamber by a shower-head like apparatus. Optical emission spectroscopy and electrical diagnostics were implemented to monitor the discharge characteristics during deposition of plasma activated coatings. The active discharge volume ($A_{act}l_{act}$), total discharge volume (V_{disc}), total gas volume ($A_{gas}l_{gas}$), l_{act} and l_{gas} are depicted.

exclusively confined to the active plasma region. Therefore, power losses outside the deposition area ($A_{\mathrm{act}} = 144$ cm^2) must be taken into account. The effective power coupled to the active discharge region can be written as

$$W_{\mathrm{eff}} = W \frac{A_{\mathrm{act}} l_{\mathrm{act}}}{V_{\mathrm{disc}}}, \tag{3.1}$$

where $W = W_{\mathrm{rf}} + W_{\mathrm{bias}}$ is the total power delivered to the plasma from the radiofrequency (W_{rf}) and pulsed bias ($W_{\mathrm{bias}} = \frac{1}{T}\int_0^T V_{\mathrm{bias}}(t) I_{\mathrm{bias}}(t)\, dt$, with the integral calculated over one pulse with period T) generators and $A_{\mathrm{act}} l_{\mathrm{act}}$ is the active discharge volume. Additionally, only a fraction of the gas flows through the active plasma region and contributes to the deposition of PAC onto the samples. The effective gas flow contributing to the deposition of PAC is given by

$$F_{\mathrm{eff}} = F \frac{A_{\mathrm{act}}}{A_{\mathrm{gas}}} = F \frac{A_{\mathrm{act}} l_{\mathrm{gas}}}{A_{\mathrm{gas}} l_{\mathrm{gas}}} = F \frac{A_{\mathrm{act}} l_{\mathrm{gas}}}{V_{\mathrm{gas}}}, \tag{3.2}$$

where A_{gas} is the cross-sectional area through where the gas flows and $F = F_{\mathrm{C_2H_2}} + \alpha F_{\mathrm{N_2}} + \beta F_{\mathrm{Ar}}$ is the total gas flow with α and β weighing factors that take into account the contribution of nitrogen and argon into the polymerization process [174, 184]. The effective energy per unit mass (in J/kg) that is channelled for the deposition of PAC onto the samples in the electrically biased electrode can be obtained from the equations 3.1 and 3.2

$$\Phi_d = \frac{W_{\mathrm{eff}}}{F_{\mathrm{eff}}} = \left(\frac{W_{\mathrm{rf}} + \frac{1}{T}\int_0^T V_{\mathrm{bias}}(t) I_{\mathrm{bias}}(t)\, dt}{F_{\mathrm{C_2H_2}} + \alpha F_{\mathrm{N_2}} + \beta F_{\mathrm{Ar}}} \right) \left(\frac{l_{\mathrm{act}} V_{\mathrm{gas}}}{l_{\mathrm{gas}} V_{\mathrm{disc}}} \right). \tag{3.3}$$

The degree of monomer dissociation and ionization is greater inside the active discharge since less power is coupled to regions outside the boundaries defined by $A_{\mathrm{act}}l_{\mathrm{act}}$ (but still inside V_{disc}). If all the delivered power was coupled to the active plasma region (symmetric discharge, i.e. $V_{\mathrm{disc}} = A_{\mathrm{act}}l_{\mathrm{act}}$) equation 3.3 would read

$$\Phi_d = \frac{W_{\mathrm{eff}}}{F_{\mathrm{eff}}} = \left(\frac{W_{\mathrm{rf}} + \frac{1}{T}\int_0^T V_{\mathrm{bias}}(t)I_{\mathrm{bias}}(t)\,dt}{F_{\mathrm{C_2H_2}} + \alpha F_{\mathrm{N_2}} + \beta F_{\mathrm{Ar}}}\right)\left(\frac{V_{\mathrm{gas}}}{A_{\mathrm{act}}l_{\mathrm{gas}}}\right). \tag{3.4}$$

Here, $W_{\mathrm{rf}} = 50$ W is the rf power coupled to the discharge and $W_{\mathrm{bias}} = \frac{1}{T}\int_0^T V_{\mathrm{bias}}(t)I_{\mathrm{bias}}(t)\,dt$ the additional power delivered to the plasma due to the applied pulsed voltage (V_{bias}) and current (I_{bias}) at the substrate holder. Figure 3.3 shows the typical pulse profile for $V_{\mathrm{bias}}(t)$ and $I_{\mathrm{bias}}(t)$ applied to the substrate holder for $V_{\mathrm{bias}} = -1000$ V. Here, $l_{\mathrm{act}} = 10$ cm and $l_{\mathrm{gas}} = 12.5$ cm are, respectively, the length of the active discharge region and the distance between the gas feed and the substrate and $V_{\mathrm{gas}} = 4330$ cm^3 and $V_{\mathrm{disc}} = 3464$ cm^3 are the total volumes occupied by the gas mixture and the discharge respectively. $\alpha = 0.35$ and $\beta = 0.05$ are empirical weighting factors introduced to take into account the relative energies associated with nitrogen and argon ionization thresholds [174, 184].

This work studies the influence of diluting carbon precursor molecules in the discharge exclusively through changes in $F_{\mathrm{C_2H_2}}$. Since all other parameters are kept constant, the macroscopic parameter Φ_d is shaped only by changes in V_{bias} and $F_{\mathrm{C_2H_2}}$ (see Figure 3.4a), the latter commonly measured as a volumetric flow ($Q_{\mathrm{Acetylene}}$) at standard conditions using a

mass flow controller. Results show that W_{bias} accounts for up to 19 % of the overall applied power when $|V_{\text{bias}}| = 1000$ V, delivering a maximum $\Phi_d = 6.8 \times 10^8$ J/kg at $Q_{\text{Acetylene}} = 1$ sccm. Conversely, the contribution of W_{bias} drops to only 1.7% at $|V_{\text{bias}}| = 250$ V when $\Phi_d = 2 \times 10^8$ J/kg reaches its minimum at $Q_{\text{Acetylene}} = 10$ sccm.

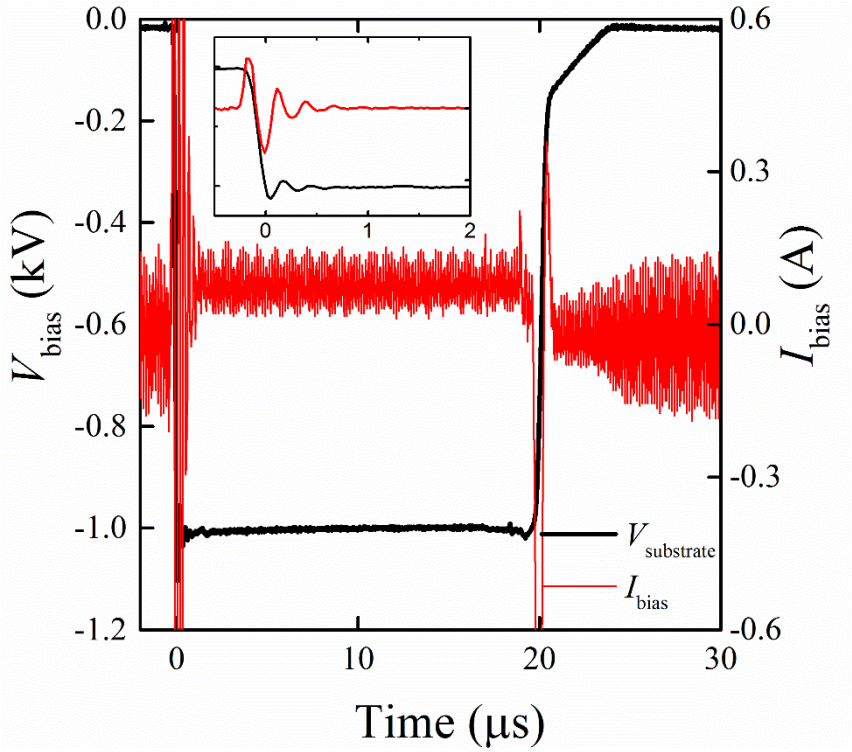

Figure 3.3: Current (I_{bias}) and voltage (V_{bias}) profiles of the high voltage pulses at -1000 V generated by the RUP 6 and applied to the bottom electrode (sample holder).

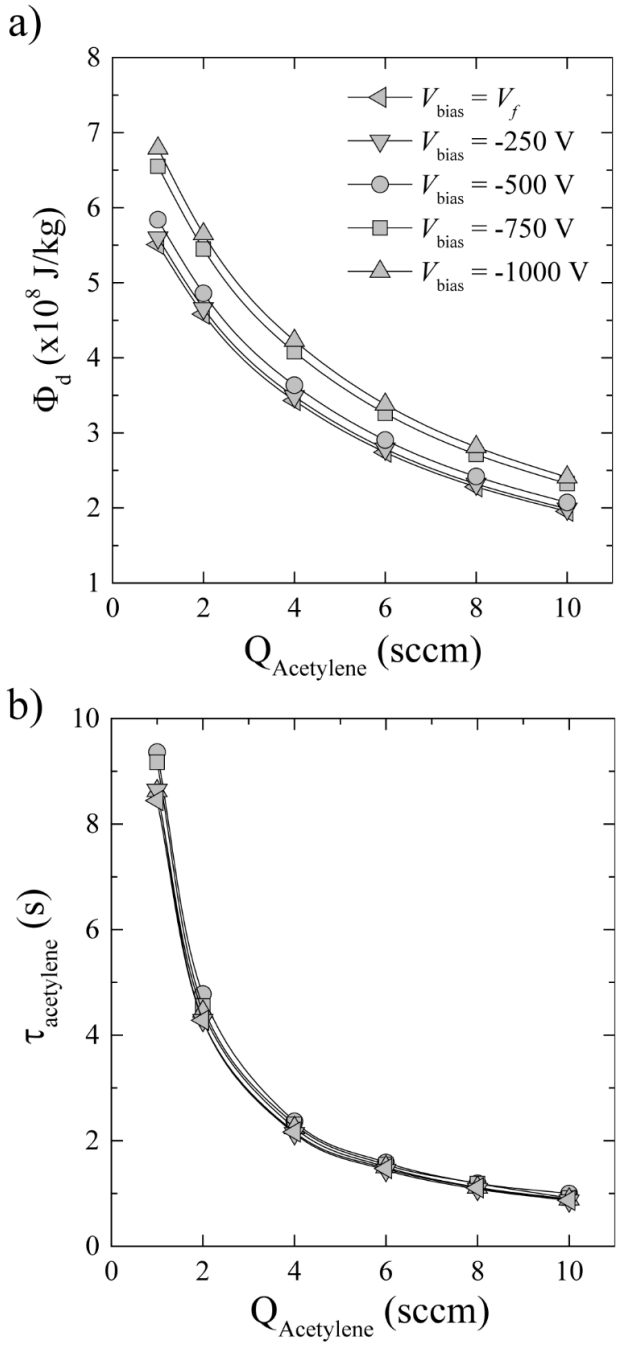

Figure 3.4: The role of process parameterization. a) Energy input per gas molecule in the plasma active discharge (Φ_d) as a function of the monomer flow rate ($Q_{Acetylene}$) for different applied pulsed bias (V_{bias}); b) Residence time of monomer molecules in the active discharge.

The adopted process parameterization allows us to understand the impact on controlling the residence time of carbon precursor molecules in the active discharge, which can be simply calculated as

$$\tau_{\text{Acetylene}}(\text{s}) = \frac{T_0 p}{p_0 T_{gas}} \frac{V_{\text{act}}}{Q_{\text{Acetylene}}(\text{sccm})/60}. \quad (3.5)$$

Here T_{gas} and p are the gas temperature and pressure in the active discharge and T_0 and p_0 are the gas temperature and pressure measured at standard conditions respectively and V_{act} is the active volume in cubic centimeters. Monomer molecules are removed from the active discharge more rapidly with increasing $Q_{\text{Acetylene}}$ (see Figure 3.4b), a consequence of the increasing pumping efficiency as adjusted to maintain a total constant pressure in the reactor across the different runs. Particularly, a tenfold increase in $Q_{\text{Acetylene}}$ yields a reduction in $\tau_{\text{Acetylene}}$ from 9.4 s (at $\Phi_d = 5.8 \times 10^8$ J/kg) to 1.0 s (at $\Phi_d = 2.1 \times 10^8$ J/kg) for $|V_{\text{bias}}|$ = 500 V. Longer transit times through the active discharge (i.e. higher $\tau_{\text{Acetylene}}$), which incidentally also take place at higher Φ_d, results in a more effective fragmentation and activation of the carbon precursor molecules. Consequently, a different population of reactive species such as ions and radicals is expected within the active discharge volume. Plasma-surface interactions and surface chemical reactions involving these reactive species modulate coating properties such as degree of cross-linking and substrate adhesion. Effects of the applied bias on $\tau_{\text{Acetylene}}$ are negligible with only small variations within the experimental uncertainty (≈ 10 %) at $Q_{\text{Acetylene}} = 1$ sccm (i.e. $\Phi_d \geq 5.5 \times 10^8$ J/kg). This latter result shows that the average gas temperature over a deposition run remains virtually unaffected (see Eq 3.5) with changes in V_{bias}.

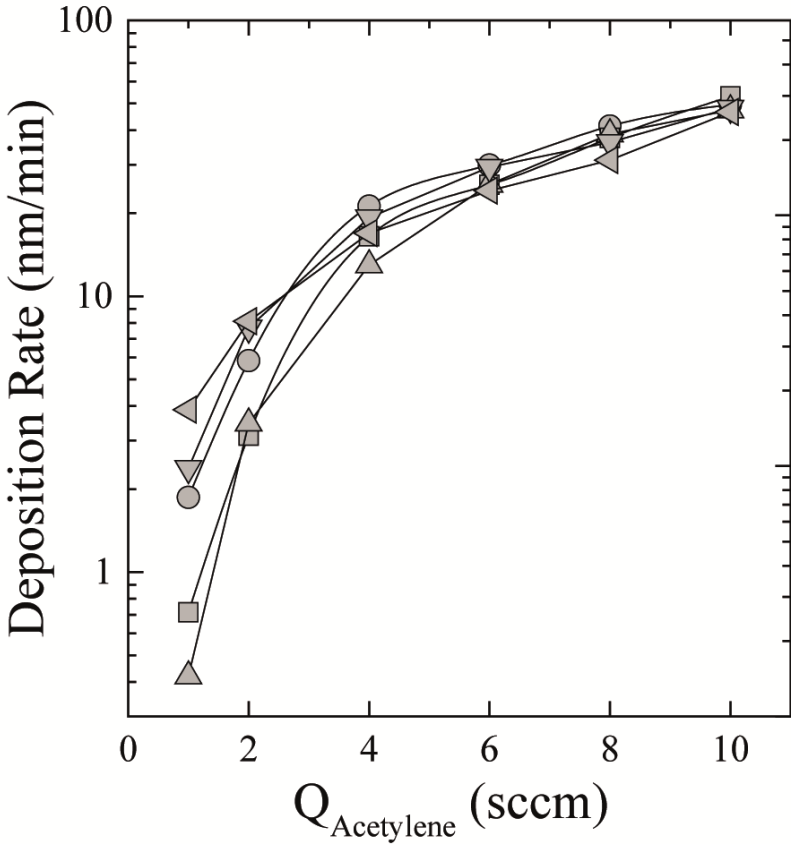

Figure 3.5: Deposition rate of plasma-activated coatings (PAC) for the complete parameterization window studied in this work. Symbols shown as inset in Figure 3.4a are also adopted in this figure.

The average PAC deposition rate is plotted as a function of $Q_{\text{Acetylene}}$ for different applied V_{bias} in Figure 3.5. Results reveal that PAC growth on the substrates is enhanced with increasing $Q_{\text{Acetylene}}$ (decreasing Φ_d), a consequence of the increased carbon precursor fraction in the discharge and the inflow rate of material towards the substrate. This trend fits with previously published results showing that the deposition rate in plasma polymerization processes scales linearly with $F_{C_2H_2}$, provided that enough energy is applied to the discharge to initiate and sustain the polymerization mechanisms [185]. Conversely, the PAC deposition rate is significantly reduced by increases in V_{bias}, particularly for $\Phi_d \geq 5.5 \times 10^8$ J/kg ($Q_{\text{Acetylene}} = 1$ sccm), and is found to be enhanced with decreasing $|V_{\text{bias}}|$. When no external bias is applied ($|V_{\text{bias}}| = V_f$) the deposition rate increases 9.2-fold to 3.38 nm s^{-1} from 0.42 nm s^{-1} at $|V_{\text{bias}}| = 1000$ V. The PAC deposition rate is fundamentally ruled by a competition between the film growth, which is dependent on the activation of the polymerization mechanisms of the carbon precursor [81], and the ablation of the growing film through sputtering by energetic ionized species. As the PAC deposition rate is suppressed significantly at higher $|V_{\text{bias}}|$ for high Φ_d it is proposed that the film ablation is predominantly regulated by the applied external electric field on the substrate holder, subsequently triggering an increase in the plasma ionization degree.

3.3.2 Optical emission spectroscopy

To support the hypothesis formulated in section 3.3.1 and further understand the physical and chemical mechanisms driving the PAC growth / ablation competition phenomena, the macroscopic description of the deposition process is combined here with optical emission

spectroscopy (OES) diagnostics. Typical emission spectra of C_2H_2/Ar/N_2 plasma discharges recorded during PAC deposition are shown in Figure 3.6. The spectra exhibit a strong emission fingerprint of N_2 molecules over the entire spectral range, with emissions from CN, NH and CH molecules as well as several atomic emission lines due to radiative transitions between different argon excited states. The N_2 fingerprint is comprised of emission bands associated with electronic, vibrational and rotational transitions within: (i) N_2 molecules of the second positive system (SPS $C^3\Pi_u \rightarrow B^3\Pi_g$, 300 nm – 385 nm); N_2^+ molecular ions of the first negative system (FNS $B^2\,\Sigma_u \rightarrow X^2\,\Sigma_g$, : 390 nm – 450 nm) and (iii) N_2 molecules of the first positive system (FPS $B^3\Pi_g \rightarrow A^3\,\Sigma_u^+$, 550 nm – 950 nm).

Measurements reveal an enhancement of up to ~4 fold (Figure 3.7a) of the normalized band intensity of N_2^+ (391.48 nm) molecular ions with increasing $|V_{\text{bias}}|$ at $Q_{\text{Acetylene}} = 1$ sccm. N_2^+ molecular ions are additionally populated when $|V_{\text{bias}}| \geq 750$ ($\Phi_d \geq 6.6 \times 10^8$ J/kg), most likely via ionization mechanisms involving electron impact collisions with ground-state N_2 molecules [186, 187]. Being positively charged, nitrogen molecular ions are accelerated by the electric field in the plasma sheath towards the growing film on the negatively biased substrate. The ions receive proportionally more energy as the applied negative potential increases, leading to the ablation of the newly deposited plasma polymer material. Film etching and ablation during plasma polymerization processes by ionic species

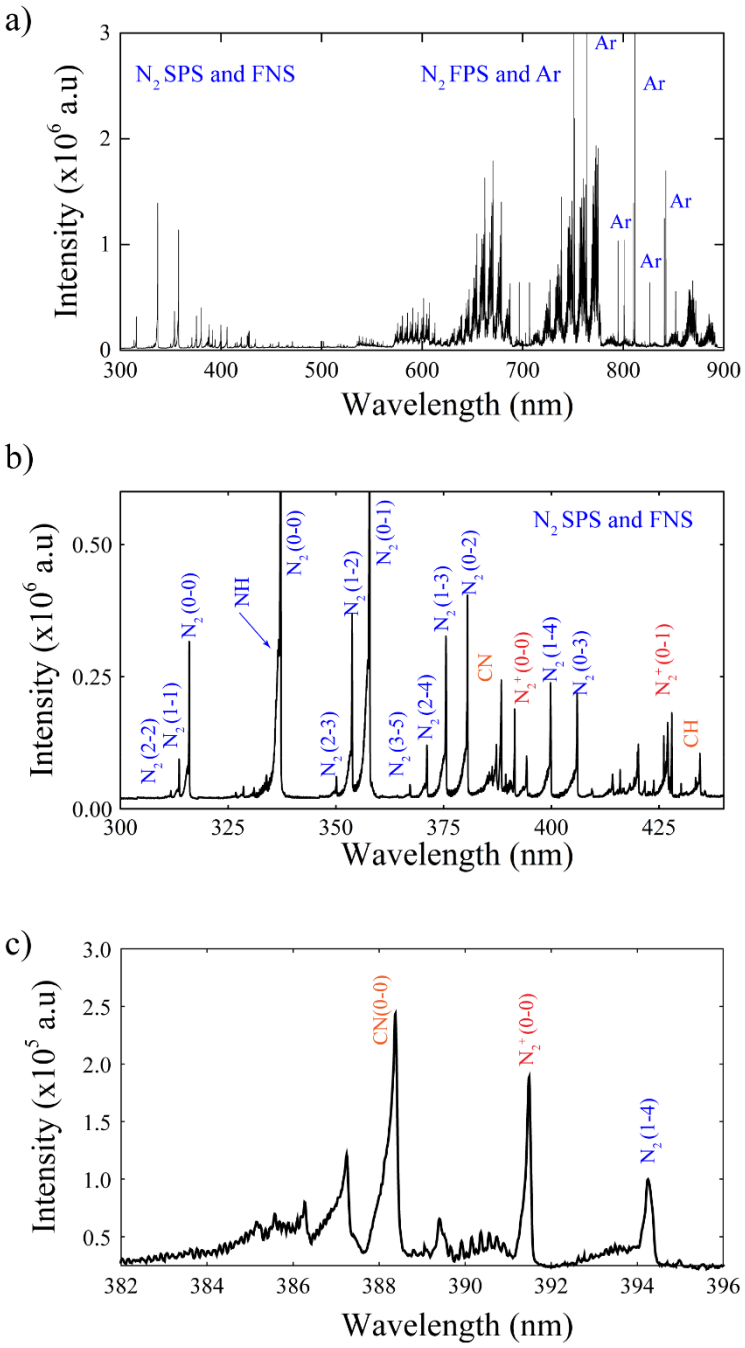

Figure 3.6: Optical emission spectroscopy diagnostics of plasma discharges during PAC deposition process. a) Typical emission spectrum of the discharge during PAC deposition in the wavelength range of 300 – 900 nm. The spectrum exhibits a strong N_2 fingerprint due to radiative transitions between various electronic, vibrational and rotational states. These transitions are assigned to the second positive system (SPS), the

first negative system (FNS) and the first positive system (FPS). Intense atomic emission lines arising from transitions between different argon excited states are also observable for higher wavelengths. b) The emission spectrum also features vibrational radiative transitions of CN radicals, NH and CH molecules. c) A zoom into the spectral window 382 – 396 nm detailing the rotational-vibrational envelope associated with of CN (0-0), N_2^+(0-0) and N_2(0-0) populations.

created in the plasma has been described as the competitive ablation and polymerization (CAP) mechanism [76].

Interestingly, CN radical molecules are found to be more abundant also with increasing $|V_{\text{bias}}|$, particularly for $Q_{\text{Acetylene}} = 1$ sccm (Figure 3.7b). CN radicals are an important precursor of carbon-nitrogen hybridizations in plasma-synthesized a-C:N:H coatings [188] and therefore its detection during film deposition can offer further insights into different PAC growth mechanisms. Increasing $|V_{\text{bias}}|$ results in extra energy available in the discharge (as shown in Fig 3.4a and 3.6) to further fragment the carbon precursor molecules and dissociate nitrogen molecules to subsequently form atomic carbon and nitrogen species. Consequently, the reaction rate of carbon and nitrogen atoms forming CN radical molecules is expected to increase. As $Q_{\text{Acetylene}}$ increases, the overall available energy per monomer unit mass in the plasma decreases and a complete fragmentation of the C≡C bonds in acetylene molecules (with an activation energy threshold of ~9 eV) to form atomic carbon becomes less probable. Accordingly, changes in CN density become less sensitive to variations in $|V_{\text{bias}}|$ for higher $Q_{\text{Acetylene}}$. The formation of CN involving atomic carbon and nitrogen is a three-body assisted reaction and although plausible, it is more likely to occur at higher pressures [189]. Another important mechanism responsible for the creation of excited CN species involves the reaction

between atomic nitrogen and CH molecules [190]. This mechanism is predicted to take place at pressures as low as 50 mTorr and OES confirms the excitation of CH species in the active discharge. Chemical etching and physical sputtering of volatile compounds at the coating surface such as −C≡N (nitrile terminations) upon ion bombardment should also be taken into consideration. CN radical molecules have been previously detected in rf discharges using nitrogen-free helium atmospheres [191]. Here, rupture of chemical bonds due to impact of energetic helium ions onto a-C:N:H coated substrates and reactor walls led to plasma-induced desorption of nitrile terminations into the discharge. The bombardment of a-C coatings by a N_2^+ beam has also been reported to promote the formation of CN hybridizations at the coating surface followed by detection of CN containing species in the discharge volume using a quadrupole mass spectrometer [192]. The boost in the emission intensity of both N_2^+ and CN species observed for $|V_{\text{bias}}| \geq 750$ V is consistent with chemical etching and physical sputtering of the coating, a hypothesis which is also supported by the significant drop in PAC deposition rate observed at these bias levels. Furthermore, a maximum in the relative emission intensity of CN species near the substrate is observed, indicating that this population is additionally excited in the vicinity of coating surface for higher $|V_{\text{bias}}|$ values due to desorption of CN hybridizations.

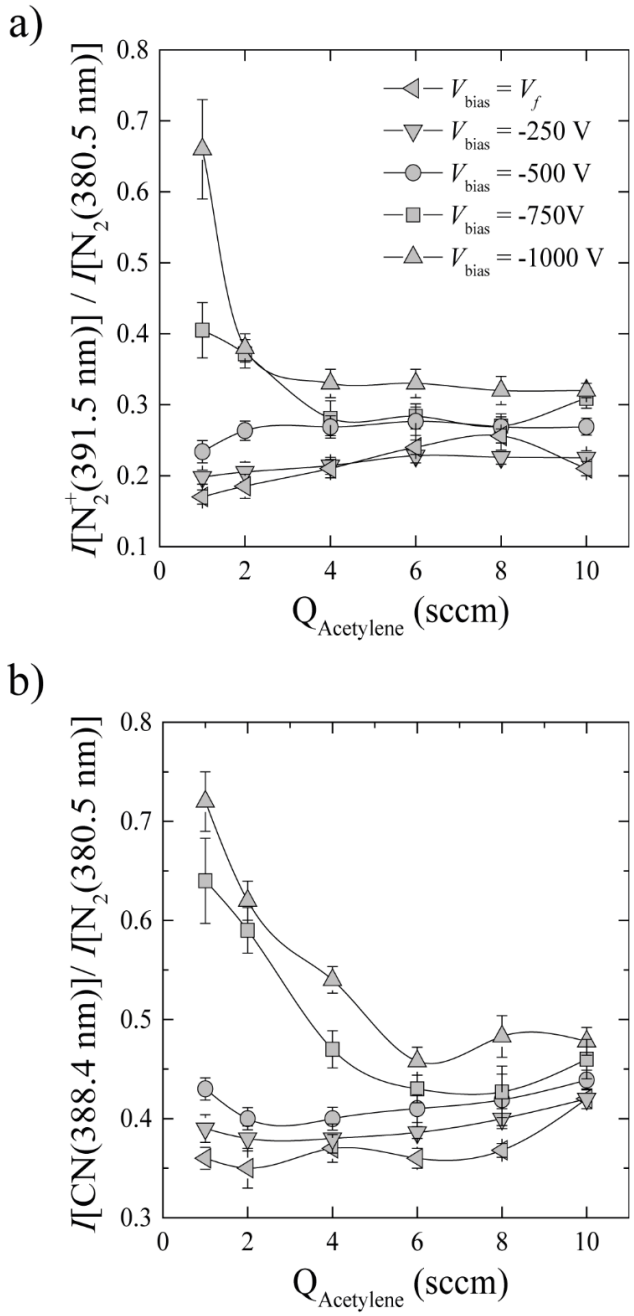

Figure 3.7: Emission intensity of (a) N_2^+ molecular ions and (b) CN radical molecules normalized to N_2 (SPS: 380.5 nm) as a function of the monomer flow rate and for different applied bias.

3.3.3 Surface elemental composition

The elemental composition of PAC surfaces was measured by XPS and its dependence on process parameters is shown in Figure 3.8. The carbon / nitrogen ratio on PAC surfaces is readily modulated within the explored ($Q_{\text{Acetylene}}$, $|V_{\text{bias}}|$) value range. The relative carbon fraction is seen to increase from a minimum of 58.4 % at ($Q_{\text{Acetylene}} = 1$ sccm, $|V_{\text{bias}}| = V_{\text{f}}$) to maximum of 82.0 % at ($Q_{\text{Acetylene}} = 10$ sccm, $|V_{\text{bias}}|$= 1000 V). Conversely, the increase in the carbon content is followed by a decrease in the nitrogen atomic fraction from 34.9 % at ($Q_{\text{Acetylene}} = 1$ sccm, $|V_{\text{bias}}| = V_{\text{f}}$) down to 11.7 % at ($Q_{\text{Acetylene}} = 10$ sccm, $|V_{\text{bias}}|$ = 1000 V). The results further indicate that PAC surfaces are oxidized when exposed to the laboratory atmosphere as oxygen was found in relative atomic concentrations up to 12.5 % for ($Q_{\text{Acetylene}} = 1$ sccm, $|V_{\text{bias}}|$ = 1000 V), however remained generally stable at other $Q_{\text{Acetylene}}$ and $|V_{\text{bias}}|$ levels. The increase in relative carbon fractions (and related decrease in nitrogen) with increasing $Q_{\text{Acetylene}}$ is expected since the relative carbon content in the plasma increases with increasing $Q_{\text{Acetylene}}$. Changes to atomic fractions between samples prepared under different V_{bias} become less significant with increasing $Q_{\text{Acetylene}}$ (decreasing Φ_d), a general trend that is consistent with the results reported in sections 3.3.1 and 3.3.2 (see Figures 3.5 and 3.7).

At higher energy inputs per monomer unit, the role of the applied bias in determining elemental composition is greater due to a higher relative content of ionized species in the plasma. At $Q_{\text{Acetylene}} = 1$ sccm, the nitrogen fraction in PAC is strikingly modulated by V_{bias} and increases 1.7-fold from 20.6 % at $|V_{\text{bias}}|$= 1000 V ($\Phi_d = 6.8 \times 10^8$ J/kg) to 34.9 % at

$|V_{\text{bias}}| = V_{\text{f}}$ ($\Phi_d = 5.5 \times 10^8$ J/kg). The trend observed in elemental composition at low $|V_{\text{bias}}|$ is followed by a modulation of the refractive index, as shown in Figure 3.9. For low bias (V_{f} and -250V) a steady increase of refractive index was observed as the carbon content increased. The major jump in refractive index observed for PAC made with high values of pulsed bias, i.e. $n = 2.24$ at $V_{\text{bias}} = -750\,\text{V}$ and $n = 2.26$ at $V_{\text{bias}} = -1000\,\text{V}$ with $Q_{\text{Acetylene}} = 1$ sccm, is likely to be caused by an increase in the density of the film induced by a greater degree of crosslinking and an associated reduction in hydrogen content (not measured in XPS). Increased ion bombardment energy during film growth is known to promote sp3 carbon bonding and facilitate the removal of incorporated hydrogen. Samples with less carbon (or high levels of nitrogen) typically had low refractive indexes.

To further understand the role played by V_{bias} in determining PAC chemical bonding configurations both XPS C(1s) and N(1s) core-levels were systematically analysed following deconvolution. The results are shown in Figure 3.10a and 3.10b respectively for $Q_{\text{Acetylene}} = 1$ sccm. The C(1s) peak features a broadening that becomes progressively asymmetric towards higher binding energies with decreasing $|V_{\text{bias}}|$. Supported by the results in Figure 3 which reveals increasing nitrogen fractions for lower $|V_{\text{bias}}|$ values, we assign this asymmetric broadening mostly to the occurrence C-N bonds. C-O bonds also contribute to this peak shoulder but not to the trend with bias since the oxygen concentration does not vary significantly with bias. Peak deconvolution and iterative fitting showed four components with centroids located at 284.97 ± 0.02 eV (C_1), 286.41 ± 0.08 eV (C_2), 287.60 ± 0.15 eV (C_3), 288.82 ± 0.19 eV (C_4). The first component at lowest binding energy corresponds to

pure carbon hybridization as well as C-H bonds while the fourth and highest binding energy peak is attributed to various COO compounds [193]. Identification and assignment of the core-level shifts between the two C-N components and the pure C-C component appears to be rather controversial within the literature. Their relative position in the spectrum seems to be vary and they have been assigned either to sp^2 and / or sp^3 C-N hybridizations [194] or according to the number of nitrogen neighbours that surround carbon atoms [195]. The assignment of these two components in the C(1s) spectrum for amorphous CN:H materials greatly depends on the local chemical environments in which the different C-N hybridizations take place [196]. Because various local chemical environments may occur in plasma polymers, the two C-N components cannot be easily identified and fixed to specific sp2 and / or sp3 C-N hybridizations. Additionally, chemical shifts caused by C-O and C=O bonds are also known to overlap with those of C-N bonds which makes the analysis and quantification even more challenging. We choose therefore to compare their relative fractions in the C(1s) spectra with the results obtained from the deconvolution of the N(1s) core-levels. Although the assignment of the two main C-N components in the XPS N(1s) peak is also somewhat controversial, the reported chemical shifts of these components are in good agreement within the literature. The XPS N1s core-level spectrum was also deconvoluted into 4 distinct components. The first peak is located at 398.33 ± 0.09 eV (N_1) and it has been assigned in the literature either to: (i) two-fold coordinated nitrogen atoms bonded to carbon atoms, such as those found in pyridinic-N surrounding vacancy defects [197] or (ii) sp^3 nitrogen atoms bonded to sp^3-hybridized carbon atoms [198]. The second component, with a peak centered at 399.28 ± 0.15 eV (N_2) has been related to both nitriles and amine groups [199], which were also identified on PAC samples by FTIR-ATR measurements (data not shown).

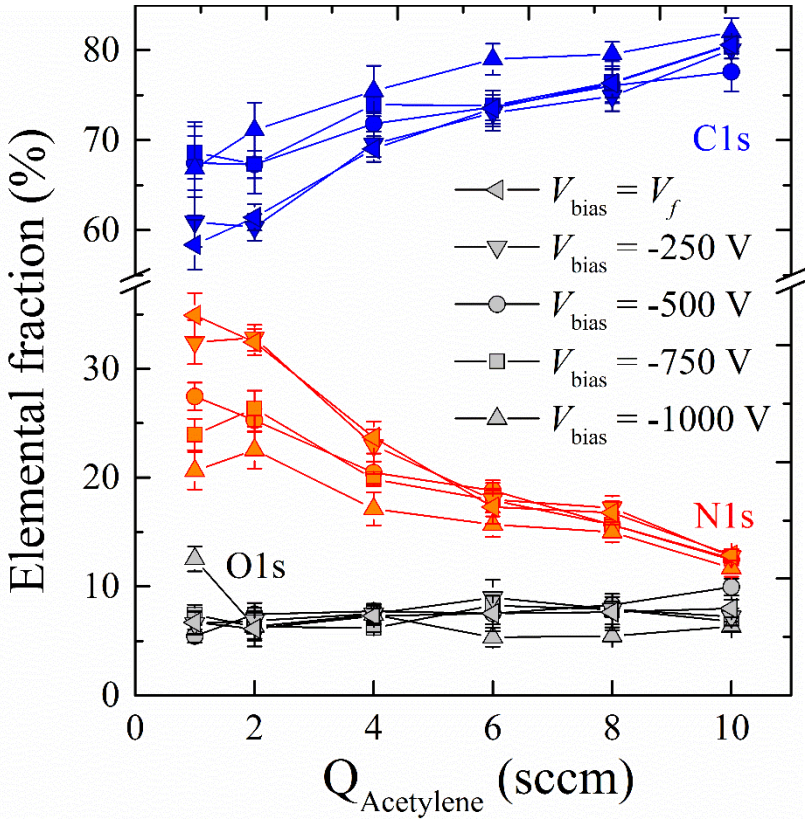

Figure 3.8: Elemental atomic fraction of carbon, nitrogen and oxygen measured by XPS for all PAC surfaces studied in this work.

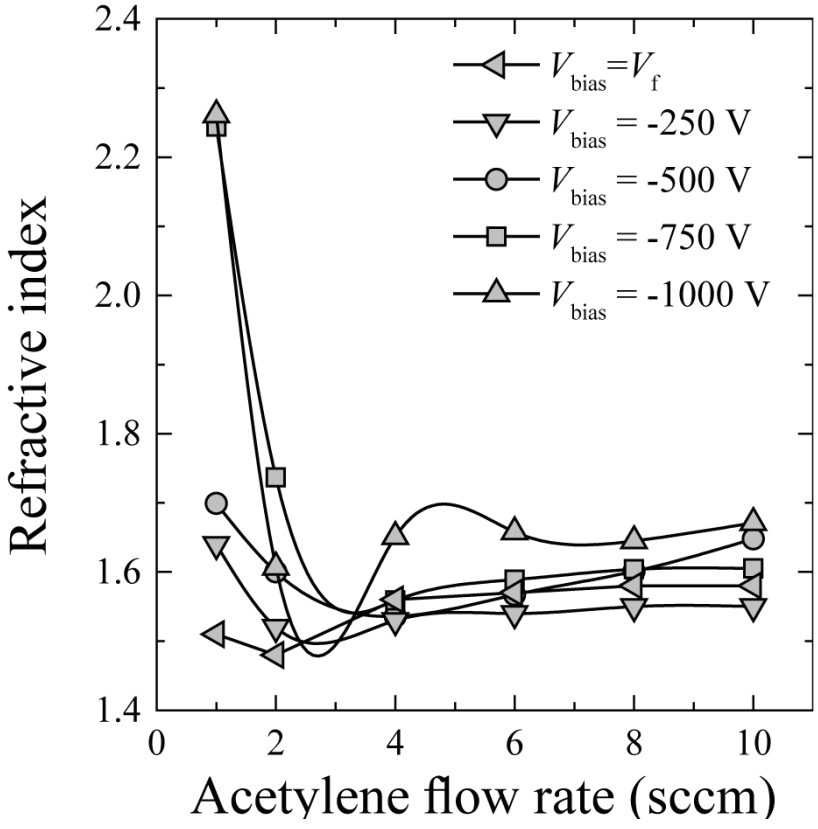

Figure 3.9: Refractive index measured by spectroscopic ellipsometry for all PAC surfaces studied in this work.

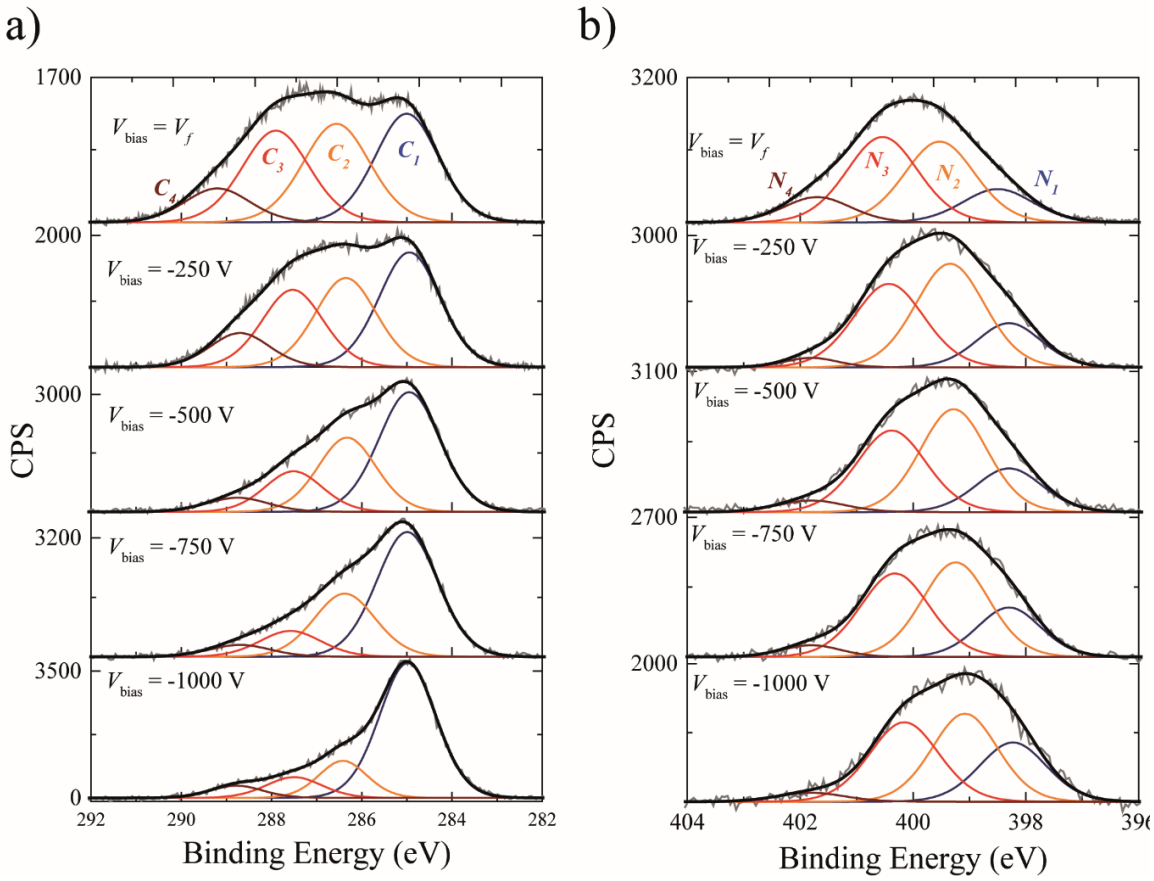

Figure 3.10: Deconvolution of C1s (a) and N1s (b) peaks for PAC surfaces prepared at $Q_{Acetylene}$ = 1 sccm ($\Phi_d \geq 5.5 \times 10^8$ J/kg). The C1s core-shell was deconvoluted into four components with peak positions located at 284.97 ± 0.02 eV (C_1), 286.41 ± 0.08 eV (C_2), 287.60 ± 0.15 eV (C_3), and 288.82 ± 0.19 eV (C_4). Measurements reveal a clear asymmetric broadening of the C1s core-shell towards higher binding energies with decreasing V_{bias} attributed to an increased number of CN hybridizations. Four components were also found for the N1s core-shell at 398.33 ± 0.09 eV (N_1), 399.28 ± 0.15 eV (N_2), 400.36 ± 0.13 eV (N_3), and 401.79 ± 0.04 eV (N_4).

The third peak centered at 400.36 ± 0.13 eV (N_3) has been generally attributed to: (i) nitrogen three-fold coordinated to sp^2 carbon atoms, like in graphitic-CN structures [198], (ii) nitrogen atoms bonded to two sp^2 and one sp^3 carbon atoms [200] or (iii) to sp^2 nitrogen atoms bonded to sp^2-hybridized carbon atoms [197]. Finally, the fourth peak at 401.79 ± 0.04 eV (N_4) is commonly attributed to nitric oxide compounds [199], also confirmed by FTIR-ATR. Taken together this compositional data suggests that for plasmas with relatively high monomer fragmentation increasing substrate bias leads to an increase in the preferential removal of nitrogen by sputtering and ablation processes.

3.3.4 Growth mechanism – correlations between coating and plasma properties

The XPS results are consistent with our main findings and conclusions for higher Φ_d and $\tau_{\text{Acetylene}}$ in section 3.3.1 (see Figures 3.4). PAC growth is governed by a competition between monomer polymerization and film etching / ablation, the latter exacerbated by the applied pulsed bias. Monomer polymerization is initiated and sustained partially via radical-assisted growth polymerization mechanisms [81] that include CN molecular radicals, as confirmed by the presence of this population in the discharge and the broadening of the C(1s) core level towards higher binding energies. Higher $|V_{\text{bias}}|$, despite enhancing the CN content in the discharge, drives an abrupt increase in the plasma ionization degree as shown by the ~2-fold decrease in the CN / N_2^+ band-head emission intensity ratios (see Figure 3.11). As PAC surfaces are bombarded with high energy N_2^+ molecular ions, nitrogen-containing compounds are preferentially sputtered / chemically etched from the C:N:H matrix. At higher applied $|V_{\text{bias}}|$ CN assemblies at the surface move from the coating surface to the plasma volume. The

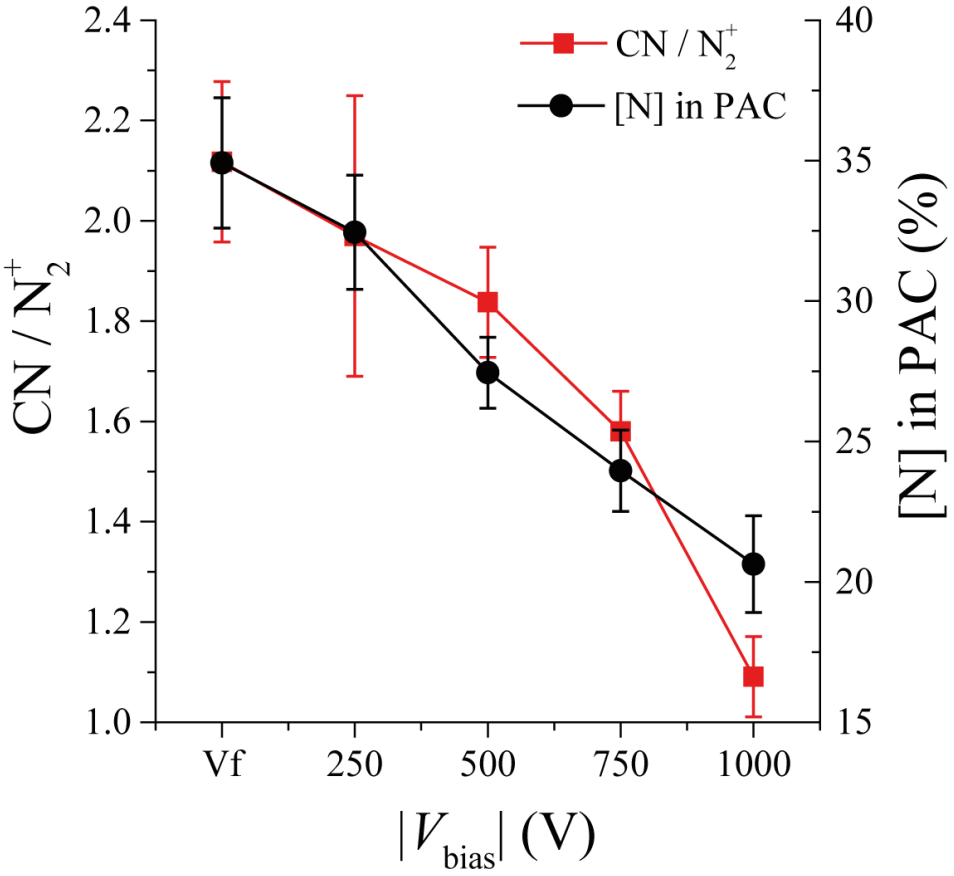

Figure 3.11: Emission intensity ratio of CN radicals to N_2^+ ions in the discharge and Nitrogen atomic fraction on PAC surfaces as a function of V_{bias} for samples prepared at $Q_{Acetylene}$ = 1 sccm ($\Phi_d \geq 5.5 \times 10^8$ J/kg). Correlations between these two datasets suggest that the overall N content in PAC is related to a balance between the formation of CN radicals in the plasma and their ablation due to energetic ion impact driven by the applied bias.

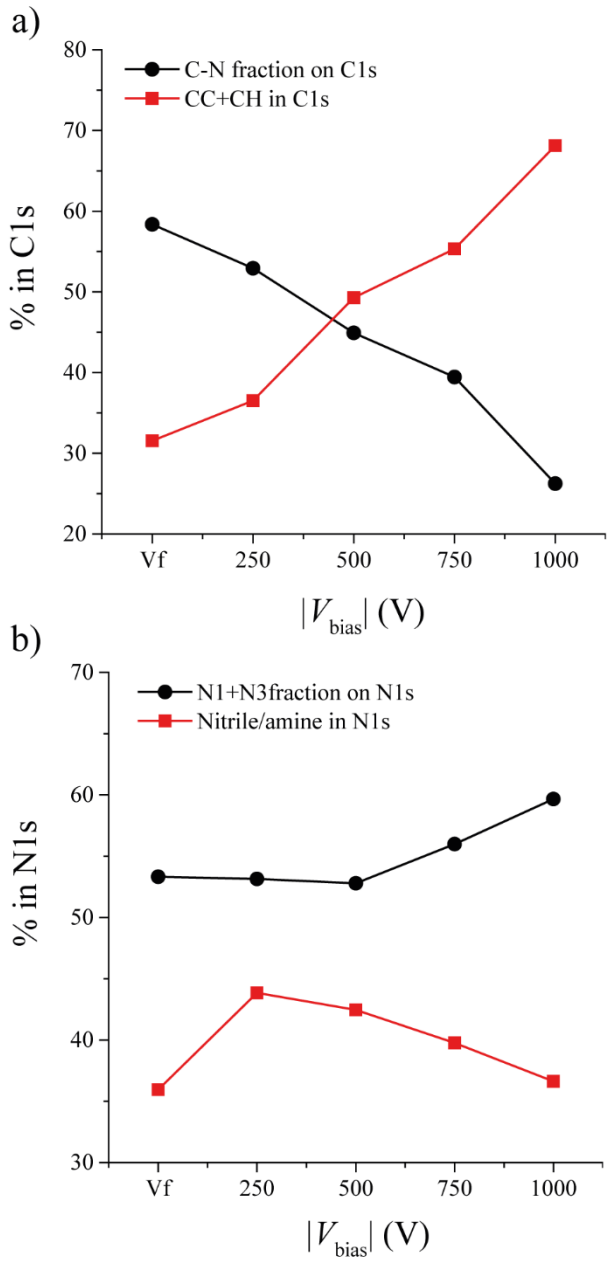

Figure 3.12: a) Atomic fractions of C_1 and C_2 + C_3 components in the C1s core-shell and b) Atomic fractions of N_2 and N_1 + N_3 components in the N1s core-shell as a function of V_{bias} for samples prepared at $Q_{Acetylene}$ = 1 sccm ($\Phi_d \geq 5.5 \times 10^8$ J/kg).

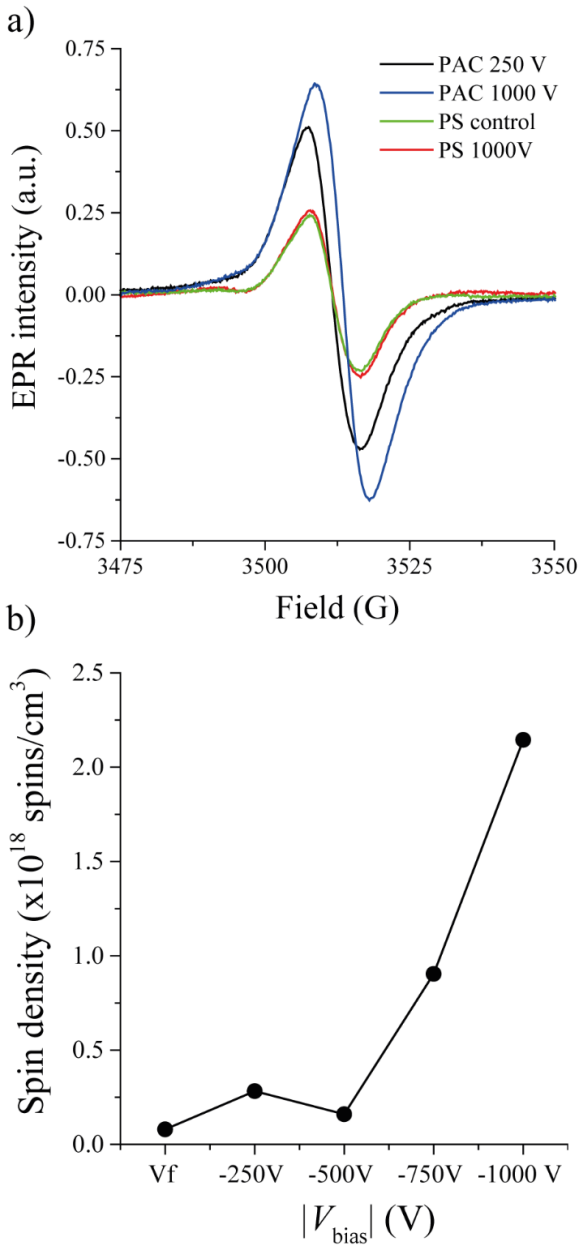

Figure 3.13: a) Electron paramagnetic resonance (EPR) spectra of PS – PAC coated substrates for V_{bias} = - 250 V (black) and V_{bias} = - 1000 V (blue) and $Q_{Acetylene}$ = 1 sccm ($\Phi_d \geq 5.5 \times 10^8$ J/kg). PS substrates treated in an argon and nitrogen plasma with V_{bias} = - 1000 V (red) show no significant difference to untreated PS samples, which indicates that unpaired electrons were introduced through PAC. B) Absolute spin density on PAC coated PS substrates at different V_{bias}.

extent of this transfer with increasing $|V_{bias}|$ is clearly illustrated by a decrease in both C_2 and C_3 XPS components in figure 3.12a, which is also followed by an increase in the emission intensity of CN radicals in the discharge. Furthermore, the decrease of N_2 (see Figure 3.12b) exemplifies the susceptibility of volatile groups such as nitrile terminations to plasma-induced desorption upon significantly increasing ion bombardment. Conversely, C-C and C-H hybridizations are less volatile and therefore less vulnerable to desorption. These assemblies account for 68% of the integrated C1s core-shell at $|V_{bias}|$= 1000 V, corresponding to 45% of PAC bonding configurations.

It has been shown in previous reports that films prepared by PP assisted with ion bombardment display a significant increase in the unpaired electron density with increasing applied bias [157]. Here, the spin density of PAC samples prepared under various V_{bias} was measured using electron paramagnetic resonance. Results plotted in Figure 3.13 fit well with previous reports [90, 157], revealing an increased radical density with increased applied bias. The relatively high baseline radical density at $V_{bias} = V_f$ (8×10^{16} spin/cm^3) is typical of plasma polymers [201, 202]. Coating exposure to ion bombardment due to substrate bias, UV radiation and radical-assisted polymerization mechanisms accounts for the inherently high spin density of PAC. The increasing propensity of ions to break bonds in the growing coating with bombardment energy accounts for the increase of the spin density with increasing pulsed bias.

3.3.5 Mechanical properties on flat substrates

The performance of implantable medical devices, such as coronary stents, that undergo extreme plastic deformation during deployment is limited by the mechanical robustness of any coating used for implant surface modification. For this reason, PAC must present an exceptional adhesion strength to metallic substrates and be able to resist peeling, cracking and further delamination following plastic deformation of the substrate. To simulate the harsh compressive and tensile stresses experienced during *in vivo* deployment, PAC SS flat sheets were severely deformed by bending and folding the samples outward and inward to very small (500 μm) radii of curvature. The ability of different PAC series to remain adhered and resist cracking and delamination after sample deformation was then qualitatively assessed by optical and electron microscopy and the results are shown in Figures 3.14a and 3.14b. Samples prepared under $\Phi_d < 4.2 \times 10^8$ J/kg ($\tau_{\text{Acetylene}} < 4.3$ s) regimes corresponding to low levels of monomer fragmentation and ionization presented very poor adhesion strengths independently of the applied $|V_{\text{bias}}|$ (Figure 3.14a shows an example of a sample prepared at $\Phi_d = 2.4 \times 10^8$ J/kg and $\tau_{\text{Acetylene}} = 1.6$ s). When the coated substrates were bent outward, with PAC outside the radius of curvature, delamination and spallation was observed and patches of the underlying metal were exposed along the deformed region. High magnification SEM images also revealed the formation of cracking featuring parallel nano- sized cracks normal to the direction of the tensile stress. Additionally, PAC topography was remarkably changed when samples were folded inward with PAC inside the radius of curvature. Elevated patches of coating were observed along the deformed region, a clear indication that peeling has occurred at the PAC / SS interface due to the applied compressive stress. Conversely, for

$\Phi_d \geq 4.6 \times 10^8$ J/kg ($\tau_{\text{Acetylene}} \geq 4.$ s), which corresponds to high levels of monomer fragmentation and ionization, PAC remained adhered to the underlying SS and did not show any topographical changes or development of cracks even at higher magnifications (see Figure 3.15b).

Enhanced adhesion strength, wear and corrosion resistance of plasma-based coatings has been attributed, in part, to enhancements in mechanical properties such as improved elasticity and hardness. To explore this hypothesis in the context of our coatings, we measured the Young's modulus of PAC coated SS substrates using nanoindentation. A typical load-displacement curve on a PAC coated SS substrate is plotted in figure 3.15, where a load of 20Mn was necessary to produce a maximum tip displacement of 600 nm. Figure 3.16a plots the reduced Young's modulus as a function of the indentation depth for the same samples tested in Figure 3.15 but in the absence of substrate deformation. An applied load of 0.02 mN produced a vertical displacement of 25.6 ± 2.0 nm on PAC prepared at $\Phi_d = 2.4 \times 10^8$ J/kg, yielding a Young's modulus of 19.39 ± 2.3 GPa. Young's moduli remained unchanged with increasing loading and indentation depths up to 41.1 ± 0.7 nm indicating that measurements up to this point are representative of PAC surfaces with minimum substrate influence. PAC stiffness is lower than typical plasma polymerized a-C:H thin films prepared in CH_4-Ar mixtures [138] and its elastic modulus is significantly lower than the 47 GPa typical of hard and elastic carbon-nitride films deposited by DC magnetron sputtering [203].

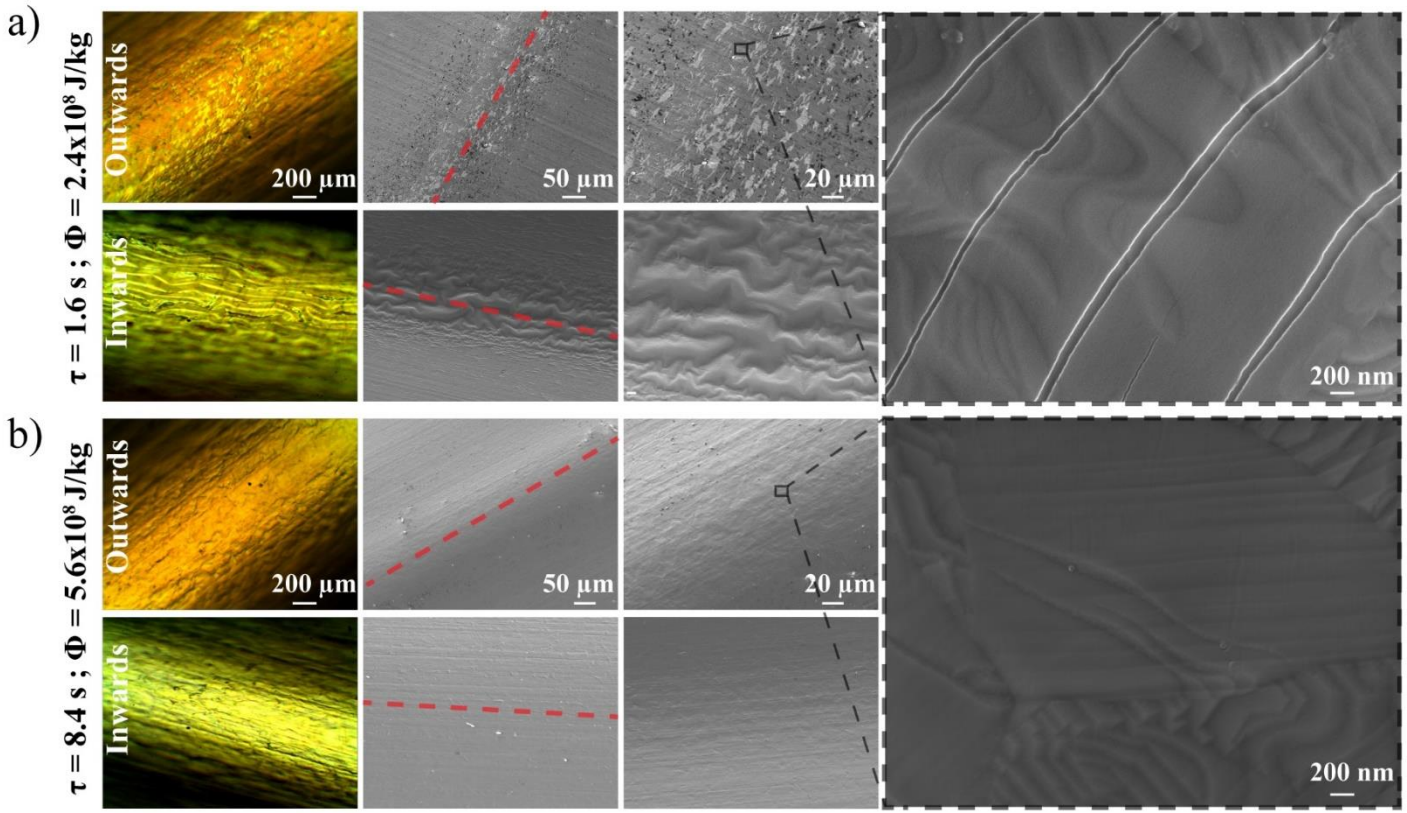

Figure 3.14: Mechanical properties of PAC under various Φ_d. a) Optical and SEM representative micrographs of PAC coated SS 316L sheets after tensile (bent outside the curvature – top images) and compressive (bent inside the curvature – bottom images) substrate deformation for samples prepared at $\Phi_d = 2.4 \times 10^8$ J/kg. Coating cracking and peeling is clearly visible in the regions of maximum deformation (red dashed-lines) and therefore maximal tensile and compressive stress respectively. b) As in a) but for PAC coated SS 316L substrates prepared at higher energy inputs ($\Phi_d = 5.6 \times 10^8$ J/kg). PAC surfaces in Figure 3.15b are mechanically robust and clearly outperform those in Figure 3.15a.

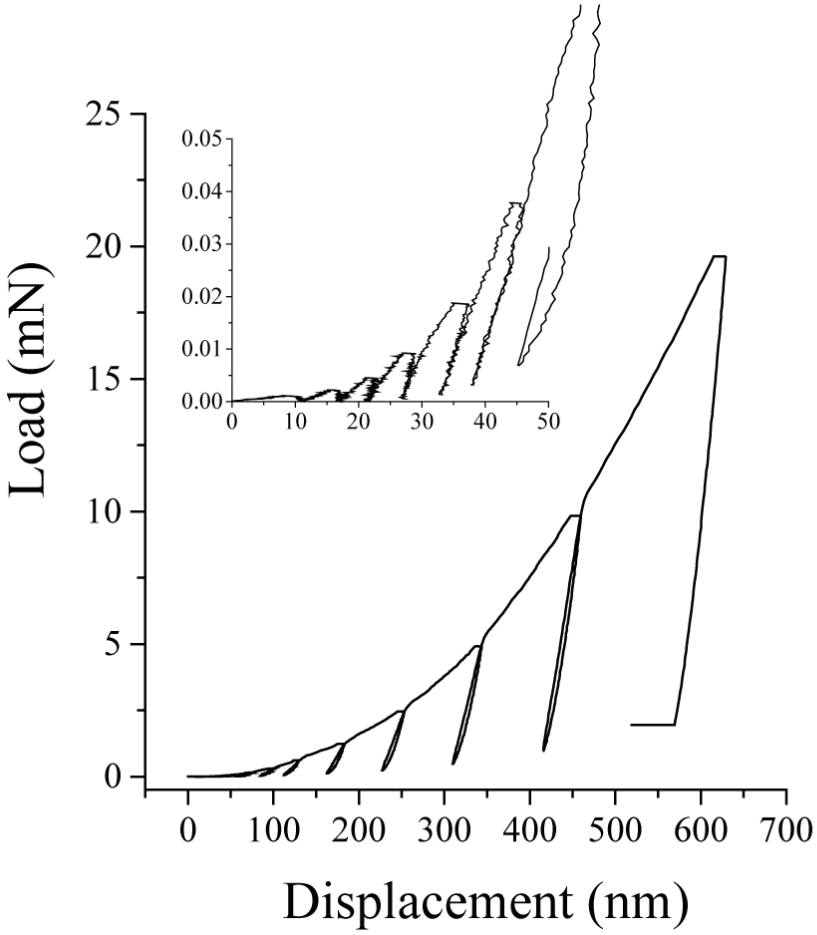

Figure 3.15: A typical load – displacement curve of PAC coated SS substrates measured by nanoindentation.

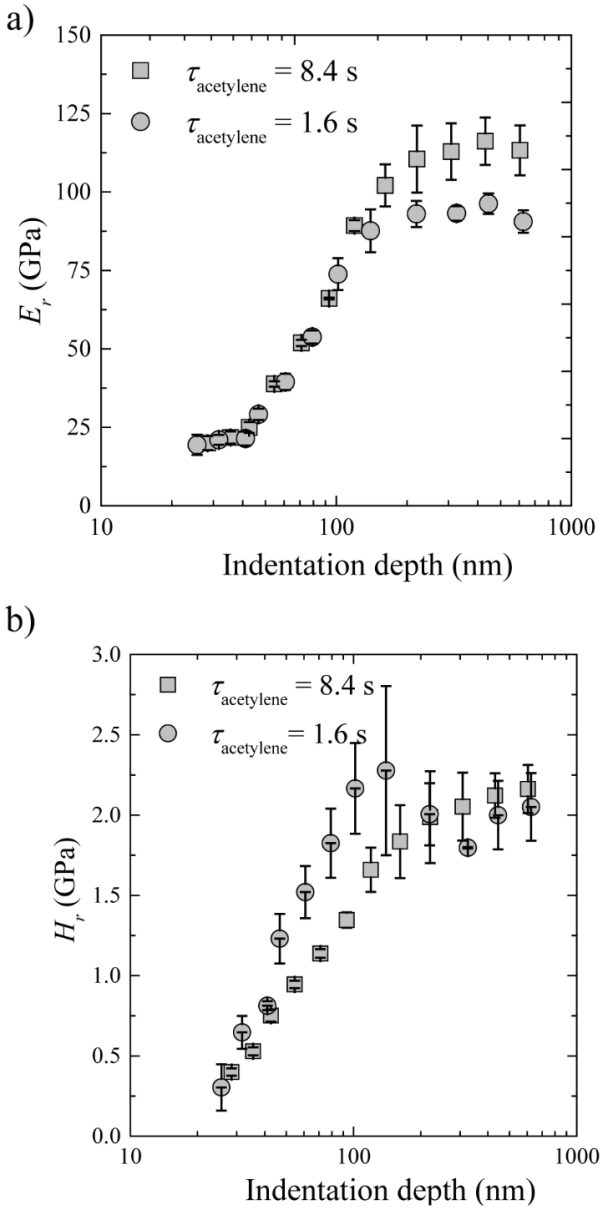

Figure 3.16: a) Reduced Young's moduli measured by nanoindentation for the same PAC surfaces tested in Figure 5a and 5b. Measurements at lower indentation depths reveal no significant differences between the moduli of the two samples, indicating a similar intrinsic coating stiffness. However, the moduli diverge for indentation depths beyond the PAC – SS interface (red dashed-line). These results suggest differences in interface structure and composition between the two samples. b) Hardness measured by nanoindentation for the same PAC surfaces tested in Figure 3.14a and 3.14b.

These results indicate that the mechanical performance and substrate adhesion of PAC under compressive and tensile deformations is not determined by its mechanical stiffness. The modulus of both PAC samples increases linearly with the applied load before it plateaus at indentation depths greater than 200 nm. However, samples prepared under higher Φ_d registered a more rapid increase and reached a maximum modulus and hardness (Figure 3.17b) of 113 GPa compared with the 91 GPa measured on lower Φ_d samples. Since the elastic modulus is similar for both PAC samples and because both were deposited on the same substrate material, the nature of the coating – metal interface must account for different elastic moduli profiles with increasing indentation depths.

Our observations suggest that stronger coating – metal interfaces are achieved when PAC is prepared under higher Φ_d, i.e. higher $\tau_{\text{acetylene}}$ values, and lower deposition rates. Increasing $\tau_{\text{Acetylene}}$ not only increases the residence time in the active discharge, promoting higher monomer fragmentation and ionization degrees, but also increases the energy input per monomer unit mass due to a lower monomer fraction in the plasma (correlated with the reduced acetylene flow rate). These findings suggest that atomic interfacial mixing (AIM) [72] accounts for the improved substrate adhesion strength. AIM modifies the substrate surface free energy to promote stronger interfacial attachment between the substrate and the deposited plasma polymer. Substrate surface modification in metals occurs mainly via enhanced bonding between metallic atoms and the deposited coating forming an organometallic compound layer at the substrate-coating interface. We have chosen SS as the substrate material since it represents an additional challenge to obtaining a superior coating

adhesion strength when compared with other metallic substrates, such as titanium, chromium or zirconium. SS does not facilitate the formation of carbide structures that would otherwise promote even higher coating adhesion strengths. Since such carbide structures are not formed in the first stages of the deposition process, the coating resilience under tensile and compressive forces rely only on its low stiffness and the atomic interfacial mixing (AIM) at the substrate / coating interface. By decoupling these two phenomena (formation of carbide structures vs AIM) it was possible to further understand significant plasma mechanisms and identify an ideal parameter window that promotes an enhanced AIM.

The extent of AIM depends on the degree of ablation of both film and substrate during the deposition process, hence on the extent of competitive ablation versus polymerization. Increased ablation of substrate / coating materials by impact from plasma energetic species promotes mixing of the two materials at the interface. Conditions of high Φ_d combined with lower deposition rates would be expected to result in greater modification of the substrate surface in the first stages of the deposition process because the samples are exposed for longer to higher levels of energetic ion bombardment and diffusion of energetic plasma species. On the contrary, low Φ_d promotes higher deposition rates resulting in rapid concealing of the substrate. Our process allows for the deposition of PAC on SS 316L with enhanced adhesion strengths, sufficient to withstand very high compressive and tensile deformations, at $\Phi_d \geq 4.6 \times 10^8$ J/kg. This value falls between the values ~10^8 J/kg and ~10^{10} J/kg observed in plasma polymerization of tetrafluoroethylene and methane respectively [72]. Further mechanical tests revealed that 40 nm thick PAC layers prepared at $5.5 \times 10^8 \leq \Phi_d \leq$

5.8×10^8 J/kg and $Q_{\text{Acetylene}} = 1$ sccm outperformed any other recipes and were able to resist the same compressive and tensile deformations even after incubation in PBS for 24 hours at 37˚C or 1 hour at 90 ˚C. Therefore, with the present choice of substrate material we were able to demonstrate that our plasma deposition process allows the one-step deposition of outstandingly robust coatings without further need for gradient or inter layers, which are commonly applied to coatings that poorly adhere to metallic substrates. Here, PAC mechanical robustness, necessary to endure typical plastic deformation of coronary stents was achieved even on substrates that do not promote the formation of carbide structures.

3.3.6 Substrate conformal coverage

The best PAC adhesion strengths are expected at $|V_{\text{bias}}| \geq 750$ V and the lowest acetylene flow rate. Under these conditions the monomer residence time increases to 9.2 s and $\Phi_d \geq 6.5 \times 10^8$ J/kg, resulting in a significant increase in the plasma ionization degree (see Figure 2b). Consequently, intensification of ablation by ion impact on the substrate drops the average deposition rate to levels below 1 nm/min, an indication of increased competitive ablation. In fact, PAC thickness could not be increased beyond 17 nm and 13 nm for samples prepared under $|V_{\text{bias}}| = 750$ V and $|V_{\text{bias}}| = 1000$ V respectively, even with increased deposition time. This shows that under these conditions an equilibrium between the film deposition rate and the ablation rate is reached, suppressing further film growth on the substrate. Limitations in PAC deposition rate introduced by excessive plasma ion bombardment at very high $|V_{\text{bias}}|$ inhibited conformal substrate coverage. High resolution SEM imaging (see Figure 3.17a)

reveals an early stage columnar-type growth [204] where coating material forms islands on the

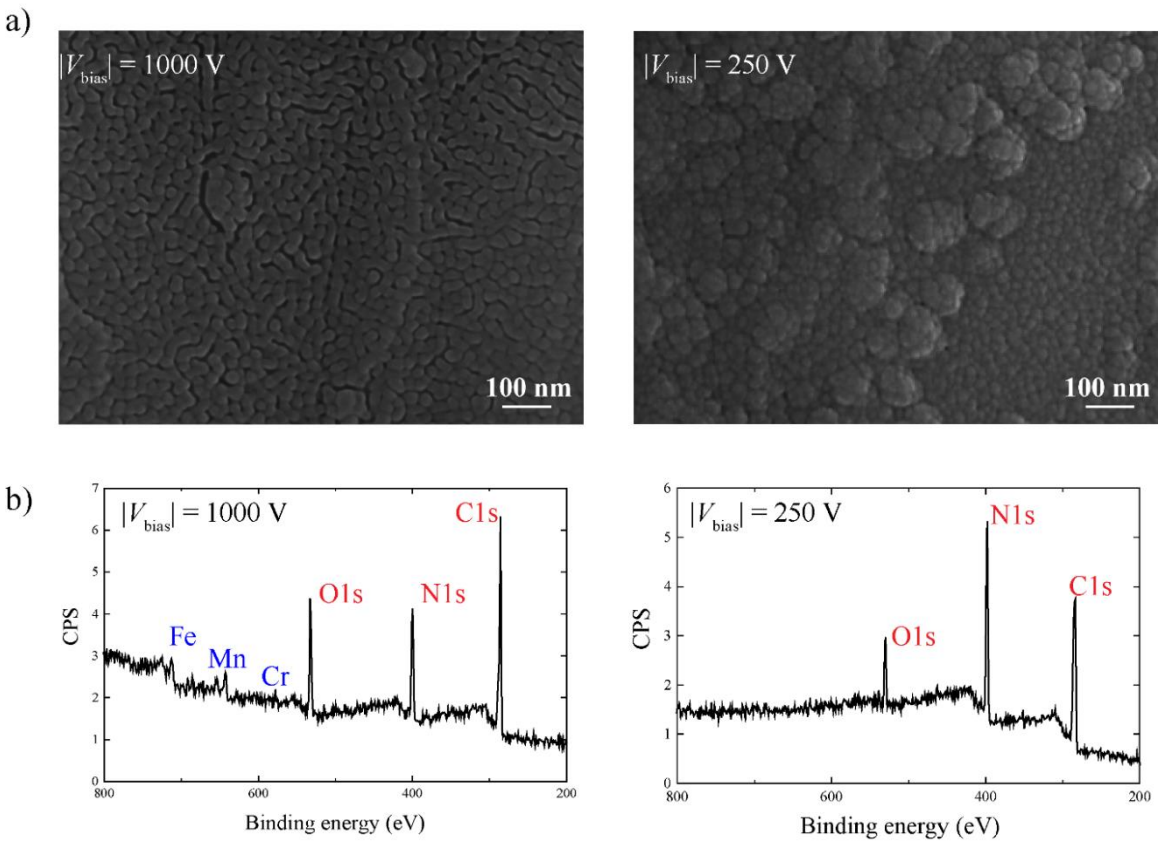

Figure 3.17: Substrate conformal coverage. a) High resolution SEM representative micrographs of PAC coated SS 316L prepared at $|V_{bias}|$ = 1000 V (left) and $|V_{bias}|$ = 250 V (right). At $|V_{bias}|$ = 1000 V the ablation rate equilibrates with the deposition rate and as a result PAC growth is suppressed to levels below 20 nm. Surfaces prepared under such conditions feature localized columnar nanostructures or islands with the underlying substrate exposed in-between them. When $|V_{bias}| \leq 500$ V the columns merge together and substrate conformal coverage is typically observed when PAC thickness is higher than 30 nm. b) XPS surveys of samples shown in Figure 6 reveal lack of conformal coverage (left), featuring Fe, Mn and Cr peaks that are typical of SS 316L materials.

substrate surface. When the film deposition rate is limited due to ablation phenomena the coalescence of the columnar structures is suppressed, preventing a total substrate coverage. Conformal substrate coverage is not achieved for PAC thickness lower than 20 nm as shown by SEM imaging and the detection of Fe, Mn and Cr in XPS surveys (Figure 7b). Wettability measurements also revealed that at $|V_{\text{bias}}| \geq 750$ V, PAC is more hydrophobic, presenting a water contact angle of ≈ 80° 10 days after deposition, while no significant changes in wettability (contact angle ≈ 65°) were observed for the remaining PAC samples, where substrate coverage was complete. When the diffusion rate of plasma reactive species that contribute to film growth is higher than the ablation rate and PAC grows beyond 30 - 40 nm, the localized columnar structures merge together giving rise to cauliflower-like nanostructures [188] that conceal the underlying metal

3.4 Conclusion

This chapter described the optimization of a technology that enables the one-step, controlled and highly reproducible fabrication of robust plasma-activated interfaces that are able to endure extreme plastic deformations of the underlying implant material imparting both tensile and compressive stress to the coating. Robust interfaces can be prepared at high energy inputs per monomer unit mass ($\Phi_d \geq 5.5 \times 10^8$ J/kg) and higher monomer residence times in the active plasma discharge ($\tau_{\text{Acetylene}} \approx 8$ s) and high nitrogen content in the feed gas mixture. Mild to medium applied pulsed bias ($|V_{\text{bias}}| \leq 500$ V) enables PAC layers to grow beyond a

critical point where total substrate coverage is achieved. Increasing the applied bias above 500 V triggers an enhancement of the plasma ionization degree where PAC growth is compromised by extensive ion bombardment involving N_2^+ molecular ions. Since PAC ablation and growth phenomena is correlated with the bombardment of energetic N_2^+ ions and the diffusion of reactive CN radicals towards the surface, respectively, in-situ screening of the emission intensity ratio between these species using OES diagnostics provides a good indicator of the growth regime. Conformal substrate coverage is usually achieved when $I_{\mathrm{CN}}/I_{\mathrm{N}_2^+} \geq 2$ and layers grow thicker than 20 nm. These coatings are highly rich in nitrogen (up to 35 at %) and also highly reactive, containing a high density of embedded radicals and surface functionalities such as amines. This enables further customized surface engineering through linker-free bioactivation using covalently immobilized bioactive molecules that can be appropriately chosen according to the application's needs.

4 BIOENGINEERING PAC FOR VASCULAR STENTS

4.1 Introduction

4.1.1 Mechanical requirements and challenges

Stents of varying size and composition are used throughout the vasculature to open vessels and restore blood flow to ischemic tissue. The dominant use is in the coronary circulation, re-opening narrowed arteries supplying the myocardium, but stents are also frequently used in the carotid artery and in the lower limbs. Accordingly, stents are an heterogenous collection of devices with significantly different materials and design characteristics. For coronary applications, stents range in diameter from 2 - 4 mm, and length from 8 - 38 mm. They are most commonly made from 316L stainless steel or alloys of cobalt-chromium or platinum-chromium to facilitate crimping, and balloon expansion for delivery. Their design can vary widely with respect to the width and number of struts, and corresponding open or closed cell design. In contrast, peripheral stents for the femoropopliteal segment are made from shape memory nickel-titanium (nitinol), have a larger diameter (4.5-10 mm) and significantly longer length (20 – 200 mm). Carotid stents are also self-expanding nitinol, with an intermediate length of 20 – 40 mm and diameter ranging from 6 – 10 mm.

In addition, comparative studies in both rabbit and porcine models represent a well-established pre-clinical and frequently used pathway for development of novel stents [205]. The models are complimentary, as each represents the best-validated approach for assessing stent thrombogenicity, endothelialisation and neointimal hyperplasia *in vivo*, respectively. Stents in these models are similar to those used for the coronaries, with the rabbit iliac model accommodating 3 mm diameter stents, of 10 mm length [206]. However, mechanistic studies

of stent performance can now also be performed in mice, using a donor-acceptor model where the stented artery of the donor mouse is grafted in the carotid of the recipient. Stents for this model are significantly smaller (0.6 mm diameter, 2.5 mm length), though also manufactured from stainless steel [207].

Taken together, the diversity of size, shape and underlying substrate make robustly and uniformly applying PAC challenging. While PAC must adhere to the underlying stent material, stent crimping and catheter balloon expansion during deployment demands a superior coating flexibility and robustness to avoid cracking, peeling and spallation. Additionally, pre-functionalization of PAC coated stents with biomolecules by incubation in solution could further exacerbate coating failure upon fenestration and accumulation of solution components at the PAC / stent interface. Since stents are complex three-dimensional objects, the deposition of mechanically robust PAC with a high degree of atomic interfacial mixing could be particularly challenging. Contrarily to two-dimensional samples, which lay flat below a stable and uniform plasma sheath, the intricate geometry of the stent is prone to form less uniform plasma sheaths and drive local changes in the plasma characteristics. This could result in the deposition of coatings with gradients in thickness and chemical/physical properties throughout the stent, which would ultimately compromise coating performance. Therefore, bioengineering PAC for stent applications is a complex task that needs to address not only physical and chemical requirements but also biocompatibility as discussed below.

4.1.2 Biocompatibility requirements

Biocompatible coatings for cardiovascular implants should be inherently non-thrombogenic and able to recruit and promote the proliferation of endothelium cells while inhibiting the attachment and overgrowth of smooth muscle cell (SMC) layers. They should fully integrate into the human vasculature by prompting healing responses to prevent implant rejection and severe immune responses post-implantation. Implant hemocompatibility can be achieved by preventing the adsorption and further denaturation of undesirable blood proteins that mediate the pathways of blood clot formation. The attachment, on the coating surface, of bioactive molecules that could prevent platelet adhesion and activation and that could be capable of further inducing favourable local cellular responses would represent a great advantage.

Although plasma synthesised carbon-based coatings were shown to retain good hemocompatibility in various *in-vitro* essays, *in-vivo* investigations to access their capacity for endothelialisation, SMC inhibition and hemocompatibility are seldom reported. Good results of these coatings in the great majority of such *in-vitro* tests were explained by the higher affinity of the surfaces to preferentially adsorb albumin over fibrinogen. However, *in-vitro* tests poorly simulate the harsh conditions of the human vasculature such as the high flow regimes of blood in arteries. High flow regimes can lead to desorption of adsorbed or weakly attached proteins. For this reason, covalent immobilization of functional bioactive molecules is preferred over their physical adsorption. Recent advances [90] showed that PECVD prepared carbon-based coatings with high concentrations of long-lived unpaired electrons can covalently immobilise biomolecules in their bioactive form directly from a

buffer solution without the need for any linking chemistry. These advances could establish a new era of truly bio-functional and -compatible cardiovascular implants.

4.1.3 Adsorption of blood protein

The biocompatibility and particularly the hemocompatibility of a blood-contacting surface are strongly affected by the affinity of the surface to adsorb specific blood proteins. The time scale on which blood proteins interact with and are adsorbed on a coating's surface is several times smaller than that of any of the interactions involving other blood components. For this reason, local cellular response to a foreign body implanted in a blood vessel will be mostly governed by the nature of the proteins adsorbed on its surface. For instance, it is known that adsorbed fibrinogen (Fib) enhances the adhesion and activation of platelets [146], triggering the coagulation pathway. Furthermore, Fib is also a fundamental element in the coagulation cascade since it is cleaved into fibrin to form an irreversible thrombus. On the other hand, albumin can inhibit the adhesion and activation of platelets, preventing the formation of a clot.

The mechanisms governing the adsorption of different blood proteins on carbon-based surfaces are not yet fully understood. The subject has driven increasing research in the last two decades and although some advances have been achieved, important questions remain unanswered. Difficulties arise in determining exactly which physical and/or chemical properties of the surfaces rule protein adsorption. Available data suggest surface roughness and surface energy, hydrogen and nitrogen fraction, sp^3 content and electrical band-gap as

possible candidates. However, these properties are generally interlinked and their decoupling is largely limited by the deposition technique used to prepare the surfaces.

It has been suggested that the adsorption of blood proteins on a DLC surface is related to the charge (electrons) transfer between the proteins and the surface [122, 208]. Protein adsorption and further denaturation occurs if the Fermi energy level of the protein is such, that electrons from its valence band are transferred to the conduction band of the coating material [208]. Therefore, hemocompatible coatings should be made with electron energy band gaps greater than those of proteins that are responsible for the formation of thrombus – such as fibrinogen, which has a band gap of 1.8 eV [209]. On the other hand, adsorption of albumin would be favourable as it can inhibit the activation of platelets on the surface of the film.

It has also been reported that surface roughness and wettability may influence the adsorption of blood proteins onto the surfaces [140, 210-212]. Albumin for instance was described to have greater affinity for more hydrophilic and rougher ta-C surfaces, made by filtered arc deposition, when compared to smoother and less hydrophilic a-C:H thin films prepared by plasma-enhanced chemical vapour deposition (PECVD) [140]. However, different chemical compositions (e.g. hydrogen content) and bonding configurations between the different samples may have also influenced protein adsorption. Based on spectroscopic ellipsometry (ES) measurements [210] it was suggested that different a-C:H coatings made by plasma magnetron sputtering can adsorb human serum albumin (HSA) and human fibrinogen (Fib) differently. The surface concentration ratio (proportional to the thickness of the adsorbed protein layer) HSA/Fib ~ 1 was higher for samples prepared with floating potential whereas

surfaces made using a negative bias presented a ratio HSA/Fib ~ 0.4. Later the same authors [145] showed that a-C:H coatings made under the same conditions presented a different behaviour with respect to HSA and Fib adsorption. The HSA/Fib thickness ratio was found to increase on samples prepared with bias, which were identified by AFM as being rougher. Berlind *et al* [212] studied HSA adsorption on different amorphous, graphitic and fullerene-like surfaces also using spectroscopic ellipsometry. They found that amorphous structures, i.e. with smoother surfaces, adsorbed more HSA when compared with graphitic and fullerene-like thin films. However, the authors could not correlate a higher HSA adsorption exclusively with the roughness of the thin films. This was because the different films also presented different chemical structure, wettability and water-binding affinities which are important parameters that also influence protein adsorption. Available data suggests that blood protein adsorption is a complex phenomenon and there is still no clear consensus on its drivers. Additional investigations are therefore necessary to understand the basic phenomena of protein / surface interactions and how different features in the surfaces can regulate differential protein absorption.

4.1.4 Surface functionalization with immobilized bioactive molecules

Recent studies found that rf-PECVD carbon-containing plasma polymers prepared with bias have the ability to covalently immobilise proteins in their bioactive form [90, 157] by reaction with radicals contained in the plasma polymers. Organic precursor plasma discharges can be used to deposit hydrophilic plasma activated radical-rich a-C:H-like coatings (PAC) if sufficient sample bias, usually up to -1kV, is provided [89]. Here, the ions formed in the plasma are accelerated with increased energy provided by the high voltage bias towards the

growing carbonised film on the substrate surface. The ion impacts promote the formation of regions of π conjugated sp^2 bonded carbon nanoclusters with extended states and a high degree of cross-linking [213]. The extended states in these π conjugated regions provide stable sites for the unpaired electrons of radicals. These unpaired electrons can hop from cluster to cluster and diffuse towards the coating surface. The content of unpaired electrons, measured by electron paramagnetic resonance spectroscopy, was found to be proportional to the bias voltage and thickness of the deposited film [157]. Colorimetric assays using immobilised horseradish peroxidase or catalase as probes have been employed to confirm the capability of PAC coatings to retain the bioactivity of the immobilised protein layer [69, 156, 214]. A variety of polyamino acids have also been found to be covalently attached to PAC surfaces via chemical bonding with unpaired electrons emerging at the film's surface [215].

Metallic substrates such as stainless steel when coated with PAC alone are significantly more hemocompatible, a property revealed by the PACs ability to considerably reduce the formation of human thrombus in different *in-vitro* assays. Blood compatibility is an essential characteristic for biocompatible cardiovascular stents and although necessary, it does not address endothelialisation and restenosis. A stable immobilization of bioactive biomolecules on the coating surface could represent a leap forward towards the true biofunctionalization of cardiovascular implants such as arterial stents. Plasma-made radical-rich coatings for stents, immobilising the appropriate biomolecule or biomolecule cocktails, to impart appropriate local biological responses to achieve full vascular integration of stents (see figure 4.1) can be envisaged. The advances discussed above suggest that chemical conjugation of proteins through the reactions of unpaired electrons with protein amino acid side chains is possible

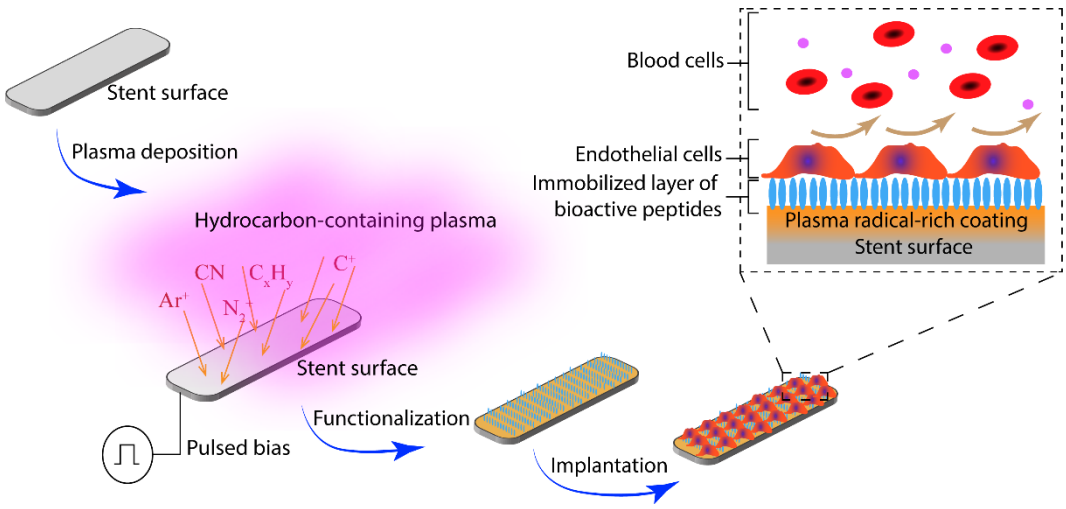

Figure 4.1. Proactive biofunctionalization of coronary stents using plasma discharges in carbon-based atmospheres. The stent is electrically biased to accelerate plasma positive ions towards the growing coating, creating therefore a radical-rich plasma activated coating (PAC). Biomolecules are then immobilized on the coating via radical bonding and they maintain a bioactive conformation after immobilization. Following stent implantation, the immobilized biomolecules induce favourable local cellular responses promoting endothelial cell migration, adhesion and proliferation on the implant surface to form a healthy endothelium. Smooth muscle cell proliferation and platelet activation is inhibited, preventing neointimal hyperplasia and the formation of thrombi to achieve favourable integration of the implanted stent in the host vasculature.

while preventing protein denaturation. It was shown that PAC surfaces could be used for the immobilization of tropoelastin in a bioactive conformation on flat stainless steel substrates [156]. Tropoelastin, being a precursor of elastin, is an important vascular protein since it participates in the correct structuring and functionalization of the whole vascular system. Elastin provides fundamental rheological properties to blood vessels, facilitates endothelialisation and constitutes (together with collagen) the sub-endothelia layer, the lamina, interfacing the intima and the media (see Figure 4.2). As an essential component of the lamina, elastin fibres play an important role in avoiding infiltration of smooth muscle cells towards inner layers of the blood vessel while promoting and regulating the growth and proliferation of luminal endothelial cells to form a healthy endothelium. Covalently immobilised tropoelastin and specific domains of tropoelastin were shown to drastically enhance the hemocompatibility of PAC coated SS substrates in *in-vitro* assays using human whole blood [216]. Endothelial cell attachment and proliferation were also improved when compared to uncoated samples.

More recently, PAC surfaces functionalised with bioactive plasmin revealed superior human blood compatibility and endothelialisation [8, 217] when compared to SS controls. Plasmin is an enzyme, derived from plasminogen, present in the blood that cleaves fibrin clots in a process called fibrinolysis. Fibrin results from the action of the protease thrombin on fibrinogen, causing it to polymerize [218]. Together with platelets, polymerized fibrin forms the hemostatic plug, mostly known as clot. When conjugated with PAC, plasmin is able to prevent the formation and deposition of fibrin complexes reducing the probability of clot development. Hemocompatibility and good *in-vitro* proliferation rates of endothelial cells

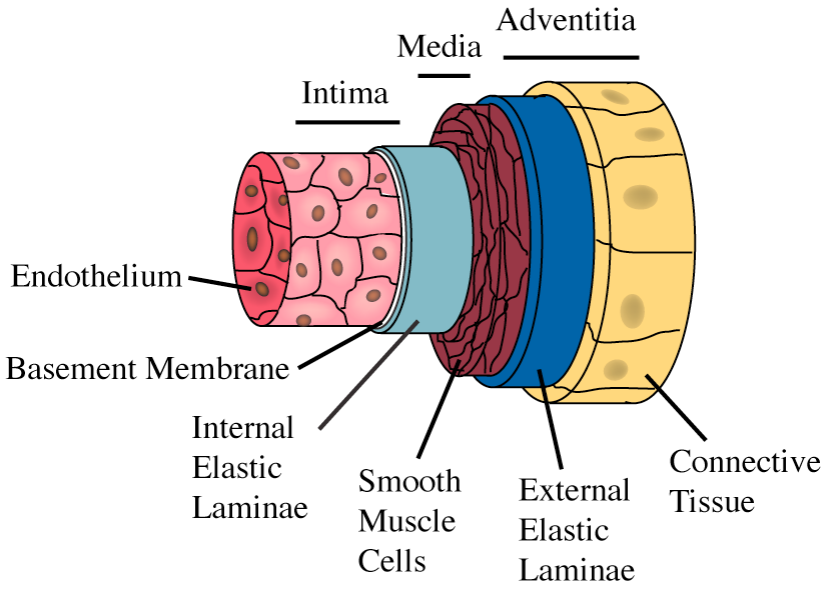

Figure 4.2. A schematic representing the structure of an artery. Image taken with permission from [219].

suggest that stents functionalised with PAC immobilised plasmin could prevent early thrombogenicity while promoting endothelialisation for stent vascular integration.

PAC conjugated with constituents of high density lipoproteins were also recently studied for hemocompatibility, endothelialisation and smooth muscle cell proliferation [6]. A low concentration of high density lipoproteins in the blood was previously associated with restenosis and thrombosis after stent deployment and coronary angioplasty. PAC was shown to covalently immobilise constituents of HDL while retaining its bioactivity. Stainless steel PAC coated substrates functionalised with HDL strikingly reduced the formation of human blood clots *in-vitro*. Moreover, HDL coated surfaces encouraged endothelialisation and prevented the over-proliferation of smooth muscle cells.

4.2 Materials and methods

4.2.1 Stent designs

In addition to flat SS flat substrates (Chapter 3), PAC was deposited on a variety of stent designs and material compositions as shown in Figure 4.3: custom laser cut 3.0 mm x 11 mm x 100 μm (stent diameter x stent length x strut length) SS stents (Laserage, USA), previously adopted in rabbit iliac models [112]; custom laser cut 0.64 mm x 2.5 mm x 70 μm SS stents (Brivant Ltd) used in carotid artery mouse model [6, 220]; 3.0 mm x 12 mm x 87 μm commercially available (Abbott Medical, USA) medical grade Cobalt Chrome alloy (20-Chromium 15-Tungsten 10 Nickel) coronary stents; custom laser cut 20 mm x 20 mm x 312 μm Nickel Titanium (NiTi) alloy (Endoluminal SCIENCES, Australia) abdominal aorta self-

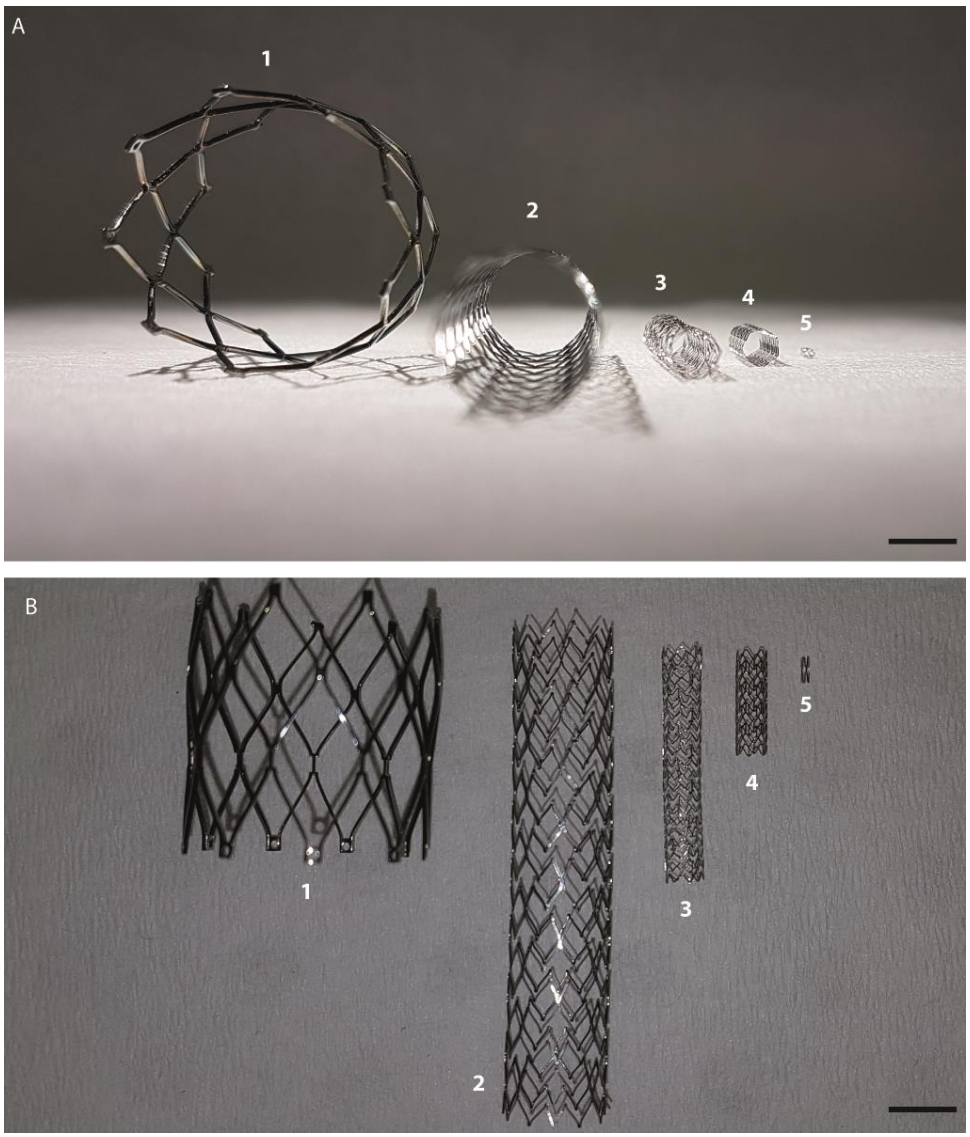

Figure 4.3. A) A photograph showing a cross-sectional view of bare metal stents of various designs, dimensions and material composition studied in this work. B) As in A but showing a top view of the stents detailing the strut design and length of each stent. From left to right stents are: (1) Self-expandable NiTi abdominal aorta stent (Endoluminal SCIENCES), (2) Self-expandable NiTi peripheral stent (Medtronic, USA), (3) Cobalt Chrome alloy coronary stent (Abbott Medical, USA), (4) SS coronary stent for rabbit iliac model (Laserage, USA) and (5) SS stents for carotid artery mouse model (Brivant Ltd). Scale bars are 4 mm (A) and 6mm (B).

expandable stents and 9.0 mm x 80 mm x 120 μm commercial available (Medtronic, USA) medical grade NiTi self-expandable peripheral stents. The stent dimensions we provided by the supplier and the strut length of all stents was measured using electron scanning microscope.

4.2.2 Stent cleaning protocol

All custom laser cut stents were subjected to a cleaning protocol with solvents in a ultrasonication bath followed by an argon plasma treatment to eliminate impurities resulting from the manufacturing process and exposure to the laboratory environment. Particularly, SS stents were cleaned using the same protocol for 2D substrates reported in section 3.2.1. A similar cleaning protocol was followed for CoCr and NiTi stents but the water rising steps were not employed to avoid surface oxidation. The discharge parameters for the argon plasma treatment were the same as used for the 2D substrates (see section 3.2.1).

4.2.3 PAC stent coating methodology

Stents were supported by conducting silver wire (see Figure 4.4A-D) and mounted on top of the electrically biased electrode using a custom-built SS holder for PAC coating and argon plasma treatment. To minimise strut shadowing caused by the silver wire, stents were hooked through one of the strut intersections located at one of the stent extremities (see detail in Figure 4.4D). The properties of different PAC formulations were extensively investigated first on custom laser cut SS coronary stents. The best PAC formulation was then applied to stents of various designs and material compositions.

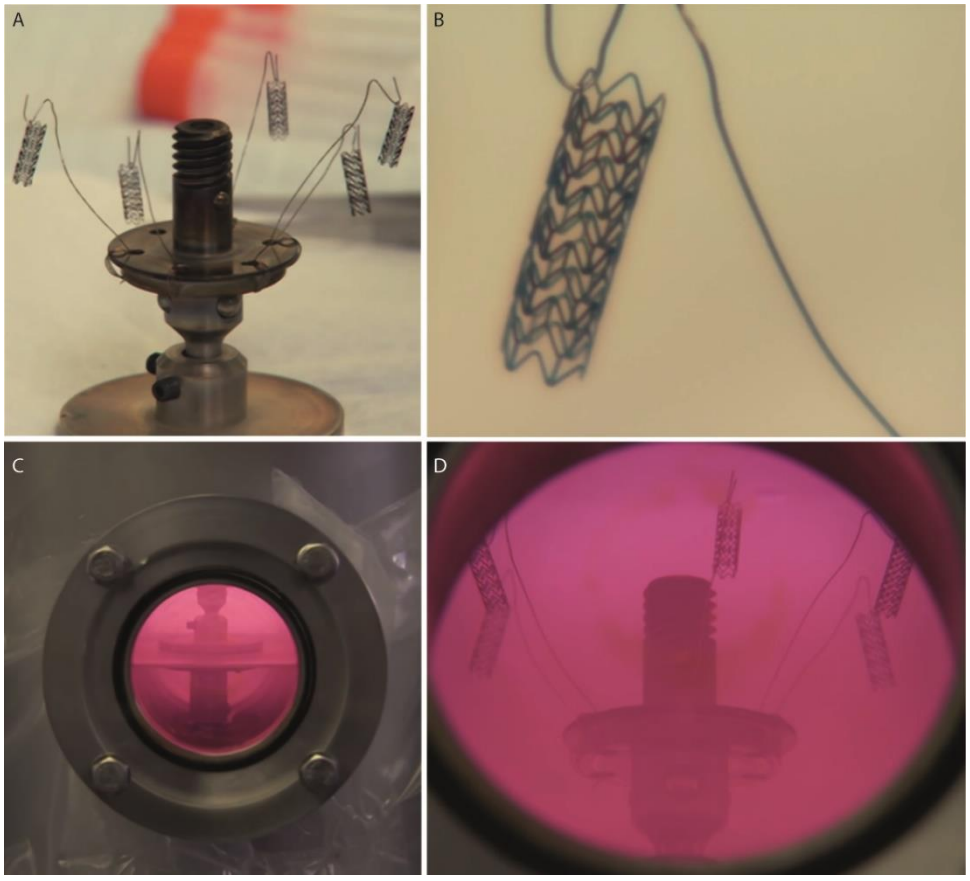

Figure 4.4. A) A photograph showing the custom-made mount used in this work to hold the stents during PAC deposition. A total of 5 stents are shown in this example but the mount can hold up to 12 stents in one deposition run. B) A zoom of the previous image detailing a SS stent (see stent number 4 in Figure 4.3) held by the fine silver wire and through the strut intersection. C) and D) Photographs showing the stent mount on top of the biased electrode through the chamber's view port during PAC deposition.

4.2.4 Stent balloon expansion

The mechanical resilience of PAC under plastic deformation was tested by crimping and expanding the stents with a balloon catheter, hence simulating stent deployment conditions during percutaneous surgery. The ability of PAC to remain on the stent following balloon expansion was further tested by pre-incubating the coated stents in a PBS solution for 24 hours at 37˚C or 1 hour at 90˚C. The stability of PAC was assessed by imaging the stents at high magnification using SEM and an optical microscope.

4.2.5 Covalent attachment of tropoelastin

Tropoelastin, the soluble pre-cursor of elastin is abundant in large blood vessels and is known to promote endothelialisation, inhibit smooth muscle cells while having good hemocompatibility [221]. We have previously employed tropoelastin (TE) as a multi-functional biomolecule to enhance endothelial cell attachment [156] and blood compatibility on early iterations of our PAC surface. We employ tropoelastin here as a probe to determine the covalent binding capacity of our optimised PAC formulations.

The detection of covalently retained tropoelastin (TE) on PAC samples performed with an ELISA assay, has been described previously [156, 214]. Briefly, recombinant human tropoelastin (Elastagen Pty Ltd) at 50µg/mL was applied to 0.8×1.2 cm samples of PAC for 90 mins. Samples were thoroughly washed and then exposed to 5% SDS (Sigma-Aldrich®) at 90 °C for 10 mins and subsequently blocked in 0.1% Casein (Sigma-Aldrich®) prior to antibody incubation. Detection of bound TE was performed after overnight incubation with a

mouse monoclonal anti-elastin antibody BA-4 (Sigma-Aldrich®) followed by a sheep anti-mouse Biotin-conjugated secondary antibody (GE Healthcare Life Sciences). A Streptavidin-HRP Conjugate was then added to the samples, allowing for colorimetric detection with ABTS (Sigma-Aldrich®) solution. The absorbance was measured at 405nm after incubation for 40 min.

4.2.6 Thrombogenicity assays

Whole blood was obtained from healthy, non-smoker, male volunteers with informed consent in accordance with the Declaration of Helsinki, who had not taken aspirin two weeks prior to donation. Approval for this work was granted by Sydney Local Health District (protocol X15-0147 & HREC/15/RPAH/203).

Platelet Rich Plasma Adhesion - Heparinized whole blood (0.5U/ml) was centrifuged for 15 min at 1000 rpm in swinging rotors. The supernatant, platelet rich plasma, was removed and incubated with each sample for 10, 30 and 60 min while rocking. Samples were washed in PBS and subsequently fixed in 2.5% glutaraldehyde in 0.1M sodium phosphate buffer and imaged by SEM.

Fibrinogen assay - A static plasma contact assay was implemented using a fluorescent fibrinogen precursor incorporated together with the plasma. Heparinized whole blood (0.2 U/ml) was centrifuged at 1000 rpm for 15 min to isolate serum. Serum and fluorescent fibrinogen (50 μg/ml) were mixed in equal volumes prior to incubation with PAC and SS samples to allow for the visualization of fibrin network formation as previously described [222]. Samples were rocked in a 24-well plate at 37°C for 60 minutes, then washed three

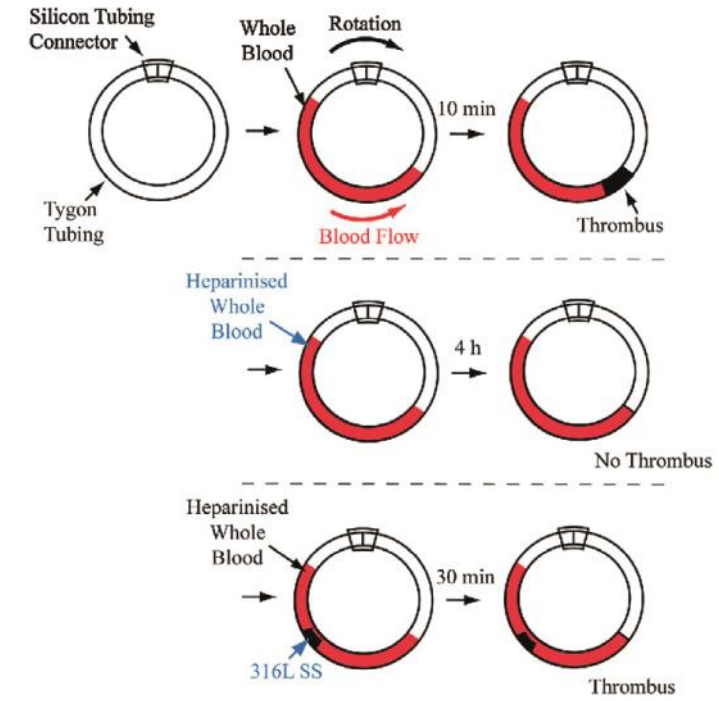

Figure 4.5. A schematic presentation of the modified Chandler loop adopted in this work. Image taken from [8].

times with PBS, before imaging with a Zeiss Axiovision Imager Z2. The fluorescent fibrinogen was tracked as it was incorporated into the growing fibrin network, allowing to image and quantify the extent of fibrin network formation. Quantification of the fluorescent intensity was calculated using Image-Pro Premier.

Thrombogenicity under flow - Evaluation of the thrombogenic potential of PAC was investigated using a modified Chandler loop (see Figure 4.5), as previously described [8]. Briefly, samples were balloon expanded into 28 cm lengths of Tygon S-50-HL tubing (SDR, Australia), connected into loops using 1cm silicone connectors and filled with heparinized whole blood (0.5 U/ml, 2.5 ml). The loops were rotated at 34 rpm at 37°C for 60 minutes. The thrombus and steel from each loop was removed for imaging and weighing.

4.2.7 Statistical analysis

Data are expressed as mean ± SEM and indicated in figures as *$p < 0.05$, **$p < 0.01$ and ***$p < 0.001$. The data were compared using ANOVA followed by Binferroni's post-hoc test using Graph-Pad Prism version 5.00 (Graphpad Software, San Diego, California) for Window.

4.3 Results and discussion

4.3.1 Mechanical performance on stents

Translation of PAC formulations onto three-dimensional samples was first studied by depositing coatings on balloon-expandable SS stents. A first set of stents was coated using

plasma parameters that yielded a low level of atomic interfacial mixing (AIM), i.e. $\Phi_d = 2.4 \times 10^8$ J/kg ($Q_{\text{acetylene}} = 8$ sccm and $V_{\text{bias}} = -500$ V), hence resulting in mechanically poor PAC formulations on two-dimensional substrates as shown in Figure 3.15B. Since the coating intrinsic stress increases at greater coating thicknesses, PAC should be prepared as thin as possible to avoid poor mechanical coupling with the stent but at the same time, it should also completely cover both inner and outer struts. At $\Phi_d = 2.4 \times 10^8$ J/kg the deposition rate is 35 nm/min measured on flat silicon wafers laying horizontally on the biased substrate. Since the stents were mounted vertically inside the chamber, it was hypothesised that a minimum PAC thickness of 40 nm should be achieved on the struts closest to the rf electrode with a deposition run of 67 seconds. To allow a complete coverage of the stents the total deposition time for this PAC formulation was set to 130 seconds. To test the mechanical properties of low AIM PAC formulations, the coated stents were manually crimped against a balloon catheter. The crimping process applies an inward radial force, resulting in a reduction of the stent internal diameter from 3 mm to 1 mm. During this process, significant tensile and compressive forces are applied to the struts, which are particularly aggravated at the intersections joining three adjacent struts. The crimped stents did not showed signs of coating failure under optical microscope imaging. Following crimping, stents were expanded using a 3 mm angioplasty balloon catheter, which restored the internal cross section of the stents to its nominal position and dimensions. The stents were then removed from the balloon and imaged under optical microscopy and SEM. Optical imaging revealed generalized peeling of PAC throughout the stent in both inner and outer struts (see Figure 4.6A-D). Peeling and spallation of PAC was observed in both optical and scanning electron microscopies, as seen by the exposure of the underlying SS and indicated by the green arrows in Figure 4.6. These

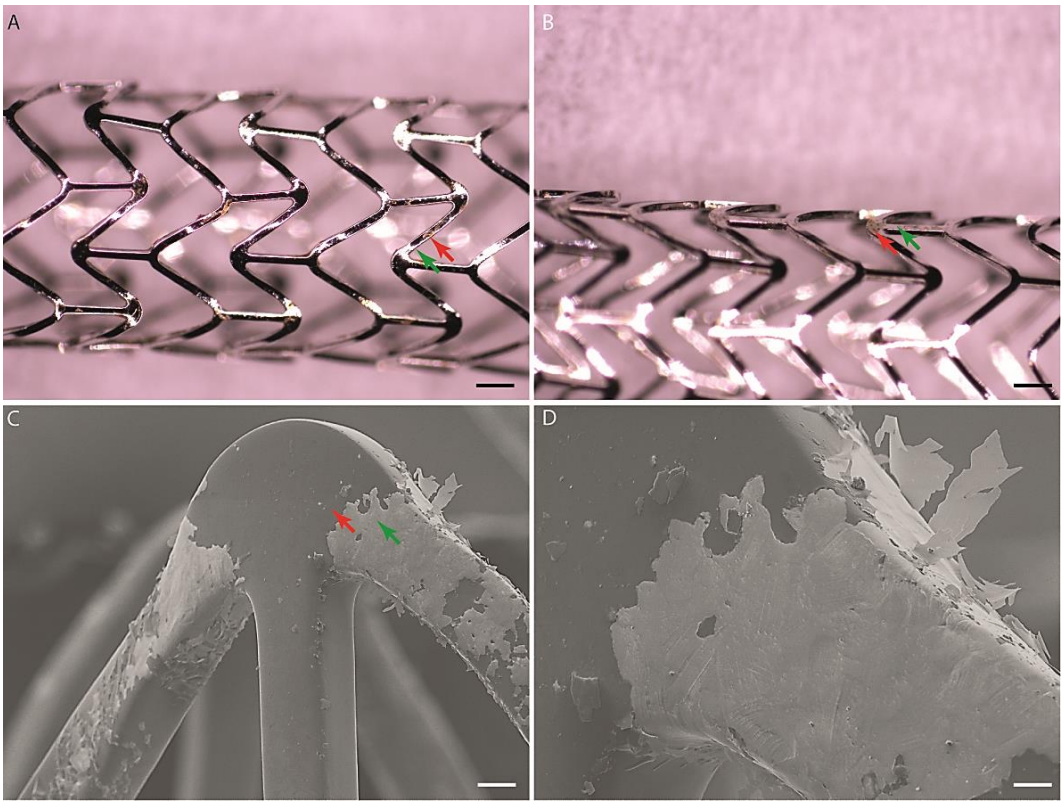

Figure 4.6. Mechanical performance of low AIM PAC on expanded SS stents. A) and B) Representative optical micrographs of SS stents coated with a thin layer (~30 nm) of PAC formulation synthesised at low energy input per monomer unit mass ($\Phi_d = 2.4 \times 10^8$ J/kg), i.e. resulting in low AIM. Following crimping and expansion with a balloon catheter, most of PAC (red arrow) peeled, hence exposing the underlying SS stent material (green arrow). C) and D) Under SEM, the exposed SS (green arrow) due to PAC (red arrow) peeling is clearly shown by the changes in the image contrast throughout the struts. Scale bars are 500 µm (A and B), 65 µm (C) and 15 µm (D).

results show that poor adhesion strength of PAC to 2D SS surfaces due to low levels of AIM are translated to more complex 3D structures.

The mechanical properties of PAC formulations synthesized with high monomer fragmentation levels was then studied by coating stents at $\Phi_d = 5.6 \times 10^8$ J/kg ($Q_{\text{acetylene}} = 1$ sccm and $V_{\text{bias}} = -250$ V), i.e. within the parameter window that delivered robust PAC on 2D SS substrates (Figure 3.15a). Since the deposition rate for the same conditions is ~2 nm/min (measured on 2D silicon wafers) and the deposition time for this round of samples was 15 minutes, PAC layers formed under these conditions should have been thicker than 30 nm in the outside struts. Visually, the coated stents presented different colors upon incidence of light at different angles, ranging from light yellow and green to dark blue and violet (Figure 4.7A and B). Optical microscopy and SEM imaging revealed that a conformal coverage of both inner and outer struts was achieved. Results in Figure 4.7 show that PAC applied to a stent under these discharge conditions is significantly more resilient, resisting crimping and further balloon expansion without cracking and delamination. Conformal PAC coverage of the underlying struts was observed even under severe plastic deformation of the stent with no signs of peeling and spallation of the coating (Figure 4.7C). At higher magnification, nano- sized cracks were observed at the strut intersections where the plastic deformation of the stent is greatest. The observed cracks were formed during expansion of the stent due to stress accommodation of the coating. Importantly, cracking propagation was not observed and the underlying stent material was not exposed after plastic deformation, showing that the integrity of PAC synthesized at high AIM can be preserved on geometrically complex samples.

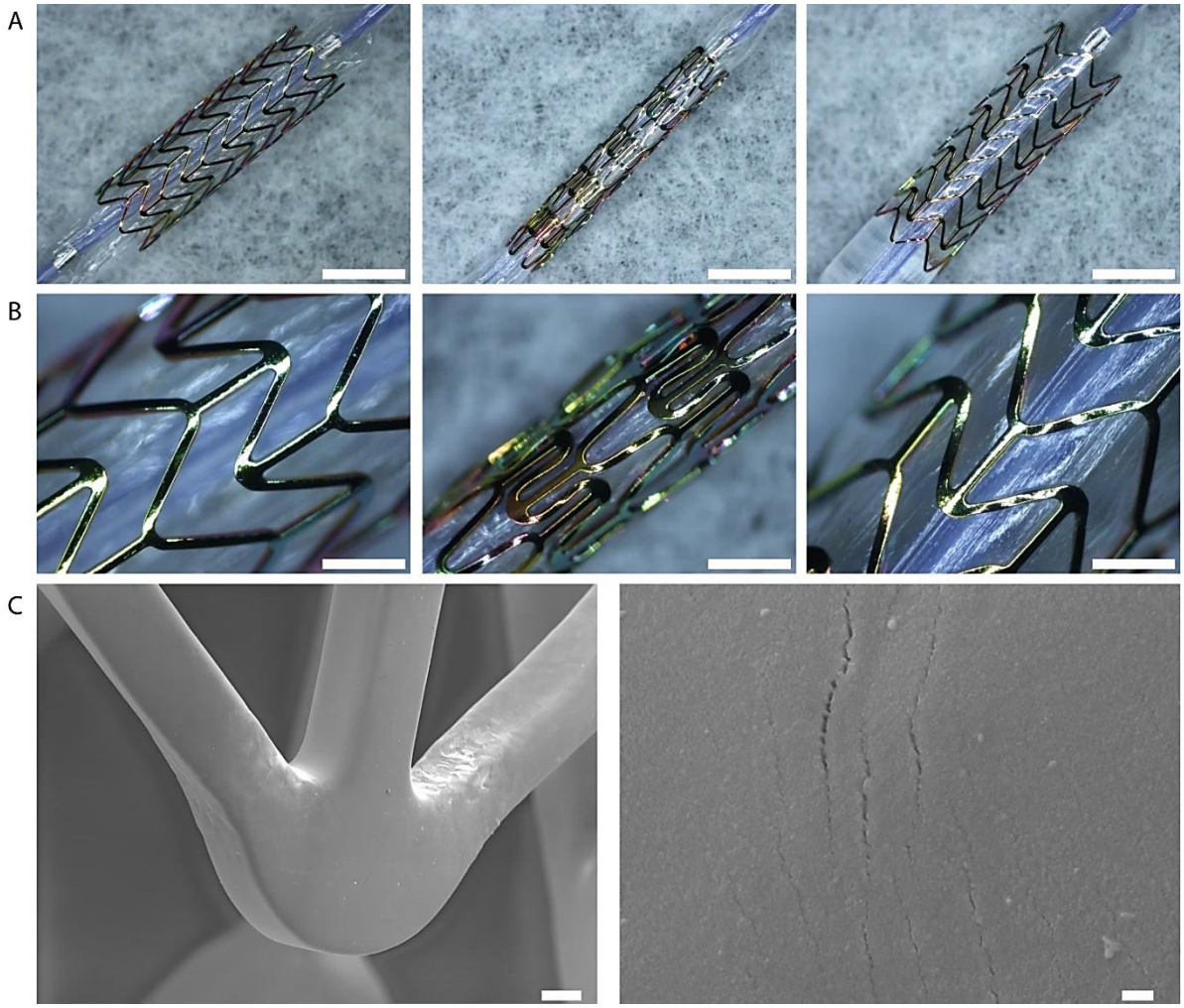

Figure 4.7. Mechanical performance of high AIM PAC on crimped and balloon expanded SS stents. A) Optical representative micrographs of SS stents coated with a thin layer (~30 nm) of PAC formulation synthesised at high energy input per monomer unit mass ($\Phi_d = 5.6 \times 10^8$ J/kg), i.e. resulting in high AIM. The images show the coated stents on a catheter balloon before (left) and after being fully crimped onto the balloon (middle); following crimping the stent undergoes a 100% expansion as shown by the image on the left. B) Same as in A) but at a higher magnification. The integrity of PAC was maintained after plastic deformation of the stent with no apparent peeling. C) SEM imaging of the expanded stent, as shown in A) and B), confirm the mechanical robustness of high AIM PAC. Localized nano-sized cracking (with no exposure of the underlying strut) is visible as a result of stress accommodation only in regions of greater plastic deformation of the stent. Scale bars are 3 mm (A), 750 µm (B) and 50 µm (left D) and 500 nm (right D).

To study the role of the deposition time and the mechanical performance of thicker PAC layers, the same mechanically resilient PAC formulation ($\Phi_d = 5.6 \times 10^8$ J/kg) was applied to a SS stent using a total deposition time of 45 minutes. The thicker PAC layer was dark blue on the outer struts, while the inner stents still showed some regions of yellow/light brown (Figure 4.8A). The characteristic darker color indicates that the PAC deposition rate is greater on the outside struts where the surfaces are more readily exposed to the plasma. An inspection of the stent under optical microscopy did not reveal signs of coating peeling (Figure 4.8A and 4.8B). Under SEM however, micro-sized cracking and delamination was observed in the regions where strain was more accentuated, by the development of plastic deformation due to torsion of the strut during stent expansion (Figure 4.8C and 4.8D). Although spallation was not propagated throughout the strut, exposure of the coating to the blood stream could aggravate delamination leading to further peeling.

The resilience of PAC formulations synthesized under high AIM conditions ($\Phi_d = 5.6 \times 10^8$ J/kg) was further studied by incubation the coated stents in a PBS solution for 24 hours before crimping and balloon expansion. Poor coating adhesion driven by an aggravation of intrinsic stress at greater thicknesses was avoided by depositing a ~30nm PAC layer on SS

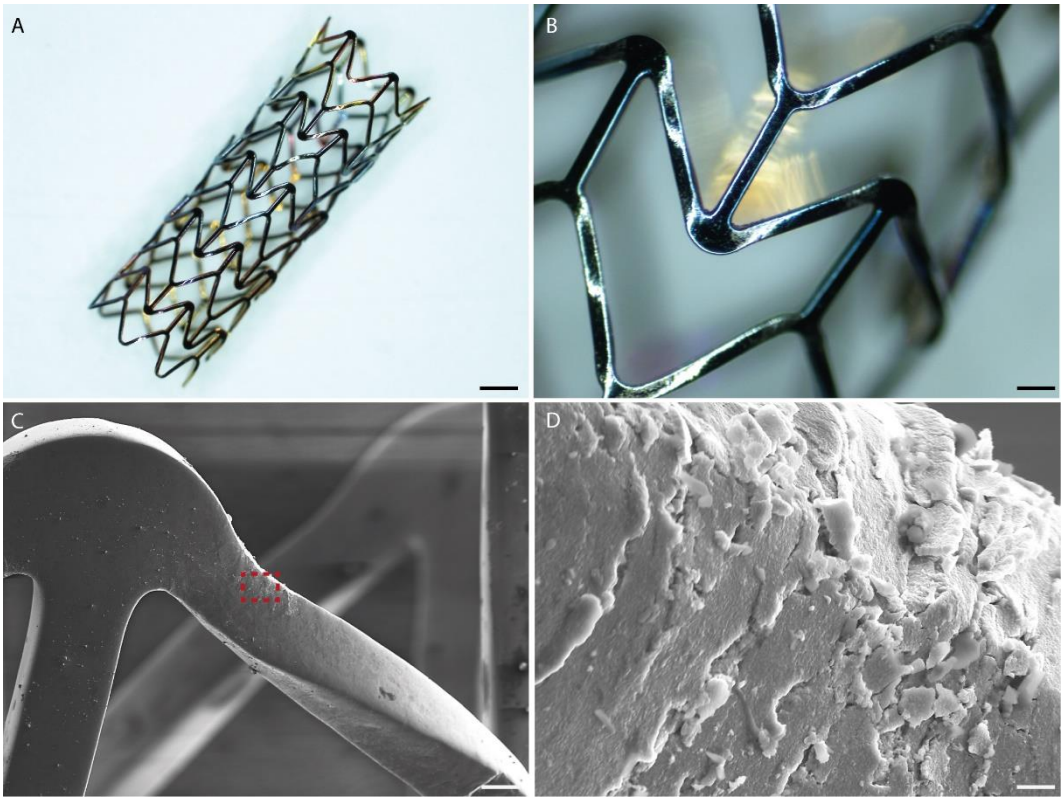

Figure 4.8. Mechanical performance of high AIM thick PAC layers on expanded SS stents. A) and B) Representative optical micrographs of SS stents coated with a thick layer (~100 nm) of PAC formulation synthesised at high energy input per monomer unit mass ($\Phi_d = 5.6 \times 10^8$ J/kg), i.e. resulting in high AIM. Following crimping and expansion with a balloon catheter, the integrity of the PAC layer (dark blue color) seems to have been preserved, showing no apparent signs of peeling and exposure of the underlying SS. C) Under SEM, microcracking was observed in the regions of aggravated plastic deformation (red square) driven by torsion of the struts during stent expansion. D) SEM of the PAC coated stent at higher magnification (red square in Figure 4.8C) shows that the underlying SS stent material was not exposed. Scale bars are 1 mm (A) 250 µm (B), 50 µm (C) and 1 µm (D).

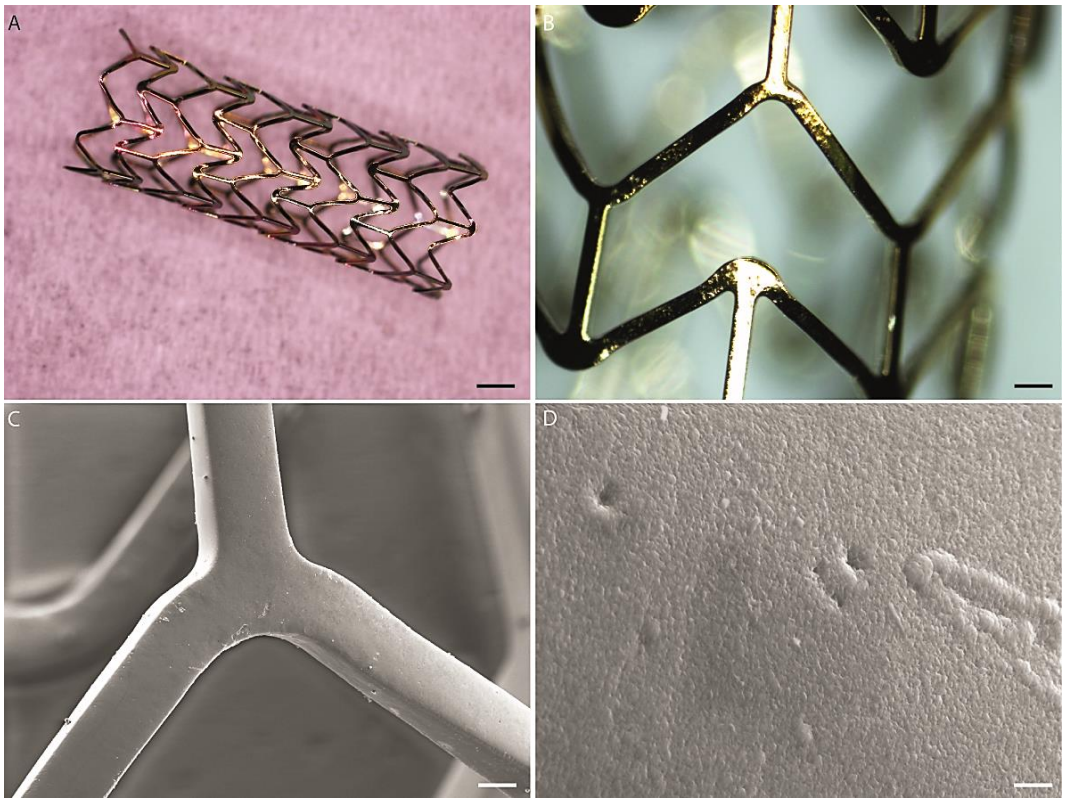

Figure 4.9. Translation of mechanically robust PAC to SS stents following incubation in solution and expansion. A) and B) Optical representative micrograph of thin PAC (~30 nm, $\Phi_d = 5.6 \times 10^8$ J/kg) coated SS stents that underwent aggressive crimping and expansion with a catheter balloon. Prior to balloon expansion, stents were incubated in PBS for 24 hours at 37˚C. C) and D) High magnification SEM imaging (right) reveals a uniform and conformal strut coverage without coating cracking and peeling. Figure D) details the PAC surface morphology on the stent at high magnification (x15000). Scale bars are 1 mm (A) 200 µm (B), 60 µm (C) and 500 nm (D).

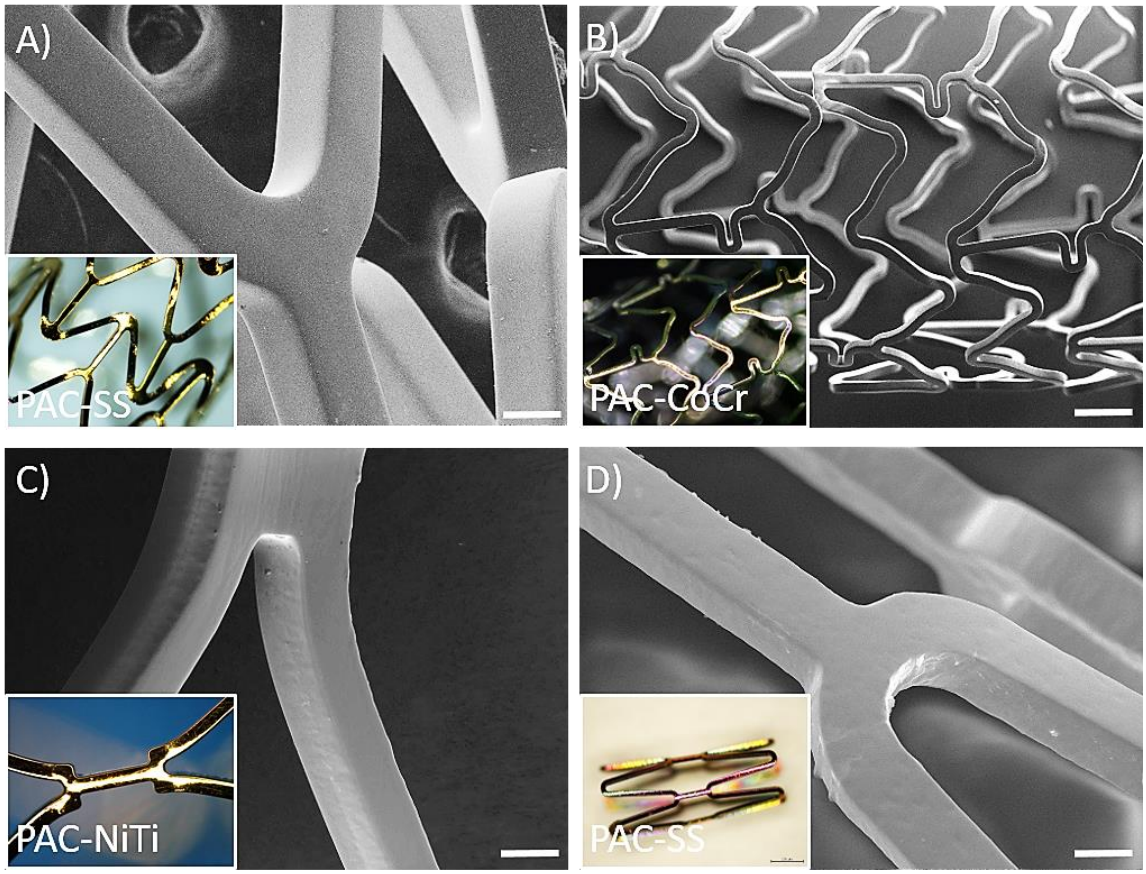

Figure 4.10. Translation of mechanically robust PAC to various stent designs, sizes and material composition including SS (A) and CoCr (B) sized coronary stents, a NiTi peripheral stent (C) and a SS mouse stent (D). All stents were subjected to plastic deformation carried out by crimping and balloon expansion. Scale bars are 100 µm (A), 600 µm (B), 270 µm (C) and 50 µm (D).

stents. Remarkably, the PAC remained adhered to the stents after a 24-hour incubation in PBS at 37˚C under flow conditions followed by aggressive crimping and expansion with a balloon catheter (Figure 4.9). These conditions simulate the harsh environments in in vivo deployment. The harsh conditions are particularly aggressive in the deployment of coronary stents, where implants undergo extensive plastic deformation and pulsating radial forces for long periods of time. A further aggravation of coating integrity upon deployment is expected by corrosion phenomena following incubation in a solution with biomolecules prior to implantation necessary for stent biofunctionalization. The results clearly demonstrate the mechanical robustness of PAC interfaces prepared under plasma conditions that promote a high degree of AIM. Results show that plasma polymerization with ion assisted bombardment allows for process simplification with cost reduction since strong PAC substrate adhesion can be achieved in a one-step process (i.e. without the need for a rate modulated co-deposition of steel and PAC to achieve a graded interface [157] prior to the deposition of pure PAC), even on non-carbide forming materials.

Mechanically robust thin PAC layers formed with high AIM ($\Phi_d = 5.6 \times 10^8$ J/kg) were further applied to stents of varied composition, including stainless steel (SS), cobalt-chromium (CoCr) and nitinol (NiTi) (Figure 4.10 A-D) and sizes appropriate for coronary (Figure 4.10A and 4.10B), peripheral (Figure 4.10C) and mouse use (Figure 4.10D). In each case, the application of a smooth, uninterrupted coating, resistant to delamination following crimping and expansion was achieved, in sharp contrast to commercial drug-eluting stents under the same conditions [111]. Stent size, composition and strut design does not appear to affect the uniform application and the mechanical properties of the coating.

While significant parameter optimization was undertaken to maximize the adhesion of PAC to stainless steel, the adhesion of PAC to carbide-forming substrates such as zirconium and titanium is even more robust [60, 223]. Other early transition metals such as chromium and niobium would be expected to similarly form additional bonds and demonstrate even greater adhesion than stainless steel. Across multiple platforms, directly relevant to commercial stents in current clinical use, these results show that PAC can be applied to and adhere robustly to stents for all applications using a one-step synthesis approach.

4.3.2 Functionalization of mechanically robust PAC with tropoelastin

So far, this thesis has demonstrated the capability of an optimized ion-assisted plasma deposition technology to deliver PAC interfaces with various surface physical and chemical properties. Further studies were focused on samples with high Φ_d, as these provide exceptional PAC substrate adhesion strengths driven by AIM phenomena, as shown in the previous section and Chapter 3. Within this range of samples, the applied pulse bias at the substrate holder explicitly modulates the nitrogen content via privileged ablation of CN hybridizations and limits the ultimate thickness of PAC layers. In this section, the biocompatibility of the best PAC surfaces, produced at $\Phi_d \geq 5.5 \times 10^8$ J/kg, is evaluated and limiting factors introduced by the applied $|V_{\text{bias}}|$ on surface biofunctionalization and blood compatibility are investigated.

The ability of PAC to covalently retain a layer of biomolecules was studied using a well-established ELISA assay following SDS washing of tropoelastin conjugated PAC interfaces

[157]. SDS is an ionic surfactant which removes any physisorbed biomolecules on surfaces whilst leaving behind those that form covalent bonds with PAC. Washing protocols with SDS at relatively high temperatures (70˚C -90˚C) have now been widely established to confirm covalent attachment of biomolecules [224, 225]. As discussed previously, tropoelastin is a component of natural elastic fibers that provide important rheological features to elastic tissues [221]. This protein features a high resistance to conformational changes [7, 226] and has been identified as a strong candidate for biofunctionalization of materials used for medical implants. Our previous experience with tropoelastin suggests that it is a strong candidate for favorably modulating recruitment of endothelial cells, while maintaining the low thrombogenicity of the underlying surface [111]. Here tropoelastin is used as a model biomolecule, representative of vascular extracellular matrix mimicking proteins increasingly used for surface functionalization.

The ELISA results reveal no significant differences of the detected levels of tropoelastin between bare SS and PAC coated SS substrates before SDS washing (Figure 4.11). However, after rigorous SDS washing at high temperatures, virtually all bound tropoelastin is removed from the SS control substrates, revealing the weakly bound nature of physically adsorbed tropoelastin on metallic substrates. Conversely, PAC surfaces prepared with $|V_{\mathrm{bias}}| = V_{\mathrm{f}}$ and $|V_{\mathrm{bias}}| = 250$ V showed, respectively, tropoelastin retention of 73 % and 72 % after SDS washing. Increasing $|V_{\mathrm{bias}}|$ further decreased tropoelastin retentions and for $|V_{\mathrm{bias}}| = 1000$ V the absorbance values were reduced to background levels.

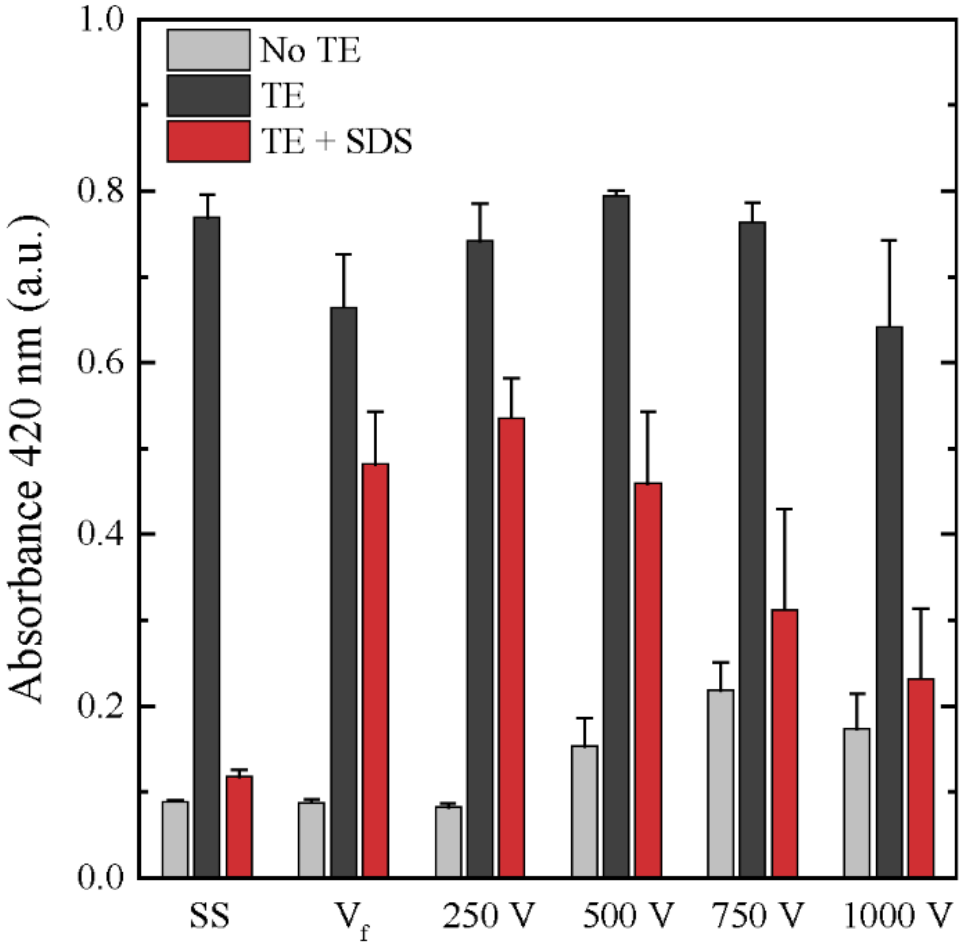

Figure 4.11. Antibody detection of retained tropoelastin on SS 316L and PAC surfaces before and after SDS washing. Samples prepared using |Vbias| ≤ 500 V retained ~70 % of the initial tropoelastin following stringent SDS washing at 90˚C. Tropoelastin was virtually eradicated from bare metal substrates, revealing the weak nature of protein-metal coupling. The decrease in tropoleastin retention for |Vbias| ≥ 750 V was associated with a lack of substrate conformal PAC coverage (as shown in Figure 3.17). This experiment was conducted with the support of Ms Elysse Filipe.

4.3.3 Hemocompatibility

Modelling the thrombogenicity of new material surfaces *in vitro* is challenging and complex. To best assess the effect of plasma parameters on the blood compatibility of PAC surfaces a panel of assays was used, separately employing platelet and leucocyte rich plasma, fluorescently labeled fibrinogen and heparinized whole blood under static and flow conditions [8]. It was initially suggested that biomaterial thrombogenicity is likely caused by plasma protein adsorption, thus resulting in the activation of the intrinsic pathway of thrombosis [166]. However, it is now known that the adsorption of plasma proteins alone is insufficient to initiate the clotting cascade and further interaction with leucocytes is necessary, with activation of the extrinsic pathway of thrombosis [166]. The advanced interplay that occurs between the two pathways (intrinsic and extrinsic) when a foreign blood contacting device is concerned has since been recognized. This highlights the importance of initial leucocyte attachment and activation on the surface of biomaterials, a step frequently overlooked in the biomaterials field. Therefore, a platelet and leucocyte rich plasma contact experiment was performed to evaluate the initial cell attachment, spreading and activation at 10, 30 and 60-minute time points. Whilst there is platelet and leucocyte attachment and spreading to the PAC surfaces even at early time points (see figures 4.12A), the lack of thrombosis evolution suggests that these cells are not in the activated state. Significant cell activation is evident in the SS control where thrombosis evolution can be seen at the 60-minute time point with significant fibrin deposition (shown in detail in figure 4.12B).

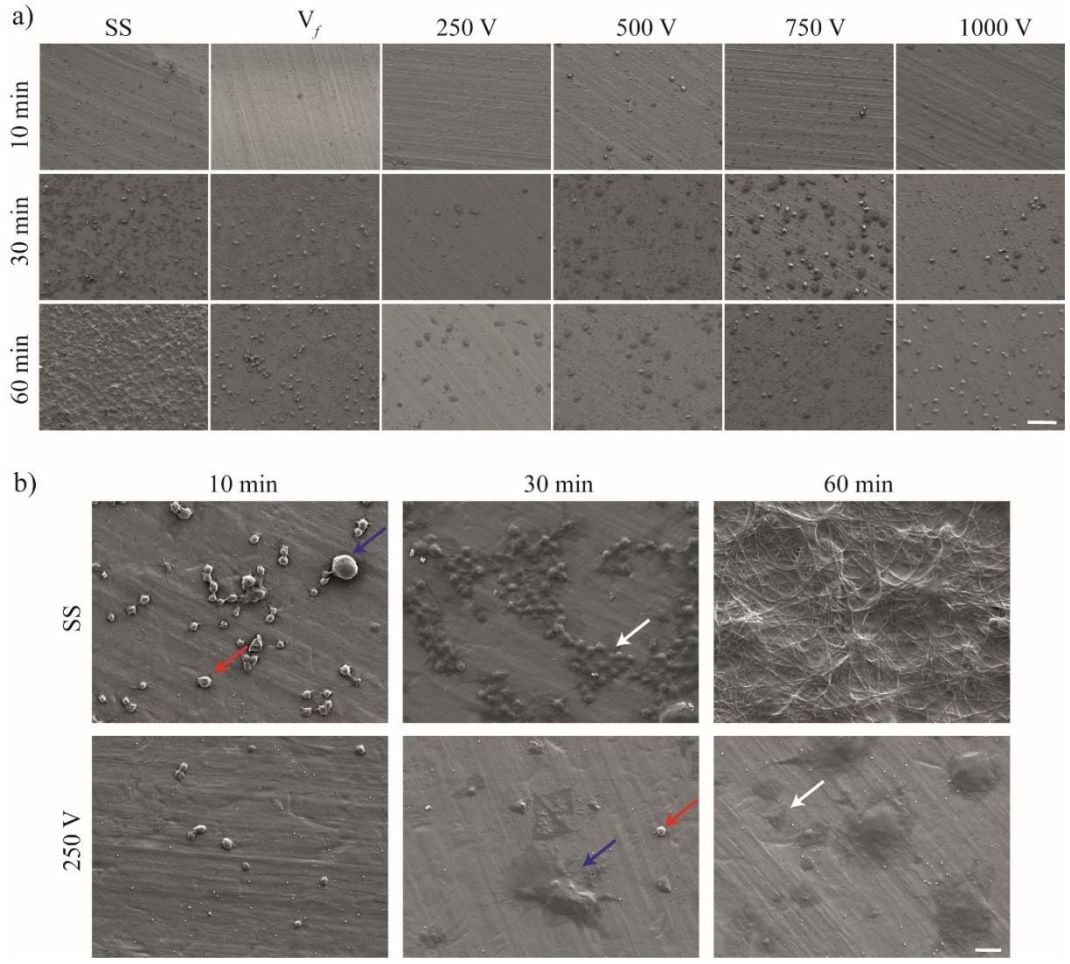

Figure 4.12. A) Representative secondary electron images of bare and PAC coated SS 2-dimensional substrates following incubation with platelet and leucocyte rich plasma for 10, 30 and 60 minutes. PAC formulations prepared at different substrate bias are screened against the bare metal. Results show that, although all PAC samples adhered platelets and leucocytes, a thrombotic plaque was only formed on the SS surface. Samples prepared at -250 V outperformed other PAC formulations. B) Comparison between PAC deposited at a substrate bias voltage of -250 V and bare SS. Platelet and leucocyte spreading was observed but they were not activated on PAC surfaces, as suggested by the lack of thrombosis evolution when compared with SS. SS surfaces clearly featured significantly more platelet spreading and platelet-platelet interaction with subsequent potential release of pro-thrombogenic molecules and the formation of fibrin networks. The arrows indicate attached (red) and spread (white) platelets and leucocytes (blue). Scale bars are 50 µm (a) and 5 µm (b).

Furthermore, significant platelet attachment, spreading and platelet-platelet and platelet-leucocyte contact is observed in the SS control, indicative of platelet activation and potentially subsequent release of pro-thrombogenic molecules. The significant lower amount of attached platelets and absence of platelet-platelet and platelet-leucocyte contact in all PAC recipes further supports the hypothesis that the PAC surfaces are supporting some cell attachment and spreading, however without their subsequent activation. It is suggested that the significantly reduced water contact angle of PAC coatings [8, 111] initiates the platelet and leucocyte attachment and spreading without inducing the same level of activation that is observed in the SS control.

The results of the platelet and leucocyte rich plasma contact experiment demonstrates the clear superiority of all PAC recipes when compared to the stainless-steel control. The assay did not clarify, nevertheless, tangible differences between PAC samples prepared under different plasmas conditions, with exception of samples prepared $|V_{\text{bias}}| = 250$ V that presented a significant reduction in platelet adhesion. Therefore, a static plasma contact assay was implemented using a fluorescent fibrinogen precursor incorporated together with the plasma [222]. The fluorescent fibrinogen provided a visual aid to the clot formation as it was incorporated into the growing fibrin network, allowing to image and quantify the extent of fibrin clot formation over a 60-minute time period. While bare SS control substrates triggered the development of dense fibrin networks, PAC strikingly reduced the development of these fibrin structures (Figure 4.13A). The least amount of fibrin was observed for PAC samples prepared with mild to medium bias voltages ($|V_{\text{bias}}| < 500$ V). Here, fluorescence mainly originated from adsorbed / immobilised fibrinogen onto PAC surfaces as only mild and mono-

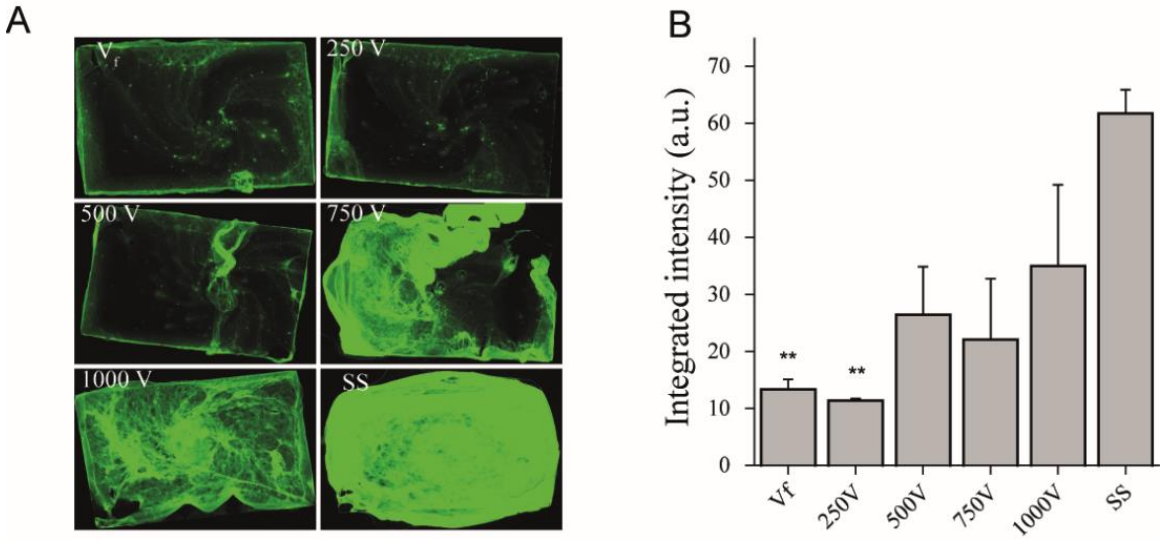

Figure 4.13. A) Sample incubation with fluorescently labelled fibrinogen in human plasma demonstrates that PAC coated SS 316L substrates ($|V_{bias}| < 500$ V; $Q_{Acetylene} = 1$ sccm) can dramatically reduce the formation of fibrin networks. B) Quantification of the fluorescently labelled fibrinogen shows that PAC formulations prepared at ($|V_{bias}| < 500$ V; $Q_{Acetylene} = 1$ sccm) adhered significantly less fibrinogen. This experiment was conducted with the support of Miss Juichien Hung.

layered immature fibrin networks were present at the edge of each sample. Fibrin network formation was enhanced at higher bias voltages. Further quantification of the integrated fluorescent intensity verified that samples synthesized at $|V_{\text{bias}}| = 250$ V and V_{f} adhered significantly less fibrinogen than bare SS and other PAC formulations as shown in Figure 4.13B.

PAC thrombosis under static conditions was further assessed with heparinized whole human blood from a single donor as shown in Figure 4.14. Based on the results obtained from the previous assays with platelet rich plasma and fluorescent fibrinogen, the PAC formulation prepared at $|V_{\text{bias}}| = 250$ V and $Q_{\text{acetylene}}$ = 1 sccm (i.e. $\Phi_d = 5.6 \times 10^8$ J/kg) was chosen for this assay. Samples were incubated with the whole blood for a period of time and subsequently washed three times in PBS to remove unattached blood to the surface. An incubation with the whole blood for 10 minutes did not result in a discernable difference between bare and PAC coated SS surfaces, where clotting was absent in both samples. At 20 minutes, the surface of PAC was still mostly clean, presenting only few and minor spots of blood randomly scattered throughout the sample. SEM imaging revealed that these blood spots were composed of small (~50 μm) and individual agglomerates of red blood cells and platelets, merged together through a monolayer of a fibrin complex. Contrarily, the entire surface of bare SS was covered by a hemostatic plug, as shown in Figure 4.14A. Under SEM, the SS surface was entirely covered by a multilayer of blood components, mostly comprised of red blood cells joined by platelets and polymerized fibrin (Figure 4.14B). By 30 minutes, while PAC surfaces were still showing signs of early stage thrombosis, a mature clot had already developed on the bare SS.

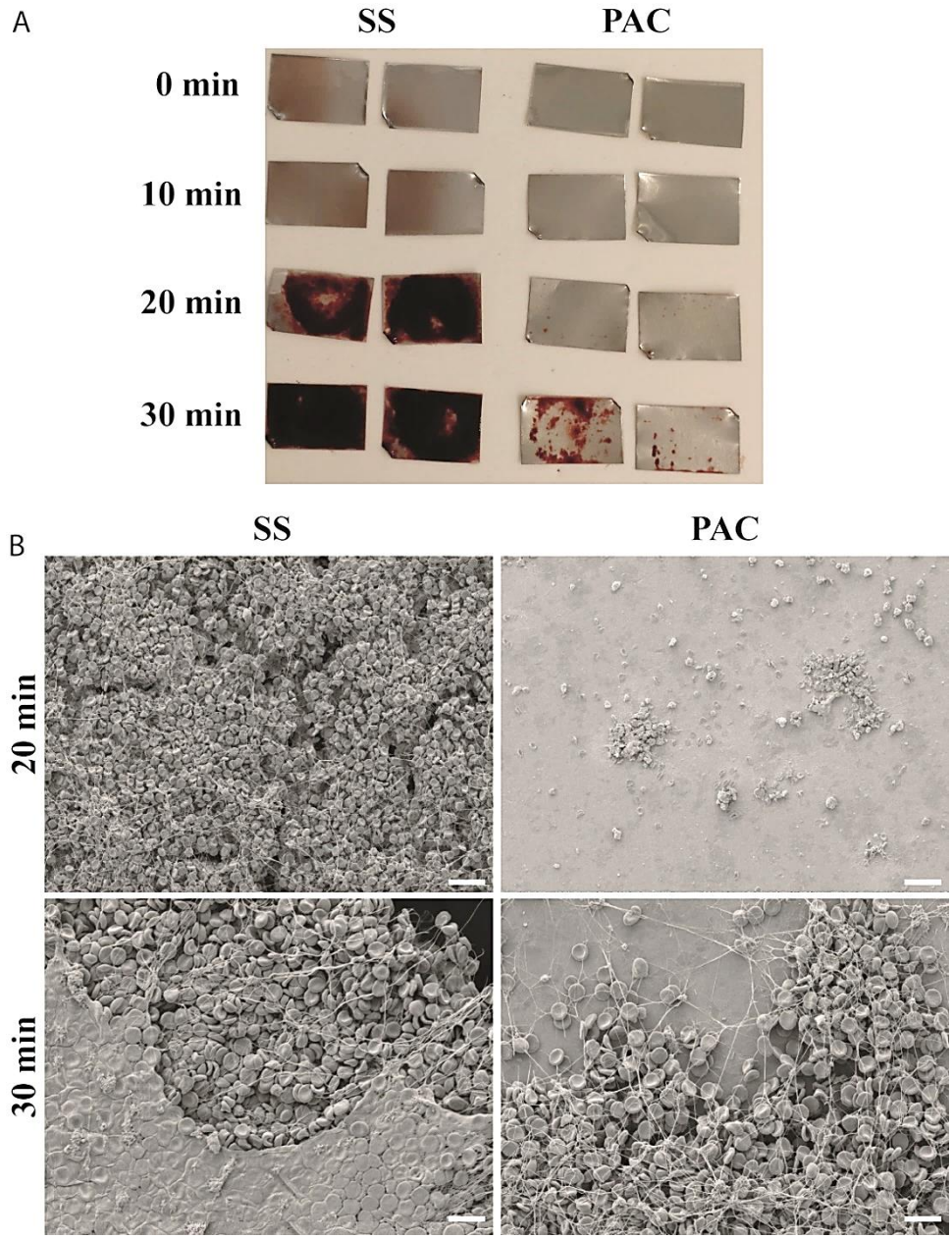

Figure 4.14. A) Representative optical images of bare and PAC coated SS upon contact with heparinized human whole blood at different time points. B) Representative secondary electron images of samples shown in A) for the 20 and 30-minute time points. The formation of a thrombotic plaque was significantly accelerated on SS samples relative to the PAC samples as shown by the agglomeration of red blood cells held together by polymerized fibrin networks. Scale bars are 40 µm (20 min) and 20 µm (30 min). This experiment was conducted with the support of Miss Juichien Hung.

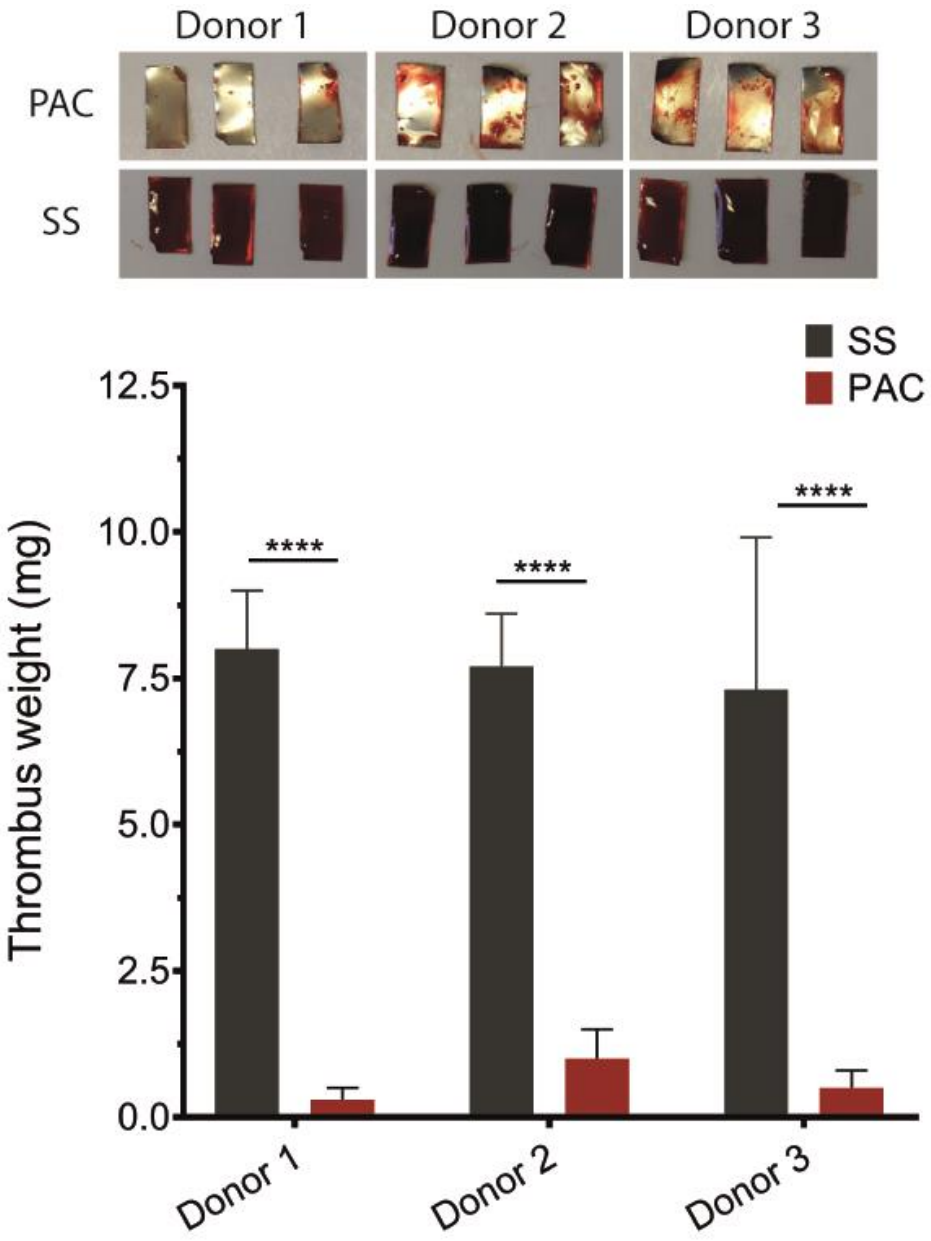

Figure 4.15. A) Representative optical images of bare and PAC coated SS upon contact with heparinized human whole blood of three different donors under static conditions. B) Quantification of the thrombus weight shows that PAC coated surfaces are significantly less thrombotic than the bare metal. This experiment was conducted with the support of Miss Juichien Hung.

Experiments under static conditions were then carried out with blood from three different donors to further assess the reproducibility of the assay and the thrombotic properties of PAC. The adhesion of blood components to both SS and PAC coated SS surfaces was evaluated by measuring thrombus weight and imaging under SEM. Pre-weighed samples were incubated with the heparinized whole blood for a total of 30 minutes and washed three times in PBS before measuring the weight of the clot. Results show that PAC coated SS samples were systematically superior, as shown in Figure 4.15A by the formation of larger hemostatic plugs on the surface of the bare metal for all donors. Quantification of the clot weight (Figure 4.15B) confirmed these observations, as SS formed clots measuring 8.0 ± 1.0 mg, 7.7 ± 0.9 mg and 7.3 ± 2.6 mg for donors 1, 2, and 3 respectively. Conversely, the clots formed on PAC surfaces were significantly smaller, weighting 0.3 ± 0.2 mg, 1.0 ± 0.5 mg and 0.5 ± 0.3 mg for donors 1, 2, and 3 respectively.

To further strengthen the hemocompatibility data, the thrombogenicity of PAC was investigated under flow conditions by incubating 2D samples with whole heparinized human blood in a modified Chandler loop [8]. The Chandler loop has been optimized to approximate coronary blood flow and is used widely in industry for assessment of the thrombogenicity of new stent platforms under flow. The modified Chandler loop was carried out by balloon expanding 0.6 cm x 1.2 cm samples inside Tygon S-50-HL tubing with a length of 28 cm. Each tube was then filled with 2.5 mL of heparinized (0.5 U/mL) whole blood and allowed to rotate at a rate of 34 rpm at 37 ˚C for a total of 60 minutes. Here, two different PAC surfaces that performed best and worst in the platelet adhesion and fibrin formation assays, $|V_{\text{bias}}| = 250$ V and $|V_{\text{bias}}| = 1000$ V, were chosen and compared against bare metal. This choice was

based on: (i) the previous hemocompatibility properties found for PAC, which shows that coatings prepared at $|V_{\text{bias}}| = 250$ V are superior than those prepared at $|V_{\text{bias}}| = 500$ V and (ii) the spin density is 3.5-fold greater than those made at $|V_{\text{bias}}| = V_{\text{f}}$. Higher spin densities provide reactive surfaces with improved sample shelf life, an essential feature when implant bioactivation is required [227]. The poor hemocompatibility of bare SS substrates was confirmed by the development of thrombi (41.9 ± 3.5 mg) after a 60-minute incubation (Figures 4.16A and 4.16B). At $|V_{\text{bias}}| = 1000$ V PAC was not significantly better than control SS substrates (35.1 ± 10.3 mg). However, at $|V_{\text{bias}}| = 250$ V, clot weight (5.4 ± 0.4 mg) was strikingly reduced by 87% compared to the bare metal samples.

The variability of the modified Chandler loop assay was evaluated under the same parameters by using blood from three different donors and carrying out experiments up to 21 months apart (Figure 4.17A and 4.17B). Here, 40 nm thick PAC layers prepared at $|V_{\text{bias}}| = 250$ V were screen against bare SS surfaces. Significant thrombus formation was again observed on the bare metal for all donors, with clot weight measuring up to 52.1 ± 12.4 mg. Contrarily, PAC was able to mitigate clot formation throughout the whole duration of the assay (60 minutes) as seen by the absence of thrombi and the clean PAC coated SS surface.

The Chandler loop assay was then carried out to study the thrombogenicity of PAC coated SS stents using serum with fluorescently labeled fibrinogen. Stents were crimped and balloon expanded inside the Tygon tubing and allowed to rotate in contact with the plasma at a rate of 34 rpm at 37 ˚C for a total of 60 minutes. Samples were then removed from the tubing, washed three times in PBS and imaged under a fluorescent microscope for detection of

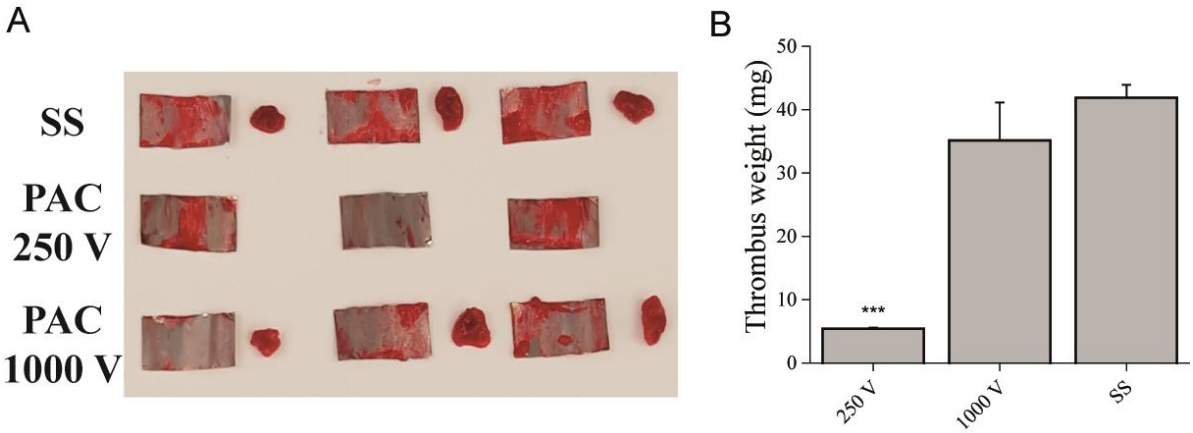

Figure 4.16. A) Representative optical images of bare and PAC coated SS upon contact with heparinized human whole blood under flow conditions. B) Thrombus weight measurements show that metallic substrates that are completely concealed by PAC (i.e. $|V_{bias}|$ = 250 V) strikingly inhibit thrombus formation.

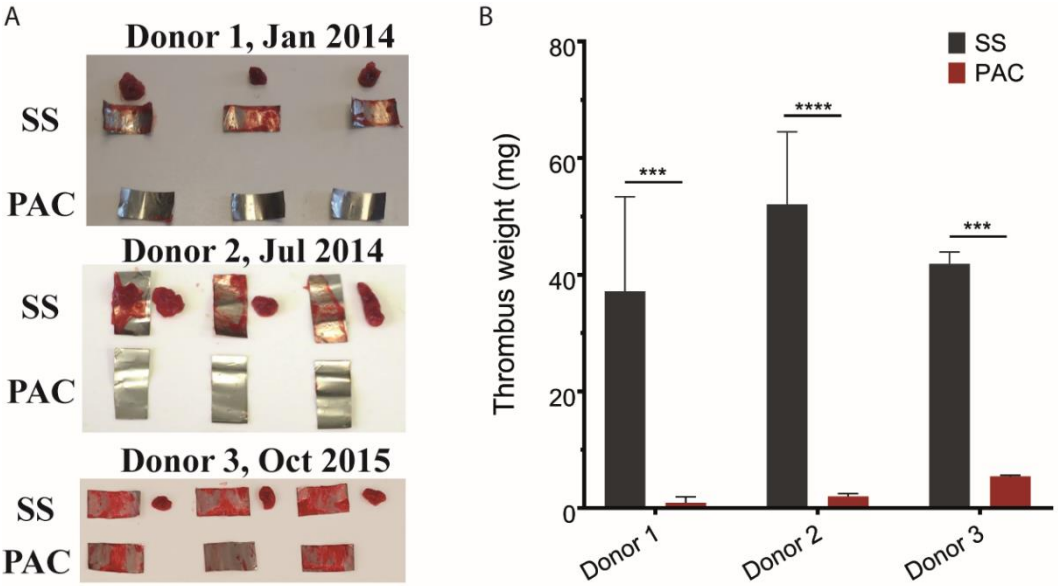

Figure 4.17. A) Representative optical images of bare and PAC ($|V_{bias}|$ = 250 V) coated SS upon contact with heparinized human whole blood. The blood was taken from three different donors and experiments were carried out under flow conditions and up to 21 months apart. B) Quantification of the thrombus weight shows that PAC coated surfaces are significantly and systematically less thrombotic under flow than the bare metal. This experiment was conducted with the support of Miss Juichien Hung.

fluorescent fibrinogen. Flow is an extremely important parameter to consider when studying the thrombotic properties of materials, particularly for 3-dimensional samples, such as stents, that are prone to create turbulent flow conditions. Therefore, this assay is paramount to screen not only the thrombogenic properties of PAC translated to 3-dimensional objects under conditions that simulate the pulsating flow of coronary arteries, but also its ability to withstand turbulent flow following stent expansion without delamination. Results in Figure 4.18 show a significant fluorescent signal on the bare SS stents from polymerization of fibrinogen and subsequent formation of fibrin networks on the surface of the struts. An observation at a higher magnification details a continuous fibrin network joining adjacent bare SS struts while PAC covered struts are visibly free of hemostatic plug.

Taken together, results of the thrombogenicity screening assays consistently show that PAC prepared at $|V_{\mathrm{bias}}| = 250$ V outperformed all other formulations and were significantly superior to bare SS surfaces. Clot formation on the surface of bare metals has been widely reported [228-230]. Metals are inherently thrombogenic, causing blood proteins to denature upon contact. The superior hemocompatible properties of PAC are most likely related with its ability to covalently bind blood proteins in their native conformation. Due to their higher mobility, blood proteins interact with a surface before cells present in the blood. Therefore, the thrombogenicity of a foreign implant is ruled by the interaction and fate of blood proteins upon interaction (physical adsorption or covalent attachment) with its surface. Results with PRP show that although platelets can attach and spread on the surface of PAC, they were probably not in an active state. The formation of fibrin networks was significant less than on

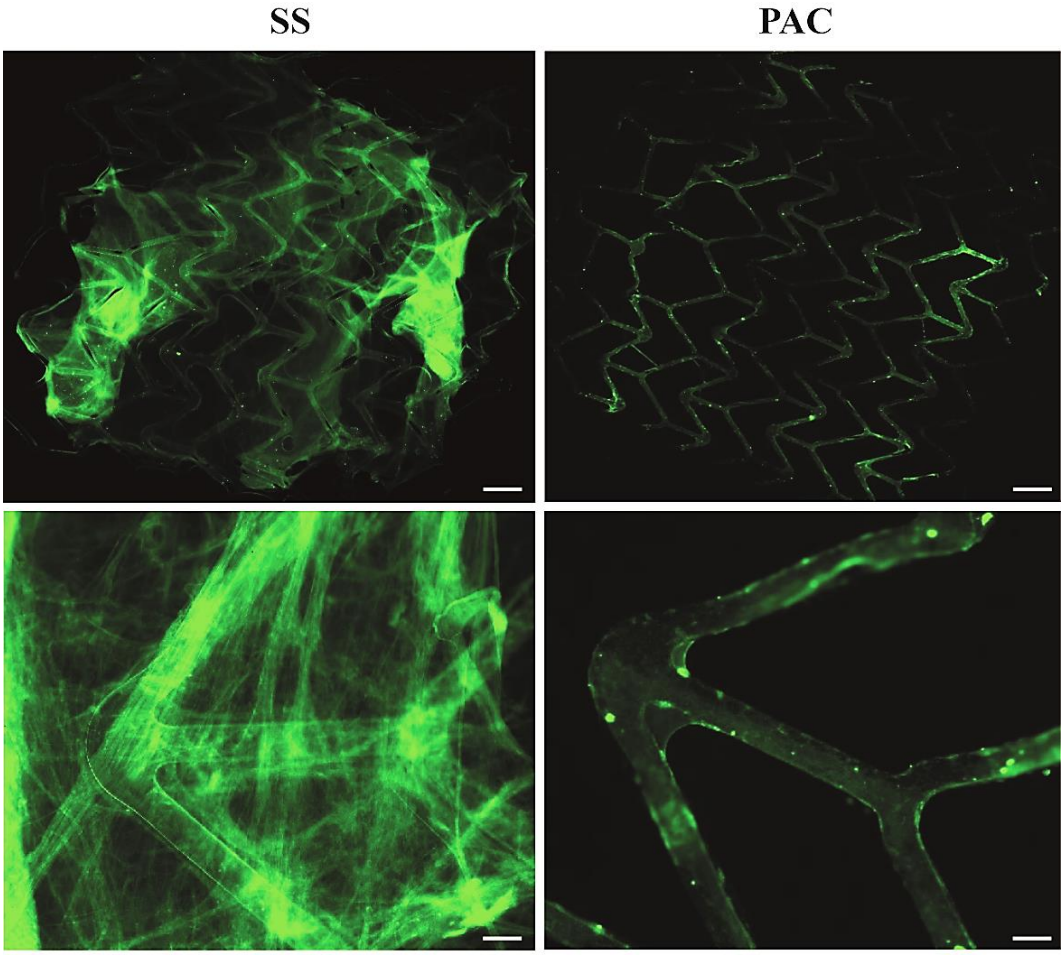

Figure 4.18. Fluorescently labelled fibrinogen imaged after stents were crimped and balloon expanded inside a loop of Tygon tubing and exposed to blood flow for 60 minutes. When translated to SS coronary stents, thin PAC layers (≈ 40 nm) prepared with at high energy per monomer unit mass ($\Phi_d = 5.6 \times 10^8$ J/kg, $|V_{bias}|$ = 250 V and $Q_{acetylene}$ = 1 sccm) can disrupt fibrin network formation upon incubation with human plasma under flow conditions. Results demonstrate that PAC is able to resist delamination, hence avoiding subsequent exposure of the stent material to blood under pulsating flow that simulates in-vivo conditions. This experiment was conducted with the support of Miss Juichien Hung.

SS, which further supports this hypothesis and suggests that either: (i) fibrinogen binds to PAC but maintains its conformation or (ii) it binds to PAC but to a lesser extent compared with other blood proteins such as albumin. On the contrary, the higher number of platelets and leucocytes observed on the surface of the bare SS, their subsequent interaction and the formation of mature fibrin networks, suggest the adsorption of unfolded albumin and fibrinogen followed by attachment and activation of platelets and development of a clot. The experiments carried out throughout this Chapter also demonstrate that PAC can be applied to a surface and maintain favorable thrombotic properties in a reproducible fashion, as demonstrated here for different donors and with PAC samples synthesized up to 21 months apart.

4.4 Conclusion

Results reported in this chapter show that plasma activated coatings (PAC) can be simply and cost-effectively synthesised for the clinical application of vascular stents using a reactive plasma polymerization process with ion-enhanced bombardment. Optimization of the plasma characteristics in Chapter 3 allowed the identification of an optimal parameter window and ultimately the deposition and translation of a mechanically resilient PAC onto 3-dimensional objects, capable of withstanding fluid immersion and the extreme plastic deformation that stents undergo during typical deployment conditions in humans. The versatility of this plasma-based synthesis platform was further demonstrated by applying PAC on a variety of stents designs with different alloy compositions, geometries and sizes. The coating resisted crimping and balloon expansion in all tested stent modes, demonstrating the potential use of PAC for rabbit iliac, mouse

carotid and human coronary and peripheral models. PAC is universally reactive, a property inherent to the synthesis in a reactive plasma, and contains radicals that diffuse over time to the surface. Due to its mildly hydrophilic properties, a wide range of biomolecules can be immobilized in their native conformation when reacting with radical groups.

Overall, the results that show a superior hemocompatibility for samples prepared at $|V_{\text{bias}}| = 250$ V and higher covalent retention of tropoelastin are consistent with the level of conformal PAC substrate coverage, as discussed in section 3.3.6 (see Figure 3.18). Exposure of the underlying SS substrate results in: (i) partial physisorption of tropoleastin as opposed to a superior covalent retention observed for totally covered substrates and (ii) clot formation triggered by contact of blood with the exposed underlying metal substrate which is innately thrombogenic. Tropoelastin retention after SDS washing has been shown to correlate linearly with the coating thickness in previous reports [157], saturating at a thickness that immobilizes a full monolayer. Thicker coatings contain higher densities of radicals that impart a superior PAC reactivity. Measurements at $|V_{\text{bias}}| = 250$ V demonstrate that 40 nm thick PAC coatings, with a measured radical density of 2.8×10^{17} spins/cm^3, provide similar tropoelastin retentions as found for highly reactive plasma immersion ion implanted polymers [215, 231]. Additionally, these same samples were further able to reduce clot formation when in contact with human blood.

5 PLASMA POLYMERISED NANOPARTICLES (NANOP^3)

The literature review and results presented throughout this chapter is published and / or will be submitted for publication in:

Nanoparticles, **Miguel Santos**, Praveesuda L. Michael, Elysse C. Filipe, Marcela M. M. Bilek and Steven G. Wise, Australian Patent Application No. 2016905306 (21 December 2016)

Miguel Santos, Praveesuda L. Michael, Elysse C. Filipe, Alex H.P. Chan, Juichien Hung, Richard P. Tan, Bob S.L. Lee, Minh Huynh, Clare Hawkins, Anna Waterhouse, Marcela M. M. Bilek and Steven G. Wise, *Plasma synthesis of carbon-based nanocarriers for linker-free immobilization of bioactive cargo*, under review at ACS Applied Nanomaterials (2017)

Miguel Santos, Praveesuda L. Michael, Elysse C. Filipe, Alex H.P. Chan, Juichien Hung, Marcela M. M. Bilek and Steven G. Wise, *Plasma polymerization of nanoparticles in dusty plasmas for applications in nanomedicine*, under preparation for submission to Scientific Reports

5.1 Introduction

5.1.1 Plasma polymerization in dusty plasmas

Plasma polymerization (PP) [128, 232] has been established as a preferred surface deposition platform in a vast range of technological and biomedical applications [4-8, 73]. The reactive environment in the plasma fragments and ionizes monomers into building blocks that polymerize and diffuse towards the plasma boundaries, i.e. surface polymerization. Ultimately, the diffusion of these reactive blocks outside the plasma results in the deposition of thin-films with modulated properties. Given the non-equilibrium properties of the plasma, in which the energy is mainly coupled to the more mobile electrons, the plasma environment can be sustained close to room temperature during the deposition process. Therefore, plasma-polymerized coatings (PPC) can be deposited on virtually any surface while preserving the mechanical characteristics of the bulk material [5]. The research to date has mainly sought to explore how the plasma process parameters can impart tailored physical, chemical or biological properties to PPC.

A far less explored domain of reactive PP is manifested in some hydrocarbon (e.g. C_2H_2 or CH_4) [233], fluorocarbon (CF_4 or C_2F_6) [234] or silane (SiH_4 or $Si_2O(CH_3)_6$) [106, 235] glow discharges, where surface polymerization (thin-film deposition) occurs simultaneously with plasma bulk polymerization, i.e. dusty plasmas [91, 95, 236]. Ionization of acetylene in the plasma for instance, triggers the continuous formation of carbonaceous nanoclusters that aggregate to form nano – to micron – sized particulates in the plasma volume, often called plasma dust. The formation of charged plasma dust

particulates plays a great role in the fundamental processes governing the discharge [236]. The electron density and temperature, floating potential and emission intensity has been reported to oscillate in discharges sustained in dust-forming radio-frequency plasma [][95, 237]. This bizarre long-time scale oscillatory phenomenon is largely related with changes to the spatial distribution of plasma dust, as the particulates are formed and subsequent removed from the plasma reactor, hence modifying the discharge characteristics.

5.1.2 Removal and collection of plasma dust particulates

The bulk of research to date in dusty plasmas has mainly focused on studying the formation mechanisms of the particles, combining both experimental diagnostic tools and theory [99]. The knowledge gain on the dynamics of dusty plasmas so far allowed the development of tools aiming to eliminate and/or remove dust particles by external manipulation. This was particularly useful in the context of magnetic confinement nuclear fusion devices [96] and in thin-film manufacturing industries [95, 238], where dust formation deteriorates process efficiency. For instance, the removal and collection of dust particles from reactors has been exemplified by the application of external electrostatic, thermophoretic or neutral gas [239] forces. Levitating dust particles have been removed from the plasma by using electrostatic probes (“plasma vacuum cleaners”) [240] and thermophoretic traps [241]. The collection of silicon-based non-spherical particles at high a mass rates (~ 2 g/hr) has been also demonstrated from organosilicon precursors in continuous downstream plasma reactor configurations [235].

5.1.3 Experimental diagnostics in dusty plasmas

The formation of particles in dusty plasmas and its impact on the discharge characteristics has been investigated using a variety of experimental diagnostics. The oscillatory behaviour of these discharges has been studied to date mainly by mass-spectrometry [242], in-situ infrared spectroscopy [243], laser light scattering [101] and optical emission spectroscopy (OES) [236]. OES for instance has been used as a non-invasive and in-situ diagnostic technique in carbonaceous dusty plasmas sustained in acetylene and methane. Reports so far have sought to investigate the evolution of the overall emission intensity by plotting the line intensity of Ar species, complemented by laser light scattering that measures the scattering (or absorbance) of an external laser beam due to the particulates. Other works have investigated the evolution of H_α line profile during the formation of dust particulates [244]. Measurements of the Doppler broadening of the H_α line in the presence of plasma dust revealed a reduction of the fast component, i.e. a reduction in the number of high-energy hydrogen atoms. The loss of high-energy hydrogen atoms was attributed to a reduction in the sheath potential and width, driven by the formation and agglomeration of negatively charged dust particulates.

As plasma dust particles have long been regarded as detrimental in plasma-based industries, the field of dusty plasmas has mainly focused in development engineering solutions aiming their removal from reactors. Contrarily, this work proposes that carbonaceous plasma dust can be tailored to function as multifunctional plasma polymerised nanoparticles ($nanoP^3$) for applications in nanomedicine. As such, this

chapter first shows that spherical nanoP^3 particles, with narrow size distribution and low aggregation, can be effectively collected from the plasma without external manipulation. It is further shown that PP technology can be operated in a suitable window of parameters to synthesize nanoP^3 in a controllable and reproducible fashion. The formation of nanoP^3 is investigated under a varied number of process (plasma) parameters, including rf coupled power, discharge pressure and gas flow ratios. Analysis of the plasma emission spectra using OES is performed during nanoP^3 synthesis, allowing the identification of relevant formation, growth and removal mechanisms of the particles in the plasma. The results reported in this chapter pave the way for process optimization, to facilitate the synthesis and collection of nanoP^3 with modulated physical, chemical and biological properties.

5.2 Materials and Methods

5.2.1 NanoP^3 synthesis and collection

NanoP^3 were synthesized in a cylindrical stainless steel capacitively coupled radio-frequency (rf) reactor as shown previously in Figures 2.1 and 2.2. The reactor was pumped down to a base pressure of ~10^{-6} Torr and $C_2H_2/N_2/Ar$ plasmas were sustained (see section 2.1) at a working pressure of 150 mTorr, unless otherwise specified.

5.2.2 NanoP^3 collection

The collection of nanoP^3 was carried out in 24 or 96 well (8.5 cm x 12.7 cm) polystyrene tissue culture-well plates (Corning, USA) and in 12 mm x 32 mm borosilicate glass sealable vials (Shimadzu, Japan). The plates (or vials) were placed on top of the substrate

holder which was electrically connected to a DC high voltage pulse generator (RUP 6-25) to provide a specific bias voltage in the range -1000 V - 0 V. Pulse frequency and time width was chosen to be 3 kHz and 20 µs respectively. Si wafers or SS flat substrates (1 cm x 1 cm) were placed on the bottom of the wells, allowing nanoP^3 trapped inside the wells to be imaged with SEM.

5.2.3 Calculation of the nanoP^3 yield

The nanoP^3 yield for each run was calculated by measuring the total mass deposited in the plates. nanoP^3 were resuspended directly from the plates under sterile conditions inside a tissue culture hood with RT-PCR Grade water (Life Technology, USA) and transferred into 1.5 mL Eppendorf tubes of known weight. nanoP^3 was pelleted down by centrifugation at 16100 G for 10 minutes. The water supernatant was then removed and samples were lyophilized overnight. The mass of each sample was calculated by subtracting the weight of the tubes without nanoP^3 from that with nanoP^3.

5.3 Results and discussion

5.3.1 Instabilities in the plasma emission

The formation of plasma dust particles inside the PP reactor (see Figure 2.1) was initially hypothesised by observing instabilities in the light emitted by the plasma during the deposition of PAC coatings. These instabilities were manifested in the form of long-time scale oscillations in the plasma apparent brightness. The oscillations were first observed by eye in discharges sustained at low acetylene flow rates (i.e. generally less than 3 sccm). Typically, the discharge glow increased gradually in intensity during the first seconds after turning on the rf generator. A sudden increase in brightness was then

observed as shown in Figure 5.1. The sudden change in the plasma apparent emission intensity occurred simultaneously with a change in the colour of the light, which suggests a change in the chemical fingerprint of the plasma, and an increase in the plasma opacity. The increase in opacity was observed by the lack of light reflected from the chamber walls on the far side of the viewport. This is best demonstrated by the white arrows in Figures 5.1a and 5.1b, where one of the access ports in the chamber was partially concealed by the plasma medium (Figures 5.1b).

The dramatic change in the apparent plasma optical characteristics in an oscillatory fashion suggests the formation plasma dust particulates. Oscillations in the light emitted by the plasma have been previously reported in acetylene-containing dusty plasmas [97, 243]. The formation, growth and removal of negatively charged particles in the positive potential of the plasma bulk is known to dramatically change the discharge characteristics [236]. The sudden increase in the plasma emission has been related to an increase in the electron temperature, necessary to compensate a reduction in the electron density due to their diffusion towards the particles. Evidence of dust particle formation in the plasma reactor is confirmed in the next section by developing a non-invasive particle collection method.

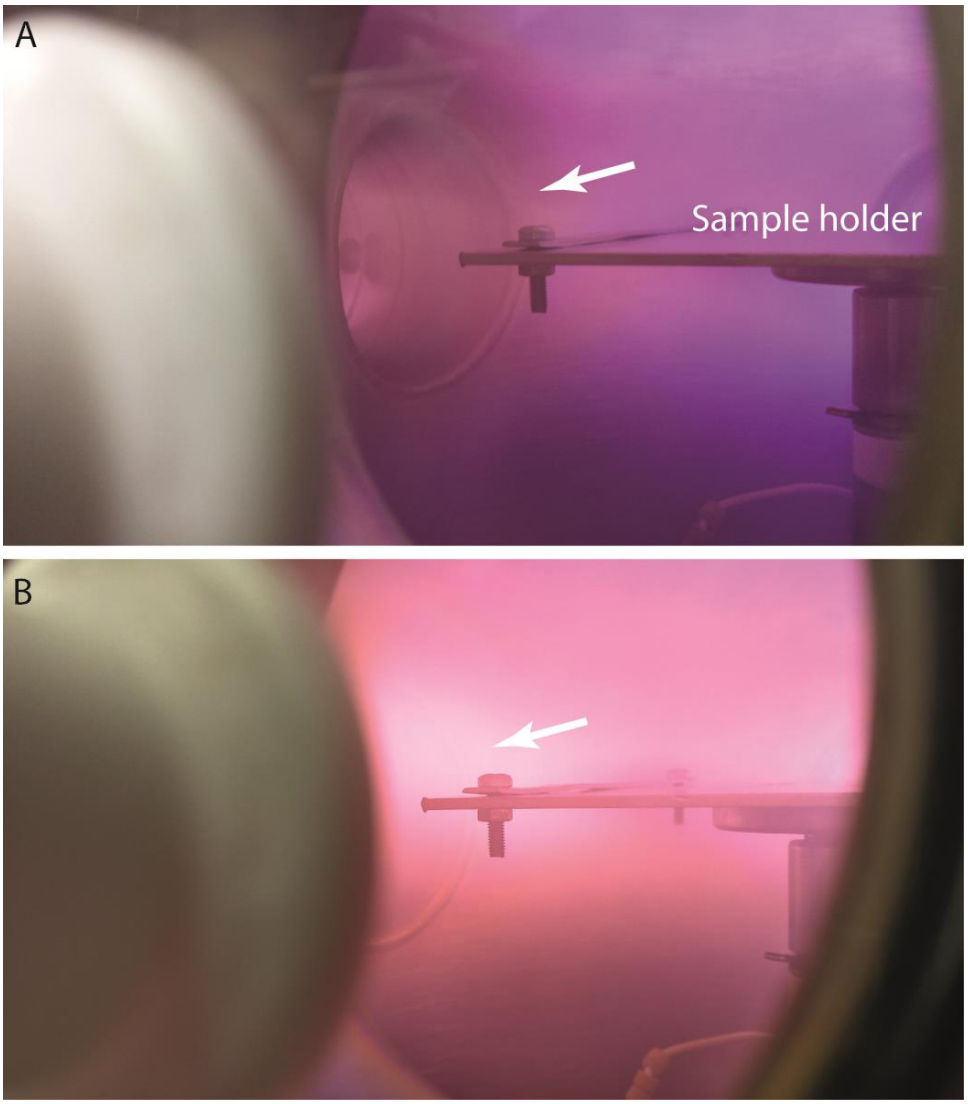

Figure 5.1. Images of $C_2H_2/N_2/Ar$ plasmas taken at different instants show a dramatic change in the discharge emission intensity, colour and opacity as it transitions from a dust-free (A) to a dusty plasma regime (B).

5.3.2 Passive collection of plasma polymerized nanoparticles (nanoP^3) in dusty plasmas

Results presented in the previous section offer indirect evidence for the formation, growth and removal of plasma dust particulates (nanoP^3) via bulk (volume) plasma polymerization. However, such particulates were not detected on the surface of PAC coated samples placed on the biased sample holder. Surface characterization with secondary electron microscopy (SEM) carried on both flat and three-dimensional samples in Chapters 3 and 4 exhibited a particle-free uniform PAC coating, as shown in Figures 3.15, 3.18, 4.7 – 4.10, 4.12 and 4.14. One possible explanation for the lack of dust particulates on the PAC coated substrates could be explained by electrostatic repulsion between the negatively charge particulates and the pulsed bias sample holder, which acquires a negative potential relative to the positive plasma potential. Under these conditions, the total electrostatic force acting on each particle dominates the gravitational force and the vertical components of the neutral and ion drag forces (see section 1.2.4). Therefore, the particulates are repelled from the surface of the substrate and are likely dragged out of the discharge by the horizontal component of the ion drag force.

To collect the dust particulates, 1cm x 1cm silicon wafer substrates were placed on a floating potential substrate holder, i.e. without pulsed bias. Switching off the negative pulsed bias reduces the confinement of the particles, since the only component of the electrostatic force arises from the potential difference between the plasma bulk and the electrode under floating conditions. One should note that PAC has been previously deposited under similar discharge conditions but high-resolution SEM pictures did not show the presence of dust particulates on the surface of the samples (Figure 4.12a).

However, these samples were characterised by SEM in the context of studying the adhesion of platelets and leucocytes upon contact with human blood. Therefore, incubation of the substrates with blood and subsequent sample processing likely removed particulates accumulated during the deposition of PAC.

Cross-sectional SEM imaging shows that a 10-minute exposure of the silicon substrates to the plasma resulted in the deposition of a ~200 nm thick PAC layers (Figure 5.2a), which were decorated by spherical particles uniformly distributed on the surface (Figures 5.2b – 5.2d). The particles had an apparent narrow size distribution, with an average diameter measured on the image focal plane of 260 nm. The embedding of the particles into the PAC matrix disturbs the surface of the coating, as shown by the formation of a depression around each particle (inset in Figure 5.2b). The continuous growth of the coating by surface plasma polymerization around different generations of particles led to a distribution of particles buried at different depths. For the current discharge parameters, six oscillations were detected during the 10-minute run, hence indicating the formation of 6 generations of nanoparticles. Therefore, nanoparticles from earlier generations were exposed to surface polymerization for longer time periods and were therefore buried deeper within the coating. Interestingly, coating depletion was also observed in the absence of particles throughout the surface of PAC (blue arrow Figure 5.2d). These particle-free depressions were potentially formed by the ejection of loosely bound particles during the chamber venting process, exposure of the sample to atmospheric pressure and subsequent handling.

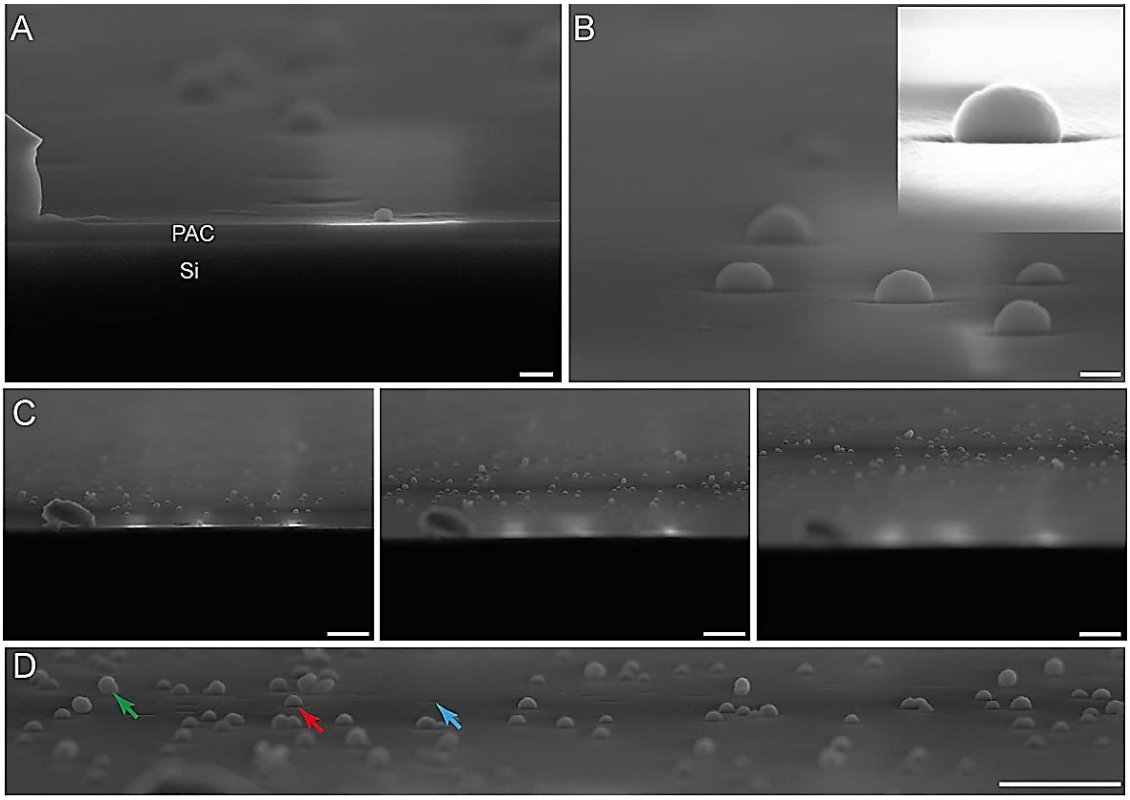

Figure 5.2. Cross-sectional SEM images of Si substrates exposed to a $C_2H_2/N_2/Ar$ plasma for 10 minutes. A PAC coating was formed on Si surface under floating potential conditions (A). The PAC coated Si wafer was decorated by spherical nanoparticles (nanoP^3) uniformly dispersed on the surface (B and C). The inset in (B) details the depletion of the coating around a buried nanoparticle. Nanoparticles formed in different cycles (or generations) were buried at different depths (green and red arrows) while some escaped from the coating as seen by particle-free depression (blue arrow.) The scale bars are (A and B) 200 nm, (C and D) 2µm.

Incidentally, free-standing particles were also observed on the surface of the coating (green arrow Figure 5.2d). The dispersion of free-standing particles on the coating surface is consistent with the ejection of particles from their initial (embedded) position or particles formed in the last cycle (oscillation). Taken together, these results show that the particles formed by bulk plasma polymerization interact poorly with the coating matrix. The lack of contact interaction could potentially arise from a strong Coulomb repulsion between the two structures. However, these results are somewhat surprising since one would expect the sintering of these structures via radical interactions. Therefore, further analysis of such structures and their interactions will be necessary to elucidate the results.

Results presented in Figure 5.2 show that while the present plasma reactor allows the deposition of PAC coatings with modulated properties, it can also be used for the synthesis and collection of dust particulates. However, the harvesting of particulates in adequate quantities for ex-situ characterization and potential use in technological and biomedical applications would require a significantly more efficient synthesis yield. Ideally, the process should be optimized to reduce surface polymerization while enhancing bulk polymerization, hence maximizing particulate formation at the detriment of coating formation. For commercial and industrial applications, the process should also be highly reproducible and compatible with high-throughput and low-cost synthesis and collection.

The collection of nanoP^3 from the plasma bulk was optimised by using a 3-dimensional entrapment device comprised of an assemble of wells as shown in Figure 5.3. The

plurality of wells is placed on top of the substrate holder (bottom electrode) to entrap nanoP^3 that fall within the boundaries of each well. Such a device can be emulated by commercially available tissue culture plates, comprised of an array of wells with varying number and sizes. The efficiency of such a device in collecting nanoP^3 was first exemplified using 8.5 cm x 12.7 cm polystyrene tissue culture plates, containing 24 wells distributed in a 4 by 6 well configuration. The depth and surface area of each well was 1.7 cm and 2 cm^2 respectively. As shown in Figure 5.4, the tissue culture plate was covered by a powder-like substance, which significantly altered the plate colour upon a 7-minute exposure to the dusty plasma. Here, the discharge was sustained with standard parameters previously optimized for the deposition of PAC. Particularly, the bias was set to -500 V which usually yields particle-free coatings on flat SS substrates (Figure 5.5a).

The ability of the device (collector) to entrap nanoP^3 was then investigated by imaging SS foils placed inside the wells. The surface of the SS foils featured a large number of nanoparticles (Figure 5.5b). In contrast, SS foils placed on the substrate holder in a flat configuration (i.e. without the collector) under the same discharge parameters only shows the deposition of a PAC coating (Figure 5.5a). Interestingly, the images did not show evidence of a coating on the surface of the samples placed in the collector, suggesting that surface polymerization does not take place on the bottom of the wells.

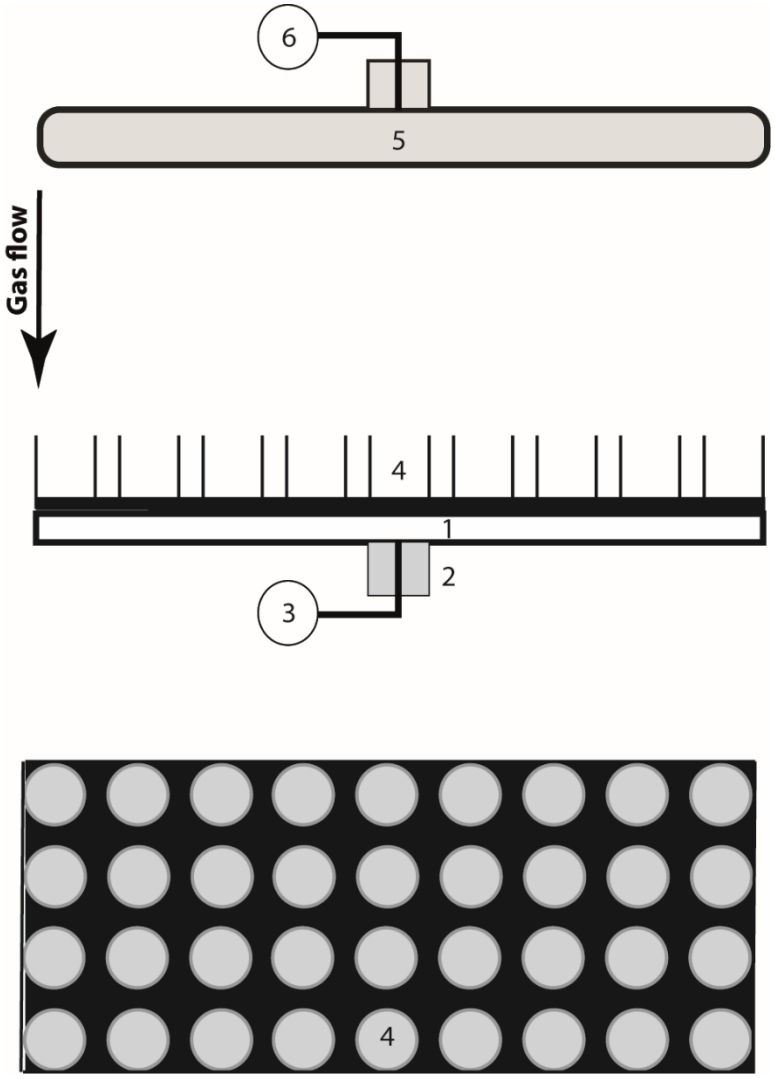

Figure 5.3. Schematic showing the bottom electrode (1), electrode support (2), pulsed high voltage power supply (3), well-shaped nanoP^3 collector (4), top rf electrode (5) and rf voltage power supply connection for top electrode (6).

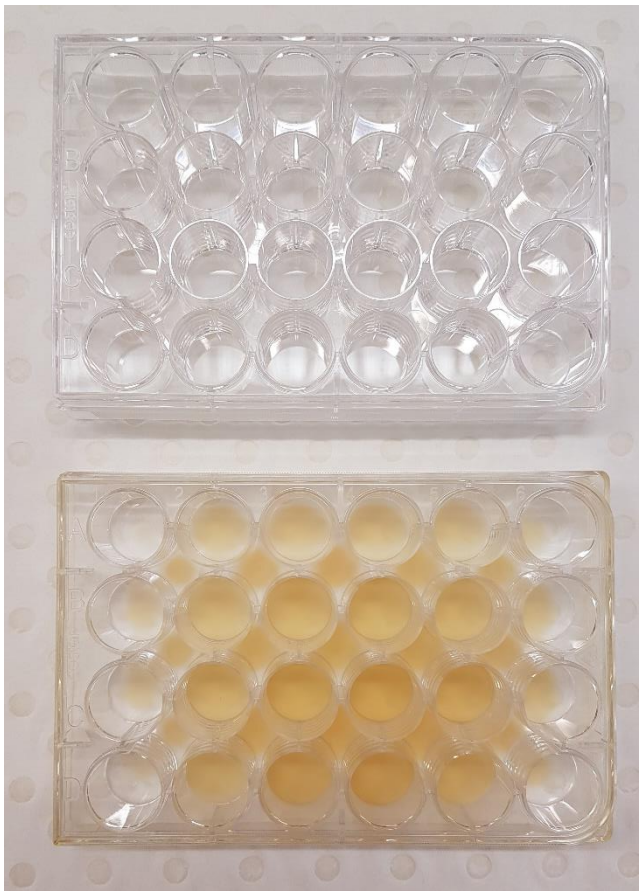

Figure 5.4. A comparison between tissue culture 24-well plates before (top) and after (bottom) exposure to a dusty $C_2H_2/N_2/Ar$ plasma for 7 minutes, i.e. 5 oscillation cycles (bottom). The collection of nanoP[3] on the bottom plate is clearly seen by the deposition of brown powder inside the wells.

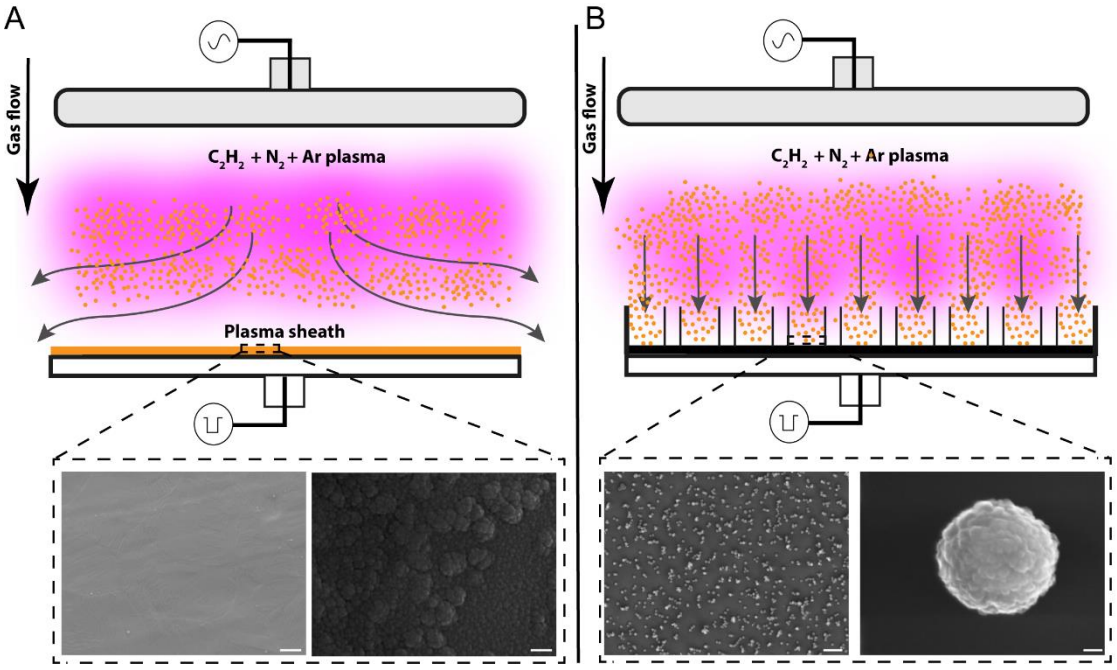

Figure 5.5. A schematic exemplifies the collection mechanism of nanoP^3 in a capacitively-coupled radio-frequency plasma sustained in a C2H2 + N2 + Ar gaseous mixture. (A) The negatively charged nanoparticles remain in the plasma positive potential and are repelled from the substrate by the electrostatic force. Here, PAC was deposited on a flat substrate supported by the bottom electrode without evidence of nanoparticles (see insets below). (B) The well-shaped nanoparticle collector coupled to the bottom electrode modifies the plasma potential. The plasma positive potential infiltrates into the collector, allowing the nanoparticles to be trapped inside the wells (see inset below). The scale bars are (A left) 2µm, (A right) 100 nm, (B left) 2µm, (B right) 20 nm.

An explanation for the large number of dust nanoP^3 entrapped in the well collector must take into account multiple considerations. It is clear by now that the electrostatic force plays fundamental role in repelling nanoP^3 from the surface of the substrates. Indeed, the electrostatic entrapment of negatively charged nanoP^3 in the positive plasma potential is further enhanced by biasing the substrate holder at negative electric potentials, as shown by the lack of nanoP^3 in the usual configuration (i.e. without the collection device). As the substrate potential increases, the electrostatic force $\boldsymbol{F}_{est}$ (which trends linearly with the particle radius r_p) on the particles also increases. Additionally, an increase in the thickness of the Debye sheath, d_{sheath}, is also expected with increasing wall (substrate) potential since $d_{sheath} = \propto {V_{bias}}^{3/4}$.

Taken together, an increase in both $\boldsymbol{F}_{est}$ and d_{sheath} results in a more efficient repulsion as all particles are now forced to take equilibrium positions further away from the surface of the substrate. Since the neutral and ion drag and gravitational forces (i.e. forces that drag particles towards the plasma boundaries) trend $\propto {r_p}^2$ and $\propto {r_p}^3$ respectively (see section 1.2.4), results show that the vertical component of these forces are dominated by $\boldsymbol{F}_{est}$. Therefore, only particles significantly larger than those formed under current discharge conditions could possibly reach the substrate by the action of gravity and drag forces. Previous research has found that dust particles levitate in equilibrium positions above the plasma sheath, where $\boldsymbol{F}_{est}$ is perfectly balanced by drag and gravitational forces [236]. In the current reactor configuration, particles levitating close to the plasma/sheath interface are expected to eventually be removed from the reactor mainly

by the action of the horizontal component of the ion drag force due to the flux of ions towards the side walls of the reactor (see Figure 5.6).

While electrostatic repulsion still takes place with the collector placed on the substrate holder, the positive plasma potential is able to penetrate the wells (see Figure 5.6). Since the vertical component of the ion and neutral drag forces is expected to be significantly larger than their horizontal components, a great majority of nanoP^3 formed in the centre of the reactor is expected to enter the boundaries of each well. Particles inside the wells continue to experience a downward force by action of the ion drag force, bringing them closer to the bottom of the collector as they grow in size and until they reach an equilibrium position or reach the bottom of the well. Therefore, the collection method proposed here allows efficient collection of dust particles by entrapment and without external manipulation.

A close inspection of a variety of substrates retrieved from inside the wells reveals a uniform distribution of aggregates formed by several individual nanoP^3. While the radius of individual (spherical) nanoP^3 was ≈ 50 – 100 nm, aggregates ranged from ~400 nm up to ~2 μm. Given that each spherical nanoP^3 acquire a significant negative net charge in the plasma, Coulomb repulsion effectively prevents particle-particle aggregation. The formation of aggregates shown in Figure 5.7a suggests that a significant reduction in the particle surface charge takes place inside the wells, which suggests that the positive plasma potential was unable to penetrate throughout the entire depth of the well. Aggregation of individual nanoP^3 was most likely triggered by a reduction of

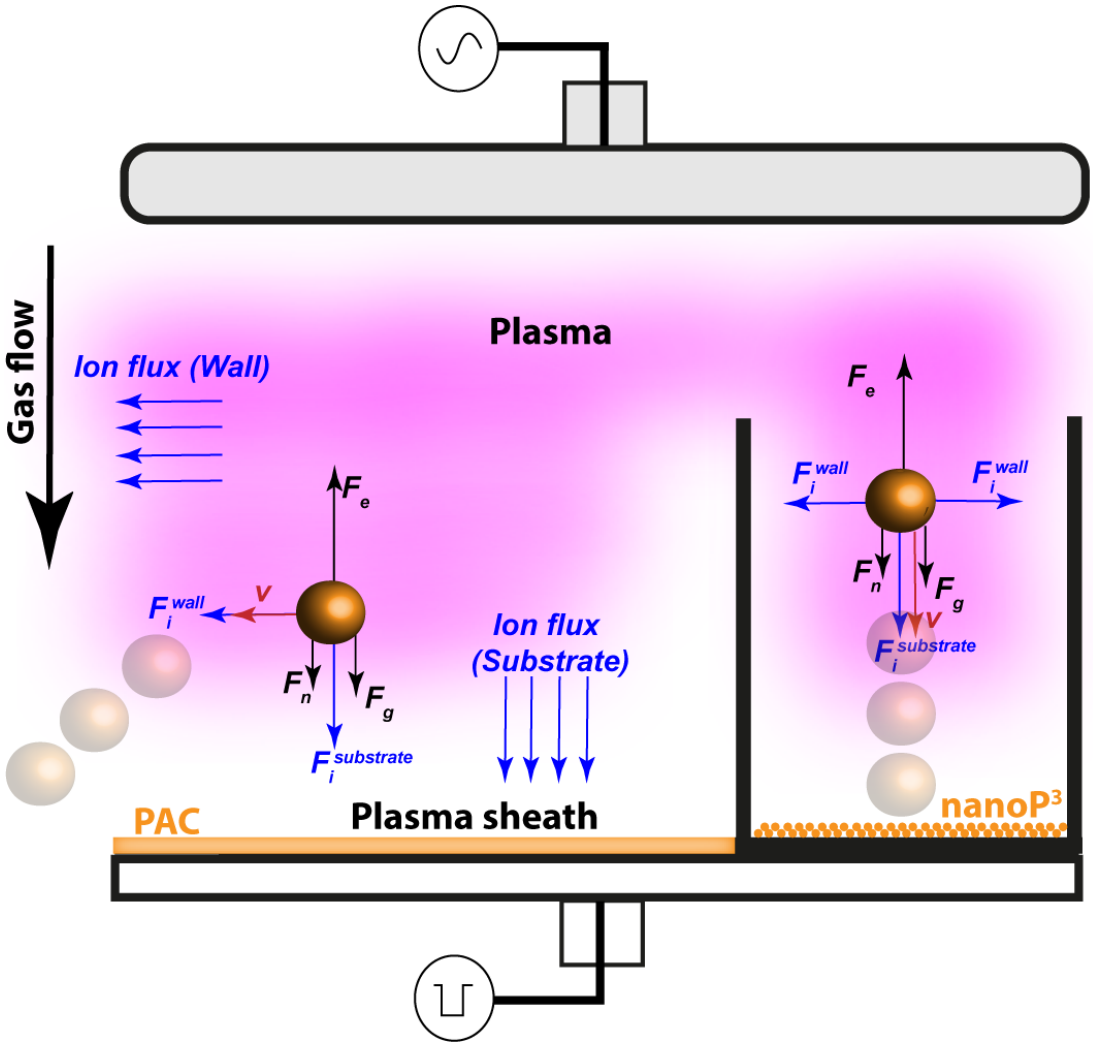

Figure 5.6. A schematic comparing the forces acting on nanoP^3 outside and inside the collector wells. The particle on the left assumes a vertical equilibrium position near the plasma sheath formed above the substrate holder. This position is defined by a balance between the electrostatic force and gravitational, neutral drag, and the vertical component of the ion drag force. The horizontal component of the ion drag force, due flux of ions towards the lateral walls of the reactor, eventually drags the nanoparticle out of the active plasma before they can reach the substrate surface. Contrarily, the particle on the left is trapped as the positive plasma potential penetrates into the well. The gravity and drag forces overcome the electrostatic force as the particle increases in size, dragging it towards the bottom of the well. Note that the horizontal components of the ion drag forces cancel each other inside the well.

the electron density in an afterglow region formed inside the well. The formation of dust particulate aggregates driven by a reduction of the surface charge has been previously reported in the afterglow region of a downstream plasma reactor [235]. Here, while the original size of the particles was ~10 nm, the resulting synthesis product was collected in ~500 nm complex conglomerates due to particle agglomeration along the reactor.

Collection of nanoP^3 was then carried out on 8.5 cm x 12.7 cm polystyrene tissue culture plates containing 96 wells each. One would expect that the length of the afterglow region should be reduced in this plate since the height of each well is now only 1.1 cm. Provided that the positive plasma potential can penetrate inside these wells to a greater extent than in the 24 well plate scenario, a reduction of the afterglow region should reduce particle aggregation. To realise this hypothesis, SEM imaging was carried out on Si wafer substrates placed inside the wells of both 24 and 96 well plates and exposed to one nanoP^3 formation cycle (the plasma was sustained at W_{rf} = 100 W and p = 150 mTorr, $Q_{acetylene}$ = 6sccm and V_{bias} = V_f). Significant formation of large particle aggregates was again confirmed on substrates placed inside the 24 well plate (inset in Figures 5.7a). The aggregates were uniformly dispersed on the surface of the Si substrate, measuring 1 – 2 μm in their longest dimension. Each aggregate was composed of spherical nanoP^3 particles with $r_p = 50$ nm, which were also found scattered around the surface amid the aggregates. The formation of large aggregates was significantly supressed in nanoP^3 collected on a 96 well plate as shown in Figures 5.7b. The results suggest that Coulomb interactions between particles prevents significant aggregation until they reach the bottom of the well. These observations are consistent with the fact that the positive

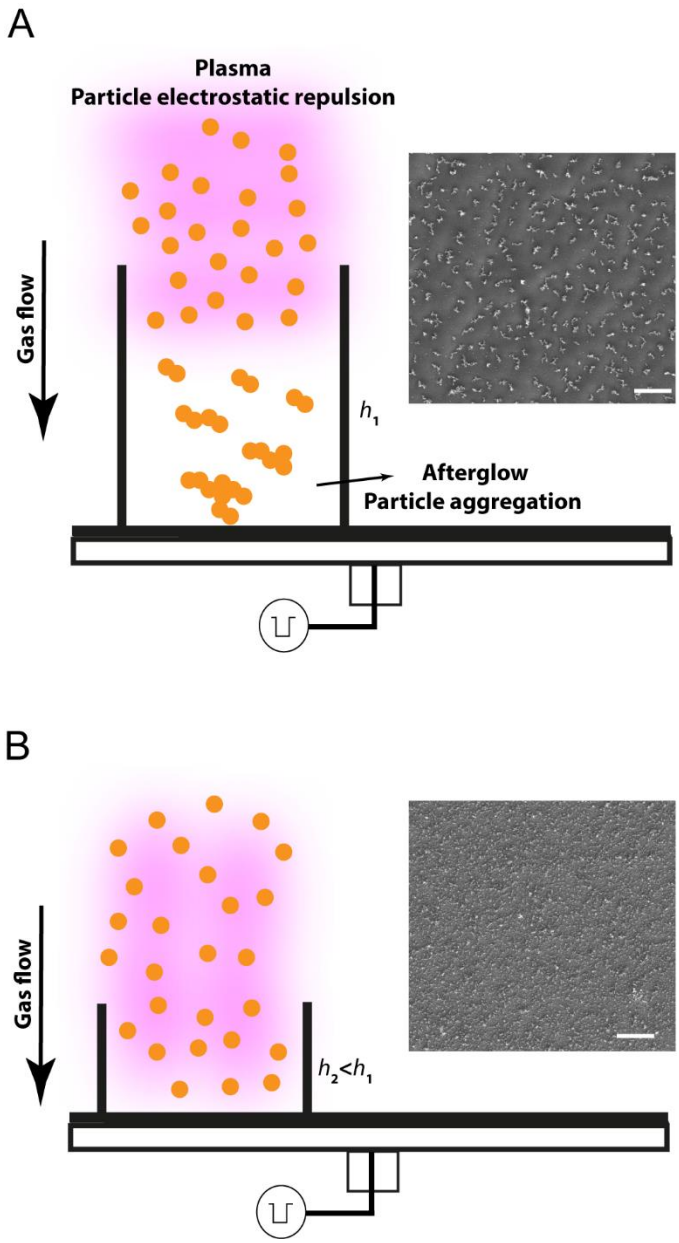

Figure 5.7. The height of the wells modulates particle aggregation. In (A), the plasma positive potential is not able to fully infiltrate towards the entire well. While the particles repel each other in the active plasma via Coulomb repulsion, the development of an afterglow region inside the well triggers particle aggregation before they reach the bottom. The inset shows an SEM image of nanoP^3 aggregates collected in a 24-well plate (h_1=17 mm). (B) The extension of the afterglow region was reduced in a 96-well plate (h_2=11 mm), allowing to collect nanoP^3 with minimal aggregation. Scale bars are 2µm.

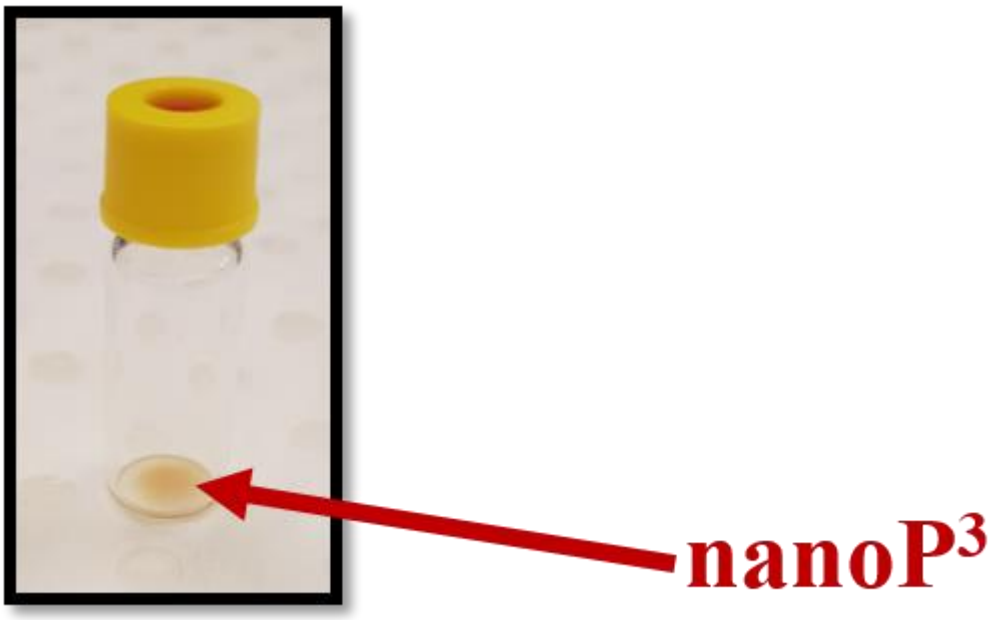

Figure 5.8. Exposure of sealable glass vials to the dusty plasma allows the collection, storage and shipping of nanoP^3 in sterile conditions

plasma potential is able to penetrate a greater fraction of the well depth, hence decreasing the total extent of the afterglow region inside the well.

The collection of nanoP^3 was further exemplified using sealable glass vials as shown in Figure 5.8. Here, accumulation of a nanoP^3 brown powder was observed on the bottom of each vial. The vials are sterilized upon exposure to the plasma and can be subsequently sealed ex-situ under a controlled and sterile environment. This proof-of-concept experiment paves the way for a nanoparticle synthesis and collection platform compatible with commercial demands. Provided that the synthesis and collection process can be stabilized for enhanced reproducibility, pre-quantification and characterization of

nanoparticles collected in the vials can be envisaged for shipping of nanoP^3 samples with tailored properties.

5.3.3 Optical emission spectroscopy as an in-situ monitoring tool during the formation of nanoP^3

While OES allows a straightforward detection of dust particulate formation in plasmas, its full potential has not yet been explored in the literature. As previously discussed, the formation and growth of dust particulates dramatically changes the characteristics of the plasma. This is best demonstrated by a reduction of the electron density which is compensated by an increase of the electron temperature to increase the ionization rate. Moreover, particle growth is enhanced by the diffusion of heavy species, i.e. ions and radicals, during the accretion phase. Consequently, a significant change of the chemical fingerprint of the plasma should be expected during the formation of the particulates. A more comprehensive analysis of the discharge emission spectra during dust particulates could therefore provide valuable information.

Here, OES was carried out to gain further knowledge of the dynamics of the radiation emitted by the plasma during the oscillations, by measuring the time evolution of active species that are expected to participate in the growth and formation of the particulates. For this purpose, high resolution spectra (0.01 nm nominal resolution) were acquired in the range 386 nm to 396 nm. This spectral window contains detailed spectral information on the rotational-vibrational band-heads of three different electronically excited molecules, which were hypothesized in this work to be paramount in describing the formation and growth of dust particulates. Figure 5.9 shows a snapshot of the spectrum

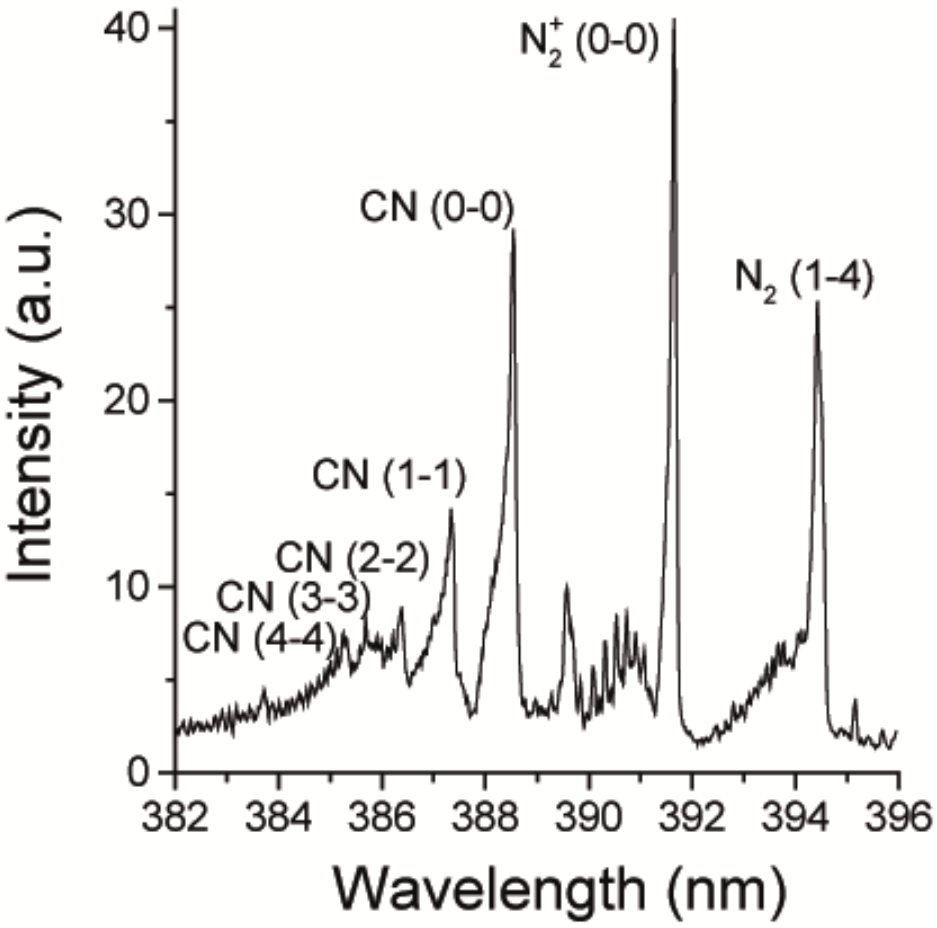

Figure 5.9. A typical emission spectrum of the C_2H_2/N_2/Ar dusty plasma in the 382 – 396 nm wavelength range.

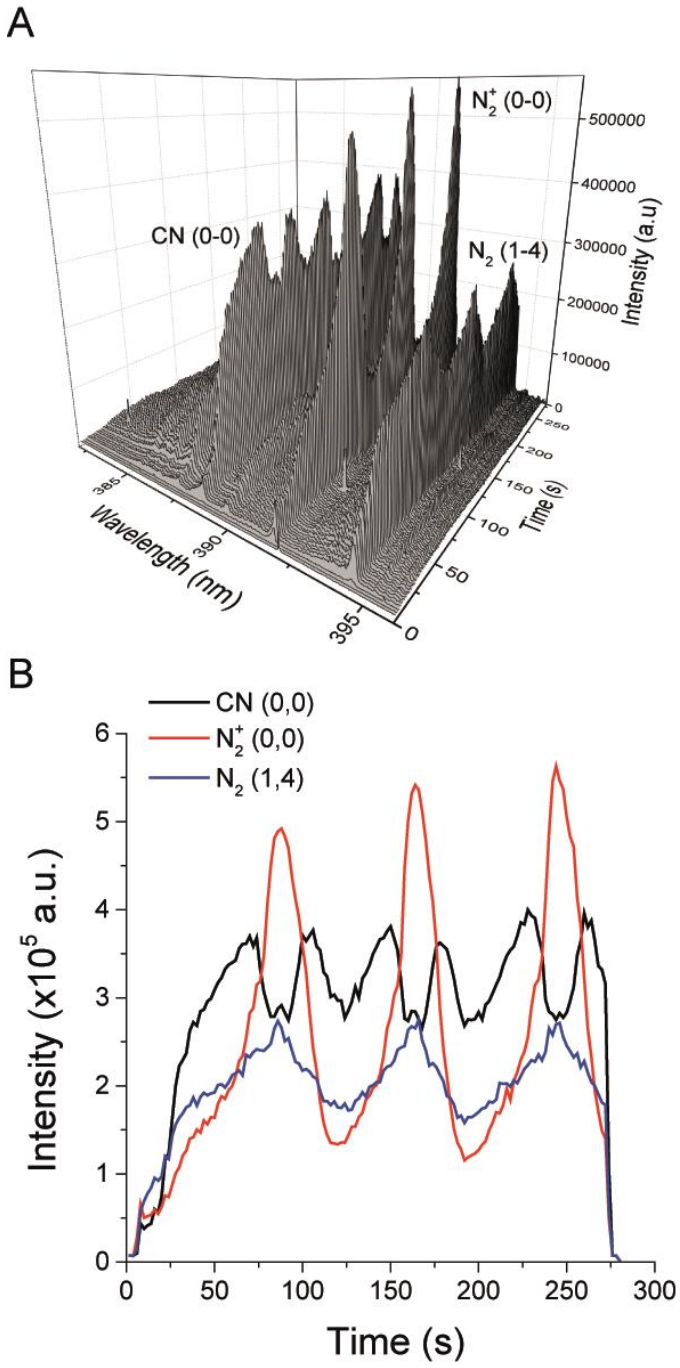

Figure 5.10. (A) Time series of the discharge emission spectra (386 – 396 nm) shows that the entire spectral envelope oscillates during the formation of nanoP^3. (B) Time-evolution of the CN (0-0), N_2^+(0-0) and N_2 (1-4) molecular rotational-vibrational band emission intensities during nanoP^3 formation (3 cycles) shows the plasma emission intensity cycles over the three phases of nanoP^3 formation, growth and collection. Surprisingly, CN emission intensity decreases in each cycle during the abrupt increase observed for the molecular ions.

acquired in plasma discharges sustained at p = 150 mTorr, P_{rf} = 50W, $V_{bias} = V_f$ and with mass flow rates set at 2, 10 and 3 sccm for acetylene, nitrogen and argon respectively.

The first molecular band arises from transitions of the CN ($B^2\Sigma^+ \rightarrow X^2\Sigma^+$) violet system between 386 nm and 389 nm. The most intense band head is centred at 388.53 nm and results from transitions between electronically excited CN radical molecules with quantum vibrational numbers υ=0, i.e. CN (0−0). The second molecular band is related with rotational-vibrational transitions of N_2^+ (0–0) molecular ions from the first negative system ($B^2\Sigma_u \rightarrow X^2\Sigma_g$) between 389 nm and 392 nm, with a band head centred at 391.64 nm. The third molecular band arises from transitions of neutral N_2 (1–4) excited molecules from the second positive system ($C^3\Pi_u \rightarrow B^3\Pi_g$) with band head centred at 394.4 nm. The time evolution of this spectral window is plotted in Figure 5.10a for a discharge duration of 300 s. As shown, the emission intensity of entire spectral envelope oscillates with time three times, a result which is consistent with the oscillations observed by eye in the overall plasma emission intensity.

To simplify the analysis, the emission intensity of each band-head was plotted as a function of time in Figure 5.10b. The emission intensity of N_2^+ (0–0) molecular ions increased monotonically, before experiencing a rapid increase at 75 s and reaching its first maximum at around 88 s. After this point, the intensity decreased steadily over 32 s reaching a minimum 120 s after ignition of the plasma. An identical pattern was then observed for the following two cycles, with consecutive maxima observed at 164 s and 244 s and a second minimum at 192 s. The average period of the oscillations was 78 s measured between consecutive maxima.

A similar oscillatory pattern was found for the N_2 (1–4) band-head transition, which oscillated in phase with N_2^+ (0–0) ions.

The change in the plasma apparent brightness observed in Figure 5.1 is driven by an overall increase in the intensity of spectral lines and rotational-vibrational bands as seen in Figures 5.10. The emission intensity is proportional to the density of the emitter state N_i and given by

$$\epsilon_i^j \propto N_i A_i^j \frac{hc}{\lambda_i^j} .$$

In a steady-state and spatially averaged approximation, the density of the emitter state N_i can be obtained by the continuity equation

$$\frac{D_i}{\Lambda^2} N_i = S_i \ .$$

The term in the left-hand side represents the loss of N_i due to diffusion where D_i is the diffusion coefficient and $\Lambda \equiv R/2.405$ is the characteristic diffusion length for a cylindrical vessel (R is the radius of the vessel). The term in the right-hand side represents the source term, which can be written in terms of the creation / loss rate coefficients related with the corresponding mechanisms of creation / loss for the emitter state. In a simplified corona model for instance, a given excited state is mostly lost by diffusion while its production is mainly driven by electron impact collision with the ground state level. Therefore, the continuity equation can be expressed as

$$\frac{D_i}{\Lambda^2} N_i = S_i \approx N_0 n_e C_0^i \ ,$$

with N_0 the number density of the ground state, n_e the electron density and

$$C_0^i \propto \int_0^\infty \sigma_0^i u f(u) du$$

the excitation coefficient for the emitter state. In the integral, σ_0^i is the electron impact excitation cross-section from the ground state, u is electron the energy and $f(u)$ is the electron energy distribution function (eedf). Since the particles behave like a sink for the more mobile electrons, the well-known quasi-neutrality equation in plasmas $n_e \approx n_i$ must be re-written in the form

$$n_e + |Z_d n_d| \approx n_i$$

where n_i and n_d are the number density of positively charged ions and dust particles respectively and Z_d the number of electrons per dust particle. The re-written quasi-neutrality equation implies that a significant reduction in the electron density takes place in the plasma as electrons are lost to the dust particles [106]. Consequently, an increase in the electron kinetic temperature is necessary to compensate the reduction in the electron density.

To compensate for electron losses by diffusion towards the growing particles, changes to the eedf are necessary to increase the ionization rate so as to sustain the plasma. Assuming one-step electron-impact collisions as the main ionization mechanism, an increase in population of higher energy electron at the tail of the eedf is required to trigger a higher ionization rate. Therefore, the increase in emission intensity of a given spectral line/or band must ultimately be driven also by changes in the eedf that result also in a bolstering of the excitation coefficient C_0^i. Since the electron kinetic temperature is generally given by

$$T_e \equiv \frac{2}{3}\langle u \rangle$$

where the brackets $\langle\,\rangle$ denote the average of the eedf over all energies, i.e. $\langle\,\rangle = \int_0^\infty \sqrt{u} f(u) du$, the same change in the eedf that drives higher C_0^i, would naturally also result in an increase in the electron temperature.

Surprisingly, an observation of the spectral time-series reveals that the CN radical molecules do not follow the same pattern along one cycle, oscillating at double the frequency registered for the N_2 (1–4) and N_2^+ (0–0) species. Particularly, a decrease in intensity was observed at around 75 s, which overlapped with the abrupt increase in the intensity of N_2^+ (0–0) species (Figure 5.10b). The intensity of CN species continued to decrease until the corresponding first maximum of the N_2^+ (0–0), before increasing to a second maximum at 105 s and then decrease again to a relative minimum at 124 s. The same oscillatory pattern for CN species repeated for the following two cycles. The relative minima registered at 88 s, 162 s and 247 s are particularly surprising since they overlap with the maxima in the overall discharge emission intensity. These results suggest that CN radical molecules are lost in the discharge at particular stages during the formation of dust particulates. This result is particularly interesting since research to date has found that the overall discharge emission intensity, driven by an increase of the electron temperature, increases with the formation of dust particulates. The following sections will combine the collection method developed in section 5.3.2 with OES to investigate the formation of nanoP^3 in the reactor. The role of the process (plasma) parameters in the formation and removal of nanoP^3 is also studied and a mechanism is proposed based on observations of the oscillation profile of N_2^+ (0–0) and CN (0–0) species.

5.3.4 Formation and growth mechanisms of nanoP^3

A more detailed screening of nanoP^3 structure with SEM showed that two groups of particles with distinctive size ranges (Figure 5.11) are formed in different growth phases. A first group of protoparticles with a size range of ~ 10 nm and a second group comprising particles with diameters ranging from ~50 nm up to ~500 nm. Results suggest that the second group of particles (larger spherical-shaped particles) are formed by the aggregation of several smaller particles from the first group – clusters. A combination of in-situ OES monitoring and SEM analysis of surface morphology of particles collected at various time points during an oscillation cycle allowed the identification of three main phases (Figure 5.12): formation and nucleation of primary carbonaceous nanoclusters (PCN) or protoparticles by radical/ion chain plasma polymerization (phase 1), rapid cluster aggregation (phase 2) and nanoP^3 removal and collection from the active plasma (phase 3).

During phase 1, the activation of the initial gaseous mixture, comprised of C_2H_2 (monomer), N_2 and Ar, is driven by collisions with energetic electrons that oscillate in the rf electric field. The activation of C_2H_2 and N_2 forms an array of different reactive species, such as ions and radicals, that recombine and nucleate to render PCN with a size of up to ~10 nm. The continuous formation and build-up of PCN in the plasma volume was observed in phase 1 by an increase in the overall plasma emission intensity over time (Figure 5.12 and 5.13). As the PCN reach a critical density in the plasma, they rapidly aggregate into highly spherical nanoP^3 (phase 2). During this second phase, the aggregation of PCN overlapped with a rapid increase in the N_2 (1 – 4) and N_2^+ emission intensities (Figures 5.13b).

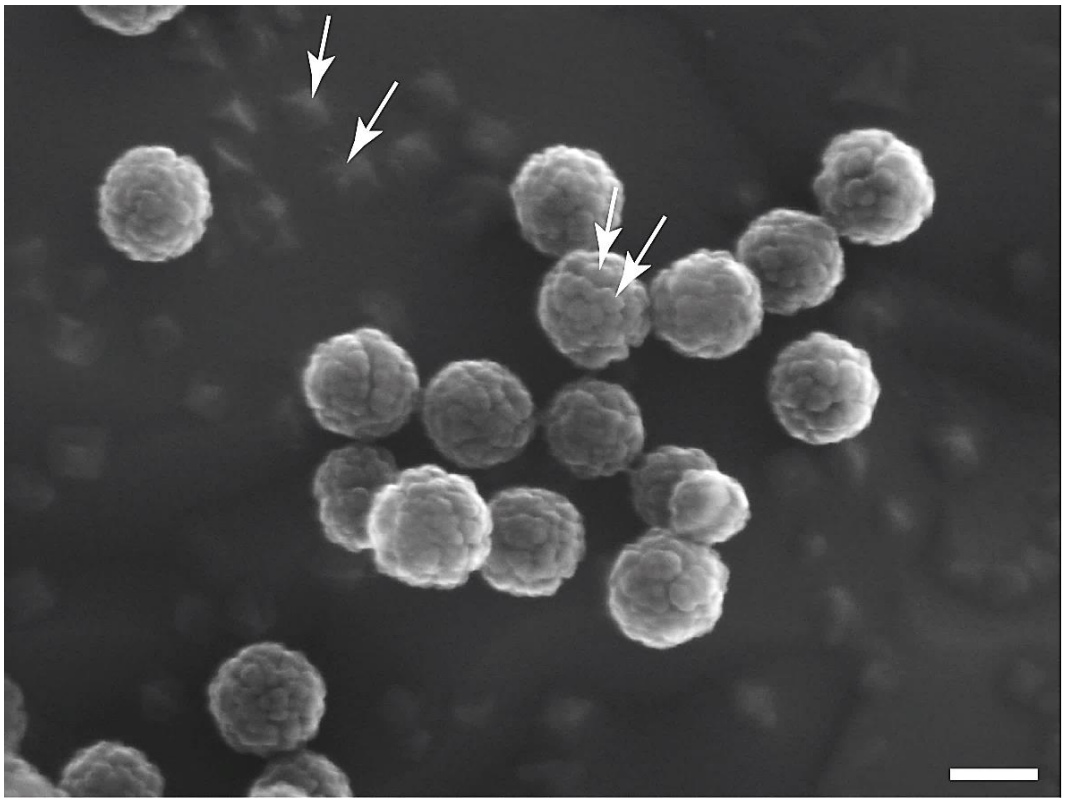

Figure 5.11. Representative SEM image detailing the surface morphology of nanoP^3. Results show that two groups of particles are formed: a first group of protoparticles (white arrows) that aggregate to into bigger and spherical nanoparticles (nanoP^3). Scale bar is 200 nm.

As discussed in the previous section, the overall increase in the emission intensity is mostly driven by a modification of the ionization profile in the plasma and potentially also by scattering of radiation by nanoP^3. Changes to the ionization profile are prompted by a reduction of the electron density, necessary to compensate for the rapid increase in the electron temperature as electrons sink into the growing particle. While the overall plasma emission intensity is expected to increase during cluster aggregation, the spectral band-head associated with CN radicals decreases in intensity during phase 2. Interestingly, the decrease in the CN population coincided with a 5-fold increase in the amount of collected particles Figure 5.13b), suggesting that the formation of nanoP^3 is assisted by accretion of radical molecules into the growing particles.

The formation and growth of PCN during phase 1 is ruled by the plasma chemical environment. The latter is essentially dependent on the type of monomer and carrier gases used to produce the discharge as well as their degree of fragmentation, dictated by the species residence time and energy input to the plasma discharge. The mechanism of formation of PCN may follow similar pathways as is the case for the PAC building block, which can be dominated by growth reactions involving either neutral reactive radicals and/or ions. Under the discharge parameters adopted in this work, radical-induced plasma polymerization may be the dominant path in phase 2, as shown by the decrease of CN radicals during the formation of nanoP^3. One should note that ion-induced growth may still play a major role in the formation and growth of carbon-based dust particles [99]. Particularly, the formation of PCN in the early stages of phase 1 may be assisted by the ion-induced chain reactions as discussed in section 1.2.4. Nevertheless, the radical-growth hypothesis, which appears to take place

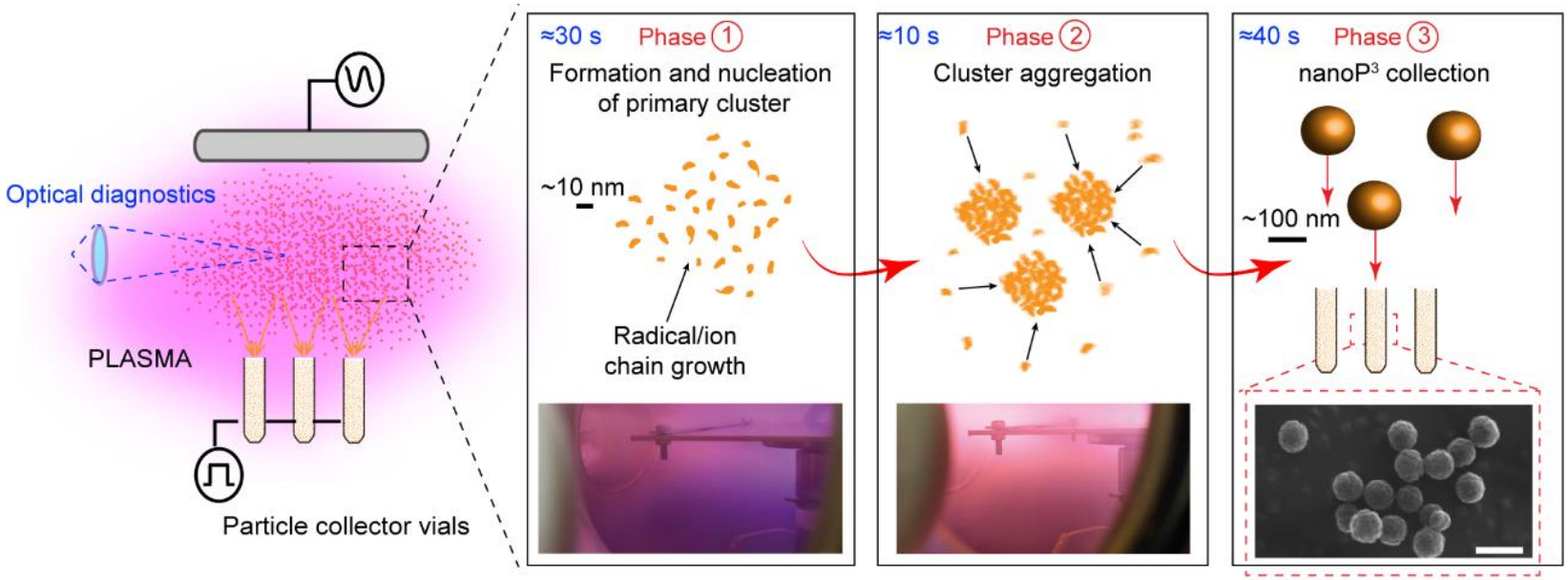

Figure 5.12. Schematic diagram showing formation, growth and collection of nanoP^3 in the plasma/gas phase. The plasma reactive chemistry determines the formation and nucleation of protoparticles or primary clusters (phase 1) that rapidly aggregate to form nanoP^3 (phase 2). When nanoP^3 reach a critical size, the gravity, neutral and ion drag forces push them out of the plasma (phase 3), enabling their collection in electrically biased collector vials (or well collectors). The time taken for each phase is indicated in blue (at the top of each phase) in seconds. Insets show images of the plasma before and during nanocluster aggregation and a SEM micrograph of nanoP^3 as collected. Scale bar = 200 nm.

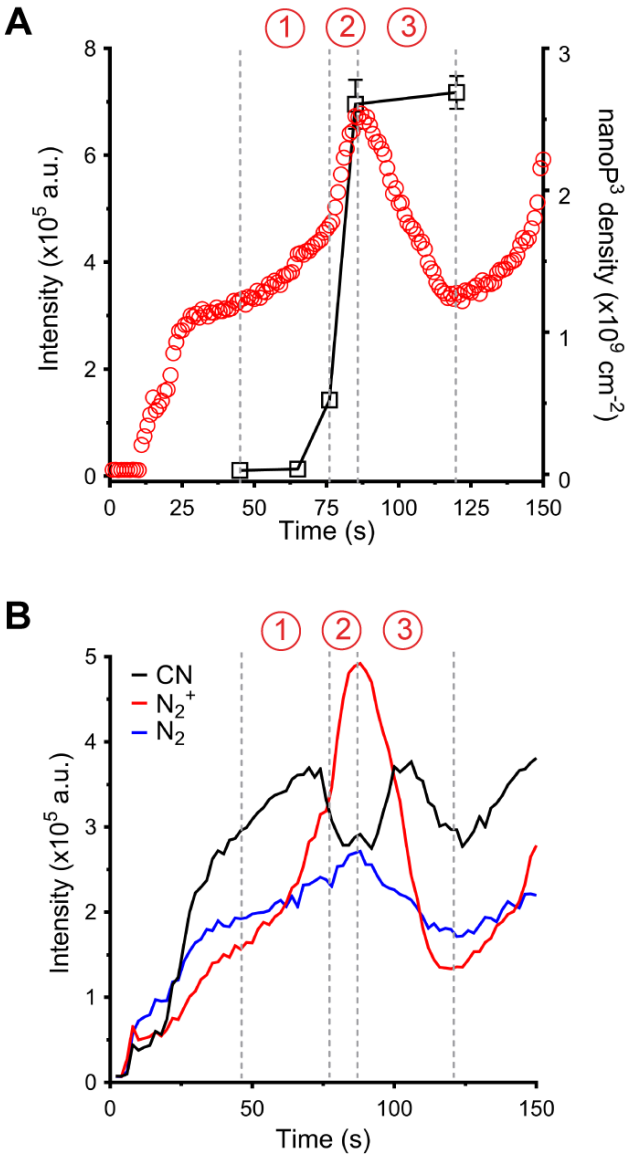

Figure 5.13. (A) Time evolution of the N_2 (0-0) band emission intensity overlaid with the density of nanoP^3 collected at different stages of the cycle. The rapid nanocluster aggregation (phase 2) coincides with an increase of both collected nanoP^3 and discharge emission intensity. (B) As in Figure 5.10b but in the 0 – 150 s time range (one nanoP^3 formation cycle). Results show that cluster aggregation coincides with a decrease in the emission intensity of CN radical species.

mainly in phase 2, is consistent with the rapid step growth polymerization model (RSGP) previously proposed in the context surface plasma polymerization of thin films (see section 1.2.3).

Cluster rapid aggregation, similar to what was observed here during phase 2, has been previously reported in many dusty plasma systems [63, 95, 101, 245]. While robust models for cluster aggregation combining both experimental and simulation efforts are still necessary, the most adopted proposition suggests Coulomb interactions between clusters of opposite charge as the most plausible mechanism [101]. When the clusters reach a critical size in the plasma (~ 10 nm) negatively and positively charged clusters start to aggregate to form the second group of larger particles (i.e. phase 2). During this phase, all the growing particles behave as a sink for electrons and ions present in the plasma, with the diffusion of charged species towards them ruled by plasma sheath dynamics. During cluster aggregation and rapid growth phases a spherical sheath is formed around the growing particles [101]. The development of this spherical sheath is most likely the reason leading to the formation of nanoP^3 with a spherical shape. Because of their higher mobility the electrons diffuse more rapidly towards the particles when compared to the positive ions. Consequently, the growing particles are charged negatively and their growth is enhanced by attracting more positively charged clusters, positive ions and neutral radicals. After reaching a critical size and density (which are dependent on the plasma parameters), the assembled negative charge on the particles surface inhibits further cluster aggregation [101].

As discussed previously, the particles acquire a negative net charged after rapid cluster aggregation, confining them to the positive plasma potential. Once the particles reach a critical size and mass other forces acting on the particles become more dominant (e.g. ion drag force, thermophoretic force, gas viscous force and gravity force) and overcome the electrostatic forces, dragging the particles away from their creation and growth zones. Under the current reactor conditions, the electrostatic force is mostly overcome by the ion drag force upon a substantial increase in the ionization degree (see equation table 1.1). In particular, the rapid increase in ion density during phase 2 (Figure 5.13b) yields a 3-fold enhancement of the ion drag force, dragging nanoP^3 out of the active plasma towards the well-shaped collector devices or glass vials. The removal of the particles leads to the formation of a particle-free zone and gives room for a new creation and growth cycle and subsequent removal of the newly formed particles (phase 3). During this phase, the overall discharge emission decreased with all spectral emission band-heads returning to typical particle-free baseline values registered at the beginning of each growth cycle (Figure 5.13a and 5.13b).

5.3.5 The role of plasma parameters in the synthesis of nanoP^3

Plasma emission spectra were systematically recorded as a function of the acetylene flow rate, rf power and discharge pressure. The substrate holder was set to floating potential, i.e. in the absence of a pulsed bias and all other process parameters were kept constant. The time evolution of the emission intensity of N_2^+ (0–0) and CN (0−0) transitions is plotted as a function of the discharge pressure in Figure 5.14 and acetylene flow rate in Figures 5.15 – 5.17 for 50 W, 75 W and 100 W respectively. Overall, the oscillatory behaviour was

consistent with previous observations at $Q_{acetylene}$ = 2 sccm, 50 W in Figure 5.10. The emission intensity of both molecular species was found to oscillate with time in a continuous and reproducible fashion, and the oscillations were significantly modulated the various process parameters. The population of molecular ions steadily increased in the discharge during the first instances for all conditions. Again, an abrupt increase in the emission intensity marking the PCN rapid aggregation in phase 2 was observed followed by a significant decrease before the start of a new cycle. The emission intensity CN (0−0) radical molecules oscillated almost in perfect phase opposition (i.e. 180˚ out of phase) to the intensity of the N_2^+ (0–0) emissions at $Q_{acetylene}$ > 2 sccm for all rf power conditions. Overall, the time delay before PCN aggregation (phase 2) decreased with increasing coupled power and acetylene flow rate. This is related to a higher availability of reactive building blocks in the plasma at earlier stages since a critical number density of PCN is necessary to trigger their aggregation. While the emission intensity for both molecular species oscillated continuously with time for all conditions tested at 50 W, damping in the oscillation amplitude was observed for $Q_{acetylene}$ > 6 sccm at 75 W and 100 W.

Modulation of the oscillations was studied by analysing and plotting relevant parameters such as period, amplitude, phase difference and symmetry of the curves along an oscillatory cycle. The period of the oscillations in particular is an important parameter since it provides information about the duration of nanoP^3 formation cycles. Here, the period was obtained by calculating the time difference between two consecutive emission maxima of the N_2^+ (0–0) species. Results show that the duration of the oscillations decreased with with increasing discharge pressure and coupled power (see Figure 5.18). The formation of nanoP^3 was

observed over wider pressure windows with increasing coupled power. Specifically, oscillations in the plasma emission were detected in the pressure range of 80 – 180 mTorr at 50 W, 80 – 200 mTorr at 75 W and 80 – 250 mTorr at 100W. The lack of oscillations for pressures below 80 W for all power conditions is related with a combination of conditions that lead to a suppression of the formation and growth of PCN and their subsequent aggregation to form nanoP^3. Firstly, at low pressures the mean-free path between particles (electrons, neutrals and ions) increases due to a reduction of the particle number density. This reduces the collision frequency and hence the probability for the formation of PCN via radical and / or ion chain reactions. Additionally, it was necessary to increase the pumping efficiency in order to lower the pressure in the reactor and maintain total gas flow rate constant throughout the set of experiments. Higher pumping efficiency reduces the residence time in the active plasma, which results in a lower degree of dissociation of the initial gaseous mixture. A decrease in the monomer activation yields a lower number of radical and ion species in the discharge, the building blocks necessary for the formation of the PCN. Conversely, the lack of oscillations observed at higher pressures for 50 and 75 W is most likely caused by a decrease in the energy per unit mass of the precursor, due to an excessive increase in the number density of gas molecules.

Figure 5.19 shows the period of the oscillations as a function of the acetylene flow rate for 50, 75 and 100 W (all other plasma parameters were kept constant). Results show that the period decreased asymptotically with increasing acetylene flow rate within the range 0.5 – 8 sccm from 256 s to 26 s and was highly modulated by the coupled power at lower flow rates. Moreover, differences in the period of oscillations are less significant with an increase of the

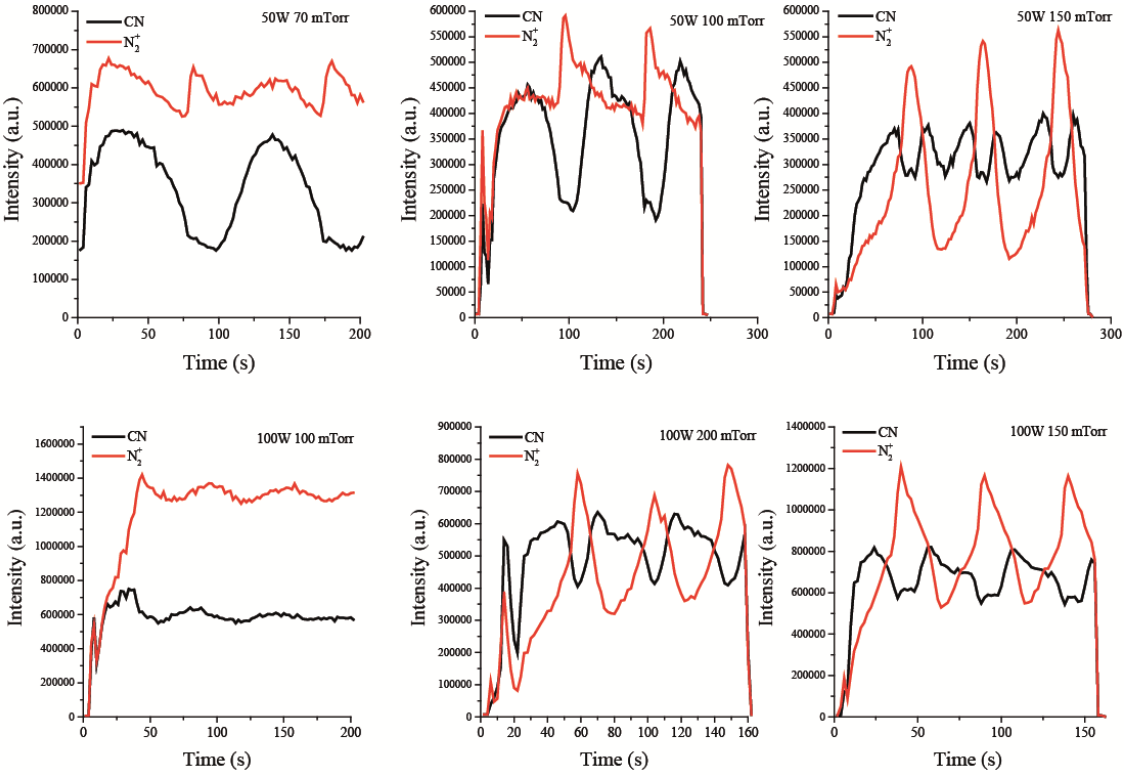

Figure 5.14. Temporal profile of the emission intensity associated with CN radical molecules and N_2^+ molecular ions during nanoparticle formation for selected working pressures and power coupled to the plasma. All other parameters were fixed at a pressure of 150 mTorr and flow rate for C_2H_2, Ar and N_2 gases of 2, 3 and 10 sccm respectively.

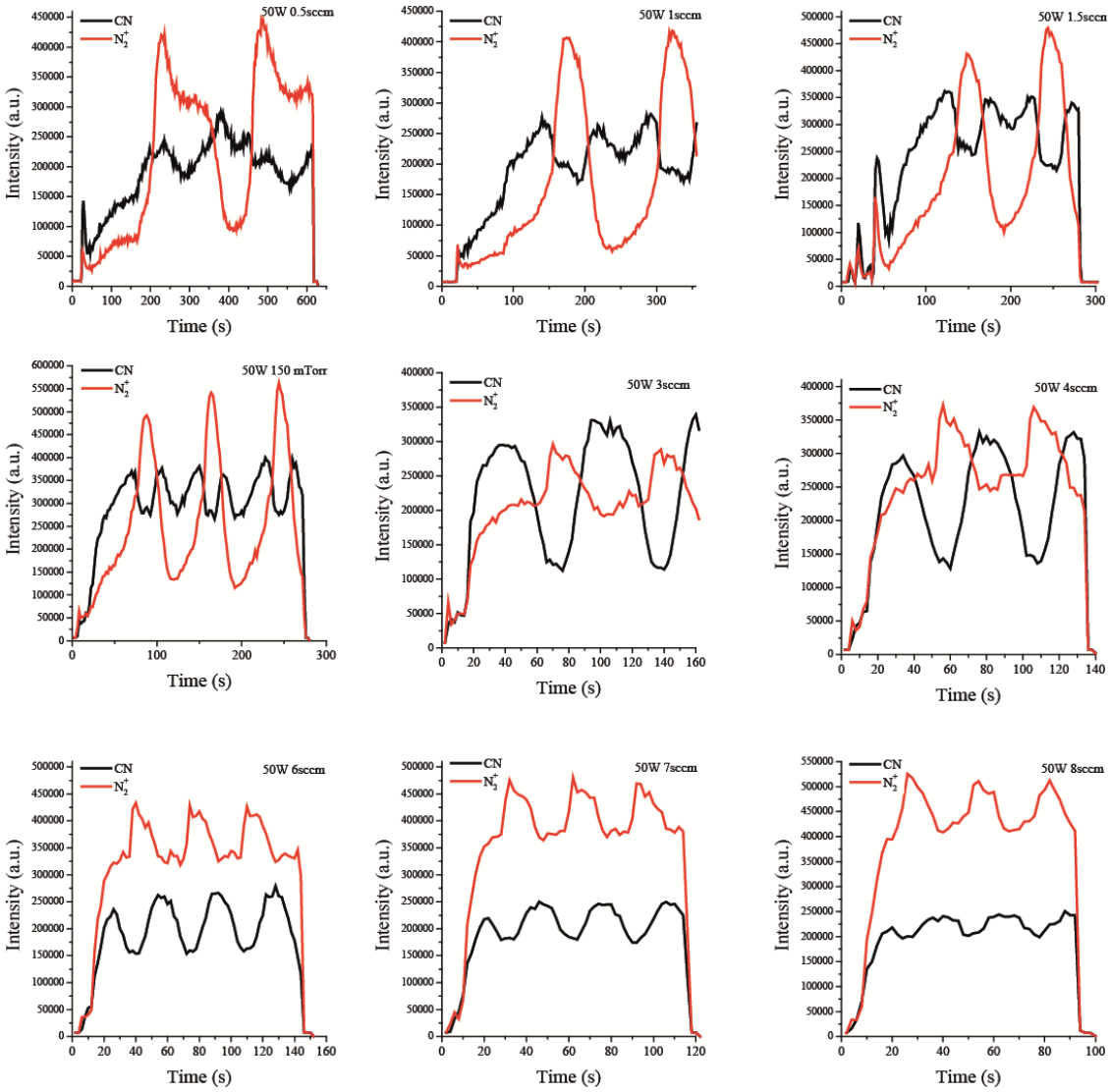

Figure 5.15. Temporal profile of the emission intensity associated with CN radical molecules and N_2^+ molecular ions during nanoparticle formation for various values of acetylene flow rate (1 – 8 sccm) at a fixed 50W coupled to the discharge, 150 mTorr and fixed flow rates for Ar and N_2 gases of 3 and 10 sccm respectively. Overall, the period and amplitude of the oscillations decrease with increasing acetylene flow rate.

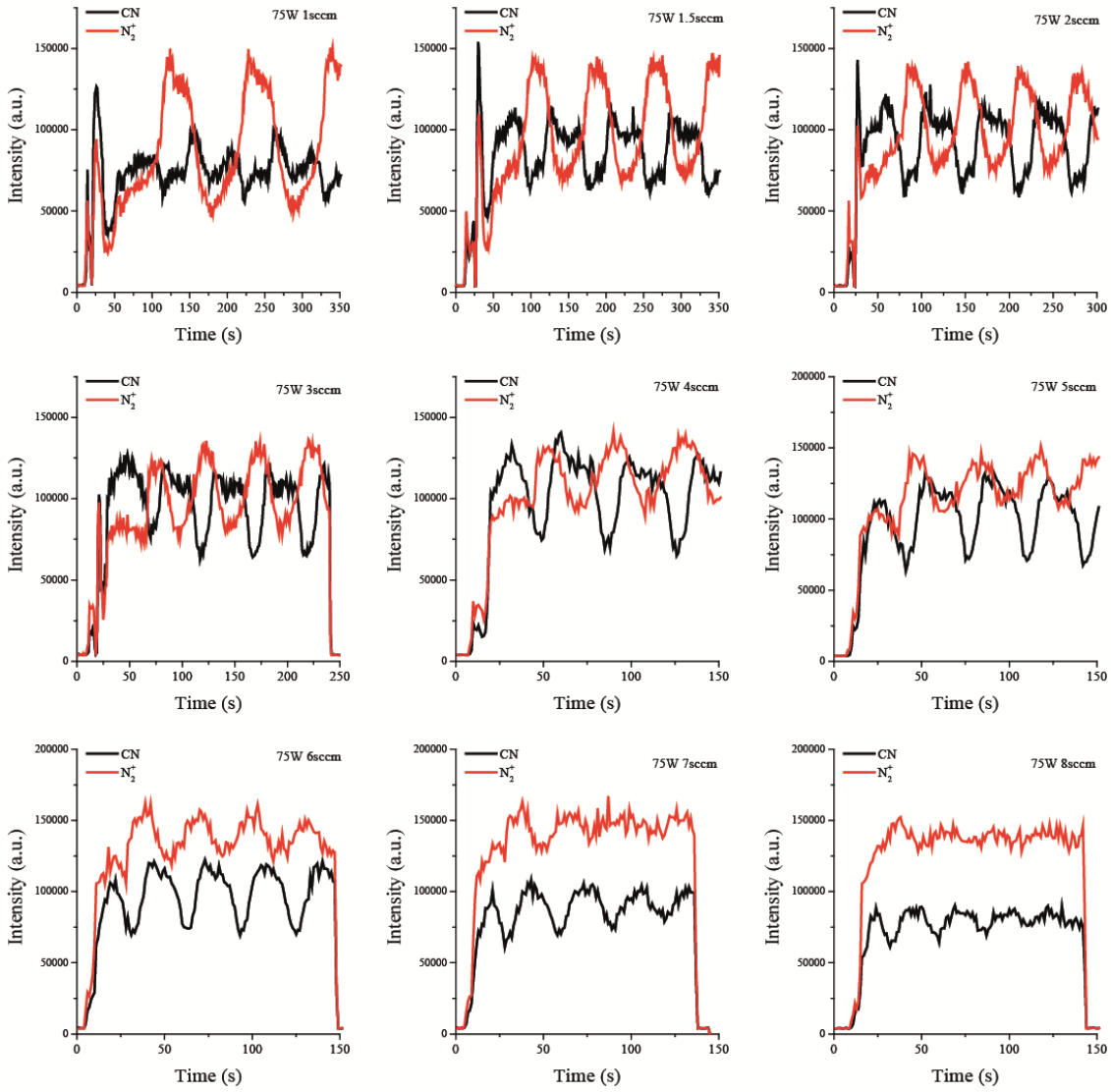

Figure 5.16. Temporal profile of the emission intensity associated with CN radical molecules and N_2^+ molecular ions during nanoparticle formation for 75W coupled to the discharge, 150 mTorr and fixed flow rates for Ar and N_2 gases of 3 and 10 sccm respectively.

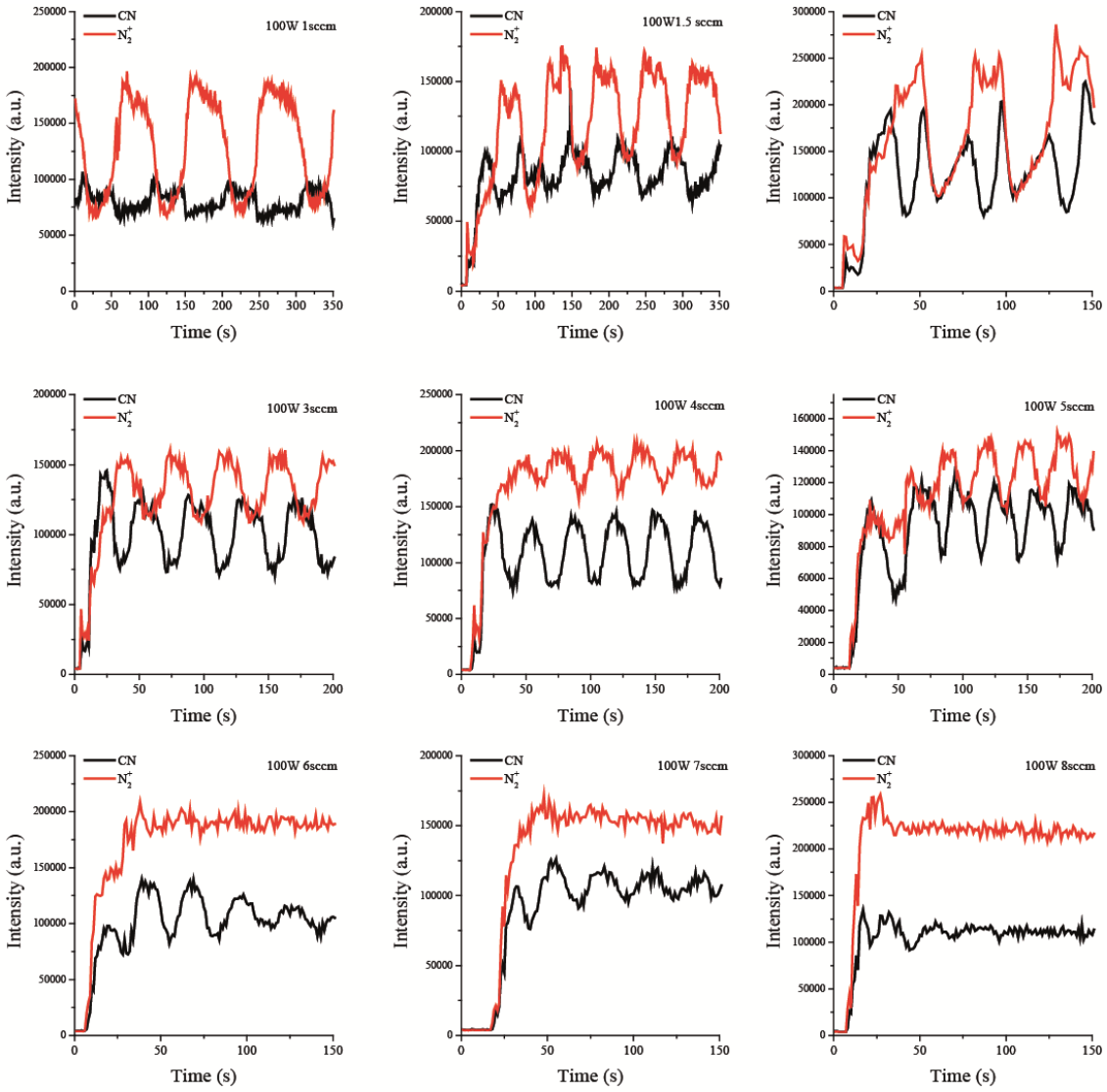

Figure 5.17. Temporal profile of the emission intensity associated with CN radical molecules and N_2^+ molecular ions during nanoparticle formation for 100W coupled to the discharge, 150 mTorr and fixed flow rates for Ar and N_2 gases of 3 and 10 sccm respectively.

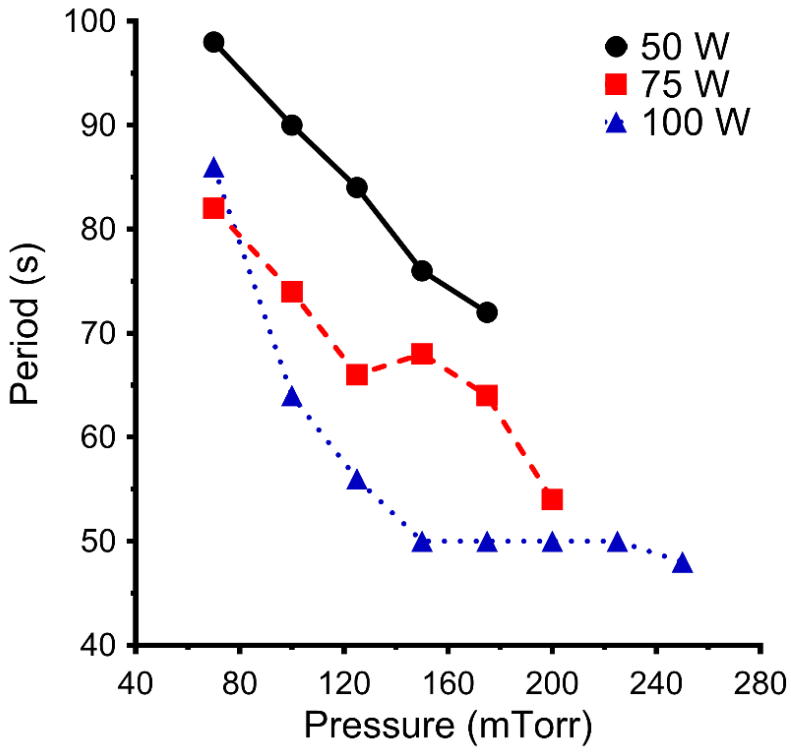

Figure 5.18. Overall, the frequency of the oscillations increases with increasing power and pressure, indicating that nanoparticles are produced at a higher rate. The pressure window at which nanoP^3 can be efficiently synthesised and collected increases with the coupled power. The pumping speed was increased in order to lower the pressure in the reactor and maintain total gas flow rate constant throughout this set of experiments.

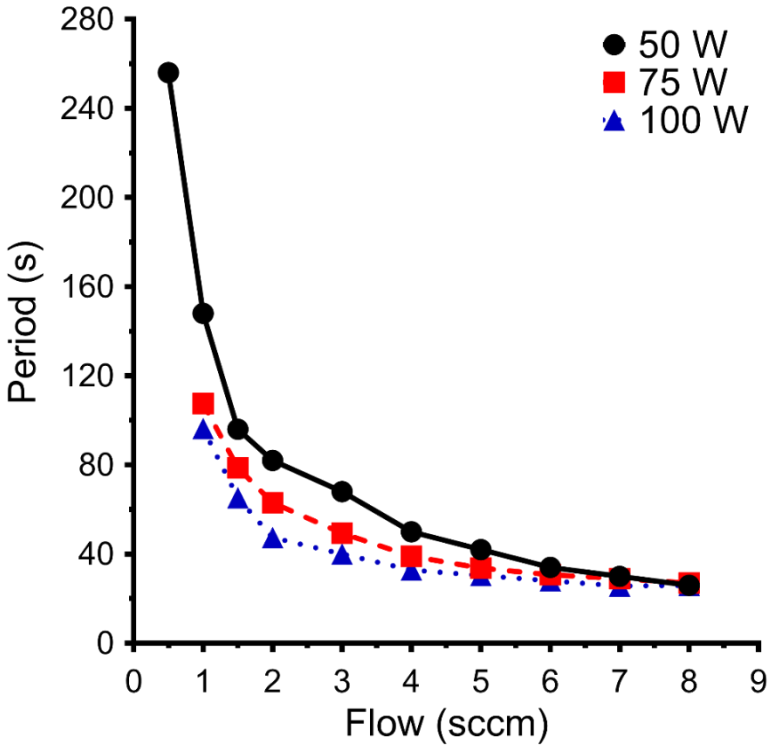

Figure 5.19. Period of the oscillations as a function of the acetylene flow rate and for 50, 75 and 100W. All other plasma parameters were kept constant. The period was calculated by averaging consecutive growth cycles (minimum of 3 cycles when possible) in Figures 5.16 – 5.18 for each condition. While decreasing monotonically with the acetylene flow rate, the period of the oscillations is only highly modulated by the coupled power at low flow rates. Differences in the nanoparticle production rate are less significant with an increase of the monomer flow rate, showing that a further excess in monomer does not contributes for nanoparticle production.

molecules and the energy per monomer unit mass decreases, contributing to an overall reduction in the number of available reactive species.

5.3.6 Process yield

As shown in Figure 5.14 – 5.17, the synthesis of nanoP^3 is an oscillatory and continuous process with collection yields proportional to the number of cycles. In order to establish a relation between the period of the oscillations and particle formation in each cycle, the total mass of nanoP^3 collected on the well collectors was the measured as a function of the acetylene flow rate and the coupled power. Results show that nanoP^3 yield (Figure 5.20) reached 3.2 g/hr m^2 and 7.7 g/hr m^2 for an acetylene flow rate of 3 sccm and rf coupled powers of 50 W and 75 W respectively. The yield was strikingly amplified to 14.4 g/hr m^2 at 100W and 6 sccm. The nanoP^3 yield per oscillation cycle follows the same trend when plotted as a function of the flow rate and coupled power (Figure 5.21). However, differences between regimes are less significant, showing that the higher yield rate is mainly driven by an increase in the period of the oscillations, i.e. occurrence of more formation cycles in the same time interval.

For all the studied rf powers, the mass yield rate profile features a maximum before it decreases to smaller values at higher monomer flow rates. The decrease in the number of nanoparticles collected at higher monomer flow rates is related to a transition in the discharge where volume polymerisation is supressed in favour of surface polymerisation.

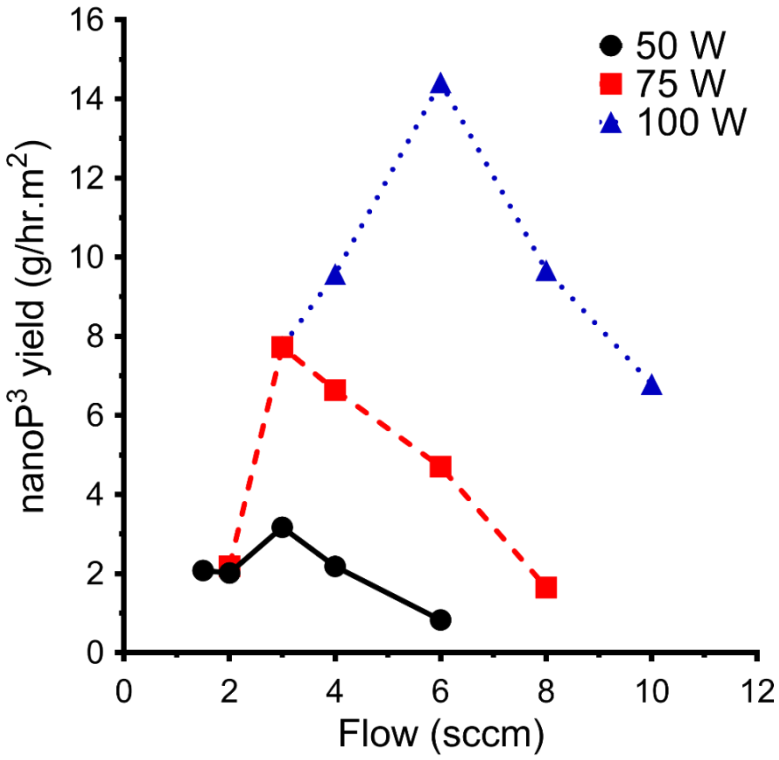

Figure 5.20. Modulation of the nanoP^3 yield showed a non-linear behaviour with the rf power and acetylene flow rate, maximizing at 14.0, 7.7 and 3.2 g/hr m^2 for 100 W (6 sccm), 75 W (3 sccm) and 50 W (3 sccm) respectively. The discharge pressure was 150 mTorr.

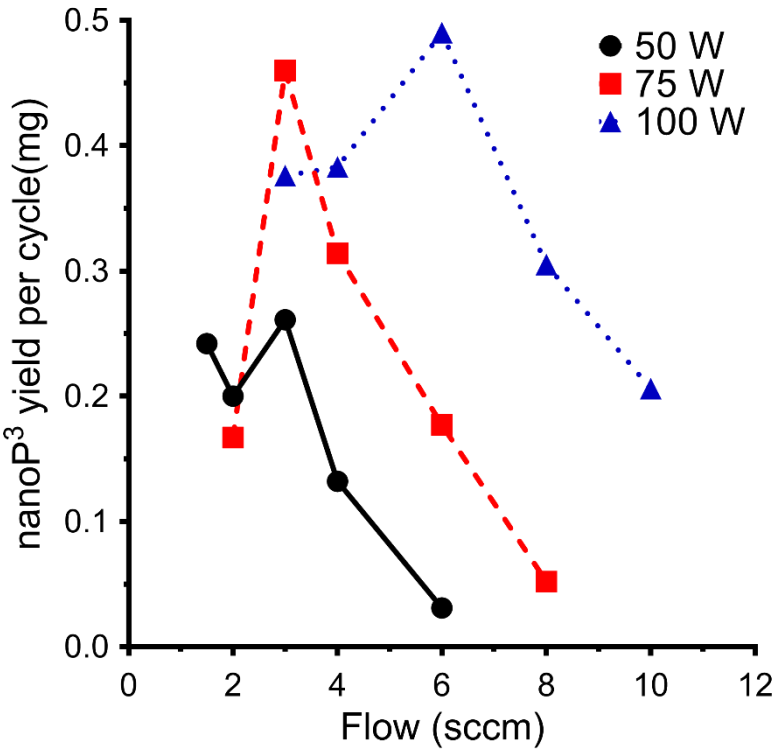

Figure 5.21. nanoP^3 mass yield per oscillation cycle as a function of the acetylene flow rate at various rf coupled powers. The discharge pressure was 150 mTorr.

A key parameter influencing this transition is again the residence time of the monomer in the discharge volume. At flow rates below the maximum yield point there is sufficient energy per monomer unit mass to effectively fragment all monomers supplied and the increasing gas flow increases the number of available reactive fragments in the discharge volume. At flow rates beyond the maximum yield point however, the power is no longer sufficient for effective fragmentation hence the proportion of the population of fragments reactive enough to form nanoparticles in the volume of the discharge decreases and the presence of an increasing population of non-reactive fragments decreases the rate of particle formation in the volume.

The transition between bulk and surface plasma polymerization is best exemplified in the Arrhenius-type plot in Figure 5.22, where the ratio between the nanoP^3 mass yield rate per collector unit area (in g s^{-1} cm^{-2}), Y_r, and the monomer flow rate F is plotted on a log scale against $(W/F)^{-1}$. The flow rate F (given in cm^3 s^{-1}) can be determined from the flow at standard conditions $Q_{\text{acetylene}}$ (measured in sccm) by

$$F = Q_{\text{acetylene}} \frac{p_0 T_{\text{gas}}}{T_0 p}$$

where T_{gas} and p are the gas temperature and pressure in the discharge and T_0 and p_0 are the gas temperature (calculated with OES diagnostics – see Chapter 2) and pressure measured at standard conditions respectively. The linear fits obtained in Figure 5.22 suggest that Y_r can be expressed as a function of the energy per monomer flow, W/F, as

$$\frac{Y_r}{F} = C \exp\left(-\frac{E_a}{W/F}\right) .$$

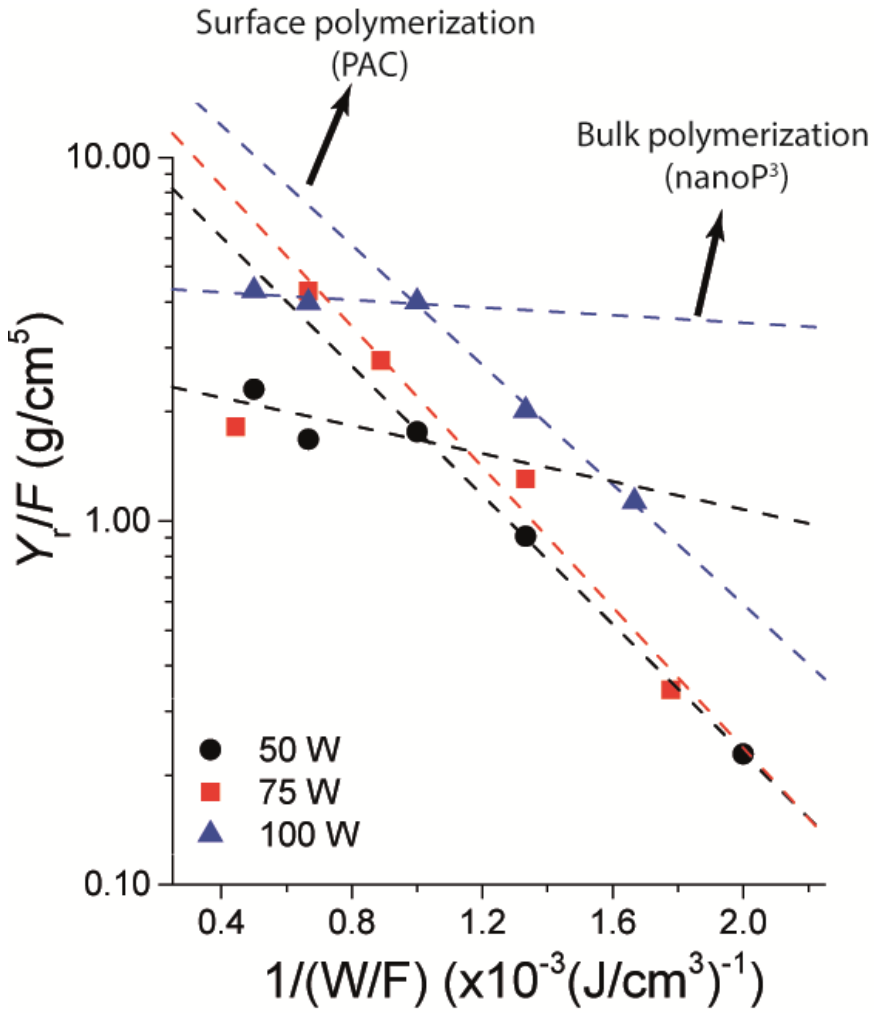

Figure 5.22. Representation of $\frac{Y_r}{F}$ in an Arrhenius-type plot, shows that the relevant macroscopic parameter that describes the formation of nanoP^3 is ∝W/F. The change in slope observed for each data set (various coupled rf powers) represents a transition in the plasma regime between bulk (dust formation) and surface (coating deposition) polymerization.

Therefore, the relevant macroscopic parameter that describes nanoP^3 production in the plasma bulk is $\propto W/F$, as is in the case of surface plasma polymerization of PAC coatings (see section 3.3). The representation of a mass deposition rate per unit area in an Arrhenius-type plot is frequently adopted to macroscopically describe plasma polymerization of thin films coatings [174]. In the previous equation, $\frac{Y_r}{F}$ gives the total nanoP^3 mass per plasma volume and unit area of the collector and therefore has units of g cm^{-5}. C is a constant (with dimensions of g cm^{-5}) that depends on the geometry of the reactor [246] and E_a is an "apparent" activation energy of the monomer used in the process per unit flow necessary to sustain plasma polymerization. E_a can be obtained by the negative of the slope of the linear fit to the Arrhenius plot. The change in slopes observed for each data set, particularly at 50 and 100 W, indicates the transition where monomer activation is channelled from bulk (nanoP^3 production) to surface (PAC deposition) polymerization. At 100 W for instance, the data points can be fitted by two linear functions, yielding $E_a = 2$ J/cm^3 and $E_a = 0.1$ J/cm^3. Since the yield rate only measures the mass of nanoP^3 collected in the well plates, higher E_a values represent the plasma regime where monomer activation is more efficiently channelled for polymerization in the plasma bulk. The significant increase in E_a at low *W*/*F* is consistent with a reduction of the nanoP^3 yield rate (Figures 5.20 and 5.21) in detriment of surface polymerization, as observed by the deposition of PAC coating outside the well collector on the rf electrode and chamber's walls. A macroscopic description similar to the one proposed here could be particularly useful in upscaling scenarios, enabling optimization of the bulk polymerization to maximize sample yield. At the highest yield rate explored in this work (150 mTorr, 100 W and $Q_{\text{acetylene}}$ = 6sccm), the cost of nanoP^3 is estimated to be around $5 per

gram. This value was calculated taking into account the cost of the raw material, i.e. acetylene, nitrogen and argon gases and electricity costs. Results in this section suggest that dusty plasmas could provide a competitive and scalable nanoparticle synthesis route compatible with commercial applications, as current commercially available functional nanoparticles are typically available for research and development applications in 1 – 10 mg vials at considerable expense (http://www.sigmaaldrich.com/materials-science/material-science products.html?TablePage=16377718).

5.4 Conclusion

This Chapter demonstrated that the surface deposition of PAC coatings, reported in Chapters 3 and 4, occurs simultaneously with the formation of plasma dust particles. The formation of dust particles by plasma bulk polymerization was first hypothesised by observing instabilities in the discharge under a specific range of process parameters. The instabilities, in the form of long-time scale oscillations observed by OES diagnostics, are driven by the formation of plasma dust nanoparticles (nanoP^3) in three main phases: protoparticle formation, rapid aggregation and nanoP^3 removal. The overall plasma emission increased significantly during phases 1 and 2, driven by an increase in the electron temperature, and followed then by a decrease in intensity as nanoP^3 are removed from the active plasma. Interestingly, the emission intensity of CN radicals, proportional to their number density in the plasma, was found to decrease significantly during the rapid aggregation phase, suggesting that nanoP^3 growth and formation is supported by these activated radical species.

A method for passive, high yield collection of nanoP^3 was also proposed. This method uses a collector device that allows the positive plasma potential to infiltrate inside a well. The negatively charged dust particles, dragged by the gravity, neutral and ion drag forces are entrapped inside the collector and eventually deposited on the bottom of the wells. It was shown that nanoP^3 aggregation is controlled by the height of the wells and the mass yield can be maximised for high-throughput and low-cost synthesis. The synthesis process was highly reproducible and easily modulated by the plasma parameters. A transition between bulk and surface polymerization was also identified by adopting a suitable macroscopic description, which could be easily adopted for process optimization in upscaling scenarios.

The synthesis of multifunctional nanoparticles in a plasma/gas phase could offer a series of benefits over traditional multi-step wet-chemistry approaches. nanoP^3 is synthesised under the same plasma environment using the same reactive building blocks as PAC. Therefore, the possibility that nanoP^3 also features the same universal binding surface as PAC, suggests that these particles could pave the way for the design of personalized nanocarriers, allowing the end user to obtain theranostic agents in a one-step incubation and according to immediate needs. As many of the favourable characteristics of nanoP^3 are inherent to the fabrication process, PP could be adopted as a nanoparticle synthesis route with great potential for broad clinical and commercial applications. This hypothesis is assessed in the Chapter 6.

6 ENGINEERING NANOP^3 AS MULTIFUNCTIONAL NANOCARRIERS

The literature review and results presented throughout this chapter is published and / or will be submitted for publication in:

Nanoparticles, **Miguel Santos**, Praveesuda L. Michael, Elysse C. Filipe, Marcela M. M. Bilek and Steven G. Wise, Australian Patent Application No. 2016905306 (21 December 2016)

Miguel Santos, Praveesuda L. Michael, Elysse C. Filipe, Alex H.P. Chan, Juichien Hung, Richard P. Tan, Bob S.L. Lee, Minh Huynh, Clare Hawkins, Anna Waterhouse, Marcela M. M. Bilek and Steven G. Wise, *Plasma synthesis of carbon-based nanocarriers for linker-free immobilization of bioactive cargo*, under review at ACS Applied Nanomaterials (2017)

Miguel Santos, Praveesuda L. Michael, Elysse C. Filipe, Alex H.P. Chan, Juichien Hung, Marcela M. M. Bilek and Steven G. Wise, *Plasma polymerization of nanoparticles in dusty plasmas for applications in nanomedicine*, under preparation for submission to Scientific Reports

Miguel Santos, Praveesuda L. Michael, Marcela M. M. Bilek and Steven G. Wise, *Fluorescent properties of plasma polymerized amorphous carbon nanoparticles*, under preparation for submission to Scientific Reports

6.1 INTRODUCTION

Over the last decade, the number of nanoparticle platforms proposed for customized nanomedicine has vastly increased [43, 44]. Nanocarriers have been designed to address a great number of clinical conditions using cocktails of drugs, nucleic acids, photosensitive dyes and diagnostic agents [45, 48, 49]. These platforms aim to control the biodistribution, enhance the efficacy, or otherwise reduce toxicity of biologics or drugs by improving solubility, half-life, or delivery [44]. Clinically available nanoparticle systems, are commonly polymeric, liposomal, and nanocrystal formulations which have largely failed to meet expectations for efficacy improvements [247]. Other commonly used platforms in development including gold, silver, iron oxide, silica and carbon-based nanoparticles share issues of cytotoxicity (limiting dose concentrations), sub-optimal cell penetration, and the requirement for complex chemical functionalization schemes to address these issues. In vivo, targeting has been uniformly poor, best exemplified for drug-delivery to tumours, where platform type, size, and charge each failed to influence the low rates of delivery [248]. As such, there is a trend towards the development of more complex, multi-functional materials, adding increased surface functionality to improve homing, imaging or delivery of drugs. With current platforms, this adds significant complexity and cost, greatly limiting the feasibility of this approach [52].

Commonly proposed nanocarriers utilize materials that are hydrophobic, bio-inactive and insoluble and thereby do not allow a direct and robust conjugation with biomolecular cargo. Functionalization strategies with chemical cross-linkers have been widely exploited to impart

surface functionalities on various nanoparticle materials such as gold, metal-oxides, ceramics, polymer nanoparticles and semiconductor quantum dots [50, 51, 249, 250]. Alternative conjugation strategies involve the pre-conjugation of molecules with the nanoparticle material during self-assembly [251]. Other approaches utilize mesoporous polymeric materials with large surface to volume ratios, which electrostatically entrap high loads of molecular cargo [55] that can be released in targeted cells upon photo-chemical stimulation [252]. However, common to all wet-chemistry approaches is the requirement for time-consuming, multi-step protocols to achieve a robust conjugation between the nanocarrier surface and the molecular cargo.

Moreover, optimization, reproducibility and control over a suitable concentration and thickness of surface coatings with functional linkers is difficult to achieve. Typically, the terminal groups of the linkers also limit the range of biomolecules that can be immobilized [51]. Such synthesis approaches rely on solvents and multiple purification steps that compromise the native conformation and functionality of the molecular cargos and present safety or disposal difficulties. The use of solvents during synthesis also requires a phase transfer to aqueous solution for biomedical applications, adding additional processing steps, such as ligand exchange and modification to stabilize and disperse the nanoparticles in solution [50]. Despite the recent rapid growth of nanomedicine research, the need for scalable nanofabrication strategies that can deliver novel products with improved performance, functionality and safety remains. Ideally, the rational design of nanoparticles should address multiple functionalization using simple approaches [45] such as direct incubation with biomolecule solutions.

Amongst carbon-based nanoparticles, nanodiamonds [253] and carbon quantum dots [254] are preferred in theranostics for their low cytotoxicity and imaging capabilities. However, while the scalable synthesis of these forms of carbon remains a challenge, post-synthesis purification can represent up to 40% of all production costs [253]. Moreover, off-the-shelf carbon-based nanoparticles also require extensive surface modification with stabilizers and functional groups for binding of molecular cargo. To address the limitations of current approaches, we have developed a novel methodology based on plasma polymerization (PP) in carbonaceous dusty plasmas. As described in the previous chapter, dusty plasmas are suspensions of solid particles immersed in ionized gases [91]. They are ubiquitous in space [92, 93] and regarded as a source of contamination in plasma-assisted manufacturing [94] and fusion devices [96]. While these impurities have been well studied and their dynamics in the plasma characterized [101, 105, 236], their potential application in theranostics has been overlooked.

This Chapter proposes for the first time that dusty plasmas can be tailored to produce multifunctional plasma polymerized nanoparticles (nanoP^3) with unique immobilization capability. It shows that PP can be operated in a suitable parameter window to synthesize nanoP^3 in a controlled fashion. By identifying relevant nanoparticle growth mechanisms, it is further demonstrated that significant features of nanoP^3, such as yield, size, aggregation, fluorescence, surface topography, chemistry and charge can be tailored and reproducibly attained. It is found that nanoP^3 retain many of the favourable surface characteristics previously reported for hydrophilic and biocompatible thin film coatings [4]. Longed-lived

radicals and functional moieties are formed and preserved within the nanoP^3 structure, enabling a simple one-step surface immobilization of bioactive cargo with wide ranges of molecular weights and chemical structures. It is also demonstrated the broad-range binding ability of nanoP^3 by simply incubating biomolecules such as drugs, fluorescent dyes, enzymes, ribonucleic acids and antibodies in aqueous solutions with the nanoparticles. nanoP^3 is readily up-taken by multiple cell lines without the need for permeabilization with negligible effect on cell proliferation and morphology.

6.2 Materials and Methods

6.2.1 NanoP^3 synthesis

NanoP^3 were synthesized and collected as previously described in section 5.2.1. Here, the acetylene, nitrogen and argon flow rates were set at 2, 10 and 3 sccm the coupled power to 50, 75 or 100 W and discharge pressure to 150 mTorr unless otherwise specified. nanoP^3 collection was carried out in tissue culture 24-well plates.

6.2.2 Scanning and transmission electron microscopy

SEM was performed with a Zeiss ULTRA Plus or a Zeiss Sigma HD FEG scanning electron microscope at acceleration voltages in the range 3 – 10 kV and a working distance between 3 and 12 mm. For TEM imaging, nanoP^3 were collected on a 300-mesh grid with an ultrathin carbon film supported by a lacey carbon film (ProSciTech) placed inside the collector vials. Sample imaging was carried out in a JEOL 2100 at an acceleration tension of 120 kV. For tomography, tilt series (±60˚) were acquired around a single axis using a 1˚ sampling

increment. Tomography alignment and reconstruction was calculated using the Composer tomography package. Segmentation and rendering were created using Avizo 9.0.

6.2.3 Laser-light scattering

Laser-light scattering was carried out for hydrodynamic size, concentration and zeta potential measurements. The hydrodynamic size distribution and concentration of nanoP^3 in RT-PCR Grade water were measured in a NanoSight NS300 laser light scattering system. For each measurement, samples were introduced into the analysis chamber and allowed to flow at a constant flow rate and temperature (24˚ C). The trajectories of nanoP^3 in the chamber were visualized and tracked using a nanoparticle tracking and analysis system (NanoSight NTA 3.0). Data for each set of samples resulted from the continuous tracking (60 second periods) of the nanoP^3 trajectories and subsequent statistical analysis of five independent measurements. The zeta potential of nanoP^3 was measured within a pH range of 2 – 10 in disposable folded capillary cells (Malvern, DTS1070) using a Zetasizer Nano ZS (Malvern Instruments, Germany). Each sample was measured at a constant temperature of 24˚ C and the zeta potential was obtained from the average of three independent series of 11 measurements each. The quality of the measurements was monitored in real time and the data was analyzed using standard procedures with the software provided by the manufacturer.

6.2.4 Electron spin resonance spectroscopy

The detection of unpaired electrons in nanoP^3 was carried out by means of ESR spectroscopy using a Bruker EMXplus X-band spectrometer. nanoP^3 were suspended from the collector vials in RT-PCR Grade water and transferred to quartz glass Suprasil flat cells with a sample

volume capacity of 150 µL. Spectra were collected with a center field of 349 mT, sampling time of 90 ms, modulation amplitude of 3 G, modulation frequency of 105 Hz and microwave frequency and power of 9.8 GHz and 25 mW respectively.

6.2.5 Fluorescence measurements

A Clariostar® microplate reader was used to measure the fluorescence emission/excitation spectra of both dry (as synthesized) and resuspended (PCR grade water) nanoP^3. The fluorescence distribution of as synthesized dry nanoP^3 in the tissue culture plates was measured by scanning each well in mapping mode. A 30 x 30 matrix was used, resulting in a 900 point/well resolution. The excitation and emission monochromators were set to 360 and 430 nm respectively, gain to 2200 and the focal weight to 9 mm. The fluorescent properties of a concentrated solution of nanoP^3 (10^{10} particles/ml) were also studied. Following resuspension of nanoP^3 in PCR grade water, the solution was transferred to a tissue culture 96-well plate and emission spectra were acquired as a function of the excitation wavelength.

6.2.6 Conjugation of nanoP^3 to various molecular cargo

Goat anti-Rat IgG-Alexa647 (abcam, ab150159 from 0.5 to 3.5 µg/mL), Goat anti-Rabbit IgG-750 (abcam, ab175733 0.5 to 3.5 µg/mL), Goat anti-Rabbit-IgG-40 nm Gold (abcam, ab119180 at 2.5 µg/mL), Goat anti-Mouse-IgG-20 nm Gold (abcam, ab27242 at 2.5 µg/mL), Goat anti-Rat-IgG-10 nm Gold (abcam, ab41512 at 2.5 µg/mL), 2,2-diphenyl-1-picrylhydrazyl (DPPH, Sigma Aldrich, from 0.5 to 10 µg/mL), Cardiogreen (Sigma Aldrich, from 0.5 to 10 µg/mL) and/or Paclitaxel-Oregon Green 488 (Invitrogen, P22310 from 0.5 to 3.5 µg/mL) were conjugated to nanoP^3 (10^9 nanoparticles/mL) in RT-PCR Grade water by

simple incubation at 4°C for 1 hour, unless specified otherwise. Highly charged Cy5 labelled peptide sequences (CY5 – CPKKKRKV – NH2, Mimotopes at 2.5 µg/mL) were conjugated to nanoP^3 (10^9 nanoparticles/mL) at pH 2, 7.4 and 10 (pH was adjusted in RT-PCR Grade water with HCl or NaOH). For all of the above molecules, the unbound cargo was washed three times with centrifugation at 16100 G for 5 minutes per wash. All washes were collected for absorbance and/or fluorescence measurements in order to calculate the amount of cargo bound to nanoP^3.

6.2.7 Quantification of molecular cargo bound to nanoP^3

The amount of molecular cargo bound to nanoP^3 following incubation was calculated using absorbance and/or fluorescence measurements of the nanoP^3 – cargo samples and their corresponding washes (cargo = 2,2-diphenyl-1-picrylhydrazyl, cardiogreen, Paclitaxel-Oregon Green 488, CY5 – CPKKKRKV – NH2 and Goat anti-Rat IgG-Alexa647). To calculate the number of cargo molecules bound to each nanoP^3 we first measured the absorbance/fluorescence of the remaining unbound cargo in the washes and interpolated the data to previously measured standard curves of the corresponding free molecular cargo. We then measured the absorbance/fluorescence of the nanoP^3 – cargo samples and subtracted the nanoP^3 background signal to confirm that the sum of the signals of unbound cargo and cargo bound to nanoP^3 matched the total amount of cargo initially added. Absorbance measurements were carried out via UV-VIS spectroscopy in a SHIMADZU UV-2550 spectrophotometer using disposable cuvettes and analyzed using UV Probe 2.33 software. The fluorescence intensity of samples and washes was measured using CLARIOstar microplate reader.

6.2.8 Conjugation and activity of Luciferase to nanoP^3

Luciferase from *Photinus pyralis* (Abcam, L9506, from 0.5 to 10 µg/mL) was conjugated to nanoP^3 (10^9 nanoparticles/mL) in RT-PCR Grade water also by simple incubation at 4°C for 1 hour. Conjugation of Luciferase to 200nm Polystyrene (ThermoFisher Scientific; R200) and 200nm gold nanoparticles (Cytodiagnostics; G-150) were performed in an identical fashion. After incubation, samples were washed 3 times with centrifugation at 16100 G, 5 mins per wash, whilst the controls were washed 3 times as per manufacturer's recommendations. All wash supernatants were collected for detection and analysis of luminescence. After incubation and wash, we added D-Luciferin (Sigma-Aldrich; A1888) containing 70 mM ATP-Mg^{2+} to all samples and washes. The luminescence and luciferase activity was detected via an IVIS system (IVIS Lumina LT, PerkinElmer) using an exposure time of 60 s.

6.2.9 Serial block face SEM sample preparation, mounting and imaging

Human Coronary Artery Endothelial cells (hCAEC, passage 4-6, Cell Applications, 300-05a) were seeded at a cell density of 10000 cells/cm^2 on circular glass cover-slips. Four hours after cell-seeding, 2.5 x 10^8 nanoparticles/mL in Human MesoEndo Endothelial growth media (Sigma-Aldrich, 811D) were added and left to incubate for 24 hours at 37°C in a 5% CO^2 incubator. An equivalent volume of DMEM-serum free media without nanoparticles were added to control samples.

Samples were prepared for serial block face SEM (SBF SEM) using a modification of the protocol previously described [255]. Samples were washed with warm PBS twice and fixed with 2.5% glutaraldehyde (ProSciTech, C001) and 2% formaldehyde (ProSciTech, C004) in 0.1M phosphate buffer pH 7.4 for 1 hr at room temperature. Samples were then washed with

0.1M phosphate buffer pH 7.4 (3 x 5 min), before post-fixation in a reduced osmium solution containing 2% osmium tetroxide (ProSciTech, C010) and 1.5% potassium ferrocyanide (Univar, 74037) in 0.1M phosphate buffer pH 7.4 for 1 hour at room temperature. Cells were subsequently washed with milliQ water (3 x 5 min) before incubating with freshly prepared and filtered 1% aqueous thiocarbohydrazide (ProSciTech, C076) for 20 minutes at room temperature. A second osmium step was applied to the samples, 2% aqueous osmium tetroxide for 30 minutes at room temperature after washing with milliQ water (3 x 5 min). Samples were then incubated in filtered 1% aqueous uranyl acetate overnight, protected from light at 4^{o}C. The following day, cells were washed in milliQ water (3 x 5 min) before incubating in freshly prepared 0.66% Walton's lead aspartate solution for 30 minutes at 60^{o}C. Cells were subsequently dehydrated using a graded ethanol series of 30, 50 and 70% (2 x 5 min each) followed by 90 and 100% ethanol (2 x 10 min each). Cells underwent a series of graded hard grade Procure 812 resin (ProSciTech, C038) in ethanol infiltration steps: 25% for 3 hours, 50% overnight, 75% for 4 hours, 100% resin overnight (twice) and finally embedded in 100% resin using BEEM capsules (ProSciTech, RB001) and allowed to polymerize at 60^{o}C for at least 48 hours. Once the resin had polymerized, samples were trimmed down to approximately 1 mm^{3} and super glued onto a 3view specimen aluminum pin (Gatan, PEP6590). The block face was sputter coated with a 10 nm layer of gold and silver, painted on all exposed side edges to enhance conductivity. Images were acquired using a variable pressure, field emission scanning electron microscope (Sigma VP, Carl Zeiss) equipped with a Gatan 3View 2XP. Backscattered electron images were collected at a fixed working distance of 4.4 mm using the following imaging parameters: 2.8 kV, 28 Pa, 30 μm aperture, 6000 x

12000 pixels, XY pixel size 6 nm, Z pixel size (slice thickness) 50 nm and pixel dwell time 1 µs.

6.2.10 Lysosome staining protocol

Human Coronary Artery Endothelial cells (hCAEC, passage 4-6, Cell Applications, 300-05a) were seeded at a cell density of 10000 cells/cm^2 on a Lab-Tek glass chamber slide (Lab-Tek, 154534). Four hours after cell seeding, 2.5x10^8 nanoP^3 were added into each well at different time points (1, 2, 4, 5, and 24 hours). At each time point, cells were stained with Lysotracker® Deep Red (ThermoFisher Scientific, L12492) according to the manufacturer's instructions at a working concentration of 75 nM for 1 hour. The cells were then fixed with 3.7% paraformaldehyde for 10 minutes and washed 3 times with PBS prior to DAPI staining. After cover-slipping, images were taken within 24 hours using a fluorescent microscope.

6.2.11 Imaging of fluorescently labelled nanoP^3 in cells

hCAEC (human Coronary Artery Endothelial Cells, Cell Applications), MCF10A (Human Mammary Epithelial Cell line) and MCF7 cells (Cancerous Human Mammary Epithelial Cell line, Sigma-Aldrich) were seeded at a density of 10000 cells/cm^2 on Lab-Tek glass chamber slides (Lab-Tek, 154534). Four hours after cell-seeding, antibody and paclitaxel conjugated nanoP^3 were incubated with cells for 24 hours. The cells were then fixed with 3.7% paraformaldehyde for 10 minutes at room temperature and washed 3 times with PBS prior to F-actin and DAPI staining of cells. For F-actin staining, cells were permeabilized with 0.01% triton-X 100 (Sigma-Aldrich, Cat) in PBS for 5 minutes. The samples were then washed 3 times in PBS, followed by incubation with Actin Red 555 ReadyProbes reagent (Life technology, R37112) for 15 minutes, as per manufacturer recommendations. The samples

were then washed 3 times in PBS. For DAPI staining of cell nuclei, cells were incubated with 1:1000 DAPI (SAPBIO, Cat) in PBS for 5 minutes at room temperature. The samples were washed 3 times in PBS prior to mounting with an aqueous fluorescent-shield mounting medium (Dako, S3023). After cover-slipping, images were taken within 24 hours using a fluorescent microscope (Zeiss Z2).

6.2.12 Cell proliferation assay

NanoP^3 cytotoxicity was evaluated for 3 different cell types: 1) human Coronary Artery Endothelial Cells (hCAEC, passage 4, Cell Applications, 300-05a); 2) Human Mammary Epithelial Cell line (MCF10A, passage 20), and; 3) Cancerous Human Mammary Epithelial Cell line (MCF7, passage 15, Sigma-Aldrich, 86012803). Cells were trypsinized and 5000 cells/cm^2 were seeded in a flat-bottomed 24-well culture plate and incubated at 37°C in a 5% CO^2 incubator. Four hours after cell seeding, serial dilutions of nanoP^3 (from 10^2 nanoparticles/well to 10^9 nanoparticles/well), were re-suspended in DMEM serum-free media, and then added into each well. After 3 and 5 days of incubation, the cell viability was evaluated using alamarBlue (Life Technologies, DAL1100). The alamarBlue reagent was added to each well as per manufacturer's recommendations and incubated for 2 hours (for hCAEC and MCF10A), and 3 hours (for MCF7). The resorufin dye catalyzed by viable cells was quantified by measuring the fluorescence at Ex/Em 530-560/590 nm on a Clariostar microplate reader. Untreated cells (DMEM serum-free media without nanoP^3) and cells treated with doxorubicin (500nM, Sigma-Aldrich, 44583) were used as controls.

6.2.13 Statistical analysis

Data are expressed as mean ± s.d. Data were analyzed using one-way ANOVA analysis of variance (Tukey's multiple comparison groups). P-Value < 0.05 were considered significant.

6.3 RESULTS AND DISCUSSION

6.3.1 Process Control of nanoP^3 properties

6.3.1.1 Aggregation

Nanoparticle stability in solution is a fundamental requisite for their use as theranostic agents. Nanoparticle aggregation significantly reduces available surface area, compromising cargo loading and efficiency, in-vivo pharmokinetics and biodistribution. In section 5.3.2, the aggregation of as synthesised nanoP^3 was significantly reduced upon collection by selecting a collector with reduced well height. As shown in Figure 6.1, the aggregation of collected nanoP^3 was further controlled by the discharge pressure, which was adjusted by tuning the pumping speed to maintain total gas flow rate constant throughout the set of experiments shown in this work. The formation of elongated aggregates was observed at discharge pressures of 70 and 100 mTorr. The size of the aggregates decreased substantially with increasing pressure, with only minimal aggregation observed at 150 mTorr. Particle aggregation was absent at 200 mTorr but the yield was significantly reduced, a result compatible with the decrease in the cycle period observed previously in Figure 5.18. The choice of the optimal discharge pressure used for nanoP^3 synthesis within the set of process parameters explored in this work was based on the balance between low aggregation and high

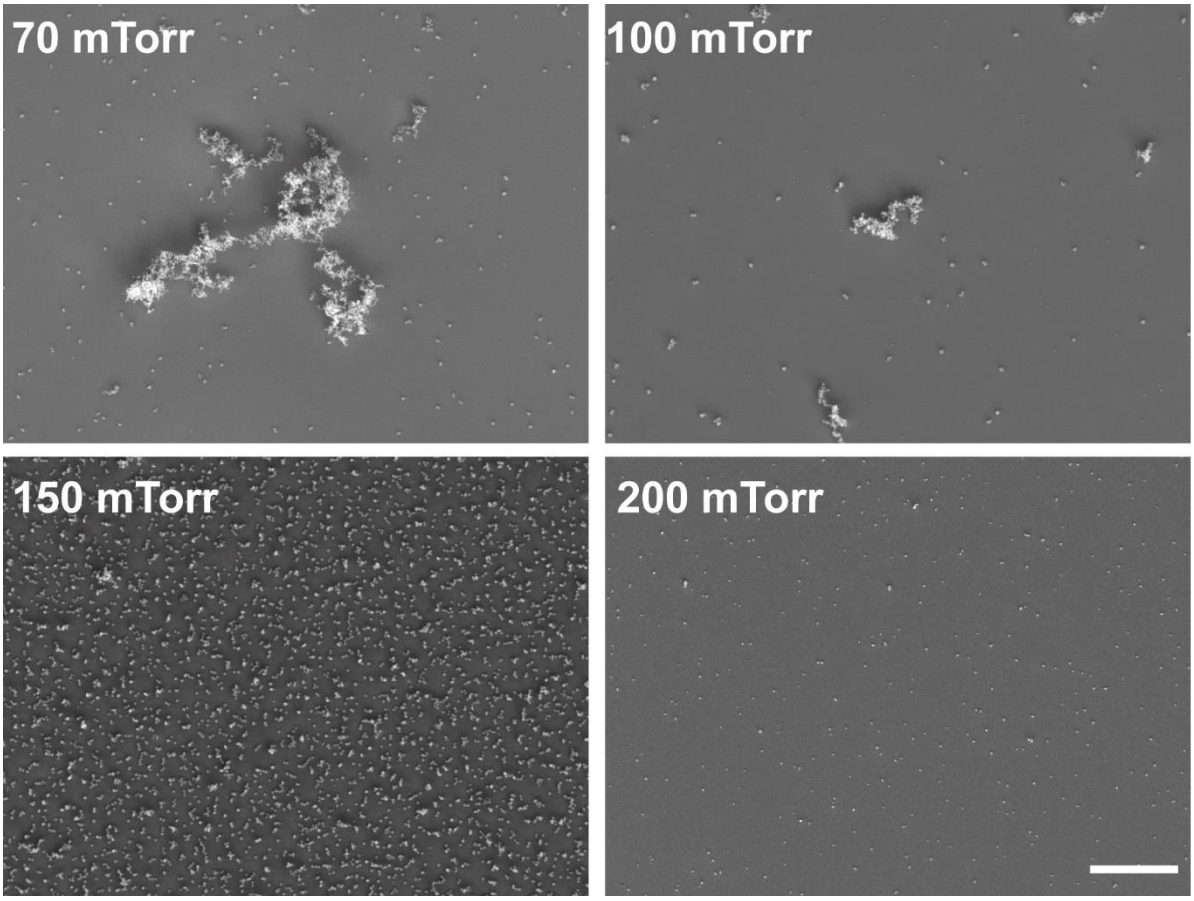

Figure 6.1. Representative secondary electron images (SEM) of nanoP^3 synthesised at various discharge pressures over one oscillation cycle at 50 W and acetylene flow rate of 3sccm. The collection time for each condition was 98 s (70 mTorr), 90 s (100 mTorr), 76 s (70 mTorr) and 69 s (200 mTorr). Elongated aggregates up to 6 µm in length were observed at 70 and 100 mTorr but were minimal at 150 mTorr and absent at 200 mTorr. The scale bar is 10µm.

particle yield. Henceforth, all nanoP^3 formulations shown in this section were synthesised with a discharge pressure of 150 mTorr.

6.3.1.2 Surface morphology and structure

The morphological features of nanoP^3, including their shape, size and surface topography, were ultimately dependent on the acetylene flow rate $Q_{acetylene}$, as shown in representative high-resolution secondary electron images in Figure 6.2. Results suggest that the flow rate determines the size of the of the initially formed PCN (or protoparticles). Increasing the flow rate increased the downstream gas and ionic drag forces, dragging PCN out of the plasma faster and suppressing their further growth and coalescence. The total flow rate, hence the residence time of the PCN in the plasma, consequently determines the resulting surface topography of nanoP^3. For instance, at $Q_{acetylene}$ = 0.5 sccm, the PCN formed in phase 1 were typically 50 – 70 nm across and their assembly in phase 2 (see section 5.3.4) formed irregularly-shaped, loosen nanoP^3 clusters (typically 350 nm across). Spherical and highly compacted nanoP^3 particles were obtained, however, through rapid aggregation of PCN smaller than 20 nm at $Q_{acetylene} \geq$ 1sccm. The formation of monodisperse populations of nanoP^3 (as suggested in Figures 5.11, 6.1 and later quantified in section 6.3.1.4) suggests that the assembly of PCN during phase 2 is thermodynamically controlled [256]. Further nanoP^3 growth and aggregation is also prevented by the build-up of a negative net charge due to electron diffusion towards the surface of the particles in the active plasma. High-resolution transmission electron microscopy (Figure 6.3) showed that the bulk structure

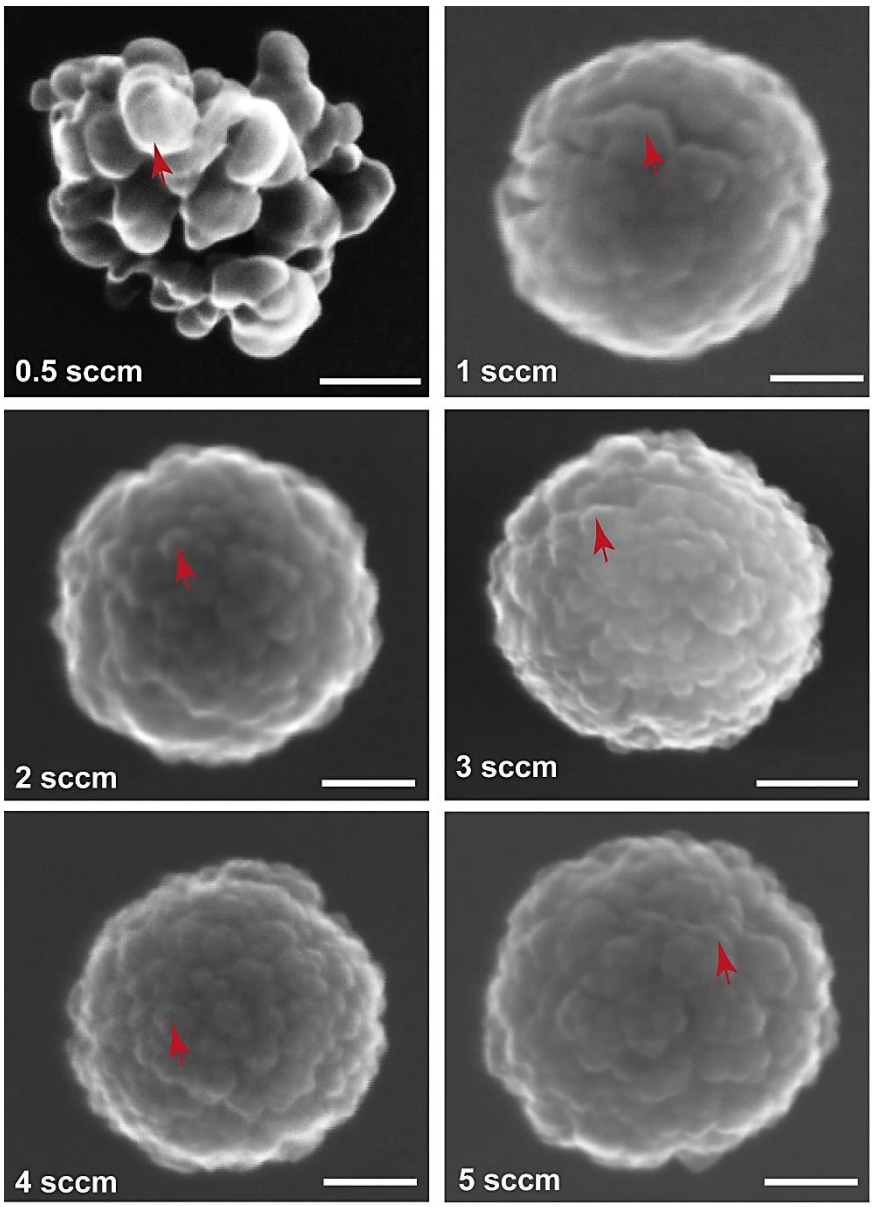

Figure 6.2. Representative high magnification SEM images of nanoP^3 synthesised at various acetylene flow rates and at a discharge pressure of 150 mTorr and coupled power of 50 W over one oscillation cycle. The topography of nanoP^3 was modulated by the size of PCN initial clusters (red arrows). Overall, the PCN decreased in size with increasing flow rate, assembling into spherical shaped and compacted nanoP^3 particles. The scale bars are (0.5 sccm) 100 nm, (1 and 3 sccm) 80 nm, (2 sccm) 90 nm and (4 and 5 sccm) 60 nm.

of nanoP^3 formed at $Q_{acetylene} \geq 1$sccm was amorphous throughout, typical of plasma polymer materials. No experimental evidence was found suggesting that PCN were crystalline in nature, contrarily to what was previously reported for small (~10 nm) dust particulates formed in silane and acetylene plasmas [95].

Static SEM and TEM images only provide a two-dimensional (2D) representation of samples, limiting visualization and analysis. Here, electron tomography was carried out to fully reveal the whole structure and morphology of nanoP^3. Electron tomography is an advanced imaging technique that makes use of a tilting sample stage which allows the capture of electron transmission images of samples from different angles (typically between -60˚ to +60 ˚). The series of tilted 2D images can be computationally aligned and reconstructed into a z-stack of images to form a three-dimensional (3D) tomogram. The resulting tomogram can be then processed by specialized processing and 3D visualization software to produce segmentation and high detailed volume and isosurface rendering of samples.

For TEM tomography, nanoP^3 were synthesized at 3scccm and 50 W in a single oscillation cycle (120 s) and were collected into a TEM copper 300 mesh grid placed on the well bottom of a 24-well tissue culture plate. An ultrathin grid carbon film (3nm thick) was chosen to maximize electron contrast between the carbon nanoP^3 matrix and the grid supporting film. Representative TEM images of nanoP^3 taken at various tilting angles of the stage are shown in Figure 6.4a (the sample stage was tilted between -66˚ and +67˚ - see full image sequence in Movie 1). Image alignment and reconstruction resulted in an electron tomogram (Figure 6.4b) comprised of a total of 900 high-resolution images of a

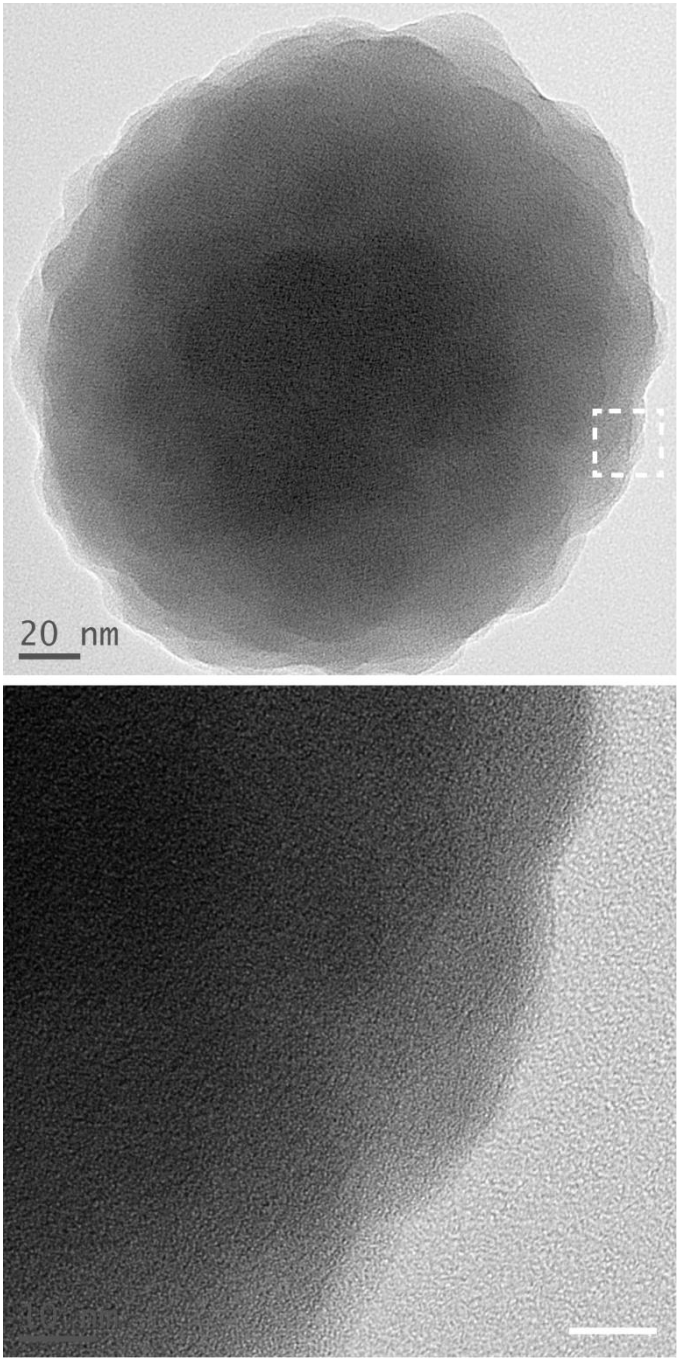

Figure 6.3. Representative high-resolution transmission electron microscopy (HR-TEM) images of nanoP^3 synthesised at 50 W, 3sccm and 150 mTorr. The scale bars are (top) 20 nm and (bottom) 10 nm.

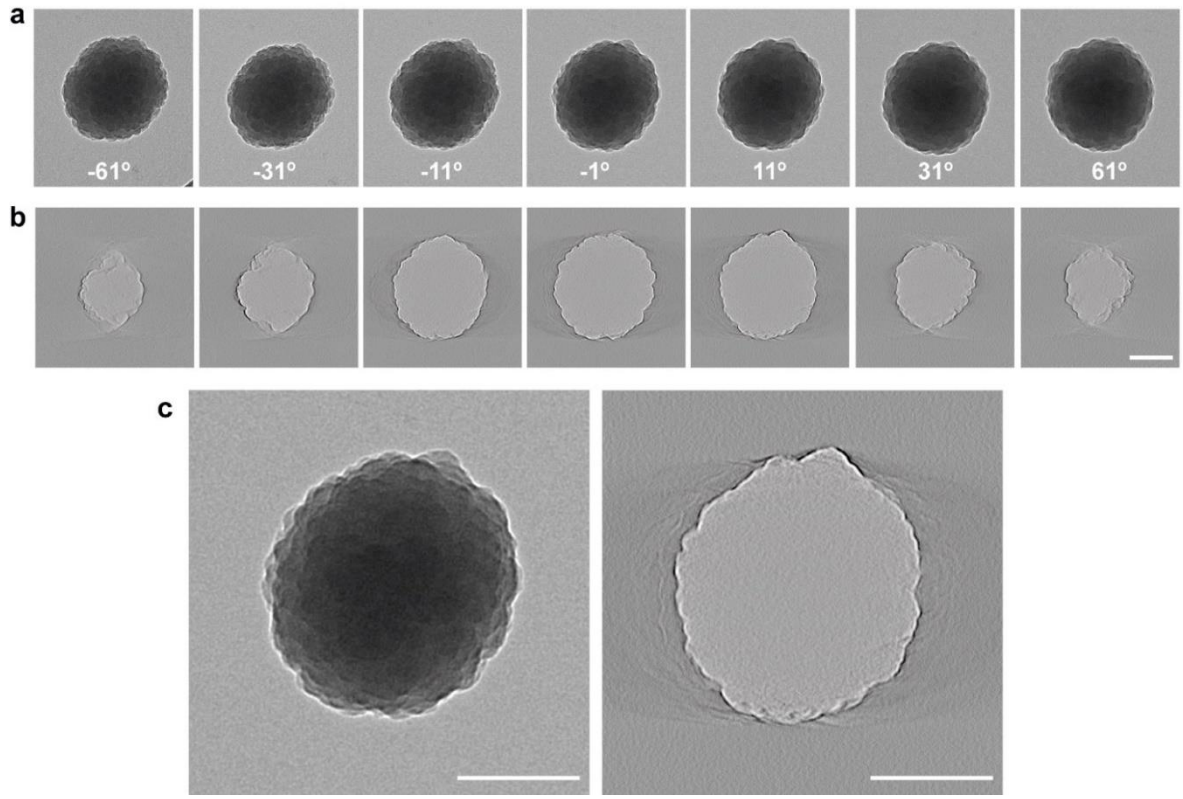

Figure 6.4. a) Representative HR-TEM images of as synthesised nanoP^3 (50 W, 3 sccm and 150 mTorr) acquired at different stage tilting angles. b) Various z-stack images from the resulting electron tomogram obtained by alignment and computer reconstruction of the 2D HR-TEM images. c) Representative images comparing the original HR-TEM image and reconstructed tomogram. Results show that nanoP^3 is formed by the aggregation of amorphous PCN (protoparticles) that assemble to form a compacted spherical structure. The scale bars are 100 nm.

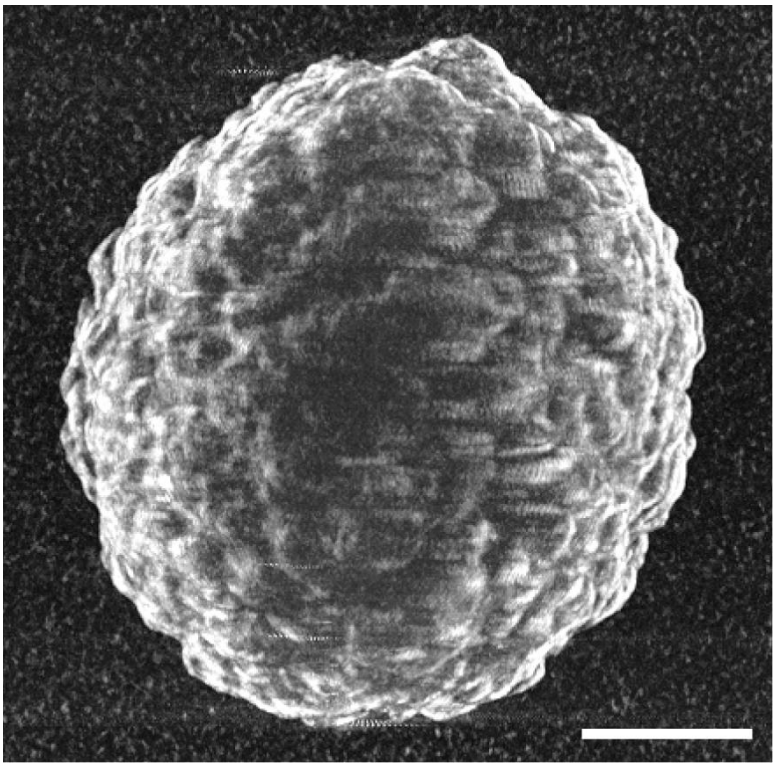

Figure 6.5. Volume rendering of nanoP^3 obtained from the electron tomogram shown in Figure 6.4. Scale bar is 100 nm.

single 200 nm diameter nanoP^3 particle, resulting in a "z-stack" image resolution of 0.29 nm (Movie S2). The electron tomogram and simulated volume rendering (Figure 6.5), are consistent with preliminary SEM observations, showing that nanoP^3 synthesized at $Q_{acetylene}$ ≥ 1sccm feature a highly compacted, solid and amorphous structure. The rapid aggregation of PCN during phase 2, and their subsequent (radical-mediated) binding, fuses the protoparticles into an assembled spherical structure. The diffusion of plasma activated radical species towards the growing particles during the aggregation phase (see Figure 5.13) further fuses the PCN, rendering a compacted nanoP^3 structure.

6.3.1.3 Chemical composition

To study the chemical composition of nanoP^3 x-ray photoelectron spectroscopy (XPS) and Fourier transform infrared spectroscopy (FTIR) were carried out. Typical XPS and FTIR survey spectra of nanoP^3 are shown in Figure 6.6 and 6.7a. FTIR spectra feature two main absorption bands located between 3680 cm^{-1} to 2450 cm^{-1} and 1770 cm^{-1} to 1050 cm^{-1} and a smaller absorbance peak attributed to stretching vibrations of nitrile groups located at ~2160 cm^{-1}. Since the two main broad bands arise from the overlap of several stretching and bending vibrations, such as C=O, C=C, C=N, NH or CH, it is not possible to precisely separate and quantify the different components due to their proximity in the spectrum. To simplify and clarify spectral analysis, the spectrum of nanoP^3 that did not contain nitrogen was also acquired by synthesizing nanoparticles in nitrogen-free C_2H_2/Ar plasmas. The infrared spectrum of this nanoP^3 formulation was mainly characterized by: (i) a strong absorption band assigned to stretching vibrations of OH (3490 cm^{-1}) and CH (2957 cm^{-1}, 2934 cm^{-1} and 2876

cm^{-1}) bonds, (ii) a broader absorption band resulting from the convolution of C=O (1705 cm^{-1}) and C=C (1631 cm^{-1}) bonds and (iii) bending vibrations of C-H bonds (1454 cm^{-1} and 1377 cm^{-1}). The incorporation of nitrogen in nanoP^3 by synthesis in C_2H_2 /Ar / N_2 plasmas was confirmed by a significant broadening of the absorption bands and occurrence of new additional peaks. New bands were observed due to stretching vibrations of NH (3340 cm^{-1} and 3340 cm^{-1}) and C≡N (2180 cm^{-1}) bonds. A significantly broader band was found at lower wavelengths, arising from the convolution of stretching vibrations of C=O (1705 cm^{-1}), C=C (1630 cm^{-1}), C=N (1578 cm^{-1}), N-O (1340 cm^{-1}), C-N (1250 cm^{-1}) and C-O (1200 cm^{-1} - 1000 cm^{-1}) as well as bending vibrations of N-H (1550 cm^{-1}) and C-H (1454 cm^{-1} and 1377 cm^{-1})). The detection of CN and NH bonds in the FTIR spectra demonstrates that the addition of non-polymerizable molecular gases (such as nitrogen) in the synthesis process provides means to straightforwardly modulate the chemical composition and surface properties of nanoP^3. The CO, OH and NO bonds were formed only upon exposure of nanoP^3 to the atmosphere, potentially driven by reaction of atmospheric oxygen with radicals formed in the plasma polymerization process.

Deconvolution of high resolution XPS C1s core-shell (Figure 6.7b) shows four components with peak positions at 284.86 eV (C_1), 286.33 eV (C_2), 287.77 eV (C_3) and 289.39 eV (C_4). These contributions were assigned to pure carbon hybridization as well as C-H bonds (C_1), sp^2 and / or sp^3 C-N hybridizations (C_2 and C_3) and COO compounds (C_4). The high resolution XPS N1s core-shell was also deconvoluted into four components located at 398.04 eV (N_1), 399.21 eV (N_2), 400.41 eV (N_3) and 402.03 eV (N_4). The first component is assigned to two-fold coordinated nitrogen atoms bonded to carbon atoms or sp^3 nitrogen atoms bonded to sp^3-

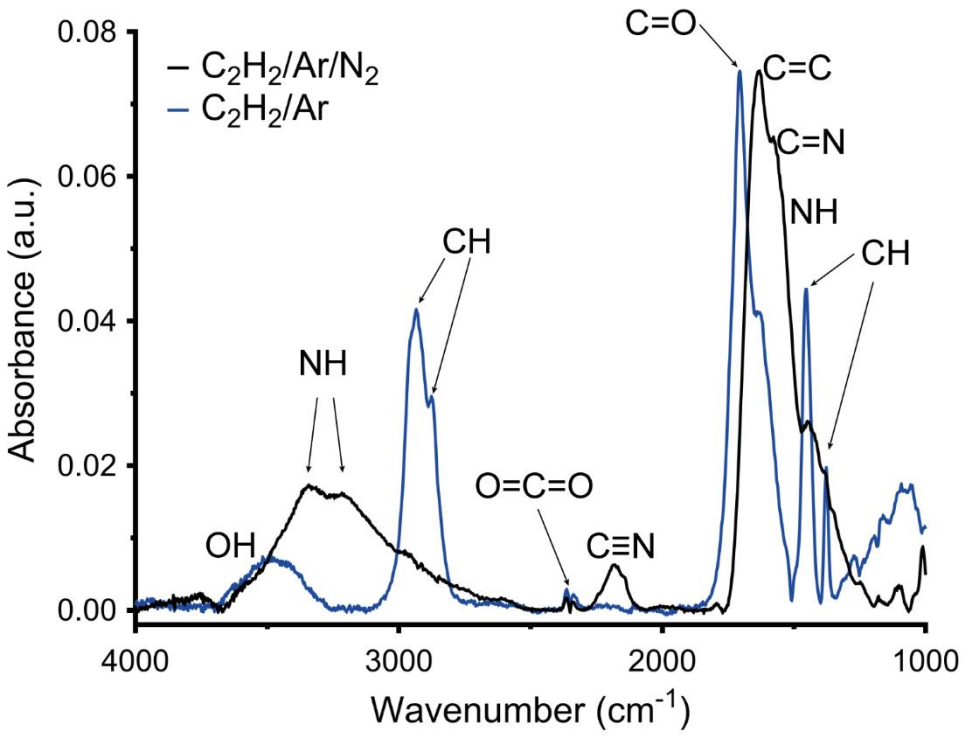

Figure 6.6. Comparison of the FTIR spectra of nanoP^3 nanoparticles formed in C_2H_2/Ar (blue line) and C_2H_2/Ar/N_2 (black line) plasma discharges. The synthesis parameters were set at 50 W, 150 mTorr for both sample sets and the flow rates to 3, 10 and 3 sccm and 3, 0 and 13 sccm for acetylene, nitrogen and argon for nanoP^3 made with C_2H_2/Ar/N_2 and C_2H_2/Ar respectively. Amines and carboxyl surface moieties are incorporated in nanoP^3 simply by adding N_2 in the gaseous mixture and by exposing nanoP^3 to air respectively

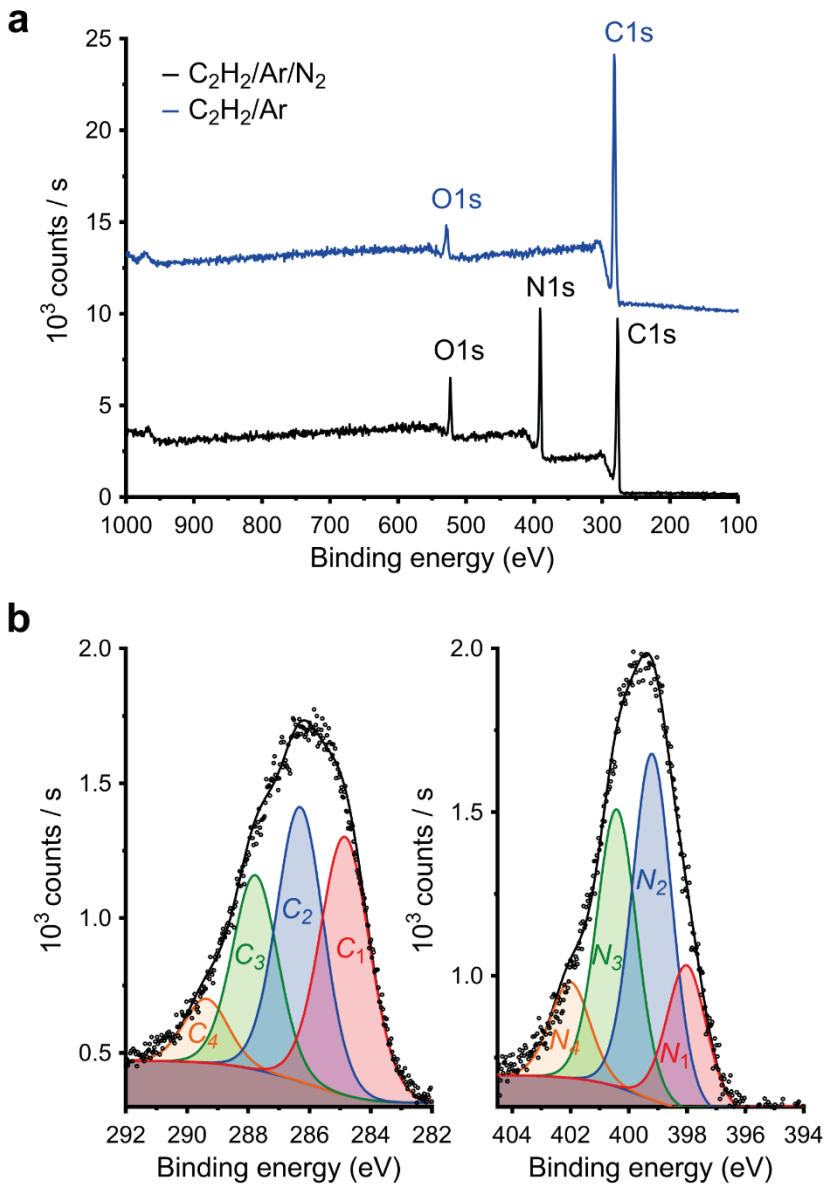

Figure 6.7. a) Comparison of the XPS survey spectra of nanoP^3 nanoparticles formed in C_2H_2/Ar (blue line) and C_2H_2/Ar/N_2 (black line) plasma discharges. The synthesis parameters were set at 50 W, 150 mTorr for both sample sets and the flow rates to 3, 10 and 3 sccm and 3, 0 and 13 sccm for acetylene, nitrogen and argon for nanoP^3 made with C_2H_2/Ar/N_2 and C_2H_2/Ar respectively. b) Deconvolution of the C 1s and N 1s XPS core levels of nanoP^3 ([C]/[N] = 2) of nanoP^3 synthesised at 50 W, 150 mTorr and acetylene flow rate of 3 sccm.

hybridized carbon atoms. The component N_2 is assigned to -C≡N and NH groups, while the component N_3 is related with nitrogen three-fold coordinated to sp^2 carbon atoms, nitrogen atoms bonded to two sp^2 and one sp^3 carbon atoms or sp^2 nitrogen atoms bonded to sp^2-hybridized carbon atoms. The fourth component N_4 is attributed to NO compounds. Overall, correlations between OES *in situ* diagnostics and *ex situ* XPS and FTIR suggest that radical molecules found in the plasma, such as CN, promote the formation of PCN and enhance the growth of nanoP^3 through radical accretion. Further, our surface characterization with FTIR and XPS suggests that nanoP^3 are three-dimensional analogues of previously reported plasma-activated amorphous coatings [61], particularly those formed under floating potential conditions ($V_{bias} = V_f$).

Further quantification of the surface chemical composition with XPS, shown in Figure 6.8, revealed that the overall carbon fraction was greater at higher $Q_{acetylene}$ (at constant W_{rf}) and decreased with increasing W_{rf} (at constant $Q_{acetylene}$). The nitrogen fraction followed the opposite trend with the plasma parameters. For instance, nitrogen fraction incorporated into as-synthesized fresh nanoP^3 was 33% at a coupled power of 50 W, increasing to 37% and 38% at 75 W and 100 W respectively. The effects of long-term storage in the elemental composition kinetics was study for nanoP^3 prepared at $Q_{acetylene}$ = 2 sccm and at constant W_{rf} = 50 W. The overall carbon relative elemental fraction was constant (≈ 62 %) over long-term storage of nanoP^3 in air and at room temperature, up to one year (see Figure 6.9). However, the nitrogen fraction decreased to ≈ 23 %, compensated by an increase in the oxygen surface content of up to ≈ 13 % one-year post-synthesis (Figure 6.9).

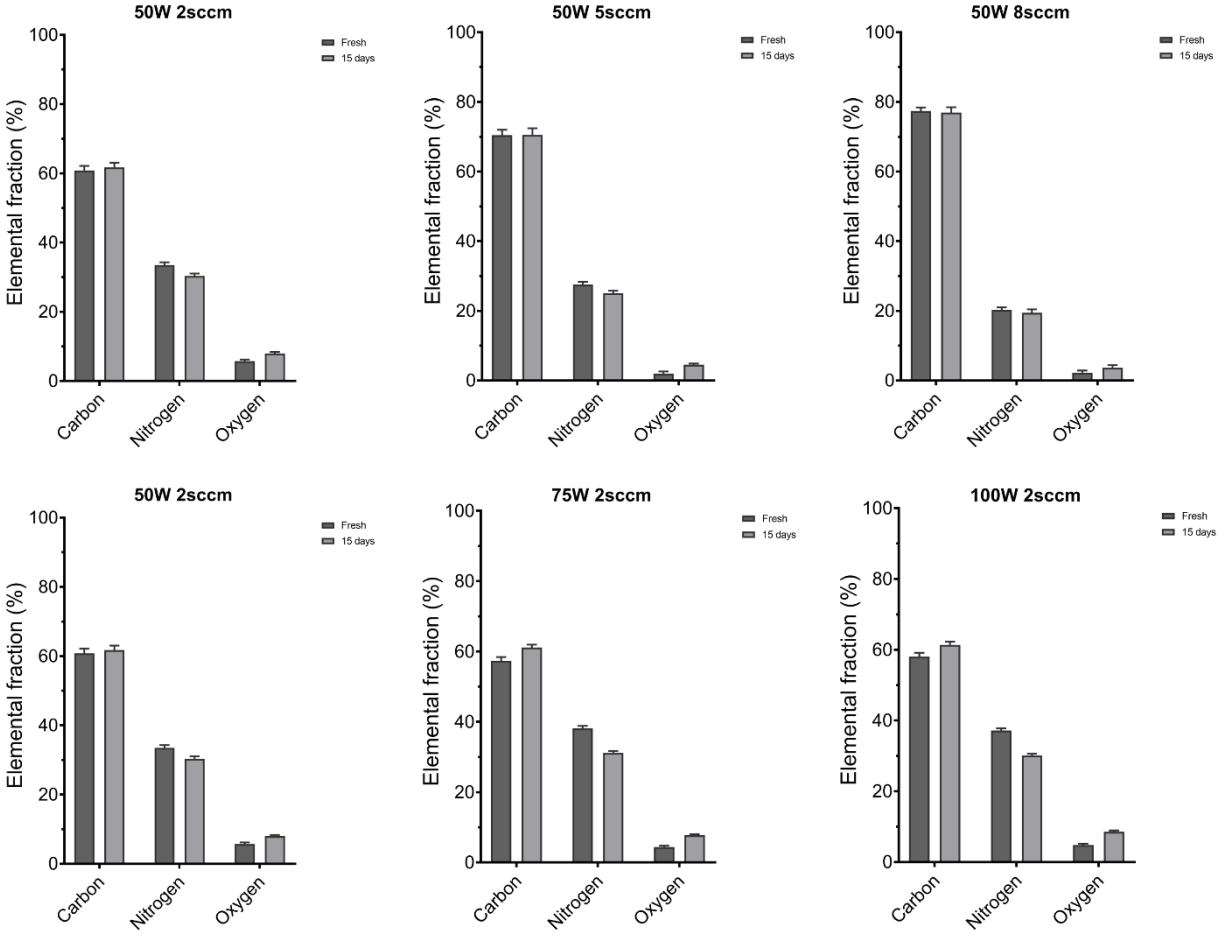

Figure 6.8. Fractional carbon, nitrogen and oxygen atomic content on nanoP^3 synthesised fresh and after 15-day storage in air at various coupled power and acetylene flow rate (discharge pressure was set at 150 mTorr).

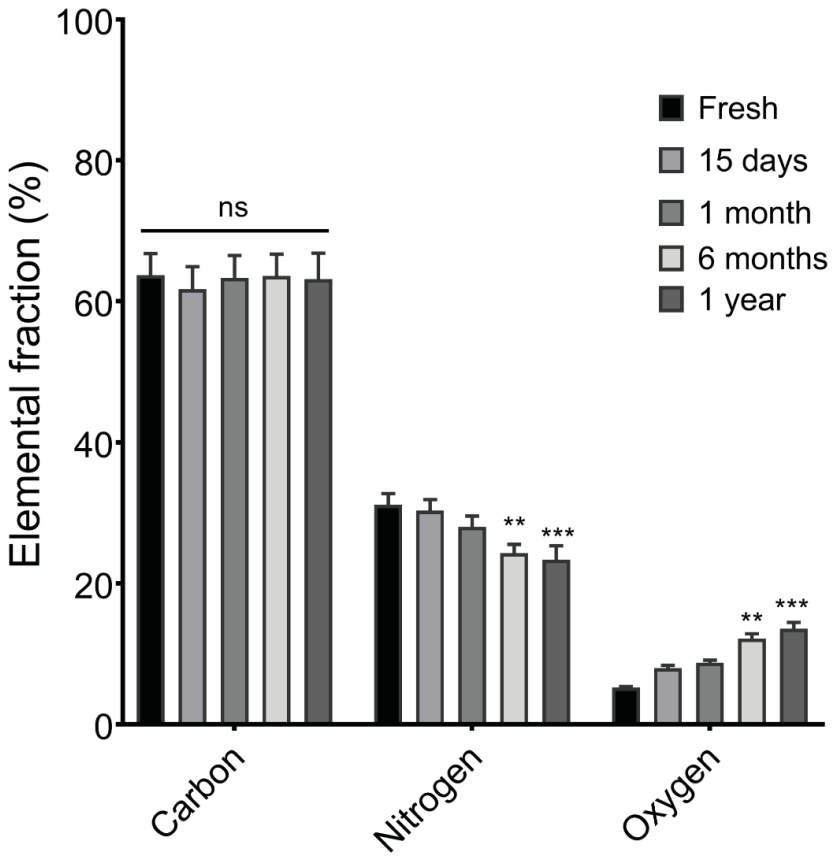

Figure 6.9. Fractional carbon, nitrogen and oxygen content on nanoP^3 (50 W, 150 mTorr and 3 sccm) at various time points and up to 1-year post synthesis.

6.3.1.4 Hydrodynamic size distribution

NanoP^3 size decreased significantly with the coupled power, measuring 86 ± 12 nm, 134 ± 21 nm and 199 ± 22 nm by SEM at the maximum yield rates for 100 W, 75 W and 50 W respectively. Since increasing the coupled power drives higher dissociation rates in the plasma, the number of reactive PCN increases. Additionally, the period of the oscillations also decreases significantly with increasing power (see Figure 5.18), which is consistent with a more rapid aggregation of PCN and hence assembly of smaller nanoP^3. The size of nanoP^3 was then studied in aqueous solution (PCR grade water) using dynamic light scattering (DLS). This technique analysis the Brownian motion of the particles by tracking their trajectory under flow. The hydrodynamic size of the nanoparticles is related with their diffusion coefficient by the Stokes – Einstein equation

$$D = \frac{k_b T}{6\pi\eta r_p}$$

where $D = \langle \overline{x,y}^2 \rangle / 4\Delta t$ is the particle diffusion coefficient, $\langle \overline{x,y}^2 \rangle$ the mean square displacement in a given time interval Δt, T and η the solution temperature and viscosity and r_p the particle radius. Since the particle diffusion coefficient (related with its mobility) in a solution depends on its size, this technique allows study of the size distribution of a nanoparticle population provided that the temperature and viscosity of the solution are known. Results show that the hydrodynamic size (Figure 6.10) of nanoP^3 populations increased significantly in solution to 135 ± 27 nm, 179 ± 29 nm and 240 ± 39 nm at the highest nanoparticle yields and for 100 W, 75 W and 50 W respectively. The “apparent” increase in hydrodynamic size, compared with as synthesized nanoP^3 measured by SEM, is inherently related with the positive net surface charge of the particles and the formation of an

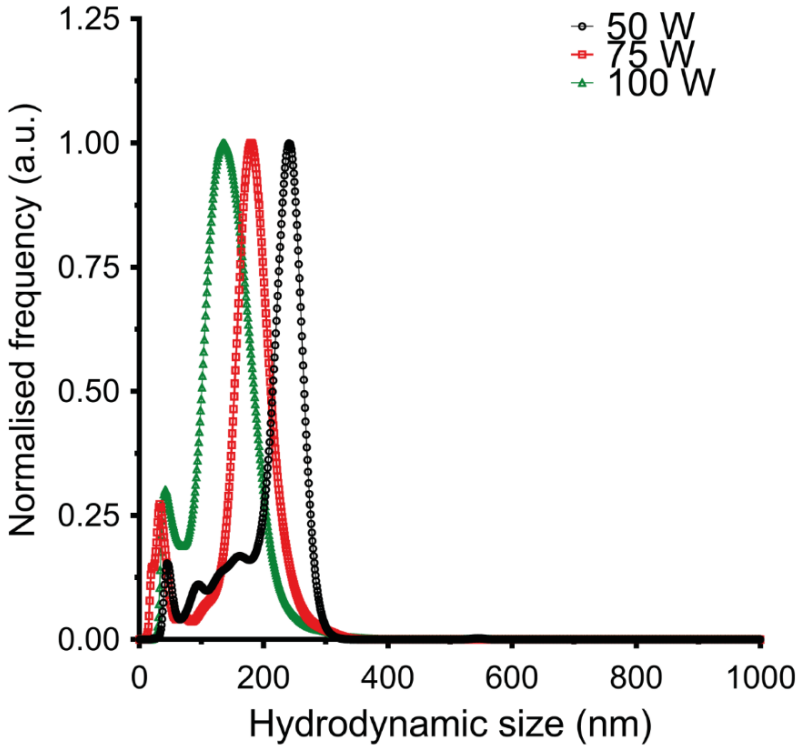

Figure 6.10. Hydrodynamic size distribution of nanoP[3] dispersed in PCR grade water analysed by dynamic light scattering (DLS) shows that particle size can be tuned by the applied rf power at the maximum yields (the acetylene flow rate was set to 3 sccm at 50 W and 75W and 6 sccm at 100W and the discharge pressure was 150 mTorr).

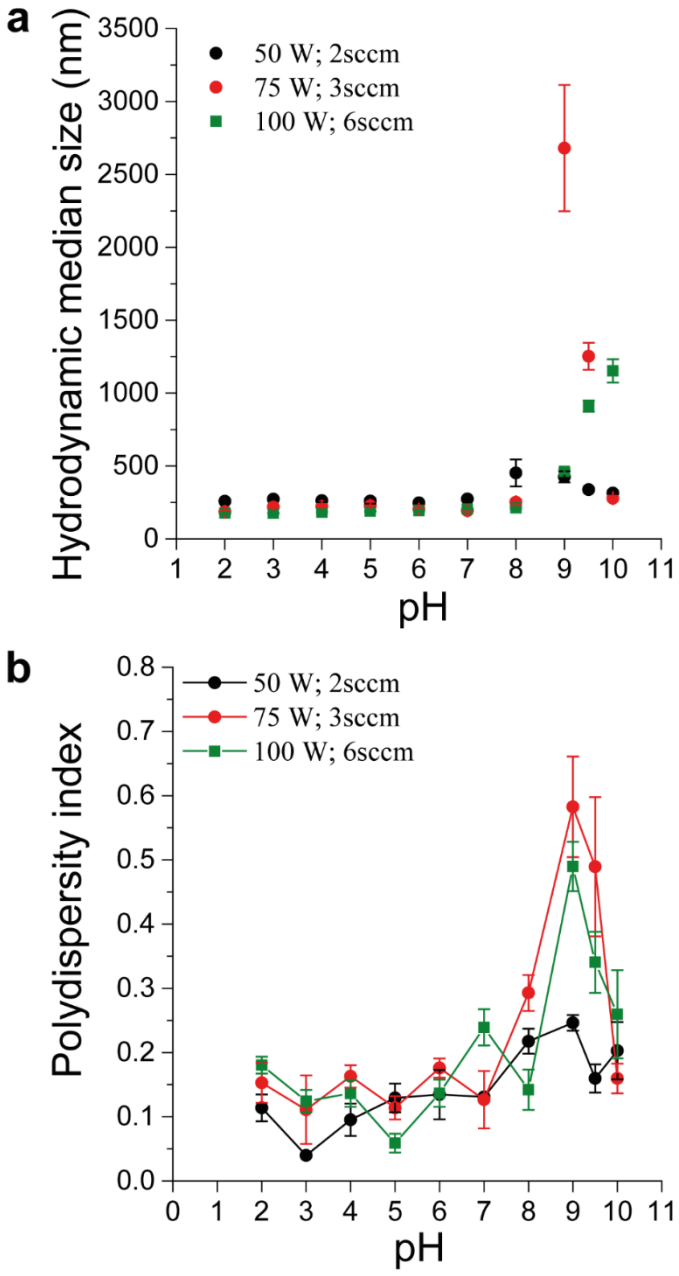

Figure 6.11. a) Hydrodynamic median size of nanoP^3 dispersed in PCR grade water as a function of the solution pH for the maximum yield rates at 50, 75 and 100 W and 150 mTorr. The size increased significantly in mildly alkaline media for all formulations due to particle aggregation. nanop^3 aggregation was reversed at higher pH (measured here up to pH 10) for formulations prepared at 50 and 75 W. b) The Polydispersity index increases with the solution pH, which consistent with particle aggregation and the results shown in Figure a).

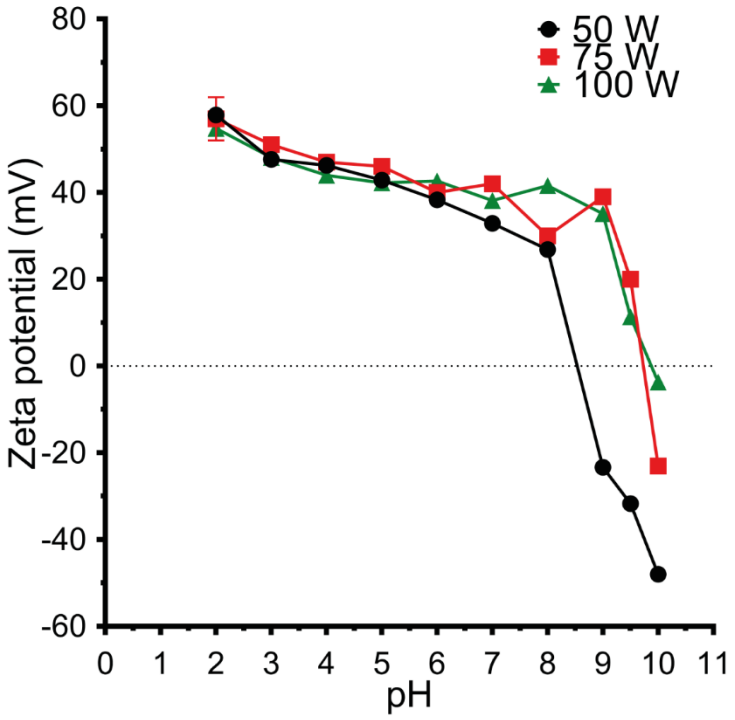

Figure 6.12. Zeta potential measurements of nanoP[3] synthesized at different applied rf power at the highest yield rates (the acetylene flow rate was set to 3 sccm at 50 W and 75W and 6 sccm at 100W and the discharge pressure was 150 mTorr) show that the surface charge of the nanoparticles can be significantly modulated in the pH range 2 – 10. All samples were positively charged ($\zeta_V > 30$ mV) and stably dispersed in aqueous solution.

extensive ionic double layer around each particle in solution. A first inner layer (Stern layer), where the anions present in solution interact more strongly with the particle surface, and a diffuse layer in which the particle-ion interaction is weaker due to the presence of both cations and anions. The extension of the ionic double layer is defined by an outer boundary within the diffuse layer, in which the ions beyond this boundary move stably in solution along with the particle. The electric potential at this boundary, measured relative to the bulk solution, is the Zeta potential, ζ_V, and is widely used as a measure of the stability of colloidal suspension. Therefore, the hydrodynamic size is a measure of the size of the particle together with the double layer. Since the particles become more sluggish as they move and drag the ions in the solution the diffusion coefficient decreases, hence yielding larger particles.

Size characterization was then investigated in aqueous solutions prepared at various pH as shown in Figure 6.11a. The size of all nanoP^3 populations remain virtually constant within the pH range of 2 – 7, showing that the particles are stable in acidic and neutral media. Particle aggregation was observed in the $8 \leq pH < 9.5$ range as demonstrated by a significant increase in the hydrodynamic size, suggesting that nanoP^3 are poorly stabilized in mildly alkaline media. The size of nanoP^3 synthesised at 50 W and 75 W decreased again for $pH \geq 9.5$, demonstrating that stabilization can be reversed in sufficiently high alkaline media. The polydispersity index is consistent with the hydrodynamic size measurements and followed the same trend with the solution pH (Figure 6.11b). Importantly, all samples were characterized by low polydispersity indices and qualified as monodisperse, measuring 0.06, 0.11 and 0.13 respectively at physiological pH. The stability of the nanoparticles in solution is discussed in

the next section in the context of their charge by measuring the zeta potential in aqueous solutions prepared at various pH.

6.3.1.5 Zeta potential

Most nanoparticle suspensions are stable electrostatically in solution when the $|\zeta_V| \geq 30$ mV. At isoelectric point, i.e. when $|\zeta_V| = 0$ mV, the stability of a nanoparticle suspension is typically compromised due to the formation of aggregates. The stability of nanoP^3 observed at low, intermediate and very high solution pH is driven by electrostatic repulsion between particles and their corresponding surrounding double layer. The zeta potential of nanoP^3 was measured to confirm this hypothesis and found that it was readily modulated by adjusting the solution's pH. It ranged from 57.8 ± 3 mV, 57.3 ± 5 mV and 54.8 ± 3 mV at pH 2 to -48.0 ± 1 mV, -23.0 ± 1 mV and -3.7 ± 1 mV at pH 10 (Figure 6.12) for nanoP^3 formulations synthesized with a coupled power of 100 W, 75 W and 50 W respectively. All nanoP^3 formulations were positively charged at neutral pH, with zeta potential higher than 30 mV, demonstrating their stability and feasibility for storage in water. Laser dynamic scattering and nanoparticle tracking analysis confirmed that all nanoparticles were stable and didn't form aggregates when dispersed in solution (see Movie S3 showing the tracking of nanoP^3 in solution). The zeta potential measurements are consistent with the results obtained for size and PDI (see table 6.1). The suspension of nanoP^3 in solution at pH < 8 is stabilized by electrostatic repulsion between positively charged particles. The buildup of positive charge around each nanoparticle is most likely driven by the protonation of amine and carboxylic groups present on the nanoP^3 surface. For 8 ≤ pH < 9.5

Table 6.1. Size of as synthesised nanoP^3 measured by SEM and hydrodynamic size and ζ_V measured by DLS for various rf coupled power (the acetylene flow rate was set to 3 sccm at 50 W and 75W and 6 sccm at 100W and the discharge pressure was 150 mTorr).

P_{rf} (W)	Size by SEM (nm)	Size by DLS (nm)	$\lvert\zeta_V\rvert$ (pH = 7)
50	199 ± 22	240 ± 39	33.9 ± 0.3
75	134 ± 21	179 ± 29	42.0 ± 1.0
100	86 ± 12	135 ± 27	38.1 ± 0.6

these surface groups become progressively more deprotonated and the particles aggregate as they reach their isoelectric point. For pH ≥ 9.5, nanoP^3 becomes negatively charge as deprotonation carboxylic groups continues, which stabilizes the nanoparticles due to the repulsion of between negatively charged particles. As shown in Figure 6.12, the isoelectric point (i.e. $\zeta_V = 0$ mV) of nanoP^3 changes for various formulations, occurring at 8 < pH < 9, 9.5 < pH < 10 and around 10 for nanoparticles produced at 50 W (3sccm), 75 W (6 sccm) and 100 W (6sccm) respectively (note that all formulations were synthesized at a discharge pressure of 150 mTorr and nitrogen and argon flow rate of 10 sccm and 3 sccm respectively). The results are consistent with the surface chemical characterization performed in the previous section. Increasing the rf coupled power increases also the overall nitrogen atomic fraction and ultimately the total number of amine groups on the surface of nanoP^3. Therefore, a higher solution pH is necessary to deprotonate the larger number of positively charged amine groups on the nanoP^3 surface. Consequently, the isoelectric point of nanoP^3 occurs at progressively higher pH with increasing nitrogen content (i.e. nanoP^3 formulations produced at higher rf coupled power). In conclusion, the stability of nanoP^3 suspended in a solution is controlled by the solution pH at which their isoelectric point occurs. The nanoP^3 isoelectric

point is ultimately driven by its surface chemistry, which is easily tuned by the plasma process parameters.

6.3.2 Radical kinetics

Since radical-chain polymerization growth (see section 1.2.3) appears to play a significant role in the formation of nanoP^3, the presence of stable radicals within the nanoparticle structure was evaluated using EPR spectroscopy. Unpaired electrons were detected within nanoP^3, as shown by the broad resonance peak (Figure 6.13a) around 348 mT (g_{factor} = 2.003), and their kinetics are controlled by temperature-dependent diffusion towards the surface (Figure 6.13b). The radical volume density was ~ 3 x 10^{16} spins/cm^3 measured 75 minutes post synthesis, decaying below 50 % of their initial value after 48 and 144 hours of storage in water at 24˚ C and 4˚ C respectively for nanoP^3 prepared at $Q_{\text{acetylene}}$ = 2 sccm and W_{rf} = 50 W (discharge pressure was set to 150 mTorr and the flow of nitrogen and argon to 10 sccm and 3 sccm respectively). The radical decay was slower for storage in air at 24˚ C, with nanoP^3 retaining 57 % of the initial radical density 240 hours post synthesis. FTIR measurements (Figure 6.14a and 6.14b) showed a significant increase in oxygen-containing functional groups (*e.g.* stretching vibrations of OH and CO bonds), which were generated by peroxyl radicals formed in surface reactions of carbon-centered radicals with atmospheric oxygen. Surface oxidation was further enhanced either by producing nanoP^3 at higher base pressures in the plasma chamber or by storing the particles in air for longer periods of time. The EPR signal detected on nanoP^3

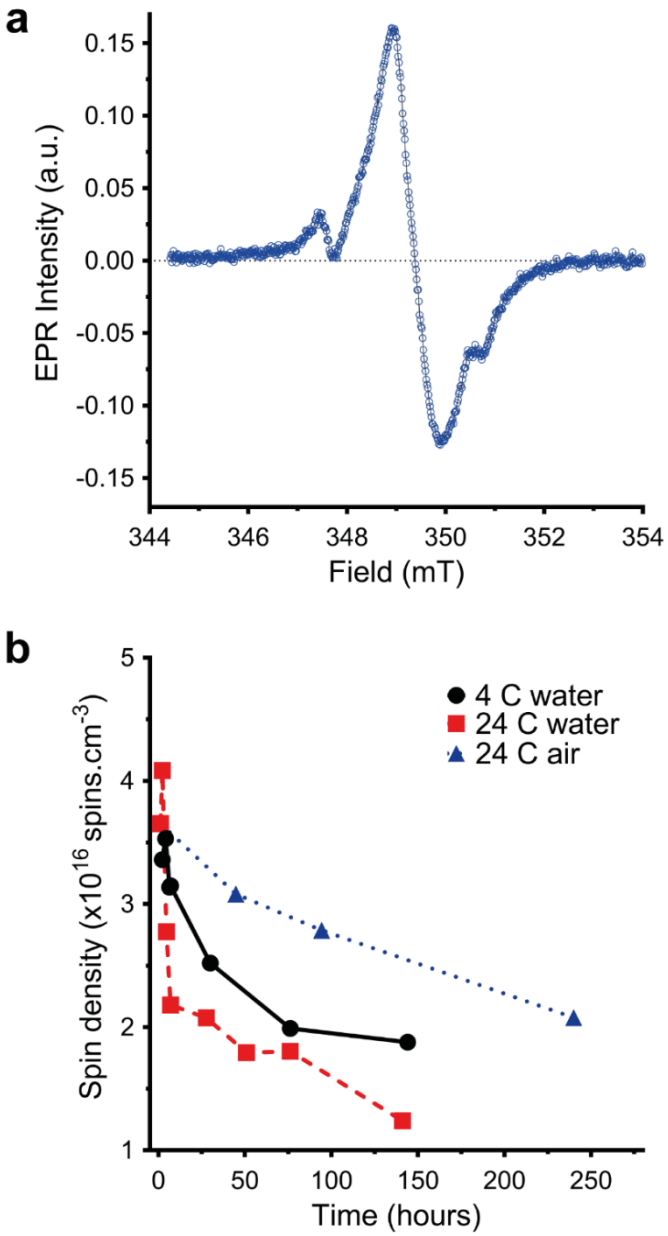

Figure 6.13. a) EPR spectroscopy confirms the presence of long-lived radicals in nanoP^3 after synthesis (3 sccm, 150 mTorr and 50W), shown here by a broad resonance peak centered around 348 mT. b) Kinetics of radicals on nanoP^3 shows that radical diffusion is temperature-activated and slower when particles are stored dry.

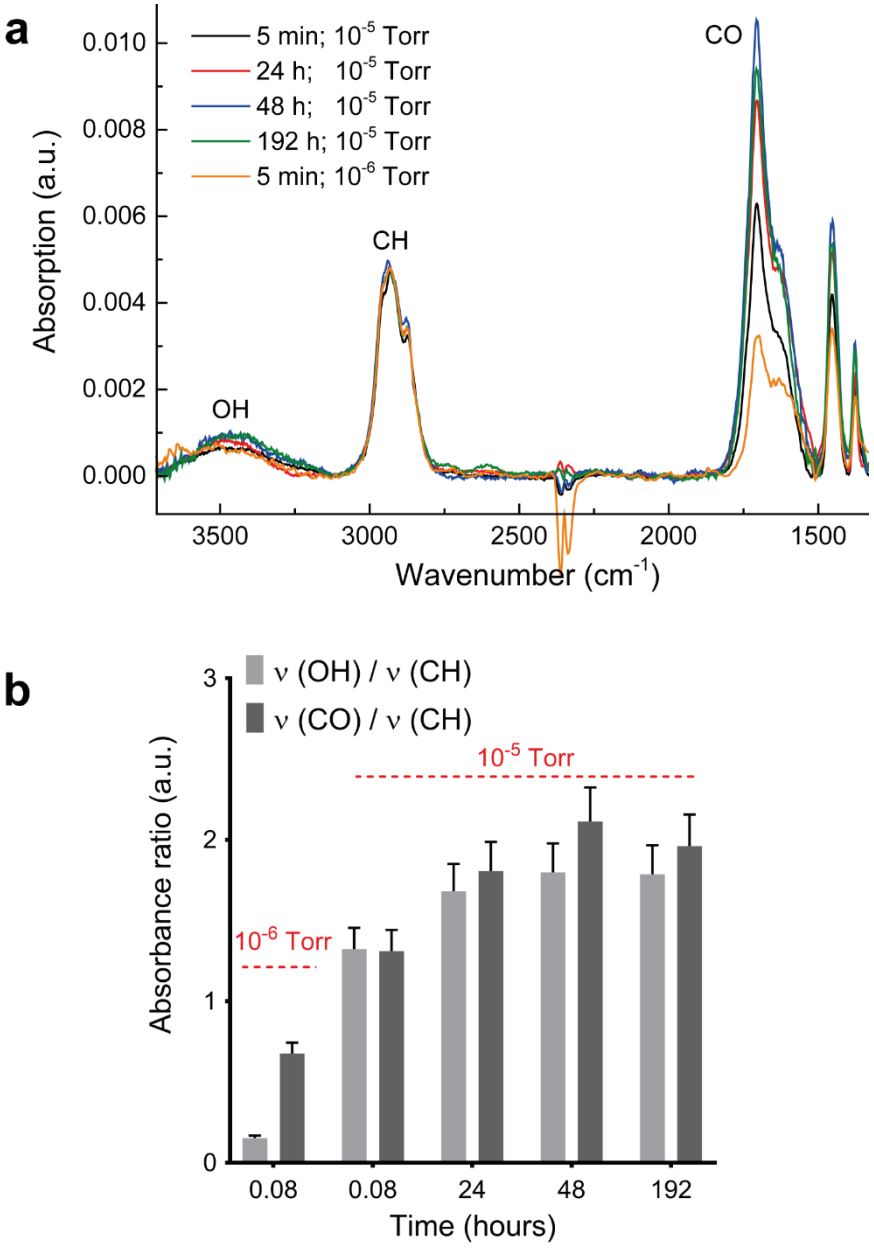

Figure 6.14. a) FTIR spectra of nanoP^3 measured at various time-points after synthesis (3 sccm, 150 mTorr and 50W) and reactor base pressure. b) Absorbance ratios between stretching vibrations of OH (3500 cm^{-1}) and CO (1700 cm^{-1}) to aliphatic CH (2900 cm^{-1}) on nanoP^3 calculated from the spectra in Figure a).

results from an excess of radical active groups that are incorporated and remain active within the nanoP^3 structure. This excess of reactive groups is consistent with the second cycle (see Figure 1.8) of the rapid step growth polymerization model (RSGP). In this cycle, polymerization is initiated and sustained by bi-radical species, which do not participate in termination reactions. Therefore, the reaction products will always contain an excess of radical species which may remain stable in the particle carbon matrix, even after the plasma is switched off. An alternative source of reactive species arises from the diffusion of radical molecules towards the particle surface, suggested by the reduction of the number density of CN radicals observed during the rapid aggregation phase (Figure 5.13b).

6.3.3 Fluorescent properties of nanoP^3

Particular modes of carbon-based nanomaterials are characterized by intrinsic and intense fluorescence, making them extremely versatile imaging platforms. The emission and excitation profiles largely depend on their physical and chemical properties including aggregation[257], dispersion in polar solvents [258], presence of nitrogen-vacancy color centers[253, 259] and surface functional groups [260]. The presence of multiple surface functionalities crosslinked with a carbon matrix suggests the possibility of nanoP^3 autofluorescence. Using steady-state emission spectroscopy, it was found that nanoP^3 dispersed in aqueous solution (or cell media) are auto-fluorescent within the UV-VIS-NIR range (Figure 6.15a), with emission profiles strongly depending on the excitation energy and intensity significantly increasing with nanoP^3 concentration in solution (Figure 6.15b). The emission profile of nanoP^3 was characterized by a shift towards higher wavelengths and a striking decrease in

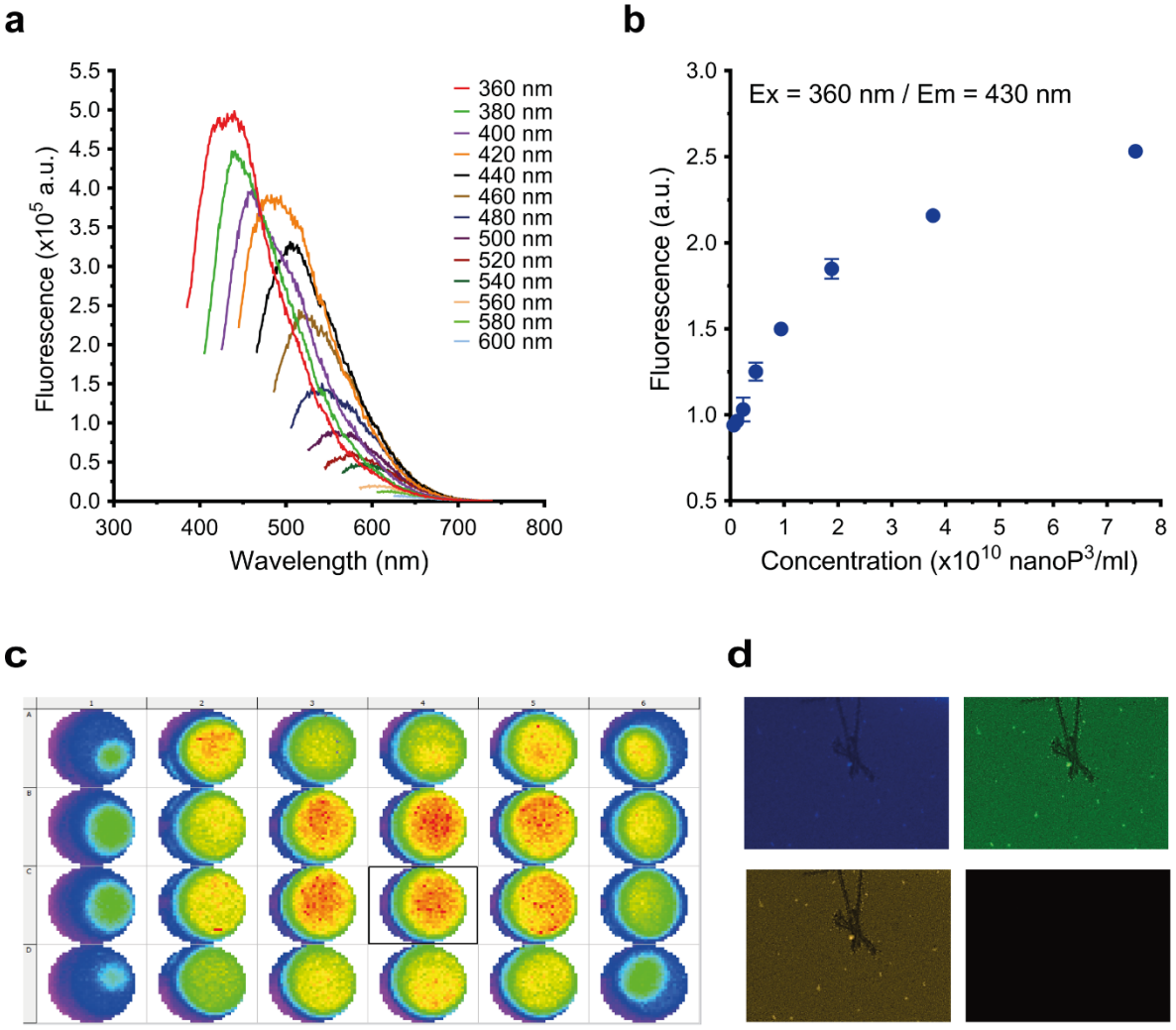

Figure 6.15. a) Steady-state spectroscopy shows that nanoP^3 (*Q* = 3, 10 and 3 sccm for acetylene, nitrogen and argon, 150 mTorr and 50W) fluoresces within the UV-VIS-NIR range. The emission profile shifts towards the red and decreases in intensity with greater excitation wavelengths. b) The fluorescence intensity was found to increase with nanoP^3 concentration in solution. c) Fluorescence mapping (excitation/emission = 360 nm / 430 nm) of as synthesised nanoP^3 collected on a 24-well tissue culture plate. d) NanoP^3 fluorescence properties were confirmed by confocal fluorescence microscopy measured in the blue, green, yellow and red channels.

the emission intensity with increasing excitation wavelengths. A maximum emission intensity was recorded for excitation wavelength of 360 nm and all emission peaks were found to be asymmetric, featuring a broadening towards larger wavelengths. A fluorescence map of the distribution of as synthesised nanoP^3 on a 24-well tissue culture plate is shown in Figure 6.15c. The wells were mapped with a microplate reader for excitation and emission wavelengths of 360 nm and 430 nm respectively. Results are consistent with the spatial distribution of nanoP3 observed previously in Figure 5.4, showing higher concentration of particles in the wells located at the center of the plate. The fluorescence properties of nanoP^3 were further confirmed by imaging as synthesized particles collected on glass substrates with an inverted fluorescence confocal microscope in various emission/excitation channels, demonstrating the versatility of nanoP^3 as an imaging agent (Figure 6.15d).

The maximum Stoke's shift (80 nm) was observed at an excitation wavelength of 360 nm, decreasing non-linearly to 25 nm at an excitation of 600 nm as shown in Figure 6.16a. Wavelength-dependent excitation is an intriguing fluorescence phenomenon characterized by a red-shift of the emission peak with increasing excitation wavelengths, and has been reported in a variety of carbon-based nanoparticles including nanodiamond, carbon nanodots [260] and graphene-oxide [257]. While a full explanation for this phenomenon remains to be elucidated, our results support the hypothesis that red-shifted emission peaks are driven by multiple discrete electronic transitions between molecular orbitals, associated with different surface functional moieties [260]. For instance, population of molecular orbital levels associated with oxygen-containing surface functional groups, such as OH, ketones C=O and ester C=O, have been suggested to induce

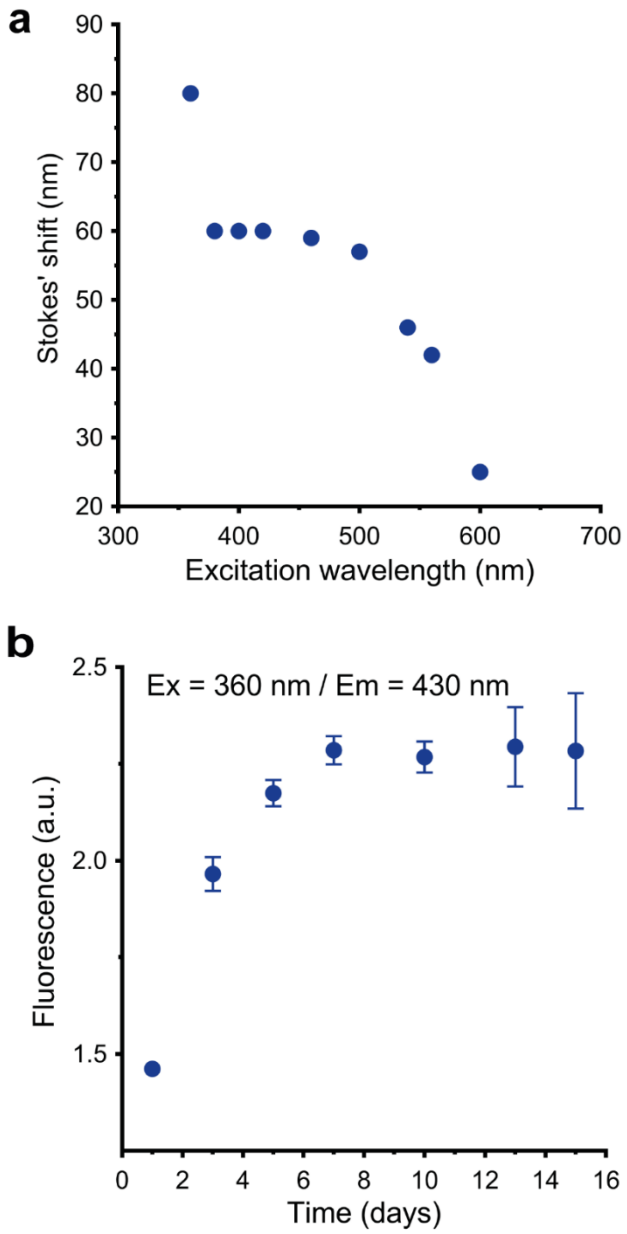

Figure 6.16. a) The maximum Stoke's shift was 80 nm for an excitation wavelength of 360 nm, decreasing to 25 nm for an excitation at 600 nm. b) The intensity of the nanoP^3 fluorescence increases in solution over time, which correlated with a continuous surface oxidation driven by radical diffusion to the particle surface (Synthesis parameters were set at *Q* = 3, 10 and 3 sccm for acetylene, nitrogen and argon, 150 mTorr and 50W).

fluorescence in nanodiamonds in the blue, green and yellow range respectively [260]. This interpretation is supported by the significant increase of the fluorescence intensity of nanoP^3 with increasing storage time (Figure 6.16b) which correlates with the formation of C=O and OH bonds due to surface oxidation (Figure 6.14a and 6.14b).

6.3.4 Linker-free, spontaneous one-step conjugation with bioactive cargo

6.3.4.1 Immobilization of wide-ranging cargo molecular weight and structure

The presence of long-lived radicals within nanoP^3 suggests the potential for direct immobilization of biomolecules by simple incubation [4, 261], giving nanoP^3 an intrinsic advantage over competing wet chemistry-based nanoparticle platforms. A radical based immobilization platform allows simultaneous attachment, without chemical intermediates, of cargo including ligands, imaging and therapeutic agents (Figure 6.17). To first exemplify and visualize the possibility of functionalization by simple incubation in solution, IgG antibodies tagged with 20 nm gold labels were incubated in water with nanoP^3 and imaged under TEM (Figure 6.18a) and electron tomography (Figure 6.18b and 6.18c – video of the tomogram in Movie S4). Single, double and triple multifunctionalization was further demonstrated on a single nanoP^3 using three different IgGs tagged with 10, 20 and 40 nm gold labels [1]. To more quantitatively understand this potential, representative conjugate classes with wide-ranging molecular weights and

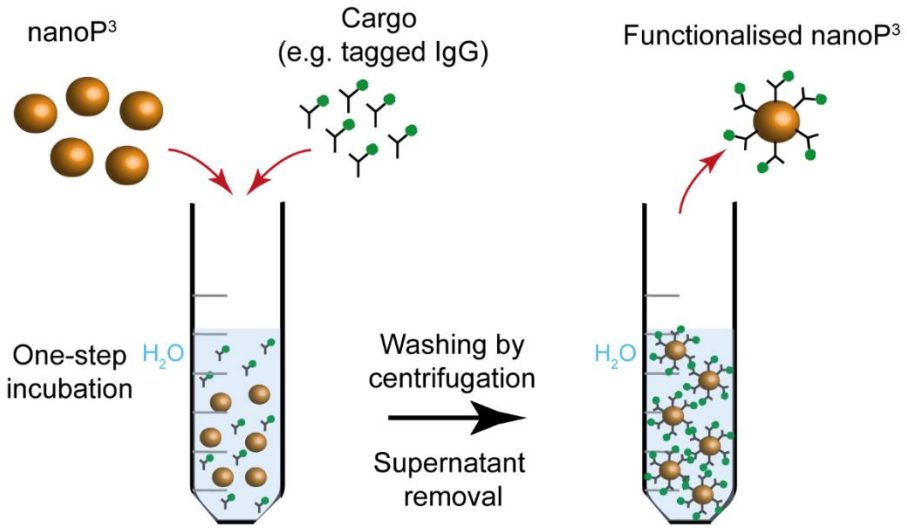

Figure 6.17. A schematic exemplifying the nanoP^3 simple and one-step solution incubation process adopted in this work. Robust immobilization of biologically active cargo is achieved by simply mixing both particles and molecules in aqueous solution.

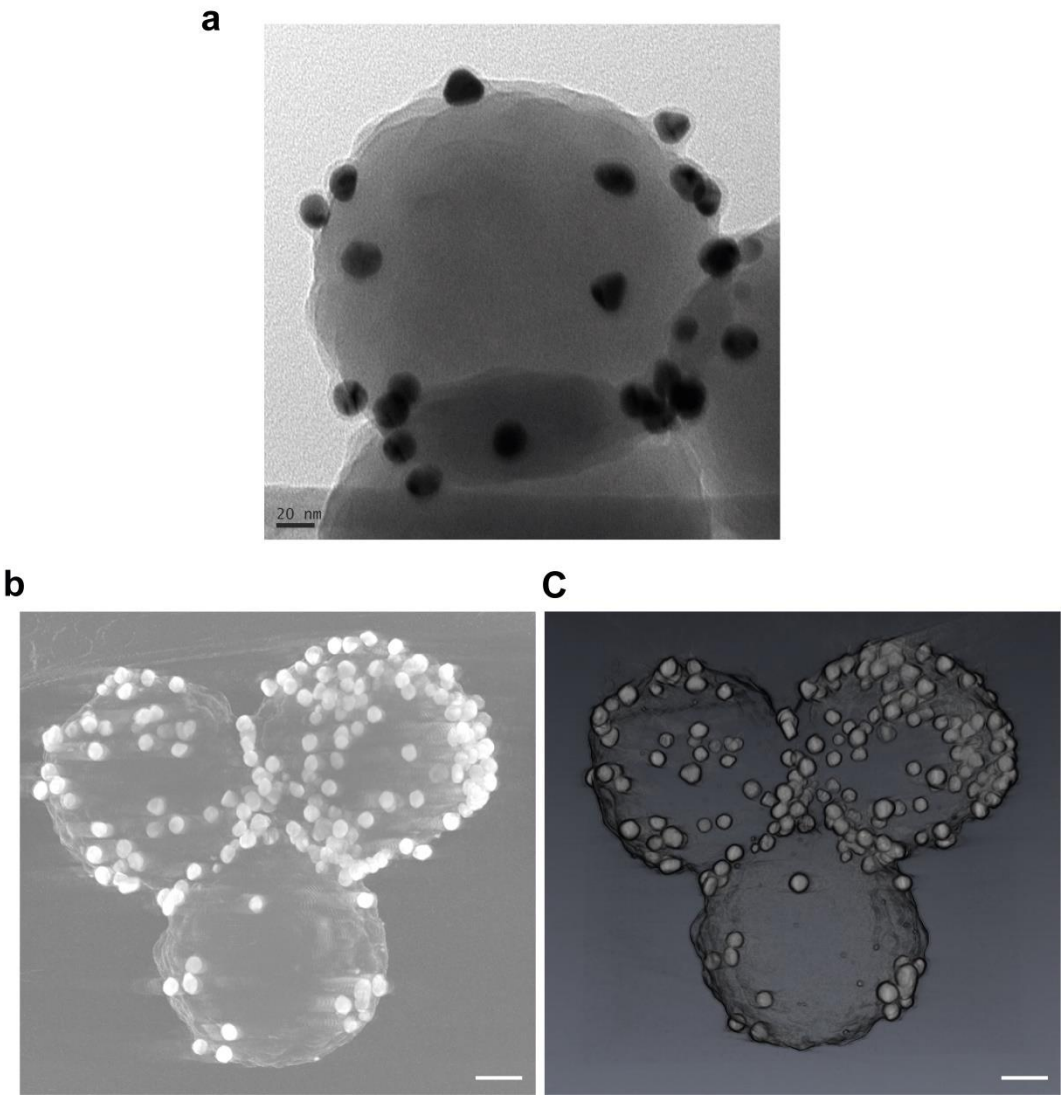

Figure 6.18. a) Representative HR-TEM images of gold-tagged IgG immobilized on the surface of a 200 nm nanoP^3 nanoparticle. a) and b) electron tomogram volume rendering reconstruction of gold-tagged IgG - nanoP^3 constructs. The plasma parameters were set at *Q* = 3, 10 and 3 sccm for acetylene, nitrogen and argon, 150 mTorr and 50W. The incubation of nanoP^3 (10^9 nanoP^3/mL) with gold labelled IgGs (3 µg/mL) was performed at room temperature, in RT-PCR grade water (Ph = 7) for 1 hour.

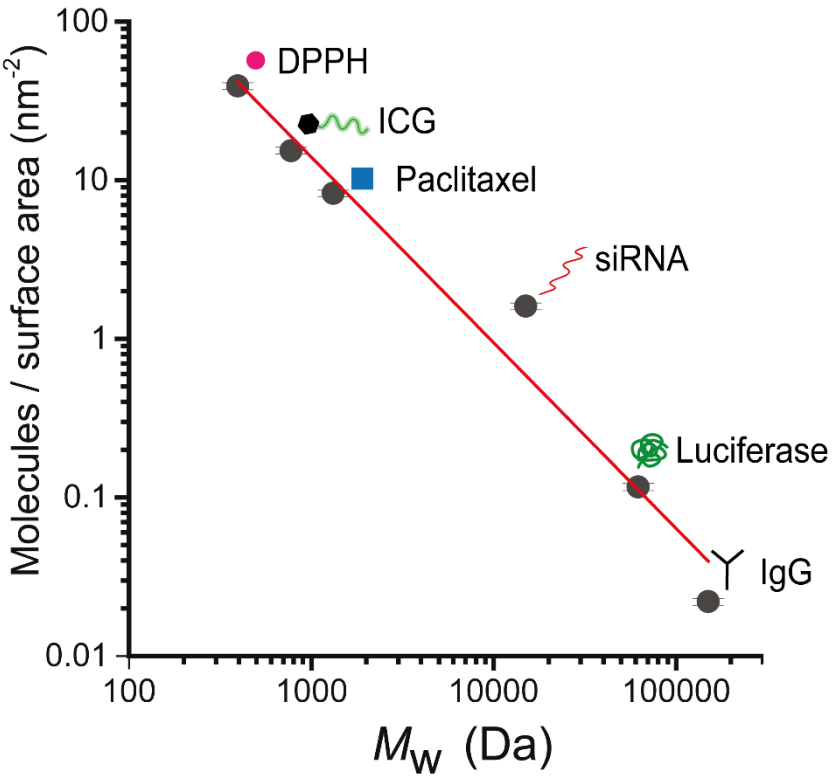

Figure 6.19. Number of cargo molecules per unit surface area of nanoP^3 at a monolayer for various cargo molecular weights, structures and biological functions. The total number of molecules bound to the nanoP^3 surface is ultimately dependent on ratio between the nanoP^3 surface area and the molecular weight of the cargo. The plasma parameters were set at Q = 3, 10 and 3 sccm for acetylene, nitrogen and argon, 150 mTorr and 50W. The incubation of nanoP^3 (10^9 nanoP^3/mL) with cargo (3 µg/mL) was performed at room temperature, in RT-PCR grade water (pH = 7) for 1 hour.

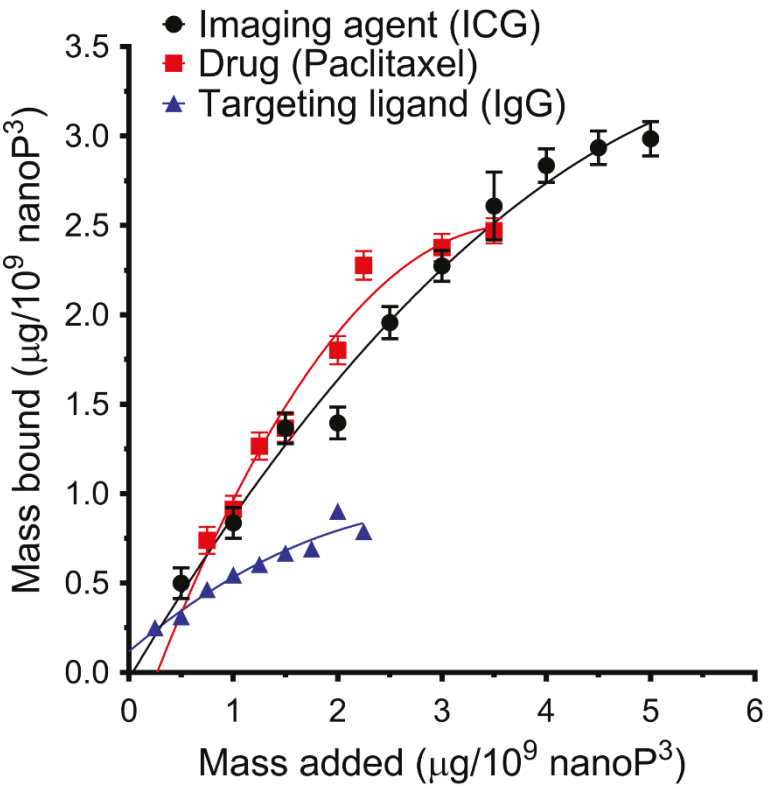

Figure 6.20. The total cargo mass bound to nanoP^3 increases with the mass added to the solution during the incubation process. Exemplification with a drug (paclitaxel), imaging agent (cardiogreen) and targeting ligand (IgG) demonstrated surface saturation at 2.3 μg, 2.9 μg and 0.8 μg respectively. The plasma parameters were set at *Q* = 3, 10 and 3 sccm for acetylene, nitrogen and argon, 150 mTorr and 50W. The incubation of nanoP^3 (10^9 nanoP^3/mL) with cargo (the mass in the x-axis was added to a total volume of 1 mL) was performed at room temperature, in RT-PCR grade water (pH = 7) for 1 hour.

structures were immobilized on nanoP^3, including an antibody (IgG, 150 kDa), enzyme (luciferase, 62 kDa), ribonucleic acid (small interfering RNA, 15 kDa), drug (paclitaxel, 1.3 kDa), fluorescent dye (cardiogreen, 0.78 kDa) and radical scavenger molecules (2,2-diphenyl-1-picrylhydrazyl, 0.39 kDa). A full monolayer of all bound conjugates was achieved by simple one-step incubation of nanoP^3 with the cargo in aqueous solution and without intermediate chemistry. The loading capacity of nanoP^3 was dependent on the available particle surface area, the molecular weight and geometry of the conjugate, as demonstrated in Figure 6.19. Overall, the number of molecules bound to nanoP^3 decreased significantly with increasing molecular weight. The amount of bound cargo was also found to increase with their concentration in solution as demonstrated in Figure 6.20. For instance, a drug (paclitaxel), imaging agent (ICG) and antibody (IgG) saturated at a monolayer respectively with 2.3 μg, 2.9 μg and 0.8 μg per 10^9 nanoP^3 after a 1 hour incubation.

6.3.4.2 Binding kinetics

The binding kinetics associated with the simple nanoP^3 conjugation process was assessed by measuring the amount of bound cargo at different incubation time points and temperatures. This was easily demonstrated by incubating nanoP^3 with the precise amount of ICG (Figure 6.21) previously calculated to saturate the nanoparticle surface at a monolayer, *i.e.* 1.9 x 10^6 ICG molecules on a single nanoP^3 particle (99 nm radius). ICG is a fluorescence dye with emission and excitation wavelengths at 805 and 830 nm respectively. Due to the low absorbance properties of tissue in this spectral window, ICG is widely used the clinic for medical diagnostics. However, ICG is characterized by a short half-life circulation in-vivo

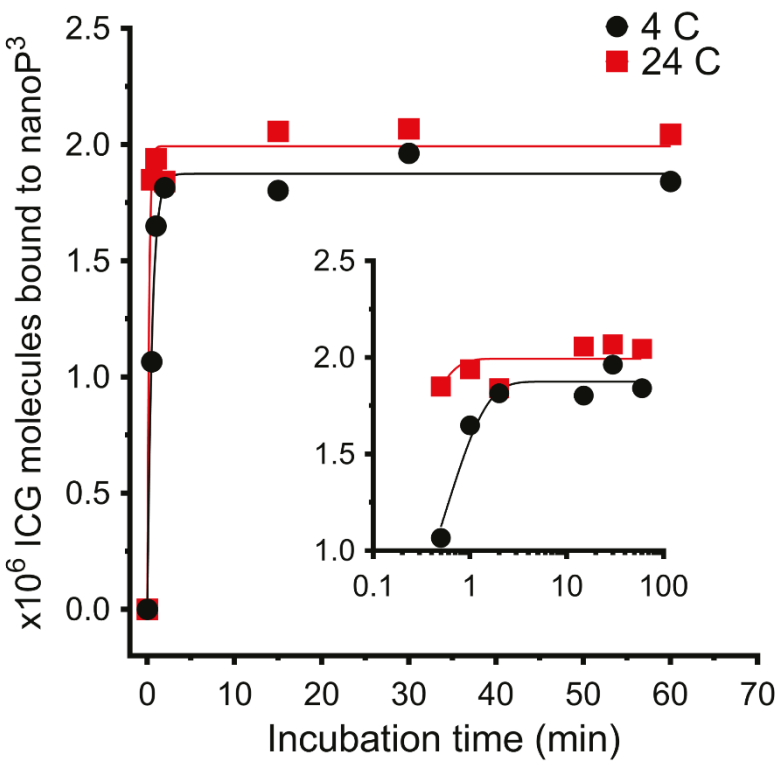

Figure 6.21. Binding kinetics experiments, exemplified here with cardiogreen, show that 90% of the total cargo was immobilized on the surface of nanoP^3 within the first 30 seconds after incubation at 24˚ C, while incubation at lower temperature (4˚ C) resulted in a 60 % binding for the same time point. Surface saturation was achieved in less than 5 minutes after incubation for both conditions. The inset shows the same data representing time in a log scale. The plasma parameters were set at *Q* = 3, 10 and 3 sccm for acetylene, nitrogen and argon, 150 mTorr and 50W. The incubation of nanoP^3 (10^9 nanoP^3/mL) with ICG (2.5 µg/mL) was performed at room temperature, in RT-PCR grade water (pH = 7) for 1 hour.

(only 4 minutes), requiring a continuous administration of the dye to avoid loss of signal. Nanoparticle-ICG constructs have been used to extend the activity of ICG. However, these platforms usually rely on weak interactions between the dye and the nanoparticle, such as electrostatic, adsorption or loading on mesoporous materials or polymer matrices and π- π stacking [262], limiting translation for its use in-vivo, or multi-step linker chemistry approaches. Here, following simple one-step incubation with nanoP^3, ICG solutions were washed by ultracentrifugation and the absorbance spectra of the washes was measured to quantify the remaining free ICG. An incubation of the cargo with nanoP^3 in water at 24˚ C resulted in an immobilization of 90% of the total cargo within the first 30 seconds. The conjugation process at 4˚ C was significantly slower, with 60 % of the total cargo immobilized after the same time-point. Nevertheless, surface saturation of the nanoparticles was achieved in less than 5 minutes for both conditions.

6.3.4.3 Shelf-life

The simple and rapid incubation process in solution shows that nanoP^3 provides a cost and time effective nanoparticle platform that does not require linker chemistry or long incubation periods. A long shelf-life and easy path to functionalization are also necessary requirements for a nanoparticle platform applicable for clinical use [45]. The binding efficiency of nanoP^3 stored for long periods of time was measured using ICG as a template molecule. Results show that the ability of nanoP^3 to immobilize cargo remains virtually constant during the first 6 months of storage in air at room temperature (Figure 6.22). A decrease of 28 % in the binding efficiency was observed for samples stored up to 16 months

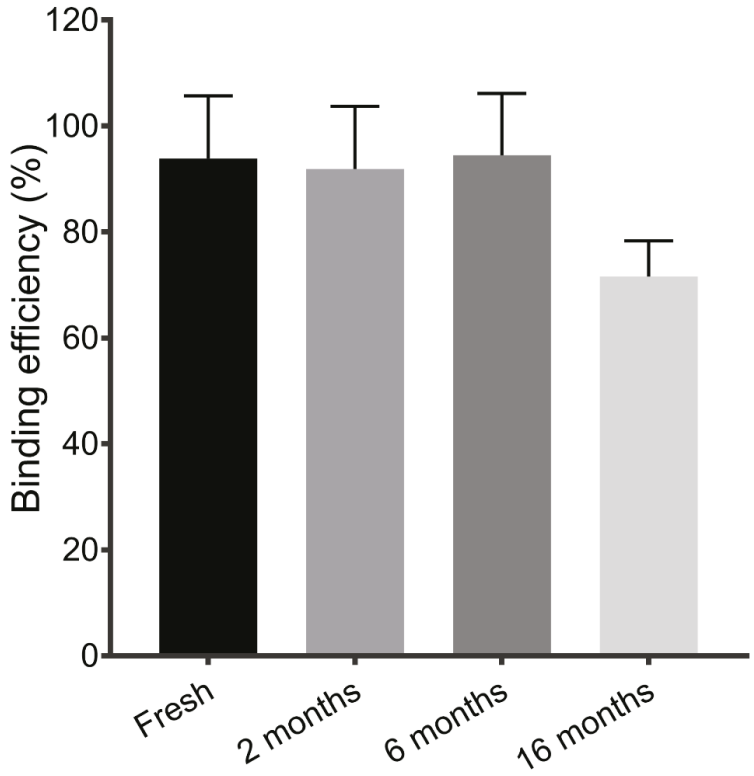

Figure 6.22. The long shelf-life of nanoP^3 was demonstrated by their ability to bind cargo (100% binding efficiency compared with fresh nanoP^3) up to 6 months of storage in air and room temperature, decreasing non-significantly by 28% after 16 months. The plasma parameters were set at *Q* = 3, 10 and 3 sccm for acetylene, nitrogen and argon, 150 mTorr and 50W. The incubation of nanoP^3 (10^9 nanoP^3/mL) with ICG (2.5 µg/mL) was performed at room temperature, in RT-PCR grade water (pH = 7) for 1 hour.

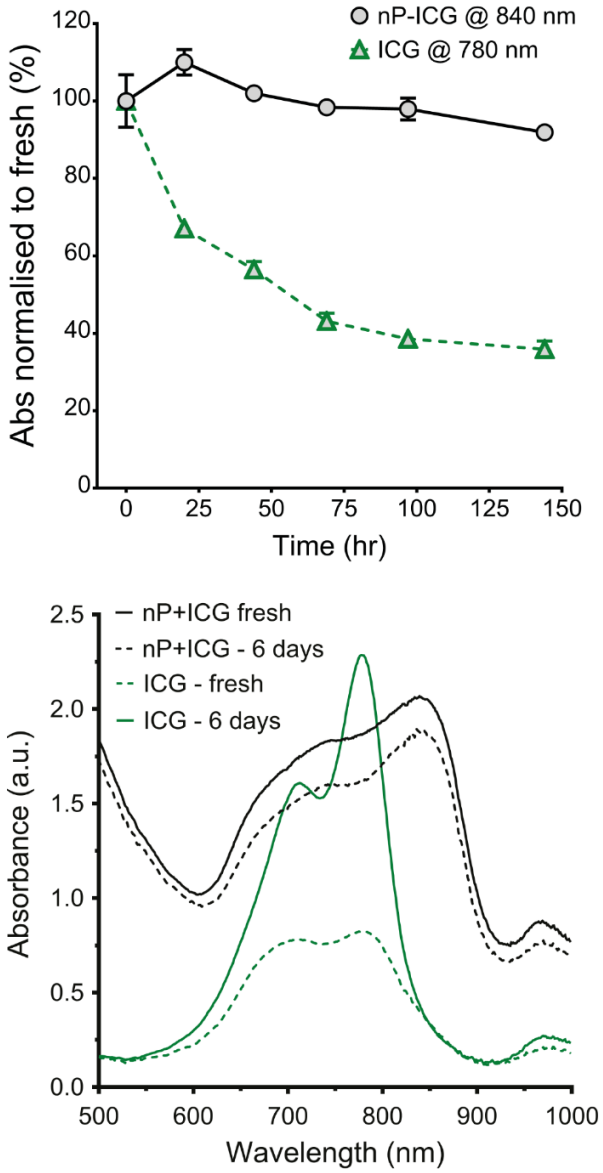

Figure 6.23. a) Kinetics of free ICG and ICG bound to nanoP^3 shows that ICG retains its activity for a significantly longer period in aqueous solution if bound to nanoP^3. The biding of ICG to the nanoP3 surface was confirmed by a 60 nm red-shift of the absorbance peak from 780 nm to 840 nm compared with free ICG in solution. b) VIS/NIR profile of free ICG and ICG conjugated nanoP^3 confirms that degradation of small cargo (< 1000 Da) is significantly delayed once immobilized to nanoP^3. The plasma parameters were set at Q = 3, 10 and 3 sccm for acetylene, nitrogen and argon, 150 mTorr and 50W. The incubation of nanoP^3 (10^9 nanoP^3/mL) with ICG (2.5 µg/mL) was performed at room temperature, in RT-PCR grade water (pH = 7) for 1 hour.

in the same conditions. However, it was still possible to fully saturate the surface of nanoP^3 by increasing the concentration of ICG in solution. Extended shelf-life could potentially be achieved by employing alternative storage approaches, including low temperature, vacuum or another non-reactive environment. The ability of nanoP^3 to retain the activity of bound ICG with storage time in aqueous solution was then tested and compared with free ICG. Degradation of free ICG was observed by a 65 ± 2 % decrease of the absorption peak at 780 nm, 144 hours after reconstitution (Figure 6.23a and 6.23b), caused by the formation of leucoforms of the dye and driven by the saturation of double bonds in the compound chain [263]. However, ICG bound to nanoP^3 retained 91 ± 2 % of its initial activity during the same period. The absorbance spectrum of nanoP^3-ICG constructs was red-shifted by 60 nm to a wavelength of 840 nm compared with free ICG (peak at 780 nm), further confirming the binding of ICG to the nanoP^3 surface. Similar red-shift have been previously reported in various nanoparticle-ICG systems [264-266]. These results show that in addition to robust immobilization of cargo, nanoP^3 can prolong the activity of some small (< 1 kDa) cargoes.

6.3.4.4 Binding modulation to highly-charged peptides

The binding of nanoP^3 to a highly-charged cargo was also investigated, using a positively charged peptide sequence bound to a Cy-5 fluorescent tag for detection (Cy-5-CPKKKRKV-NH_2), and often used as a nuclear localization sequence capable of targeting the cell nucleus. This nuclear targeting ability is mostly driven by the presence of multiple polar (cationic) amino acids, including lysine (K) and arginine (R). Initial incubations of nanoP^3 with the peptide at neutral pH did not result in the expected robust conjugation observed for more

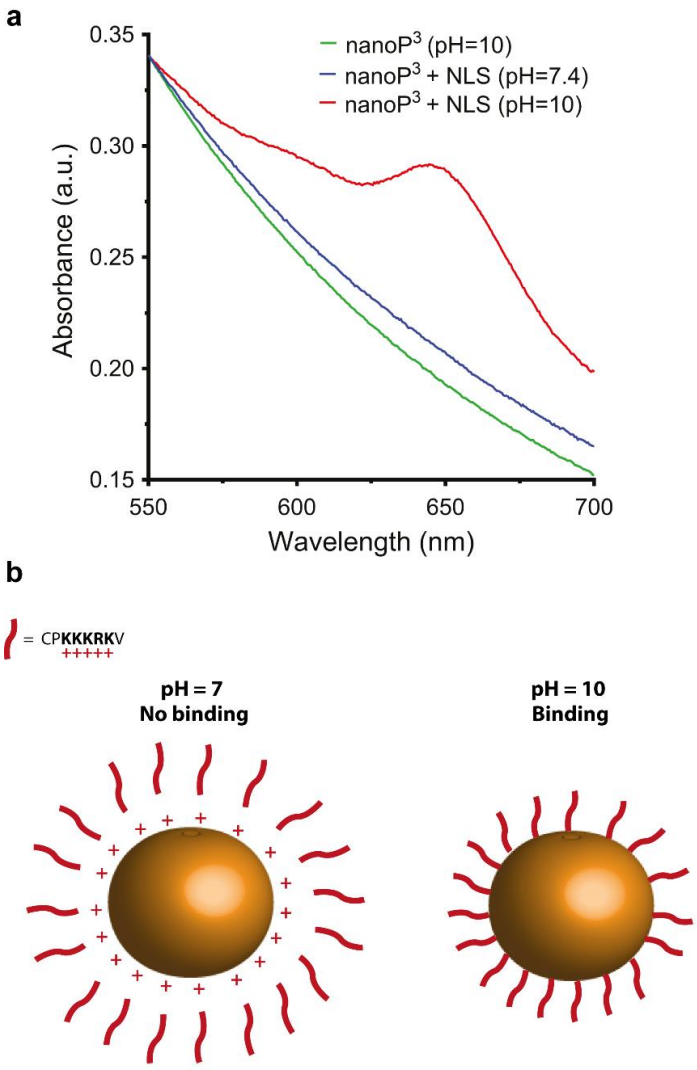

Figure 6.24. a) The binding ability of nanoP^3 to highly positively charged cargo is exemplified with a Cy-5 tagged highly-charged peptide sequence (Cy-5-CPKKKRKV), with an absorbance peak around 650 nm, at different solution pH. Binding to nanoP^3 was only achieved at higher pH, consistent with zeta potential measurements shown in Figure 6.8. b) A schematic depicting repulsion of the charged peptide from the surface of nanoP^3 due to the presence of positively charged groups (protonated amines and carboxylic acid surface groups) at neutral pH. Binding is achieved upon physical contact with the surface of nanoP^3 in alkaline media upon deprotonation of amines and carboxylic acid groups. The plasma parameters were set at Q = 3, 10 and 3 sccm for acetylene, nitrogen and argon, 150 mTorr and 50W. The incubation of nanoP^3 (10^9 nanoP^3/mL) with NLS (2.5 µg/mL) was performed at room temperature, in RT-PCR grade water for 1 hour.

neutral cargo (Figure 6.24a). Increasing solution pH to 10 was required for binding to the highly positively charged peptide. Results are consistent with the observed drop in the nanoP^3 zeta potential between pH 8 and 10, previously shown in Figure 6.8. Since the nanoP^3 is positively charged due to protonation of surface groups, and this charge is only partially screened by the negative ions in the Stern layer, the net charge at the free-solution interface is positive for pH $\leq$ 8, repelling the positively charged peptide from the surface of the particle (Figure 6.24b). As pH increases, the surface groups of the nanoparticles are progressively deprotonated and at pH > 8, when the solution transitions to highly alkaline media, the particles reach their isoelectric point and then become progressively negatively charged. In such conditions, the peptide is attracted to the surface of nanoP^3 and subsequently immobilized upon physical contact. These results generally demonstrate that manipulation of solution pH can be used to enhance the binding of charged ligands and potentially orient them on the surface should they have a dipole moment.

6.3.4.5 Retention of cargo bioactivity post-immobilization

The robust binding of cargo to nanoP^3 was further demonstrated for conformationally sensitive molecules and the results compared with that on commercial gold (GNP) and polystyrene (PS) nanoparticles using luciferase as a probe (Figure 6.25a). Luciferase is a bioluminescent enzyme, chosen to allow simultaneous study of functional activity as it is conformationally sensitive and inactive when unfolded [267]. Nanoparticles were incubated with luciferase, followed by three centrifugation washing steps after which the bioluminescence of the supernatant (Figure 6.25b) and the post-wash particles was recorded

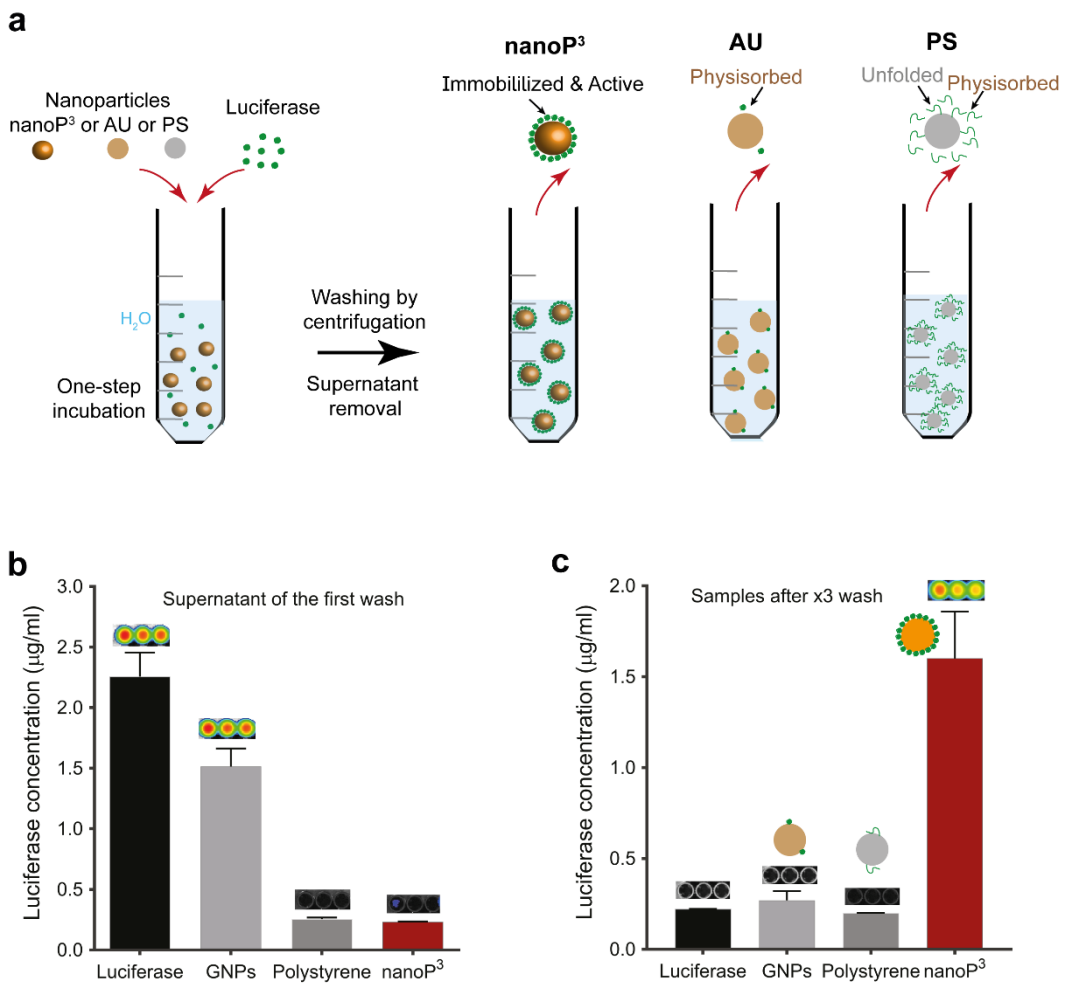

Figure 6.25. a) Schematic diagram to demonstrate the robust binding of bioluminescent luciferase facilitated by nanoP^3 in a simple one-step incubation in aqueous solution. Conjugation with luciferase is also compared with commercial gold (GNP) and polystyrene (PS) nanoparticles. Following multiple washes, luciferase bioluminescence, requiring both binding and bioactivity was quantified. b) Evaluation of the supernatant from the first wash step showed a significant presence of luciferase for the GNP sample, suggesting non-binding of the enzyme to the GNPs. c) Whilst in the final post-wash samples, only nanoP^3 showed a positive signal, indicating retention of bioactive luciferase on the surface of these nanoparticles. The absence of signal for PS suggests unfolding of the enzyme. The plasma parameters were set at Q = 3, 10 and 3 sccm for acetylene, nitrogen and argon, 150 mTorr and 50W. The incubation of nanoP^3 (10^9 nanoP^3/mL) with luciferase (1.0 µg/mL) was performed at room temperature, in RT-PCR grade water for 1 hour.

(Figure 6.25c). The assay demonstrated that nanoP^3 provides a robust immobilization while preserving luciferase activity without any pre-functionalization with chemical cross-linking intermediates. Conversely, signal was detected in the first wash for gold nanoparticles, which require thiol mediated bonds to achieve covalent binding [268], and absent from polystyrene under all conditions due to suspected unfolding and associated loss of activity (Figure 6.25b).

6.3.5 Interaction of nanoP^3 with cells

The interaction of nanoP^3 with multiple cell types was also investigated. Penetration of the cell membrane, subsequent access to the cytoplasm and low toxicity are necessary requisites for nanoparticles to be useful in delivery of bioactive or therapeutic agents [269]. Positively charged nanoparticle platforms including gold, quantum dots and dendrimers can penetrate the negatively charged cell membrane, but can leave behind membrane pores which increase cell death [270]. Specialized nanoparticle shapes, including rods, needles and discs can also pass inside cells at a greater rate than traditional spherical architectures [271]. In the most recent studies, it is the protein corona adsorbed to the nanoparticle surface which determines cellular interactions making the nature of surface interactions with serum proteins of critical importance [272]. However, further analysis through fluorescence-based assays for protein quantification revealed that the nanoparticles adsorbed serum proteins on the surface through electrostatic and hydrophobic complementarity, which allowed the nanoparticle to interface with the cell membrane. Here, unfunctionalized 99 nm (radius) nanoP^3 penetrated the membrane of human coronary artery endothelial cells (hCAECs) and accumulated in small

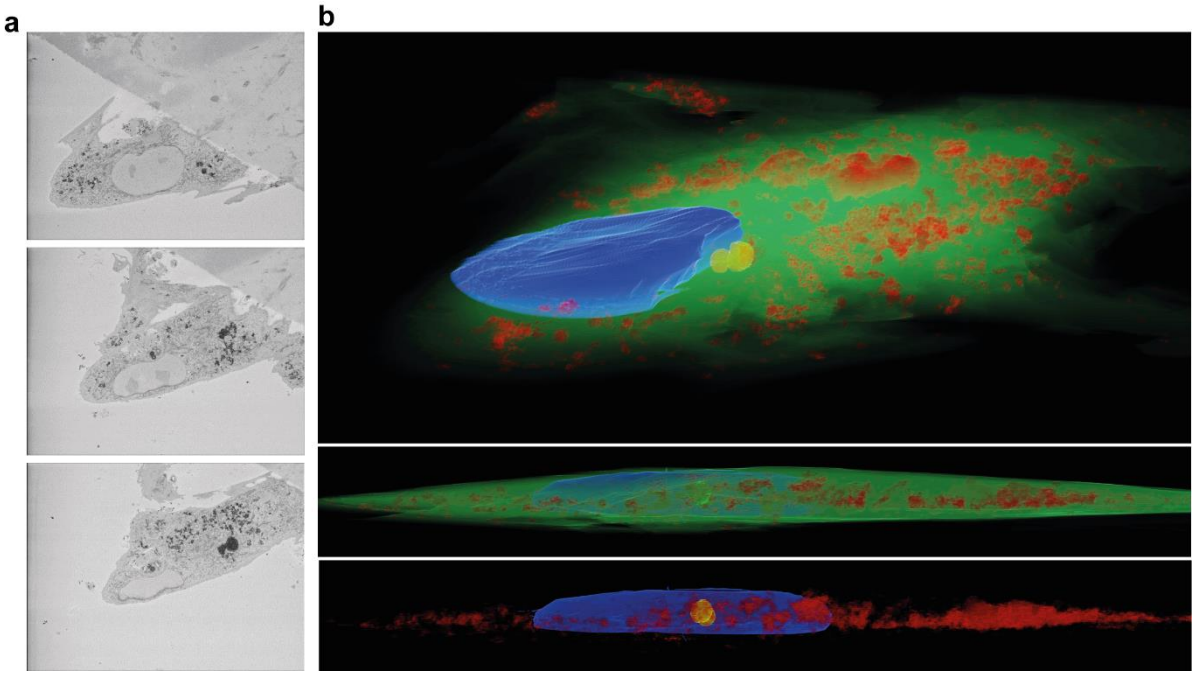

Figure 6.26. a) 3View SEM demonstrates nanoP^3 inside the cell membrane of human coronary artery endothelial cells, appearing as dark spheres outside of the nucleus. b) 3D reconstruction of the 3View sections shows a homogenous distribution of nanoP^3 (red) in the cytoplasm (green). The cell nucleus is shown in blue. The nanoP^3 synthesis parameters were set at Q = 3, 10 and 3 sccm for acetylene, nitrogen and argon, 150 mTorr and 50W. 3View SEM was acquired with the technical support of Dr Minh Huynh and cell culture experiments were performed with the support of Mrs Praveesuda Michael and Dr Minh Huynh.

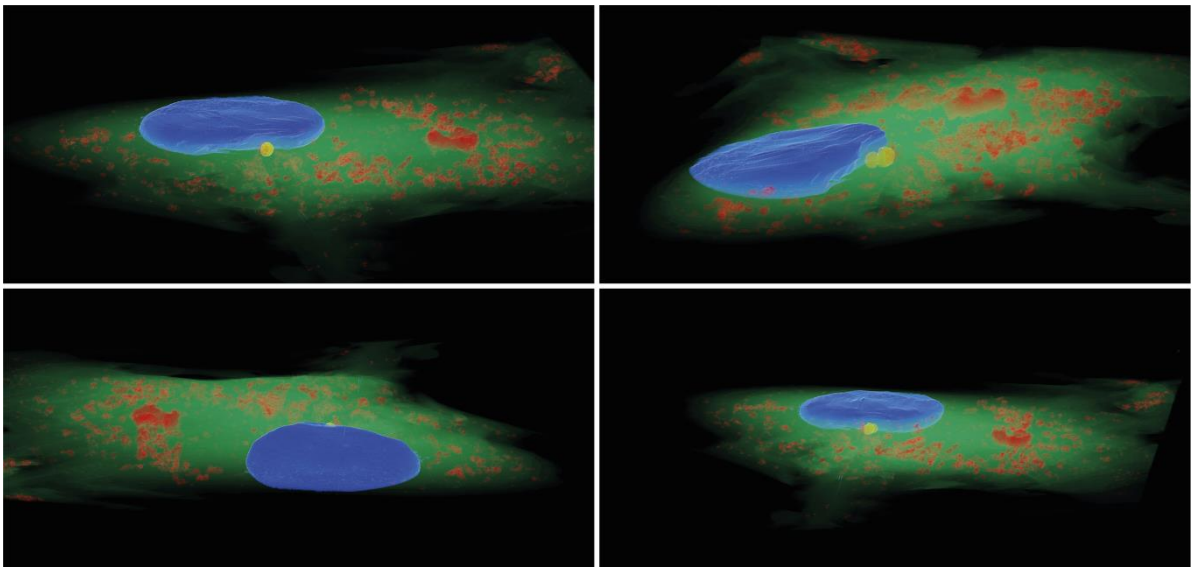

Figure 6.27. As in Figure 6.26b viewed from different orientations. Cell culture experiments were performed with the support of Mrs Praveesuda Michael.

clusters within the cytoplasm after 24 hours of incubation, observed using serial block face (SBF) SEM (Figure 6.26a). SBF SEM facilitates serial sectioning of single cells inside the scanning electron microscope, providing definitive evidence for the presence of nanoP^3 inside the cell membrane. Reconstruction of multiple slices shows the clear presence of nanoP^3, appearing as dark spheres outside of the nucleus (see Movie S5). 3D rendering of the SBF SEM images best shows the distribution of nanoP^3 inside the cell membrane (Figure 6.26b and 6.27). These results indicate that nanoP^3 readily cross the cell membrane without the requirement for surface functionalization with cell penetrating agents, in contrast to gold [273] and polymer-based [274] platforms which require peptide-mediated conjugation. While nanoP^3 are positively charged at physiological pH it is likely that they rapidly conjugate serum proteins when added to the cell media, consistent with their binding behavior described above, and that these attached proteins drive interactions with the cell membrane. While further studies will determine the preferred pathway of cell internalization for differently sized nanoP^3, further assays were performed to determine if they are recycled once inside the cell, or if they are able to reach the cytosol.

Lysosomes are the destination organelles for particles internalized by the general endocytosis pathway, responsible for the processing and recycling of unwanted intracellular material. Confinement of nanoparticles in membrane bounded vesicles, including lysosomes, can prevent release into the cytosol, degrade biological cargo and potentially lead to cellular excretion *via* exocytosis [275]. The relatively rapid lysosomal escape of carriers designed to influence cell function is therefore crucial to their efficacy [276]. Current vectors that enable the lysosomal escape of macromolecules such as viruses, fusogen peptides, cationic lipids,

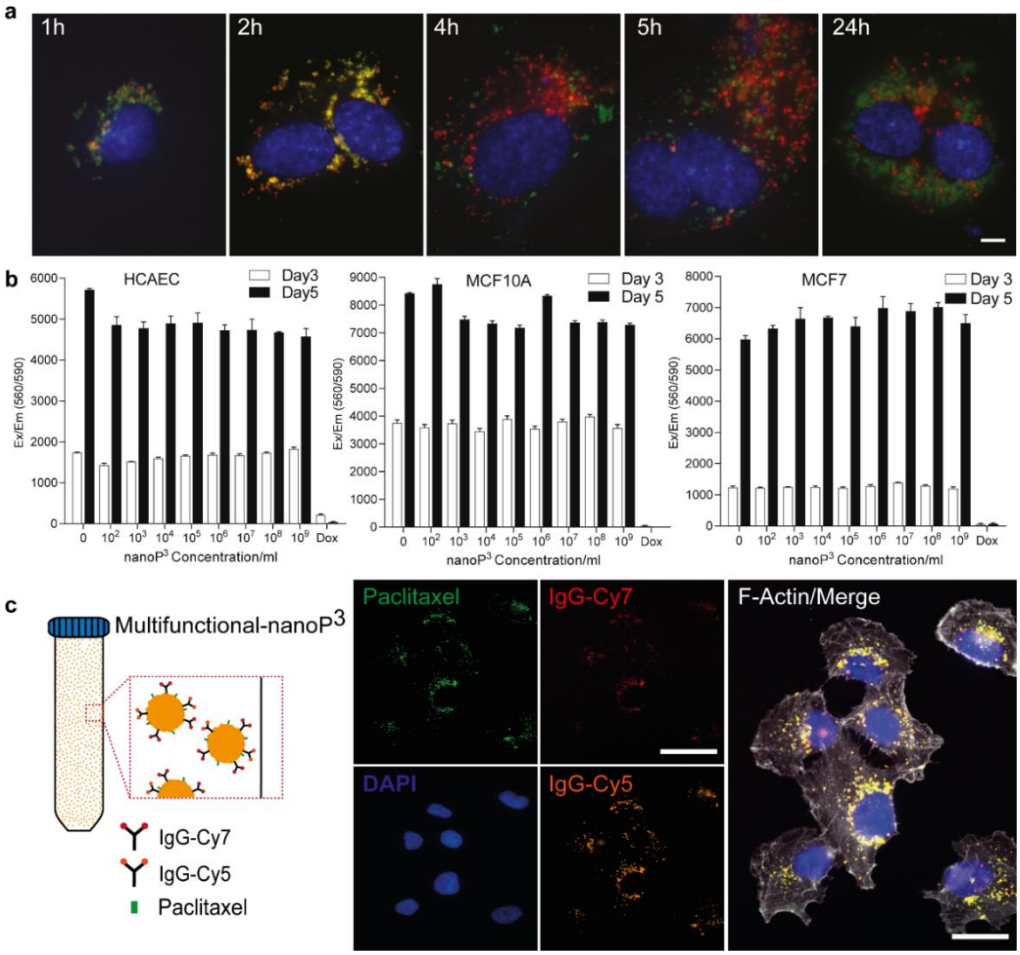

Figure 6.28. a) LysoTracker® staining (red) was used to label acidic organelles including lysosomes, while autofluorescent nanoP^3 were also imaged (green). After 2 hours, co-localization is strongest before separation of staining at 4 and 5 hours, suggesting nanop^3 escape lysosomal compartmentalization. d) Cytotoxicity of nanoP^3 was evaluated in 3 different cell types (i) endothelial cells (hCAECs), (ii) MCF10A, and (iii) MCF7. After 3 and 5 days incubation at increasing nanoP^3 concentrations (up to 10^9 particles/3.2mm^2), no significant reduction in viability was detected and proliferation rates appeared comparable to cell only controls. Doxorubicin (dox) was used as a negative control for cell growth. e) nanoP^3 co-functionalized with paclitaxel (green), IgG-Cy7 (red) and IgG-Cy5 (orange) entered MCF7 cells following incubation, accumulating in the cytoplasm. Scale bar = 20 µm. The nanoP^3 synthesis parameters were set at Q = 3, 10 and 3 sccm for acetylene, nitrogen and argon, 150 mTorr and 50W. The incubation of nanoP^3 (10^9 nanoP^3/mL) with cargo (1.0 µg/mL) was performed at room temperature, in RT-PCR grade water for 1 hour. Cell culture experiments were performed with the support of Mrs Praveesuda Michael.

and cationic polymers are limited by their immunogenicity, toxicity and by their ability to carry only limited classes of therapeutic agents [277]. Lysotracker (a lysosome-staining red fluorescent dye) was used to stain the lysosomes, and the autoflourescence of nanoP^3 was used to determine their co-localization (Figure 6.28a). One hour after incubation, few lysosomes were observed within the cells, increasing in number by two hours. Co-localization of nanoP^3 with lysosomes at 2 hours was significant, reflected in the abundant yellow staining in the image. By 4 hours, green nanoP^3 is clearly observed outside of the lysosomes, increasingly so at 5 hours. At the latest timepoint of 24 hours nanoP^3 is clearly separate from the stained lysosomes. These data suggest that nanoP^3 can escape lysosome compartmentalization by 4 hours.

Further nanoP^3 incubation with hCAECs, epithelial MCF10A or human breast adenocarcinoma cells (MCF7) for up to 5 days did not significantly affect cell proliferation, with up to $3.1x10^8$ particles per mm^2 (Figure 6.28b). Rates of growth were marginally lower in HCAECs for all nanoparticle concentrations, somewhat variable for MCF10A with no clear trend for concentration and unchanged for MC7 compared to cell only controls. Cell morphology also appears unaffected after 3 and 5 days in culture, demonstrating that nanoP^3 were well tolerated in multiple cell types at high concentrations. In contrast, several of the most commonly used nanoparticle platforms, including gold [278], silver [279] and zinc oxide (ZnO) [280] carry concerns regarding toxicity, influenced by size, shape and surface functionalities.

The addition of multiple functionalities to nanoparticles without the requirement for post synthesis modification and purification would break one of the critical impasses preventing timely clinical translation of new therapies. Transfer of multiple cargo into cells was demonstrated using paclitaxel-488, IgG-Cy5 and IgG-Cy7 as triple functionalized nanoP^3 in MCF10A (Figure 7e), MCF7 and hCAECs. Confocal imaging showed the presence of paclitaxel (green), IgG-Cy5 (red) and IgG-Cy7 (orange) co-localized within the cell membrane (Figure 6.28c). These data show that multiple cargo can be carried across the cell membrane when bound to nanoP^3, appearing to remain bound after entry. As it is not expected that the surface of nanoP^3 was fully saturated with cargo at the incubation concentrations used (see Figure 6.28b), the presence of additional serum proteins on the surface is likely to have played a role in interactions with the cell. While the results presented earlier demonstrated the retention of luciferase bioactivity bound to nanoP^3, consistent with our previous findings of conformation retention on plasma polymerized surfaces, retention of antibody/drug functionality once inside the cell was not determined in this first proof-of-concept experiment. Further studies are required to validate that intracellular activity is retained. The current data set suggests that nanoP^3 are effective carriers to transport ligands to the cytosol, but not the nucleus and that the covalent binding to the platform prevents cargo release once inside the cell. Future work will determine the utility of cleavable intermediates, well validated in other systems [281] to facilitate intracellular release and nuclear transport for payloads with this additional requirement.

6.4 CONCLUSION

This chapter demonstrated that the synthesis of multifunctional nanoparticles by plasma bulk polymerization in acetylene dusty plasmas may offer a series of benefits over current multi-step wet-chemistry approaches. It was shown that the physical and chemical properties of nanoP^3, including aggregation, surface topography, size distribution, charge, surface chemistry and fluorescence can be modulated by appropriate choice of process parameters. NanoP^3 retain a similar surface activity characteristic of thin film coatings synthesized by surface plasma polymerization. Functional radical groups activated in excess during the formation of initial PCN clusters (protoparticles), and further diffusion of active radical molecules during rapid cluster aggregation, are preserved within the nanoP^3 carbon matrix. This unique radical-rich surface chemistry, allows for robust immobilization of cargo without the need for intermediate functionalization and purification steps, and combined with a long active shelf life, has great potential to overcome many of the major limitations of currently proposed nanoparticle platforms. The robust and versatile immobilization features of nanoP^3 were demonstrated here using a library of biomolecules of wide ranging structures, molecular weights and biological functions. Importantly, the biological activity and conformation of the molecules is preserved on the nanoP^3, as suggested by the immobilization of the bioluminescent enzyme luciferase. Immobilization of highly-charged cargo was achieved by lowering the zeta-potential of the particles significantly below their isoelectric point, as demonstrated with the robust binding of polycationic peptide sequences in highly alkaline media. NanoP^3 is readily internalised by various cells, escape lysosomal compartmentalisation with no evidence of cytotoxicity, facilitating the delivery of multiple

cargo across the membrane. The universal binding surface of nanoP^3 paves the way for the design of personalized nanocarriers, allowing the end user to obtain theranostic agents in a one-step incubation and according to immediate needs. As many of the favorable characteristics of nanoP^3 are inherent to the fabrication process, this work proposes plasma bulk polymerization in reactive dusty plasmas as a nanoparticle synthesis route with valuable potential for broad clinical and commercial applications.

7 FINAL REMARKS

This thesis extensively explores the synthesis, characterization and optimization of biofunctionalisable nanomaterials produced by plasma polymerization in reactive gaseous mixtures. The first part, reported in Chapters 3 and 4, deals with the deposition of carbon-based plasma activated coatings (PAC) on medical grade substrates, and particularly on cardiovascular stents. An optimal plasma polymerization window of parameters was identified, enabling the reproducible synthesis of PAC coatings that combine exceptional mechanical properties with an easily functionalisable and haemocompatible surface. This ideal window of parameters was identified through the development a control feedback strategy combining in-situ and non-invasive optical emission spectroscopy (OES) measurements, a plasma macroscopic description and extensive physical and chemical characterization of the coatings. Process optimization was driven by multiple physical, chemical and biological considerations, necessary to address current clinical demands.

Mechanically robust PAC coatings are obtained under high energy input per unit monomer mass, Φ_d, and high monomer residence times $\tau_{\text{Acetylene}}$ in the active plasma. In particular, PAC formulations prepared at $\Phi_d \geq 5.5 \times 10^8$ J/kg (corresponding to $Q_{\text{Acetylene}} \leq 2$ sccm and a rf power of 50 W), $\tau_{\text{Acetylene}} \approx 8$ s and $250\ \text{V} \leq |V_{\text{bias}}| \leq 500\ \text{V}$ can be grown uniformly on SS substrates with robust adhesion. The enhanced adhesion of PAC at higher monomer fragmentation regimes is consistent with previously reported thin-film growth models, such as the competitive ablation and polymerization (CAP) and rapid step growth polymerization (RSGP) models [70, 128]. In this work, the implementation of OES diagnostics shows that PAC ablation is driven by the bombardment of ions, such as N_2^+

molecular ions, which compromise coating growth when $|V_{\text{bias}}| \geq 750$ V. PAC ablation was confirmed by a simultaneous reduction of the coating deposition rate and an increase in the number density of CN molecular radicals excited in the plasma, the latter caused by preferential sputtering of these hybridizations upon the bombardment of N_2^+ molecular ions. Robust PAC-substrate interlayers are achieved at an equilibrium between coating ablation and deposition rates for $|V_{\text{bias}}| \leq 500$ V and $Q_{\text{Acetylene}} \leq 2$ sccm, a deposition parameter window that yields emission intensity ratios between CN radical molecules and N_2^+ ions in the plasma of $I_{\text{CN}}/I_{N_2^+} \geq 2$.

While substrate adhesion is further enhanced by the bombardment of energetic ions at mildly applied substrate bias ($|V_{\text{bias}}| \leq 500$ V), this process also generates an excess of radical groups in the coating bulk. Mechanically resilient PAC are created with high fractional nitrogen atomic content (33%) and a radical density (2.8×10^{17}spins/cm^3) at $|V_{\text{bias}}| = 250$ V. Radicals that diffuse towards the PAC surface over time are utilised to bioactivate the coating through the immobilization of biofunctional molecules. The linker-free immobilization of bioactive molecules on coatings developed in this work include tropoelastin, plasmin and apoliprotein A-I and has been exemplified in several publications [4, 6-8]. Additionally, these PAC formulations were tested in an assemble of thrombogenic assays, demonstrating significant reduction in platelet adhesion and activation as well as suppression of thrombus formation under both static and flow conditions.

Resilient, biofunctional and haemocompatible PAC was translated to medical grade stents of various designs and alloy compositions, demonstrating the versatility of the coating deposition process. Overall, the exceptional substrate adhesion of PAC developed here represents an advance over previous works, where coating adhesion to the stents was achieved through the application carbon-metal graded layers that require more time-consuming and multi-step plasma deposition platforms [157]. In-vivo experiments in rabbits and ex-vivo pre-clinical trials in non-human primates are being undertaken to further assess the biocompatible properties of PAC (unpublished data not shown here).

This thesis further explores for the first-time plasma polymerised nanoparticles (nanoP^3), synthesized in acetylene dusty plasmas under similar conditions as PAC, as multifunctional nanocarriers for applications in nanomedicine. Chapters 5 and 6 carry out a pioneering and comprehensive synthesis, collection and analysis of the physical, chemical, optical, biocompatible and surface binding properties of nanoP^3. The continuous and cyclic formation of nanoP^3 was first observed as oscillations in the plasma emission spectrum during the deposition of PAC. OES measurements allowed the identification of key growth mechanisms in the formation of nanoP^3, such as the diffusion of CN radicals excited in the plasma towards the growing particles. The presence of CN hybridizations in the particles was confirmed by XPS and FTIR measurements, while ESR showed the presence of long-lived radicals. Importantly, it was shown that nanoP^3 could potentially be adopted as a new, cost-effective and multifunctional theranostic platform. The radical-rich surface of nanoP^3 allows the linker-free immobilization of biologically functional cargo in a one-step incubation process and without the requirement for traditional step-wise linker-chemistry. The nanoP^3 binding

versatility was demonstrated by using a panoply of molecules that include small radical scavengers such as DPPH, widely available drugs like paclitaxel, oligonucleotide acids (silencing RNA), imaging dyes (cardiogreen) and antibodies. Further experiments using cardiogreen as a template cargo molecule show that the binding kinetics are fast, with 90% of the cargo present in solution binding to nanoP^3 within only 30 seconds of incubation at room temperature. Complete surface saturation is observed in less than 5 minutes independent of the solution's temperature. The particles have a long shelf life with immobilization efficiency unaltered up to at least 6 months of storage in air and room temperature compared with freshly produced nanoP^3.

Additionally, it was shown that the central features of nanoP^3 can be modulated by selection of appropriate parameters in the plasma polymerization process. NanoP^3 are reproducibly synthesized with modulated features, such as surface morphology, aggregation, size distribution, surface charge and chemistry by generating plasma discharges at suitable pressure, gas flow rate and coupled power. For instance, the morphology and the size are dependent on the initial size of smaller clusters (or protoparticles) that aggregate to form nanoP^3 in the initial and intermediate stages of the formation cycle. Particularly, increasing the acetylene flow rate and coupled power yields smaller clusters, which translate into smaller and more spherical nanoP^3.

While the use of flat substrates results in the deposition of particle-free PAC coatings, this work shows that nanoP^3 can be efficiently collected in dusty plasmas by using three dimensional substrates, such as cylindrical wells. Since the particles are negatively charged

and are electrostatically stabilized by Coulomb repulsion in the active plasma, the aspect ratio of the wells determines the degree to which the plasma can penetrate the well, which ultimately modulates the aggregation of as-synthesized nanoP^3. Incidentally, nanoP^3 aggregation upon collection was significantly suppressed by using collector devices, emulated here with tissue culture well plates, with relatively shorter wells. When suspended in aqueous solution directly from the wells, the nanoparticles acquire a positive net charge at physiological pH due to the protonation of surface functional groups such as amines. Increasing the solution pH to highly alkaline media renders negatively charged nanoP^3 as deprotonation of surface carboxylic acid groups becomes more dominant. Since the aggregation and instability of nanoP^3 is modulated by the solution pH at which the particles reach their isoelectric point (i.e. neutral surface charge), the surface chemistry of nanoP^3 can be engineered such that the nanoparticles have sufficiently high net charge to repel each other in solution. For instance, the solution pH at which the isoelectric point occurs increases significantly for nanoP^3 synthesised with larger nitrogen atomic fractions, as a more alkaline medium is necessary to deprotonate a larger amount of surface amine groups. Besides controlling the stability in solution, this feature is particularly useful when binding of highly charged cargo to the nanoparticles is required, as shown in this work through the binding of highly positively charged peptides in highly alkaline media. Surface charge tunability of nanoP^3 could be further explored in future work to orient polar cargo which require the active site to be readily available on the particle surface following immobilization.

Overall, the process is compatible with scale-up to high throughput, low-cost commercial production, demonstrated by the high nanoP^3 mass yield obtained at high coupled power and

high monomer flow rate (100 W and acetylene flow rate of 6 sccm). The estimated cost of nanoP^3 is only $5 per gram, including raw material (acetylene, nitrogen and argon gases) and electricity costs. This places nanoP^3 as a strong competitive alternative platform to commercial nanoparticles, typically available at 30000-fold the production cost of nanoP^3. Taken together, the data demonstrates that nanoP^3 uniquely offers a simple, rapid, cost-effective platform for the delivery of multiple bioactive agents, with significant implications for improving the efficacy of molecular cargo. The universal binding features of nanoP^3 combined with their low cytotoxicity and intracellular trafficking properties are required features, paramount in facilitating the translation of nanoparticle-based therapy libraries into the commercial and clinical domain. Plasma dust nanoparticles are ubiquitous in space, commonly observed in reactive plasmas but have long been regarded as detrimental to many manufacturing and energy processes. As the bulk of research has sought only to study the dynamics and mechanisms of formation, ultimately to eliminate these plasma nanoparticles, their potential in theranostics has been so far overlooked. By demonstrating the unanticipated use of plasma dust in theranostics, however, these findings represent a paradigm shift that spans the fields of plasma physics, materials science, nanotechnology and nanoparticle synthesis.

Finally, this work should be regarded as part of a wider interdisciplinary research program. The synthesis and characterization of nanoP^3 paves the way for future developments in nanomedicine and tissue engineering. In particular, the findings reported in this thesis have inspired substantial research aiming to explore the use of nanoP^3 as nanocarriers in multiple applications, including cancer and cardiovascular research, gene therapy and diagnostics as

well as multifunctionalization of three-dimensional scaffolds for tissue engineering (unpublished data not shown). Optimal nanoP^3 formulations may substantially differ in size, chemical composition and nanoparticle shape, depending on specific applications. Therefore, the synthesis of nanoP^3 can be further explored outside the process parameter windows reported here and by using gaseous mixtures containing alternative monomers and carrier gases. The transition observed in the discharge between bulk (nanoP^3 formation) and surface plasma polymerization (PAC deposition) could be also further explored, envisaging the one-step synthesis and characterization of coating-nanoparticle hybrid structures as exemplified in Figure 5.2.

REFERENCES

1. Miguel Santos, P.L.M., Elysse C. Filipe, Alex H.P. Chan, Juichien Hung, Richard P. Tan, Bob S.L. Lee, Minh Huynh, Clare Hawkins, Anna Waterhouse, Marcela M. M. Bilek and Steven G. Wise, *Plasma synthesis of carbon-based nanocarriers for linker-free immobilization of bioactive cargo.* ACS Appl Nanomaterials, 2017. **1**(2): p. 580-594.
2. Miguel Santos, P.L.M., Marcela M. M. Bilek and Steven G. Wise, *Plasma polymerization of nanoparticles in dusty plasmas for applications in nanomedicine.* under preparation for submission to Scientific Reports 2018.
3. Miguel Santos, P.L.M., Marcela M. M. Bilek and Steven G. Wise, *Fluorescent properties of plasma polymerized amorphous carbon nanoparticles.* under preparation for submission to Scientific Reports, 2018.
4. Santos, M., et al., *Mechanically Robust Plasma-Activated Interfaces Optimized for Vascular Stent Applications.* ACS Appl Mater Interfaces, 2016. **8**(15): p. 9635-50.
5. Santos, M., M.M.M. Bilek, and S.G. Wise, *Plasma-synthesised carbon-based coatings for cardiovascular applications.* Biosurface and Biotribology, 2015. **1**(3): p. 146-160.
6. Vanags, L.Z., et al., *Plasma activated coating immobilizes apolipoprotein A-I to stainless steel surfaces in its bioactive form and enhances biocompatibility.* Nanomedicine: Nanotechnology, Biology and Medicine. **13**(7): p. 2141-2150.
7. Yeo, G.C., et al., *Plasma-Activated Tropoelastin Functionalization of Zirconium for Improved Bone Cell Response.* ACS Biomaterials Science & Engineering, 2016. **2**(4): p. 662-676.
8. Wise, S.G., et al., *Immobilization of bioactive plasmin reduces the thrombogenicity of metal surfaces.* Colloids and Surfaces B: Biointerfaces, 2015. **136**: p. 944-954.
9. Santos, M., et al., *11 - Simple one-step covalent immobilization of bioactive agents without use of chemicals on plasma-activated low thrombogenic stent coatings A2 - Wall, J. Gerard*, in *Functionalised Cardiovascular Stents*, H. Podbielska and M. Wawrzyńska, Editors. 2018, Woodhead Publishing. p. 211-228.
10. Ratner, B.D., *A paradigm shift: biomaterials that heal.* Polymer International, 2007. **56**(10): p. 1183-1185.
11. *Organization for Economic Co-operation and Development*. 2011; Available from: http://www.oecd.org/. (Figures 4.7.1 and 4.7.2)
12. *Centers for Disease Control and Prevention*. 2013; Available from: http://www.cdc.gov/nchs/fastats/inpatient-surgery.htm.
13. *World Health Organization, Cardiovascular disease*. 2011; Available from: http://www.who.int/mediacentre/factsheets/fs317/en/.
14. Serruys, P.W., M.J. Kutryk, and A.T. Ong, *Coronary-artery stents.* N Engl J Med, 2006. **354**(5): p. 483-95.

15. Honda, Y. and P.J. Fitzgerald, *Stent thrombosis: an issue revisited in a changing world.* Circulation, 2003. **108**(1): p. 2-5.
16. Kornowski, R., et al., *In-stent restenosis: Contributions of inflammatory responses and arterial injury to neointimal hyperplasia.* Journal of the American College of Cardiology, 1998. **31**(1): p. 224-230.
17. Dani, S., et al., *Biodegradable-polymer-based, sirolimus-eluting Supralimus stent: 6-month angiographic and 30-month clinical follow-up results from the series I prospective study.* EuroIntervention, 2008. **4**(1): p. 59-63.
18. Han, Y., et al., *Sustained clinical safety and efficacy of a biodegradable-polymer coated sirolimus-eluting stent in "real-world" practice: Three-year outcomes of the CREATE (multi-center registry of EXCEL biodegradable polymer drug eluting stents) study.* Catheterization and Cardiovascular Interventions, 2012. **79**(2): p. 211-216.
19. Vranckx, P., et al., *Biodegradable-polymer-based, paclitaxel-eluting Infinnium stent: 9-Month clinical and angiographic follow-up results from the SIMPLE II prospective multi-centre registry study.* EuroIntervention, 2006. **2**(3): p. 310-7.
20. Kandzari, D.E., et al., *Late-Term Clinical Outcomes With Zotarolimus- and Sirolimus-Eluting Stents: 5-Year Follow-Up of the ENDEAVOR III (A Randomized Controlled Trial of the Medtronic Endeavor Drug [ABT-578] Eluting Coronary Stent System Versus the Cypher Sirolimus-Eluting Coronary Stent System in De Novo Native Coronary Artery Lesions).* JACC: Cardiovascular Interventions, 2011. **4**(5): p. 543-550.
21. Krucoff, M.W., et al., *A New Era of Prospective Real-World Safety Evaluation: Primary Report of XIENCE V USA (XIENCE V Everolimus Eluting Coronary Stent System Condition-of-Approval Post-Market Study).* JACC: Cardiovascular Interventions, 2011. **4**(12): p. 1298-1309.
22. Stone, G.W., et al., *Long-Term Safety and Efficacy of Paclitaxel-Eluting Stents: Final 5-Year Analysis From the TAXUS Clinical Trial Program.* JACC: Cardiovascular Interventions, 2011. **4**(5): p. 530-542.
23. Curfman, G.D., et al., *Drug-eluting coronary stents--promise and uncertainty.* N Engl J Med, 2007. **356**(10): p. 1059-60.
24. Chen, J.P., et al., *Drug-Eluting Stent Thrombosis The Kounis Hypersensitivity-Associated Acute Coronary Syndrome Revisited.* Jacc-Cardiovascular Interventions, 2009. **2**(7): p. 583-593.
25. Lee, B.S., et al., *Surface grafting of blood compatible zwitterionic poly(ethylene glycol) on diamond-like carbon-coated stent.* Journal of Materials Science-Materials in Medicine, 2011. **22**(3): p. 507-514.
26. Cho, H.H., et al., *The behavior of vascular smooth muscle cells and platelets onto epigallocatechin gallate-releasing poly(l-lactide-co-ε-caprolactone) as stent-coating materials.* Biomaterials, 2008. **29**(7): p. 884-893.
27. Hibbert, B., S. Olsen, and E. O'Brien, *Involvement of Progenitor Cells in Vascular Repair.* Trends in Cardiovascular Medicine, 2003. **13**(8): p. 322-326.
28. Aoki, J., et al., *Endothelial Progenitor Cell Capture by Stents Coated With Antibody Against CD34: The HEALING-FIM (Healthy Endothelial Accelerated Lining*

Inhibits Neointimal Growth-First In Man) Registry. Journal of the American College of Cardiology, 2005. **45**(10): p. 1574-1579.
29. Beijk, M.A.M., et al., *Genous™ endothelial progenitor cell capturing stent vs. the Taxus Liberté stent in patients with de novo coronary lesions with a high-risk of coronary restenosis: a randomized, single-centre, pilot study.* European Heart Journal, 2010. **31**(9): p. 1055-1064.
30. Lei, J., et al., *Nitric oxide, a protective molecule in the cardiovascular system.* Nitric Oxide, 2013. **35**(0): p. 175-185.
31. Garg, U.C. and A. Hassid, *Nitric oxide-generating vasodilators and 8-bromo-cyclic guanosine monophosphate inhibit mitogenesis and proliferation of cultured rat vascular smooth muscle cells.* The Journal of Clinical Investigation, 1989. **83**(5): p. 1774-1777.
32. Dubey, R.K., et al., *Nitric oxide inhibits angiotensin II-induced migration of rat aortic smooth muscle cell. Role of cyclic-nucleotides and angiotensin1 receptors.* The Journal of Clinical Investigation, 1995. **96**(1): p. 141-149.
33. Ziche, M., et al., *Nitric oxide mediates angiogenesis in vivo and endothelial cell growth and migration in vitro promoted by substance P.* The Journal of Clinical Investigation, 1994. **94**(5): p. 2036-2044.
34. McCall, T.B., et al., *Synthesis of nitric oxide from L-arginine by neutrophils. Release and interaction with superoxide anion.* Biochem J, 1989. **261**(1): p. 293-6.
35. Radomski, M.W., R.M. Palmer, and S. Moncada, *Endogenous nitric oxide inhibits human platelet adhesion to vascular endothelium.* Lancet, 1987. **2**(8567): p. 1057-8.
36. McNamara, D.B., et al., *L-arginine inhibits balloon catheter-induced intimal hyperplasia.* Biochem Biophys Res Commun, 1993. **193**(1): p. 291-6.
37. Yoon, J.H., et al., *Local Delivery of Nitric Oxide from an Eluting Stent to Inhibit Neointimal Thickening in a Porcine Coronary Injury Model.* Yonsei Med J, 2002. **43**(2): p. 242-251.
38. Lin, C.-E., et al., *Combination of Paclitaxel and Nitric Oxide as a Novel Treatment for the Reduction of Restenosis.* Journal of Medicinal Chemistry, 2004. **47**(9): p. 2276-2282.
39. Nieman, K., et al., *Multislice computed tomography angiography for noninvasive assessment of the 18-month performance of a novel radiolucent bioresorbable vascular scaffolding device: the ABSORB trial (a clinical evaluation of the bioabsorbable everolimus eluting coronary stent system in the treatment of patients with de novo native coronary artery lesions).* J Am Coll Cardiol, 2013. **62**(19): p. 1813-4.
40. Tamai, H., et al., *Initial and 6-month results of biodegradable poly-l-lactic acid coronary stents in humans.* Circulation, 2000. **102**(4): p. 399-404.
41. Serruys, P.W., et al., *A bioabsorbable everolimus-eluting coronary stent system (ABSORB): 2-year outcomes and results from multiple imaging methods.* Lancet, 2009. **373**(9667): p. 897-910.
42. William M Wilson, N.L.C., *Advances in coronary stent technology: current expectations and new developments.* Research Reports in Clinical Cardiology, 2013. **4**.

43. Chou, L.Y., K. Ming, and W.C. Chan, *Strategies for the intracellular delivery of nanoparticles.* Chem Soc Rev, 2011. **40**(1): p. 233-45.
44. Petros, R.A. and J.M. DeSimone, *Strategies in the design of nanoparticles for therapeutic applications.* Nature Reviews Drug Discovery, 2010. **9**(8): p. 615-627.
45. Peer, D., et al., *Nanocarriers as an emerging platform for cancer therapy.* Nat Nano, 2007. **2**(12): p. 751-760.
46. Jo, H. and C. Ban, *Aptamer-nanoparticle complexes as powerful diagnostic and therapeutic tools.* Exp Mol Med, 2016. **48**: p. e230.
47. Dahlman, J.E., et al., *In vivo endothelial siRNA delivery using polymeric nanoparticles with low molecular weight.* Nat Nano, 2014. **9**(8): p. 648-655.
48. Weissleder, R., M. Nahrendorf, and M.J. Pittet, *Imaging macrophages with nanoparticles.* Nat Mater, 2014. **13**(2): p. 125-138.
49. Pu, K., et al., *Semiconducting polymer nanoparticles as photoacoustic molecular imaging probes in living mice.* Nat Nano, 2014. **9**(3): p. 233-239.
50. Sperling, R.A. and W.J. Parak, *Surface modification, functionalization and bioconjugation of colloidal inorganic nanoparticles.* Philosophical Transactions of the Royal Society A: Mathematical, Physical and Engineering Sciences, 2010. **368**(1915): p. 1333-1383.
51. Yu, M.K., J. Park, and S. Jon, *Targeting strategies for multifunctional nanoparticles in cancer imaging and therapy.* Theranostics, 2012. **2**(1): p. 3-44.
52. Cheng, Z.L., et al., *Multifunctional Nanoparticles: Cost Versus Benefit of Adding Targeting and Imaging Capabilities.* Science, 2012. **338**(6109): p. 903-910.
53. Rogers, W.B., W.M. Shih, and V.N. Manoharan, *Using DNA to program the self-assembly of colloidal nanoparticles and microparticles.* Nature Reviews Materials, 2016. **1**(3).
54. Zhang, Y.G., et al., *A general strategy for the DNA-mediated self-assembly of functional nanoparticles into heterogeneous systems.* Nature Nanotechnology, 2013. **8**(11): p. 865-872.
55. Ashley, C.E., et al., *The targeted delivery of multicomponent cargos to cancer cells by nanoporous particle-supported lipid bilayers (vol 10, pg 389, 2011).* Nature Materials, 2011. **10**(6): p. 476-476.
56. Wang, H., et al., *A biomimetic hybrid nanoplatform for encapsulation and precisely controlled delivery of therasnostic agents.* Nature Communications, 2015. **6**.
57. Zhang, J. and R.D. Misra, *Magnetic drug-targeting carrier encapsulated with thermosensitive smart polymer: core-shell nanoparticle carrier and drug release response.* Acta Biomater, 2007. **3**(6): p. 838-50.
58. Lee, S.M., et al., *"Clickable" Polymer-Caged Nanobins as a Modular Drug Delivery Platform.* Journal of the American Chemical Society, 2009. **131**(26): p. 9311-9320.
59. Gref, R., et al., *'Stealth' corona-core nanoparticles surface modified by polyethylene glycol (PEG): influences of the corona (PEG chain length and surface density) and of the core composition on phagocytic uptake and plasma protein adsorption.* Colloids and Surfaces B: Biointerfaces, 2000. **18**(3–4): p. 301-313.
60. Yeo, G.C., et al., *Plasma-Activated Tropoelastin Functionalization of Zirconium for Improved Bone Cell Response.* Acs Biomaterials Science & Engineering, 2016. **2**(4): p. 662-676.

61. Santos, M., et al., *Mechanically Robust Plasma-Activated Interfaces Optimized for Vascular Stent Applications.* Acs Applied Materials & Interfaces, 2016. **8**(15): p. 9635-9650.
62. Lieberman, M.A. and A.J. Lichtenberg, *Principles of plasma discharges and materials processing*. 2nd ed. 2005, Hoboken, N.J.: Wiley-Interscience. xxxv, 757 p.
63. Shukla, P.K. and A.A. Mamun, *Introduction to dusty plasma physics*. 2002, Bristol: Institute of Physics Publishing.
64. Bogaerts, A., et al., *Gas discharge plasmas and their applications.* Spectrochimica Acta Part B: Atomic Spectroscopy, 2002. **57**(4): p. 609-658.
65. Park, G.Y., et al., *Atmospheric-pressure plasma sources for biomedical applications.* Plasma Sources Science and Technology, 2012. **21**(4): p. 043001.
66. Yasuda, H. and T. Hsu, *Some aspects of plasma polymerization investigated by pulsed R.F. discharge.* Journal of Polymer Science: Polymer Chemistry Edition, 1977. **15**(1): p. 81-97.
67. Yang, P., et al., *Haemocompatibility of hydrogenated amorphous carbon (a-C:H) films synthesized by plasma immersion ion implantation-deposition.* Nuclear Instruments and Methods in Physics Research Section B: Beam Interactions with Materials and Atoms, 2003. **206**(0): p. 721-725.
68. Hadar, M.-L., et al., *Effect of Radio-Frequency and Low-Frequency Bias Voltage on the Formation of Amorphous Carbon Films Deposited by Plasma Enhanced Chemical Vapor Deposition.* Plasma Science and Technology, 2014. **16**(10): p. 954.
69. Yin, Y., et al., *Protein immobilization capacity and covalent binding coverage of pulsed plasma polymer surfaces.* Applied Surface Science, 2010. **256**(16): p. 4984-4989.
70. Biederman, H., *Plasma Polymer Films*. 2004: Imperial College Press.
71. Vasudev, M.C., et al., *Exploration of Plasma-Enhanced Chemical Vapor Deposition as a Method for Thin-Film Fabrication with Biological Applications.* ACS Applied Materials & Interfaces, 2013. **5**(10): p. 3983-3994.
72. Yasuda, H.K., et al., *Atomic Interfacial Mixing to Create Water Insensitive Adhesion.* The Journal of Adhesion, 1982. **13**(3-4): p. 269-283.
73. Yasuda, H. and M. Gazicki, *Biomedical applications of plasma polymerization and plasma treatment of polymer surfaces.* Biomaterials, 1982. **3**(2): p. 68-77.
74. Yasuda, H., *Glow discharge polymerization.* Journal of Polymer Science: Macromolecular Reviews, 1981. **16**(1): p. 199-293.
75. Yasuda, H., *Plasma Polymerization*. 1985: Academic Press, INC.
76. Yasuda, H. and T. Hsu, *Plasma polymerization investigated by the comparison of hydrocarbons and perfluorocarbons.* Surface Science, 1978. **76**(1): p. 232-241.
77. Yasuda, H. and C.R. Wang, *Plasma Polymerization Investigated by the Substrate-Temperature Dependence.* Journal of Polymer Science Part a-Polymer Chemistry, 1985. **23**(1): p. 87-106.
78. Yu, Q.S., C. Huang, and H.K. Yasuda, *Glow characterization in direct current plasma polymerization of trimethylsilane.* Journal of Polymer Science Part a-Polymer Chemistry, 2004. **42**(5): p. 1042-1052.

79. Suwa, T., et al., *Plasma polymerization in direct current glow: Characterization of plasma-polymerized films of benzene and fluorinated derivatives.* Microelectronics Technology, 1995. **614**: p. 471-484.
80. Schwarz, J., M. Schmidt, and A. Ohl, *Synthesis of plasma-polymerized hexamethyldisiloxane (HMDSO) films by microwave discharge.* Surface and Coatings Technology, 1998. **98**(1): p. 859-864.
81. Friedrich, J., *Mechanisms of Plasma Polymerization – Reviewed from a Chemical Point of View.* Plasma Processes and Polymers, 2011. **8**(9): p. 783-802.
82. D'Agostino, R., *Plasma deposition, treatment, and etching of polymers*. 1990, Boston: Academic Press.
83. Khelifa, F., et al., *Free-Radical-Induced Grafting from Plasma Polymer Surfaces.* Chemical Reviews, 2016. **116**(6): p. 3975-4005.
84. Groenewoud, L.M.H., et al., *Pulsed Plasma Polymerization of Thiophene.* Langmuir, 2000. **16**(15): p. 6278-6286.
85. Thiry, D., et al., *Plasma diagnostics for the low-pressure plasma polymerization process: A critical review.* Thin Solid Films, 2016. **606**: p. 19-44.
86. Han, L.M., R.B. Timmons, and W.W. Lee, *Pulsed plasma polymerization of an aromatic perfluorocarbon monomer: Formation of low dielectric constant, high thermal stability films.* Journal of Vacuum Science & Technology B: Microelectronics and Nanometer Structures Processing, Measurement, and Phenomena, 2000. **18**(2): p. 799-804.
87. Hynes, A.M., M.J. Shenton, and J.P.S. Badyal, *Pulsed Plasma Polymerization of Perfluorocyclohexane.* Macromolecules, 1996. **29**(12): p. 4220-4225.
88. Rinsch, C.L., et al., *Pulsed Radio Frequency Plasma Polymerization of Allyl Alcohol: Controlled Deposition of Surface Hydroxyl Groups.* Langmuir, 1996. **12**(12): p. 2995-3002.
89. Bilek, M.M.M., *Biofunctionalization of surfaces by energetic ion implantation: Review of progress on applications in implantable biomedical devices and antibody microarrays.* Applied Surface Science, 2014. **310**(0): p. 3-10.
90. Bilek, M.M., et al., *Free radical functionalization of surfaces to prevent adverse responses to biomedical devices.* Proc Natl Acad Sci U S A, 2011. **108**(35): p. 14405-10.
91. Langmuir, I., C.G. Found, and A.F. Dittmer, *A New Type of Electric Discharge: The Streamer Discharge.* Science, 1924. **60**(1557): p. 392-4.
92. Goertz, C.K., *Dusty Plasmas in the Solar-System.* Reviews of Geophysics, 1989. **27**(2): p. 271-292.
93. Verheest, F., *Dusty plasmas in application to astrophysics.* Plasma Physics and Controlled Fusion, 1999. **41**: p. A445-A451.
94. Selwyn, G.S., J. Singh, and R.S. Bennett, *In situ laser diagnostic studies of plasma-generated particulate contamination.* Journal of Vacuum Science & Technology A: Vacuum, Surfaces, and Films, 1989. **7**(4): p. 2758-2765.
95. Bouchoule, A., *Dusty plasmas : physics, chemistry, and technological impacts in plasma processing*. 1999, Chichester: Wiley.

96. Winter, J., *Dust in fusion devices - a multi-faceted problem connecting high- and low-temperature plasma physics.* Plasma Physics and Controlled Fusion, 2004. **46**: p. B583-B592.
97. Winter, J., et al., *Dust formation in Ar/CH4 and Ar/C2H2 plasmas.* Plasma Sources Science & Technology, 2009. **18**(3).
98. Hong, S., J. Berndt, and J. Winter, *Growth precursors and dynamics of dust particle formation in the Ar/CH 4 and Ar/C 2 H 2 plasmas.* Plasma Sources Science and Technology, 2003. **12**(1): p. 46.
99. Ming, M., et al., *New pathways for nanoparticle formation in acetylene dusty plasmas: a modelling investigation and comparison with experiments.* Journal of Physics D: Applied Physics, 2008. **41**(22): p. 225201.
100. Bouchoule, A. and L. Boufendi, *Particulate formation and dusty plasma behaviour in argon-silane RF discharge.* Plasma Sources Science & Technology, 1993. **2**(3): p. 204-213.
101. Watanabe, Y., *Formation and behaviour of nano/micro-particles in low pressure plasmas.* Journal of Physics D-Applied Physics, 2006. **39**(19): p. R329-R361.
102. Kobayashi, H., M. Shen, and A.T. Bell, *Effects of Reaction Conditions on the Plasma Polymerization of Ethylene.* Journal of Macromolecular Science: Part A - Chemistry, 1974. **8**(2): p. 373-391.
103. Kobayashi, H., A.T. Bell, and M. Shen, *Formation of an amorphous powder during the polymerization of ethylene in a radio-frequency discharge.* Journal of Applied Polymer Science, 1973. **17**(3): p. 885-892.
104. De Bleecker, K., A. Bogaerts, and W. Goedheer, *Detailed modeling of hydrocarbon nanoparticle nucleation in acetylene discharges.* Physical Review E, 2006. **73**(2): p. 026405.
105. Fridman, A.A., et al., *Dusty plasma formation: Physics and critical phenomena. Theoretical approach.* Journal of Applied Physics, 1996. **79**(3): p. 1303-1314.
106. Stoffels, W.W., et al., *Electron density fluctuations in a dusty Ar/SiH4 rf discharge.* Journal of Applied Physics, 1995. **78**(8): p. 4867-4872.
107. Shukla, P.K. and B. Eliasson, *Colloquium: Fundamentals of dust-plasma interactions.* Reviews of Modern Physics, 2009. **81**(1): p. 25-44.
108. Wu, S., et al., *Plasma-modified biomaterials for self-antimicrobial applications.* ACS Appl Mater Interfaces, 2011. **3**(8): p. 2851-60.
109. Morent, R., et al., *Plasma Surface Modification of Biodegradable Polymers: A Review.* Plasma Processes and Polymers, 2011. **8**(3): p. 171-190.
110. Choudhury, D., et al., *Fabrication and characterization of DLC coated microdimples on hip prosthesis heads.* Journal of Biomedical Materials Research Part B: Applied Biomaterials, 2014: p. n/a-n/a.
111. Waterhouse, A., et al., *The immobilization of recombinant human tropoelastin on metals using a plasma-activated coating to improve the biocompatibility of coronary stents.* Biomaterials, 2010. **31**(32): p. 8332-8340.
112. Waterhouse, A., et al., *In vivo biocompatibility of a plasma-activated, coronary stent coating.* Biomaterials, 2012. **33**(32): p. 7984-7992.

113. Maguire, P.D., et al., *Mechanical stability, corrosion performance and bioresponse of amorphous diamond-like carbon for medical stents and guidewires.* Diamond and Related Materials, 2005. **14**(8): p. 1277-1288.
114. Yang, Z., et al., *A Novel Technique Toward Bipolar Films Containing Alternating Nano–Layers of Allylamine and Acrylic Acid Plasma Polymers for Biomedical Application.* Plasma Processes and Polymers, 2011. **8**(3): p. 208-214.
115. Coad, B.R., et al., *Functionality of Proteins Bound to Plasma Polymer Surfaces.* ACS Applied Materials & Interfaces, 2012. **4**(5): p. 2455-2463.
116. Truica-Marasescu, F. and M.R. Wertheimer, *Nitrogen-Rich Plasma-Polymer Films for Biomedical Applications.* Plasma Processes and Polymers, 2008. **5**(1): p. 44-57.
117. Qi, P., et al., *Multifunctional Plasma-Polymerized Film: Toward Better Anticorrosion Property, Enhanced Cellular Growth Ability, and Attenuated Inflammatory and Histological Responses.* ACS Biomaterials Science & Engineering, 2015. **1**(7): p. 513-524.
118. Wise, S.G., et al., *Plasma-based biofunctionalization of vascular implants.* Nanomedicine (Lond), 2012. **7**(12): p. 1907-16.
119. Aisenberg, S. and R. Chabot, *Ion-Beam Deposition of Thin Films of Diamondlike Carbon.* Journal of Applied Physics, 1971. **42**(7): p. 2953-2958.
120. Dearnaley, G. and J.H. Arps, *Biomedical applications of diamond-like carbon (DLC) coatings: A review.* Surface and Coatings Technology, 2005. **200**(7): p. 2518-2524.
121. Love, C.A., et al., *Diamond like carbon coatings for potential application in biological implants—a review.* Tribology International, 2013. **63**(0): p. 141-150.
122. Roy, R.K. and K.-R. Lee, *Biomedical applications of diamond-like carbon coatings: A review.* Journal of Biomedical Materials Research Part B: Applied Biomaterials, 2007. **83B**(1): p. 72-84.
123. Hauert, R., *A review of modified DLC coatings for biological applications.* Diamond and Related Materials, 2003. **12**(3–7): p. 583-589.
124. Cui, F.Z. and D.J. Li, *A review of investigations on biocompatibility of diamond-like carbon and carbon nitride films.* Surface and Coatings Technology, 2000. **131**(1–3): p. 481-487.
125. Ali, N., et al., *Human microvascular endothelial cell seeding on Cr-DLC thin films for heart valve applications.* Journal of Materials Engineering and Performance, 2006. **15**(2): p. 230-235.
126. Robertson, J., *Diamond-like amorphous carbon.* Materials Science and Engineering: R: Reports, 2002. **37**(4–6): p. 129-281.
127. McKenzie, D.R., *Tetrahedral bonding in amorphous carbon.* Reports on Progress in Physics, 1996. **59**(12): p. 1611.
128. Hynek Biederman, Y.O., *Plasma polymerization processes*. 1992: Elsevier.
129. Alakoski, E., et al., *Load-Bearing Biomedical Applications of Diamond-Like Carbon Coatings - Current Status.* The Open Orthopaedics Journal, 2008. **2**: p. 43-50.
130. McKenzie, D.R., et al., *Hydrogen-free amorphous carbon preparation and properties.* Diamond and Related Materials, 1994. **3**(4–6): p. 353-360.
131. Fallon, P.J., et al., *Properties of filtered-ion-beam-deposited diamondlike carbon as a function of ion energy.* Physical Review B, 1993. **48**(7): p. 4777-4782.

132. Ivanov-Omskii, V.I., A.V. Tolmatchev, and S.G. Yastrebov, *Optical properties of amorphous carbon films deposited by magnetron sputtering of graphite.* Semiconductors, 2001. **35**(2): p. 220-225.
133. Onoprienko, A.A. and I.B. Yanchuk, *Temperature dependence of the mechanical properties of amorphous carbon films deposited by magnetron sputtering.* Powder Metallurgy and Metal Ceramics, 2006. **45**(3-4): p. 190-195.
134. Wang, Y., et al., *Microstructure, mechanical and tribological properties of graphite-like amorphous carbon films prepared by unbalanced magnetron sputtering.* Surface and Coatings Technology, 2011. **205**(8–9): p. 3058-3065.
135. Shi, J.R., R. Ji, and S.N. Piramanayagam, *Corrosion performance of thin hydrogenated amorphous carbon films prepared by magnetron sputtering.* Diamond and Related Materials, 2007. **16**(9): p. 1716-1721.
136. Dai, H., et al., *Analysis of hydrogenated amorphous carbon films deposited by middle frequency pulsed unbalanced magnetron sputtering.* Journal of Non-Crystalline Solids, 2013. **363**(0): p. 77-83.
137. Romyani, G., J. Tapati, and R. Swati, *Transparent polymer and diamond-like hydrogenated amorphous carbon thin films by PECVD technique.* Journal of Physics D: Applied Physics, 2008. **41**(15): p. 155413.
138. Bruno, P., et al., *Mechanical properties of PECVD hydrogenated amorphous carbon coatings via nanoindentation and nanoscratching techniques.* Surface and Coatings Technology, 2004. **180–181**(0): p. 259-264.
139. Morshed, M.M., et al., *DLC films deposited by a neutral beam source: adhesion to biological implant metals.* Surface and Coatings Technology, 2003. **169–170**(0): p. 254-257.
140. Ma, W.J., et al., *DLC coatings: Effects of physical and chemical properties on biological response.* Biomaterials, 2007. **28**(9): p. 1620-1628.
141. Erdemir, A., et al., *Friction and wear performance of diamond-like carbon films grown in various source gas plasmas.* Surface and Coatings Technology, 1999. **120–121**(0): p. 589-593.
142. Z. M. Zeng, X.B.T., T. K. Kwok, B. Y. Tang, M. K. Fung and P. K. Chub, *Effects of plasma excitation power, sample bias, and duty cycle on the structure and surface properties of amorphous carbon thin films fabricated on AISI440 steel by plasma immersion ion implantation.* J. Vac. Sci. Technol. A, 2000. **18**(5): p. 2164.
143. Zhang, S., et al., *Residual stress characterization of diamond-like carbon coatings by an X-ray diffraction method.* Surface and Coatings Technology, 1999. **122**(2–3): p. 219-224.
144. Ward, L., et al., *The Effect of Bias Voltage and Gas Pressure on the Structure, Adhesion and Wear Behavior of Diamond Like Carbon (DLC) Coatings With Si Interlayers.* Coatings, 2014. **4**(2): p. 214-230.
145. Lousinian, S. and S. Logothetidis, *Optical properties of proteins and protein adsorption study.* Microelectronic Engineering, 2007. **84**(3): p. 479-485.
146. Yang, P., et al., *Activation of platelets adhered on amorphous hydrogenated carbon (a-C:H) films synthesized by plasma immersion ion implantation-deposition (PIII-D).* Biomaterials, 2003. **24**(17): p. 2821-2829.

147. McLaughlin, J.A. and P.D. Maguire, *Advances on the use of carbon based materials at the biological and surface interface for applications in medical implants.* Diamond and Related Materials, 2008. **17**(4–5): p. 873-877.
148. Kushner, V.V.a.M.J., *Scaling of hollow cathode magnetrons for ionized metal physical vapor deposition.* J. Vac. Sci. Technol. A, 2006. **A**(5).
149. D E Siegfried, D.C.a.D.G. *Reactive Cylindrical Magnetron Deposition of Titanium Nitride and Zirconium Nitride Films*. in *39th Annual Technical Conference Proceedings*. 1996.
150. Glocker, D.A. *Principles and Applications of Hollow Cathode Magnetron Sputtering Sources*. in *38th Annual Technical Conference Proceedings* 1995.
151. Azzi, M., et al., *Corrosion performance and mechanical stability of 316L/DLC coating system: Role of interlayers.* Surface and Coatings Technology, 2010. **204**(24): p. 3986-3994.
152. Chandra, L., et al., *The effect of exposure to biological fluids on the spallation resistance of diamond-like carbon coatings on metallic substrates.* Journal of Materials Science: Materials in Medicine, 1995. **6**(10): p. 581-589.
153. Shin, H.S., et al., *Biocompatible PEG Grafting on DLC-coated Nitinol Alloy for Vascular Stents.* Journal of Bioactive and Compatible Polymers, 2009. **24**(4): p. 316-328.
154. Kim, J.H., et al., *Comparison of diamond-like carbon-coated nitinol stents with or without polyethylene glycol grafting and uncoated nitinol stents in a canine iliac artery model.* The British Journal of Radiology, 2011. **84**(999): p. 210-215.
155. Kim, H.-J., et al., *Mechanical stability of the diamond-like carbon film on nitinol vascular stents under cyclic loading.* Thin Solid Films, 2008. **517**(3): p. 1146-1150.
156. Yin, Y., et al., *Acetylene plasma polymerized surfaces for covalent immobilization of dense bioactive protein monolayers.* Surface and Coatings Technology, 2009. **203**(10–11): p. 1310-1316.
157. Yin, Y., et al., *Covalently Bound Biomimetic Layers on Plasma Polymers with Graded Metallic Interfaces for in vivo Implants.* Plasma Processes and Polymers, 2009. **6**(10): p. 658-666.
158. Boufendi, L., et al., *Dusty plasma for nanotechnology.* Journal of Physics D-Applied Physics, 2011. **44**(17).
159. Bonitz, M., N.J.M. Horing, and P. Ludwig, *Introduction to complex plasmas*. Springer series on atomic, optical, and plasma physics,. 2010, Heidelberg ; New York: Springer. xvii, 447 p.
160. Kovacevic, E., et al., *A candidate analog for carbonaceous interstellar dust: Formation by reactive plasma polymerization.* Astrophysical Journal, 2005. **623**(1): p. 242-251.
161. Pendleton, Y.J., et al., *Near-Infrared Absorption-Spectroscopy of Interstellar Hydrocarbon Grains.* Astrophysical Journal, 1994. **437**(2): p. 683-696.
162. Pendleton, Y.J. and L.J. Allamandola, *The organic refractory material in the diffuse interstellar medium: Mid-infrared spectroscopic constraints.* Astrophysical Journal Supplement Series, 2002. **138**(1): p. 75-98.

163. Contreras, C.S. and F. Salama, *Laboratory Investigations of Polycyclic Aromatic Hydrocarbon Formation and Destruction in the Circumstellar Outflows of Carbon Stars.* Astrophysical Journal Supplement Series, 2013. **208**(1).
164. Eisberg, R.M. and R. Resnick, *Quantum physics of atoms, molecules, solids, nuclei, and particles*. 2nd ed. 1985, New York: Wiley.
165. Mavadat, M., et al., *Determination of ro-vibrational excitations of N 2 (B , v ') and N 2 (C , v ') states in N 2 microwave discharges using visible and IR spectroscopy.* Journal of Physics D: Applied Physics, 2011. **44**(15): p. 155207.
166. Gorbet, M.B. and M.V. Sefton, *Biomaterial-associated thrombosis: roles of coagulation factors, complement, platelets and leukocytes.* Biomaterials, 2004. **25**(26): p. 5681-703.
167. Lau, A.K., et al., *Probucol promotes functional reendothelialization in balloon-injured rabbit aortas.* Circulation, 2003. **107**(15): p. 2031-6.
168. Yu, Y., et al., *Bioengineering stents with proactive biocompatibility.* Interventional Cardiology, 2015. **7**(6): p. 571-584.
169. Mauri, L., et al., *Twelve or 30 months of dual antiplatelet therapy after drug-eluting stents.* N Engl J Med, 2014. **371**(23): p. 2155-66.
170. Liu, C.L., P.K. Chu, and D.Z. Yang, *In vitro evaluation of diamond-like carbon coatings with a Si/SiCx interlayer on surgical NiTi alloy.* Nuclear Instruments and Methods in Physics Research Section B: Beam Interactions with Materials and Atoms, 2007. **257**(1–2): p. 132-135.
171. Wei, C. and J.-Y. Yen, *Effect of film thickness and interlayer on the adhesion strength of diamond like carbon films on different substrates.* Diamond and Related Materials, 2007. **16**(4–7): p. 1325-1330.
172. Wei, C., Y.-S. Wang, and F.-C. Tai, *The role of metal interlayer on thermal stress, film structure, wettability and hydrogen content for diamond like carbon films on different substrate.* Diamond and Related Materials, 2009. **18**(2–3): p. 407-412.
173. Falub, C.V., et al., *A quantitative in vitro method to predict the adhesion lifetime of diamond-like carbon thin films on biomedical implants.* Acta Biomaterialia, 2009. **5**(8): p. 3086-3097.
174. Hegemann, D., et al., *Macroscopic Description of Plasma Polymerization.* Plasma Processes and Polymers, 2007. **4**(3): p. 229-238.
175. Hegemann, D., et al., *Growth Mechanism of Oxygen-Containing Functional Plasma Polymers.* Plasma Processes and Polymers, 2010. **7**(11): p. 889-898.
176. Sharma, A.K., *Reproducibility in Glow-Discharge Polymerization.* Journal of Polymer Science Part a-Polymer Chemistry, 1986. **24**(11): p. 3077-3087.
177. Myung, S. and H. Choi, *Chemical structure and surface morphology of plasma polymerized-allylamine film.* Korean Journal of Chemical Engineering, 2006. **23**(3): p. 505-511.
178. Denis, L., et al., *Synthesis of Allylamine Plasma Polymer Films: Correlation between Plasma Diagnostic and Film Characteristics.* Plasma Processes and Polymers, 2009. **6**(3): p. 199-208.
179. Thierry, B., et al., *Theoretical background of optical emission spectroscopy for analysis of atmospheric pressure plasmas.* Plasma Sources Science and Technology, 2015. **24**(6): p. 064003.

180. Aragón, C. and J.A. Aguilera, *Characterization of laser induced plasmas by optical emission spectroscopy: A review of experiments and methods.* Spectrochimica Acta Part B: Atomic Spectroscopy, 2008. **63**(9): p. 893-916.
181. Oliver, W.C. and G.M. Pharr, *Measurement of hardness and elastic modulus by instrumented indentation: Advances in understanding and refinements to methodology.* Journal of Materials Research, 2004. **19**(01): p. 3-20.
182. Jamesh, M.I., et al., *Graded metal carbon protein binding films prepared by hybrid cathodic arc — Glow discharge plasma assisted chemical vapor deposition.* Surface and Coatings Technology, 2015. **265**: p. 222-234.
183. Hegemann, D., *Influence of pressure on an asymmetric, radio frequency discharge with methane.* Thin Solid Films, 2006. **515**(4): p. 2173-2178.
184. Hegemann, D. and M.-M. Hossain, *Influence of Non-Polymerizable Gases Added During Plasma Polymerization.* Plasma Processes and Polymers, 2005. **2**(7): p. 554-562.
185. Yasuda, H. and C.E. Lamaze, *Polymerization in an electrodeless glow discharge. II. Olefinic monomers.* Journal of Applied Polymer Science, 1973. **17**(5): p. 1519-1531.
186. Alves, L.L., et al., *Capacitively coupled radio-frequency discharges in nitrogen at low pressures.* Plasma Sources Science and Technology, 2012. **21**(4): p. 045008.
187. Alves, L.L. and L. Marques, *Fluid modelling of capacitively coupled radio-frequency discharges: a review.* Plasma Physics and Controlled Fusion, 2012. **54**(12): p. 124012.
188. Sarra-Bournet, C., et al., *Effect of C2H4/N2 Ratio in an Atmospheric Pressure Dielectric Barrier Discharge on the Plasma Deposition of Hydrogenated Amorphous Carbon-Nitride Films (a-C:N:H).* Plasma Chemistry and Plasma Processing, 2010. **30**(2): p. 213-239.
189. Dilecce, G., et al., *CN(B 2 Σ +) formation and emission in a N 2 –CH 4 atmospheric pressure dielectric barrier discharge.* Plasma Sources Science and Technology, 2009. **18**(1): p. 015010.
190. Iwai, T., M.I. Savadatti, and H.P. Broida, *Mechanisms of Populating Electronically Excited CN in Active Nitrogen Flames.* The Journal of Chemical Physics, 1967. **47**(10): p. 3861-3874.
191. Durrant, S.F., E.C. Rangel, and M.A. Bica de Moraes, *Optical emission study of reaction mechanisms in the deposition of nitrogen-containing amorphous hydrogenated carbon films.* Journal of Vacuum Science & Technology A, 1995. **13**(4): p. 1901-1906.
192. Hammer, P. and W. Gissler, *Chemical sputtering of carbon films by low energy N2+ ion bombardment.* Diamond and Related Materials, 1996. **5**(10): p. 1152-1158.
193. Briggs, D., *Surface analysis of polymers by XPS and static SIMS*. Digitally printed 1st pbk. ed. Cambridge solid state science series. 2005, Cambridge ; New York: Cambridge University Press. xiv, 198 p.
194. Marton, D., et al., *Carbon Nitride Deposited Using Energetic Species: A Two-Phase System.* Physical Review Letters, 1994. **73**(1): p. 118-121.
195. Ronning, C., et al., *Carbon nitride deposited using energetic species: A review on XPS studies.* Physical Review B, 1998. **58**(4): p. 2207-2215.

196. Muhl, S. and J.M. Méndez, *A review of the preparation of carbon nitride films.* Diamond and Related Materials, 1999. **8**(10): p. 1809-1830.
197. Snis, A. and S.F. Matar, *Electronic density of states, $1s$ core-level shifts, and core ionization energies of graphite, diamond, ${\mathrm{C}}_{3}{\mathrm{N}}_{4}$ phases, and graphitic ${\mathrm{C}}_{11}{\mathrm{N}}_{4}$.* Physical Review B, 1999. **60**(15): p. 10855-10863.
198. Johansson, Å. and S. Stafström, *A Δ-self-consistent-field study of the nitrogen 1s binding energies in carbon nitrides.* The Journal of Chemical Physics, 1999. **111**(7): p. 3203-3208.
199. Rodil, S.E., et al., *Nitrogen Incorporation into Tetrahedral Hydrogenated Amorphous Carbon.* physica status solidi (a), 1999. **174**(1): p. 25-37.
200. Vinu, A., et al., *Preparation and Characterization of Well-Ordered Hexagonal Mesoporous Carbon Nitride.* Advanced Materials, 2005. **17**(13): p. 1648-1652.
201. Haupt, M., J. Barz, and C. Oehr, *Creation and Recombination of Free Radicals in Fluorocarbon Plasma Polymers: An Electron Spin Resonance Study.* Plasma Processes and Polymers, 2008. **5**(1): p. 33-43.
202. Ershov, S., et al., *Free Radical Generation and Concentration in a Plasma Polymer: The Effect of Aromaticity.* ACS Applied Materials & Interfaces, 2014. **6**(15): p. 12395-12405.
203. Gammon, W.J., et al., *Hard and elastic amorphous carbon nitride thin films studied by ${}^{13}\mathrm{C}$ nuclear magnetic resonance spectroscopy.* Physical Review B, 2002. **66**(15): p. 153402.
204. Thornton, J.A., *Influence of apparatus geometry and deposition conditions on the structure and topography of thick sputtered coatings.* Journal of Vacuum Science & Technology, 1974. **11**(4): p. 666-670.
205. Virmani, R., et al., *Drug eluting stents: are human and animal studies comparable?* Heart, 2003. **89**(2): p. 133-8.
206. Joner, M., et al., *Endothelial Cell Recovery Between Comparator Polymer-Based Drug-Eluting Stents.* Journal of the American College of Cardiology, 2008. **52**(5): p. 333-342.
207. Ali, Z.A., et al., *Increased in-stent stenosis in ApoE knockout mice: insights from a novel mouse model of balloon angioplasty and stenting.* Arterioscler Thromb Vasc Biol, 2007. **27**(4): p. 833-40.
208. Chen, J.Y., et al., *Antithrombogenic investigation of surface energy and optical bandgap and hemocompatibility mechanism of Ti(Ta+5)O2 thin films.* Biomaterials, 2002. **23**(12): p. 2545-2552.
209. Gutmann F, K.H., *Modern Bioelectrochemistry*. 1986: New York: Plenum Press.
210. Logothetidis, S., et al., *Haemocompatibility studies on carbon-based thin films by ellipsometry.* Thin Solid Films, 2005. **482**(1–2): p. 126-132.
211. Lousinian, S. and S. Logothetidis, *In-situ and real-time protein adsorption study by Spectroscopic Ellipsometry.* Thin Solid Films, 2008. **516**(22): p. 8002-8008.
212. Berlind, T., et al., *Protein adsorption on thin films of carbon and carbon nitride monitored with in situ ellipsometry.* Acta Biomaterialia, 2011. **7**(3): p. 1369-1378.
213. Bilek, M.M.M., et al., *Depth-Resolved Structural and Compositional Characterization of Ion-Implanted Polystyrene that Enables Direct Covalent*

Immobilization of Biomolecules. The Journal of Physical Chemistry C, 2015. **119**(29): p. 16793-16803.
214. Bax, D.V., et al., *Linker-free covalent attachment of the extracellular matrix protein tropoelastin to a polymer surface for directed cell spreading.* Acta Biomaterialia, 2009. **5**(9): p. 3371-3381.
215. Bax, D.V., et al., *Binding of the cell adhesive protein tropoelastin to PTFE through plasma immersion ion implantation treatment.* Biomaterials, 2011. **32**(22): p. 5100-5111.
216. Hiob, M.A., et al., *The use of plasma-activated covalent attachment of early domains of tropoelastin to enhance vascular compatibility of surfaces.* Biomaterials, 2013. **34**(31): p. 7584-7591.
217. Wise, S.G., et al., *TCT-433 Plasmin Immobilization for Reduced Thrombogenicity of Metallic Implants.* Journal of the American College of Cardiology, 2014. **64**(11, Supplement): p. B127.
218. Tanaka, K.A., N.S. Key, and J.H. Levy, *Blood coagulation: hemostasis and thrombin regulation.* Anesth Analg, 2009. **108**(5): p. 1433-46.
219. Waterhouse, A., *Bioengineering a coronary stent with covalently immobilised tropoelastin*, in *School of Molecular Bioscience*. 2011, University of Sydney.
220. Ali, Z.A., et al., *Increased In-Stent Stenosis in ApoE Knockout Mice. Insights from a Novel Mouse Model of Balloon Angioplasty and Stenting.* Arteriosclerosis, Thrombosis, and Vascular Biology, 2007.
221. Wise, S.G., et al., *Tropoelastin: A versatile, bioactive assembly module.* Acta Biomaterialia, 2014. **10**(4): p. 1532-1541.
222. Leslie, D.C., et al., *A bioinspired omniphobic surface coating on medical devices prevents thrombosis and biofouling.* Nat Biotech, 2014. **32**(11): p. 1134-1140.
223. Akhavan, B., S.G. Wise, and M.M. Bilek, *Substrate-Regulated Growth of Plasma-Polymerized Films on Carbide-Forming Metals.* Langmuir, 2016.
224. Vandenberg, E., et al., *Protein immobilization of 3-aminopropyl triethoxy silaneglutaraldehyde surfaces: Characterization by detergent washing.* Journal of Colloid and Interface Science, 1991. **143**(2): p. 327-335.
225. Bilek, M. and D. McKenzie, *Plasma modified surfaces for covalent immobilization of functional biomolecules in the absence of chemical linkers: towards better biosensors and a new generation of medical implants.* Biophysical Reviews, 2010. **2**(2): p. 55-65.
226. Dyksterhuis, L.B., et al., *Tropoelastin as a thermodynamically unfolded premolten globule protein: The effect of trimethylamine N-oxide on structure and coacervation.* Archives of Biochemistry and Biophysics, 2009. **487**(2): p. 79-84.
227. Wakelin, E.A., et al., *Bio-Activation of Polyether Ether Ketone Using Plasma Immersion Ion Implantation: A Kinetic Model.* Plasma Processes and Polymers, 2015. **12**(2): p. 180-193.
228. Baier, R.E. and R.C. Dutton, *Initial events in interactions of blood with a foreign surface.* Journal of Biomedical Materials Research, 1969. **3**(1): p. 191-206.
229. Palmaz, J.C., *Intravascular stents: tissue-stent interactions and design considerations.* American Journal of Roentgenology, 1993. **160**(3): p. 613-618.

230. Seeger, J.M., et al., *Hydrophilic surface modification of metallic endoluminal stents.* Journal of Vascular Surgery, 1995. **22**(3): p. 327-336.
231. Wakelin, E.A., et al., *Mechanical Properties of Plasma Immersion Ion Implanted PEEK for Bioactivation of Medical Devices.* ACS Applied Materials & Interfaces, 2015. **7**(41): p. 23029-23040.
232. Yasuda, H.K., *PLASMA POLYMERIZATION*. 2012: Elsevier Science.
233. Winter, J., et al., *Dust formation in Ar/CH 4 and Ar/C 2 H 2 plasmas.* Plasma Sources Science and Technology, 2009. **18**(3): p. 034010.
234. Anderson, H.M., et al., *Particles in C 2 F 6 -CHF 3 and CF 4 -CHF 3 etching plasmas.* Plasma Sources Science and Technology, 1994. **3**(3): p. 302.
235. Roth, C., et al., *Nanoparticle Synthesis and Growth in a Continuous Plasma Reactor from Organosilicon Precursors.* Plasma Processes and Polymers, 2012. **9**(2): p. 119-134.
236. Berndt, J., et al., *Some Aspects of Reactive Complex Plasmas.* Contributions to Plasma Physics, 2009. **49**(3): p. 107-133.
237. Bouchoule, A., *Dusty Plasmas.* Physics World, 1993. **6**(8): p. 47-51.
238. Boufendi, L. and A. Bouchoule, *Industrial developments of scientific insights in dusty plasmas.* Plasma Sources Science & Technology, 2002. **11**(3a): p. A211-A218.
239. Hinz, A.M., et al., *Versatile particle collection concept for correlation of particle growth and discharge parameters in dusty plasmas.* Journal of Physics D: Applied Physics, 2015. **48**(5): p. 055203.
240. Winter, J., V.E. Fortov, and A.P. Nefedov, *Radioactive dust levitation and its consequences for fusion devices.* Journal of Nuclear Materials, 2001. **290**(Supplement C): p. 509-512.
241. Kovačević, E., et al., *Formation and material analysis of plasma polymerized carbon nitride nanoparticles.* Journal of Applied Physics, 2009. **105**(10): p. 104910.
242. Ch, D., et al., *Investigations of CH 4 , C 2 H 2 and C 2 H 4 dusty RF plasmas by means of FTIR absorption spectroscopy and mass spectrometry.* Journal of Physics D: Applied Physics, 1999. **32**(15): p. 1876.
243. Kovačević, E., et al., *Infrared fingerprints and periodic formation of nanoparticles in Ar/C2H2 plasmas.* Journal of Applied Physics, 2003. **93**(5): p. 2924-2930.
244. Stefanovic, I., et al., *Hα emission in the presence of dust in an Ar-C 2 H 2 radio-frequency discharge.* New Journal of Physics, 2003. **5**(1): p. 39.
245. Yu, A.M., M.A. Olevanov, and T.V. Rakhimova, *Dust particle coagulation mechanism in low-pressure plasma: rapid growth and saturation stage modeling.* Plasma Sources Science and Technology, 2008. **17**(1): p. 015013.
246. Hegemann, D., C. Oehr, and A. Fischer, *Design of functional coatings.* Journal of Vacuum Science & Technology A: Vacuum, Surfaces, and Films, 2005. **23**(1): p. 5-11.
247. Bobo, D., et al., *Nanoparticle-Based Medicines: A Review of FDA-Approved Materials and Clinical Trials to Date.* Pharm Res, 2016. **33**(10): p. 2373-87.
248. Wilhelm, S., et al., *Analysis of nanoparticle delivery to tumours.* Nature Reviews Materials, 2016. **1**(5).
249. Bilan, R., et al., *Quantum dot surface chemistry and functionalization for cell targeting and imaging.* Bioconjug Chem, 2015. **26**(4): p. 609-24.

250. Bohara, R.A., N.D. Thorat, and S.H. Pawar, *Role of functionalization: strategies to explore potential nano-bio applications of magnetic nanoparticles.* RSC Advances, 2016. **6**(50): p. 43989-44012.
251. Xing, P. and Y. Zhao, *Multifunctional Nanoparticles Self-Assembled from Small Organic Building Blocks for Biomedicine.* Adv Mater, 2016. **28**(34): p. 7304-39.
252. Wang, H., et al., *A biomimetic hybrid nanoplatform for encapsulation and precisely controlled delivery of theranostic agents.* 2015. **6**: p. 10081.
253. Mochalin, V.N., et al., *The properties and applications of nanodiamonds.* Nat Nano, 2012. **7**(1): p. 11-23.
254. Lim, S.Y., W. Shen, and Z. Gao, *Carbon quantum dots and their applications.* Chemical Society Reviews, 2015. **44**(1): p. 362-381.
255. Deerinck, T.J., Bushong, E. A., Thor, A. & Ellisman, M. H., *NCMIR Methods for 3D EM: A new protocol for preparation of biological specimens for serial block face scanning electron microscopy.* National Center for Microscopy and Imaging Research, 2010.
256. Xia, Y., et al., *Self-assembly of self-limiting monodisperse supraparticles from polydisperse nanoparticles.* Nat Nano, 2011. **6**(9): p. 580-587.
257. Sharma, A., et al., *Origin of Excitation Dependent Fluorescence in Carbon Nanodots.* The Journal of Physical Chemistry Letters, 2016. **7**(18): p. 3695-3702.
258. Cushing, S.K., et al., *Origin of Strong Excitation Wavelength Dependent Fluorescence of Graphene Oxide.* ACS Nano, 2014. **8**(1): p. 1002-1013.
259. Hsiao, W.W.-W., et al., *Fluorescent Nanodiamond: A Versatile Tool for Long-Term Cell Tracking, Super-Resolution Imaging, and Nanoscale Temperature Sensing.* Accounts of Chemical Research, 2016. **49**(3): p. 400-407.
260. Xiao, J., et al., *Fluorescence Origin of Nanodiamonds.* The Journal of Physical Chemistry C, 2015. **119**(4): p. 2239-2248.
261. Bilek, M.M.M., et al., *Free radical functionalization of surfaces to prevent adverse responses to biomedical devices.* Proceedings of the National Academy of Sciences, 2011. **108**(35): p. 14405-14410.
262. Sheng, Z., et al., *Indocyanine Green Nanoparticles for Theranostic Applications.* Nano-Micro Letters, 2013. **5**(3): p. 145-150.
263. Lajunen, T., et al., *Indocyanine Green-Loaded Liposomes for Light-Triggered Drug Release.* Molecular Pharmaceutics, 2016. **13**(6): p. 2095-2107.
264. Niu, C., et al., *Near-infrared induced phase-shifted ICG/Fe3O4 loaded PLGA nanoparticles for photothermal tumor ablation.* Scientific Reports, 2017. **7**(1): p. 5490.
265. Zheng, X., et al., *Indocyanine Green-Containing Nanostructure as Near Infrared Dual-Functional Targeting Probes for Optical Imaging and Photothermal Therapy.* Molecular Pharmaceutics, 2011. **8**(2): p. 447-456.
266. Zheng, X., et al., *Enhanced Tumor Treatment Using Biofunctional Indocyanine Green-Containing Nanostructure by Intratumoral or Intravenous Injection.* Molecular Pharmaceutics, 2012. **9**(3): p. 514-522.
267. Nakatsu, T., et al., *Structural basis for the spectral difference in luciferase bioluminescence.* Nature, 2006. **440**(7082): p. 372-376.

268. Conde, J., et al., *Design of Multifunctional Gold Nanoparticles for In Vitro and In Vivo Gene Silencing.* ACS Nano, 2012. **6**(9): p. 8316-8324.
269. Tonga, G.Y., K. Saha, and V.M. Rotello, *25th Anniversary Article: Interfacing Nanoparticles and Biology: New Strategies for Biomedicine.* Advanced Materials, 2014. **26**(3): p. 359-370.
270. Verma, A. and F. Stellacci, *Effect of Surface Properties on Nanoparticle–Cell Interactions.* Small, 2010. **6**(1): p. 12-21.
271. Barua, S. and S. Mitragotri, *Challenges associated with penetration of nanoparticles across cell and tissue barriers: A review of current status and future prospects.* Nano Today, 2014. **9**(2): p. 223-243.
272. Fleischer, C.C. and C.K. Payne, *Nanoparticle–Cell Interactions: Molecular Structure of the Protein Corona and Cellular Outcomes.* Accounts of Chemical Research, 2014. **47**(8): p. 2651-2659.
273. Tiwari, P.M., et al., *Enhanced intracellular translocation and biodistribution of gold nanoparticles functionalized with a cell-penetrating peptide (VG-21) from vesicular stomatitis virus.* Biomaterials, 2014. **35**(35): p. 9484-9494.
274. Steinbach, J.M., Y.-E. Seo, and W.M. Saltzman, *Cell penetrating peptide-modified poly(lactic-co-glycolic acid) nanoparticles with enhanced cell internalization.* Acta Biomaterialia, 2016. **30**(Supplement C): p. 49-61.
275. Chu, Z., et al., *Rapid endosomal escape of prickly nanodiamonds: implications for gene delivery.* 2015. **5**: p. 11661.
276. Chu, Z., et al., *Unambiguous observation of shape effects on cellular fate of nanoparticles.* 2014. **4**: p. 4495.
277. PANYAM, J., et al., *Rapid endo-lysosomal escape of poly(dl-lactide-co-glycolide) nanoparticles: implications for drug and gene delivery.* The FASEB Journal, 2002. **16**(10): p. 1217-1226.
278. Chuang, S.-M., et al., *Extensive evaluations of the cytotoxic effects of gold nanoparticles.* Biochimica et Biophysica Acta (BBA) - General Subjects, 2013. **1830**(10): p. 4960-4973.
279. Lee, Y.-H., et al., *Cytotoxicity, oxidative stress, apoptosis and the autophagic effects of silver nanoparticles in mouse embryonic fibroblasts.* Biomaterials, 2014. **35**(16): p. 4706-4715.
280. Luo, M., et al., *Reducing ZnO nanoparticle cytotoxicity by surface modification.* Nanoscale, 2014. **6**(11): p. 5791-5798.
281. Wong, P.T. and S.K. Choi, *Mechanisms of Drug Release in Nanotherapeutic Delivery Systems.* Chemical Reviews, 2015. **115**(9): p. 3388-3432.